THE D.C. DISC-ARMATURE ELECTRIC MOTOR

by

P. Campbell, B.Sc.(Warwick), M.A.(Cambridge).

A thesis submitted for the degree of Doctor of Philosophy

to

The University of Warwick,

based upon research conducted in

the Department of Engineering.

December 1974.

THE D.C. DISC-ARMATURE ELECTRIC MOTOR

by

P. Campbell, B.Sc.(Warwick), M.A.(Cambridge).

A thesis submitted for the degree of Doctor of Philosophy

to

The University of Warwick,

based upon research conducted in

the Department of Engineering.

December 1974.

CONTENTS.

CONTENTS.

LIST OF TABLES.

LIST OF FIGURES.

LIST OF FIGURES.

ACKNOWLEDGEMENTS.

The work described in this thesis was carried out over a period of three years at the University of Warwick. There are many people there, in the Engineering Department, who have assisted and contributed in a number of ways, and it is difficult to list them all here. I must thank them all, though, for a most enjoyable and rewarding time.

In particular, I am indebted to those in the University Workshops, for their patience, skill, and endurance in producing the hardware for my project. Also, my thanks are extended to my supervisor, Mr. A.E. Corbett, and to all my colleagues for helpful discussions and advice. There are many individuals and organisations outside the university who have spent much time considering my problems, allowing me the use of their facilities, or giving essential equipment. To them I am grateful, as also to the Science Research Council, for supporting me for those three years.

For the past year I have been on the academic staff of the Cambridge University Engineering Department, and I am most grateful for their tolerance while I have been writing this thesis. Finally, I must thank my wife, Caroline, without whose support this work would have taken much longer to complete.

DECLARATION.

Most of the work described in this thesis was the sole responsibility of the author. The exceptions are some past or collaborative work, and these are made clear in the text by the use of references. A number of articles and papers have been published

on this research (References 19 to 31). No reprints are submitted, though, since all the relevant features are included in the text of the thesis.

Peter Campbell

SUMMARY

This thesis develops the theory relating to the d.c. Disc-Armature electric motor, and uses two particular machines as examples.

Considerable importance is attached to the calculation of the field due to the permanent magnet poles, and both direct and iterative methods are employed. For the determination of e.m.f. and torque in the axial-field machine, the flux density at any point is inseparable from its radius, and a "moment of flux density" is defined to account for this. By considering the individual armature conductors, the fluctuations of e.m.f. and torque during rotation are found. These calculations are used to select the optimum dimensions for the machine and its components, for particular design criteria.

The design of the machine is discussed, and certain problems receive particular attention. These include the realisation of the full magnetic field, and the materials for a rotating flux return ring. For the latter, iron powder compacts are found to be convenient, having the lowest power losses.

The fan motor incorporates such a return ring, and its performance agrees well with the theoretical predictions. For the high coercivity magnets used, the field calculations are also quite accurate. The wheel motor's operation reveals a peculiarity of the commutation in this type of machine, and indicates an important area for further study.

SUMMARY

This thesis develops the theory relating to the d.c. Disc-Armature electric motor, and uses two particular machines as examples.

Considerable importance is attached to the calculation of the field due to the permanent magnet poles, and both direct and iterative methods are employed. For the determination of e.m.f. and torque in the axial-field machine, the flux density at any point is inseparable from its radius, and a "moment of flux density" is defined to account for this. By considering the individual armature conductors, the fluctuations of e.m.f. and torque during rotation are found. These calculations are used to select the optimum dimensions for the machine and its components, for particular design criteria.

The design of the machine is discussed, and certain problems receive particular attention. These include the realisation of the full magnetic field, and the materials for a rotating flux return ring. For the latter, iron powder compacts are found to be convenient, having the lowest power losses.

The fan motor incorporates such a return ring, and its performance agrees well with the theoretical predictions. For the high coercivity magnets used, the field calculations are also quite accurate. The wheel motor's operation reveals a peculiarity of the commutation in this type of machine, and indicates an important area for further study.

LIST OF PRINCIPAL SYMBOLS.

a	number of parallel armature paths.
c	clearance between armature and main pole face.
d	conductor overall diameter.
d_c	diameter of copper in conductor.
d_1, d_2	inner & outer diameters of active length of conductors.
$e_{i,j}$	e.m.f. in conductor element.
e_j	e.m.f. in conductor at angular position j.
i,j,k	subscripts describing radial, angular, and axial positions.
l	length of an active conductor.
l_c	total length of conductor in armature.
l_g	air gap length.
l_m	magnet length.
n	number of conductor elements of length δr in active length ; number of conductor layers.
n, n'	normals to magnet surface.
p	number of poles.
p'	brush pressure.
r_i	radius corresponding to i.
t	thickness of armature disc.
v	linear velocity of conductor at its average radius.
v_c	linear velocity of commutator.
w	conductor angular velocity.
A_b	total brush contact area.
A_c	specific electric loading.
A_{pp}	active area of pole pitch.
$\underline{B}$	flux density.

LIST OF PRINCIPAL SYMBOLS.

a	number of parallel armature paths.
c	clearance between armature and main pole face.
d	conductor overall diameter.
d_c	diameter of copper in conductor.
d_1, d_2	inner & outer diameters of active length of conductors.
$e_{i,j}$	e.m.f. in conductor element.
e_j	e.m.f. in conductor at angular position j.
i,j,k	subscripts describing radial, angular, and axial positions.
l	length of an active conductor.
l_c	total length of conductor in armature.
l_g	air gap length.
l_m	magnet length.
n	number of conductor elements of length δr in active length ; number of conductor layers.
n, n'	normals to magnet surface.
p	number of poles.
p'	brush pressure.
r_i	radius corresponding to i.
t	thickness of armature disc.
v	linear velocity of conductor at its average radius.
v_c	linear velocity of commutator.
w	conductor angular velocity.
A_b	total brush contact area.
A_c	specific electric loading.
A_{pp}	active area of pole pitch.
$\underline{B}$	flux density.

$\overline{B}$	specific magnetic loading.
$B_{i,j}$	flux density at point i,j.
B_j	flux density at angular position j.
B_m	magnet flux density.
B_w	angular pitch of brush.
B_x	flux density in axial direction.
C_l	number of conductors/layer.
E	total armature e.m.f.
E_c	average conductor e.m.f.
H	magnetising force.
H_g	magnetising force in the air gap.
H_m	magnetising force of magnet.
H_x	magnetising force in axial direction.
I	armature current.
I_c	conductor current.
J	current density.
J_c	conductor current density.
M	intrinsic magnetisation.
M_s	pole strength on magnet face.
N	rotational speed.
$\overline{P}$	moment of flux density.
$\overline{P}_j$	moment of flux density at angular position j.
Q	total I^2R heat in armature.
Q_c	I^2R heat in conductor.
R, R_a	armature resistance.
R_1, R_2	inner and outer radii of active length of conductors.

$\overline{B}$	specific magnetic loading.
$B_{i,j}$	flux density at point i,j.
B_j	flux density at angular position j.
B_m	magnet flux density.
B_w	angular pitch of brush.
B_x	flux density in axial direction.
C_1	number of conductors/layer.
E	total armature e.m.f.
E_c	average conductor e.m.f.
H	magnetising force.
H_g	magnetising force in the air gap.
H_m	magnetising force of magnet.
H_x	magnetising force in axial direction.
I	armature current.
I_c	conductor current.
J	current density.
J_c	conductor current density.
M	intrinsic magnetisation.
M_s	pole strength on magnet face.
N	rotational speed.
$\overline{P}$	moment of flux density.
$\overline{P}_j$	moment of flux density at angular position j.
Q	total I^2R heat in armature.
Q_c	I^2R heat in conductor.
R, R_a	armature resistance.
R_1, R_2	inner and outer radii of active length of conductors.

S_w angular pitch of commutator segment.

T armature torque.

T' output torque.

T_j armature torque at angular position j.

V_c copper volume.

V_m magnet volume.

Z total number of armature conductors.

Z_p number of conductors in winding path.

Z_s number of conductors in series in armature.

α pole arc.

α' pole arc/pole pitch ratio.

δ displacement angle of conductors from radial line.

τ pole pitch.

ϕ total flux per pole.

$\phi_{i,j}$ flux at point i,j.

ϕ_j flux over active length at angular position j.

ψ magnetic potential.

1: INTRODUCTION.

On the 8th. of May, 1967, an application was made to patent the design of a new type of electric motor (Reference 1). The University of Warwick, and the author's supervisor, were involved in the formulation of that patent. It stated that the invention was "particularly suitable for the direct driving of the wheel of an electrically powered road vehicle".

The most novel feature of this motor (Figure 1.1) is its armature. The active conductors run radially from the axis of the machine, so that an axial field system is required. The coils are connected as a double layer winding, the complete armature being disc-shaped. This assembly is made possible by bending up the ends of the coils, so that they no longer lie in the plane of the disc. One side of each coil is longer than the other, by an amount that makes it possible for the end-windings to nest closely together (Figure 1.2). Finally, the winding is connected to the commutator, and the complete armature is encapsulated in epoxy resin, giving it mechanical strength.

The axial field is provided by permanent magnets, located to one side of the armature disc. They are bonded to a mild steel ring, adjacent poles having opposite directions of magnetisation. The magnetic circuit is completed on the remote side of the armature disc by another stationary mild steel ring.

The first application of the Disc-Armature motor was two years after its invention, when it was used to propel an electric lawn-mower. The test results on this machine (Reference 2) are shown in Figure 1.3. When delivering its normal output power of 1¼ H.P., the efficiency of 76% is rather disappointing. Permanent magnets require no magnetising current during motor operation, and the

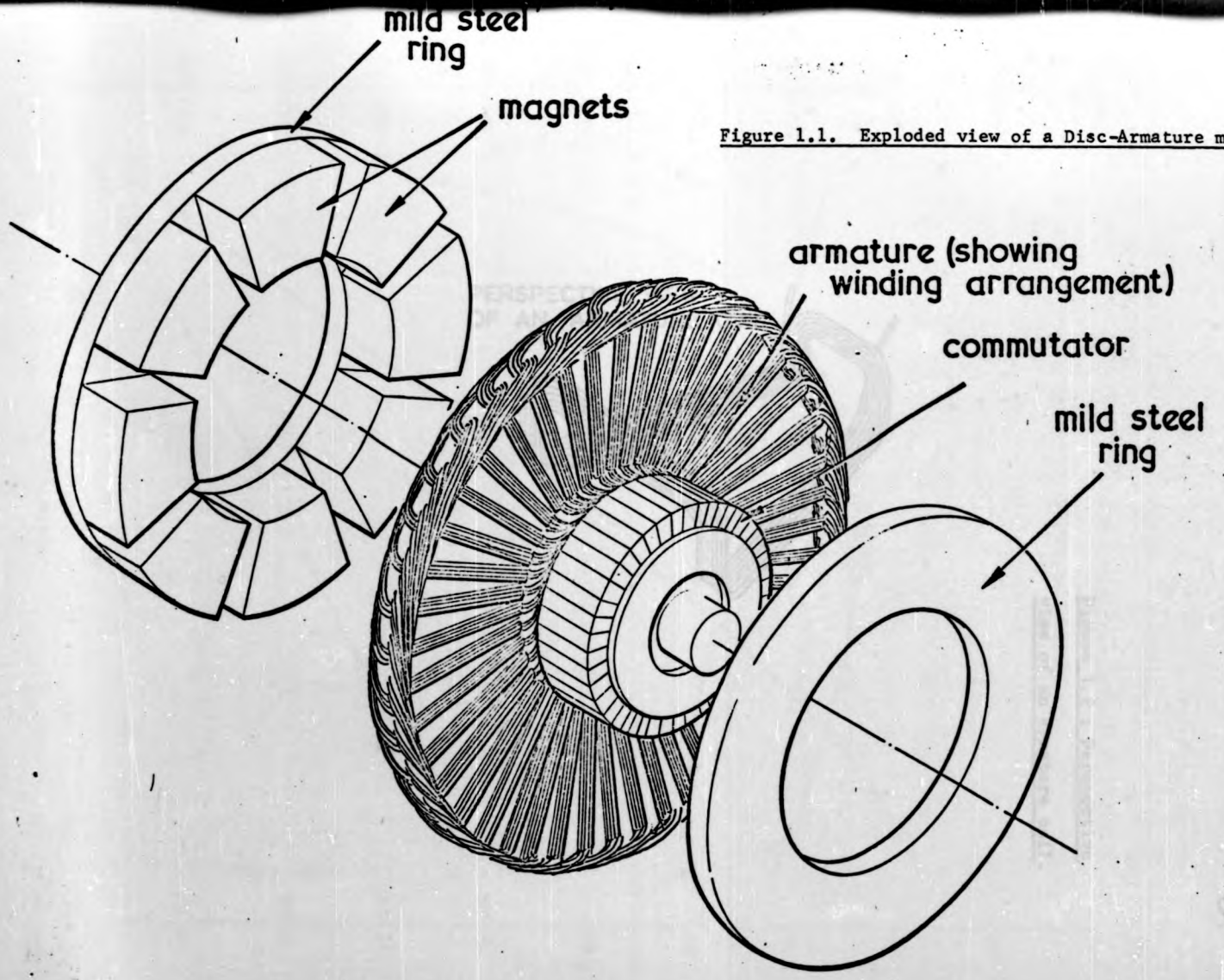

Figure 1.1. Exploded view of a Disc-Armature motor.

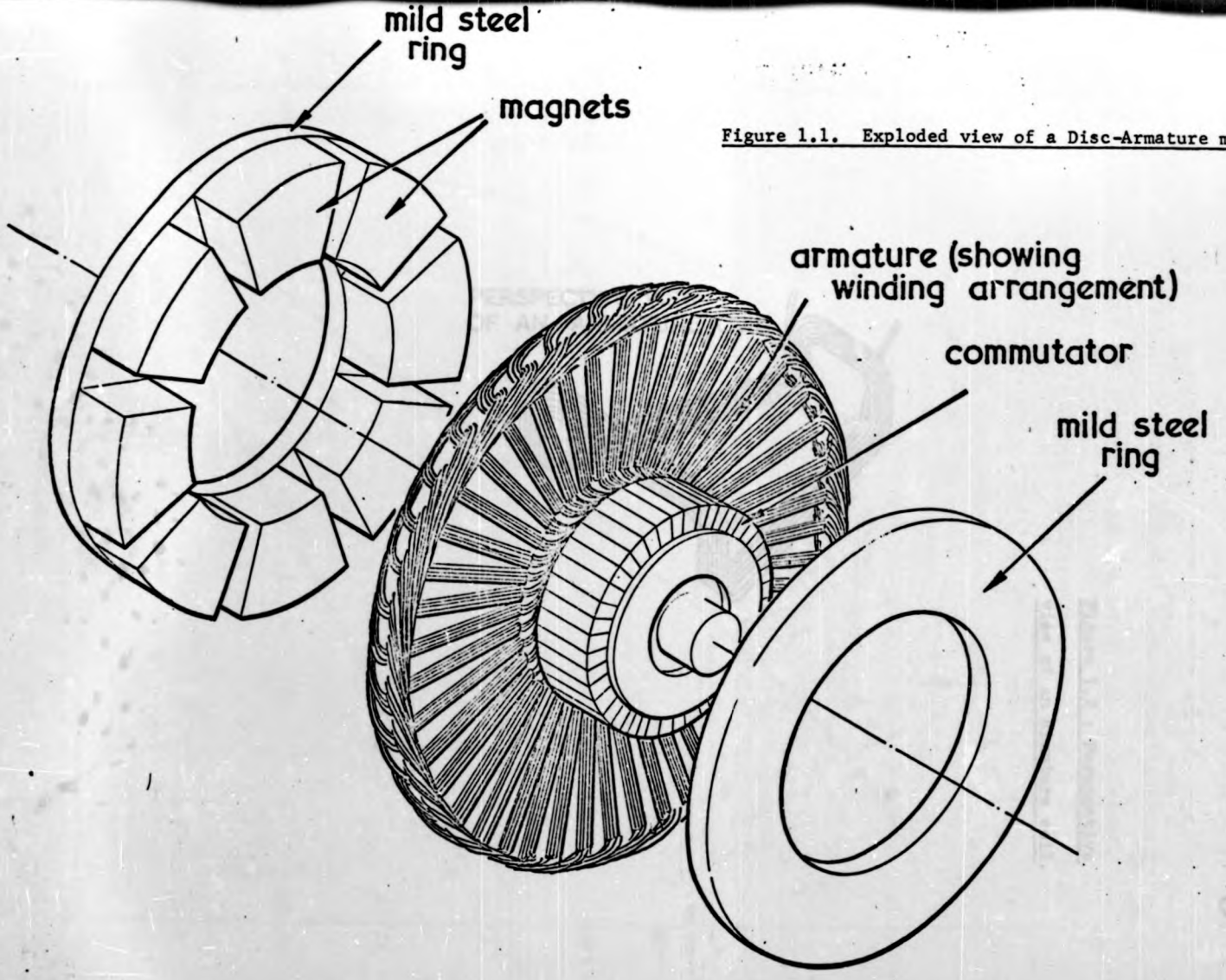

Figure 1.1. Exploded view of a Disc-Armature motor.

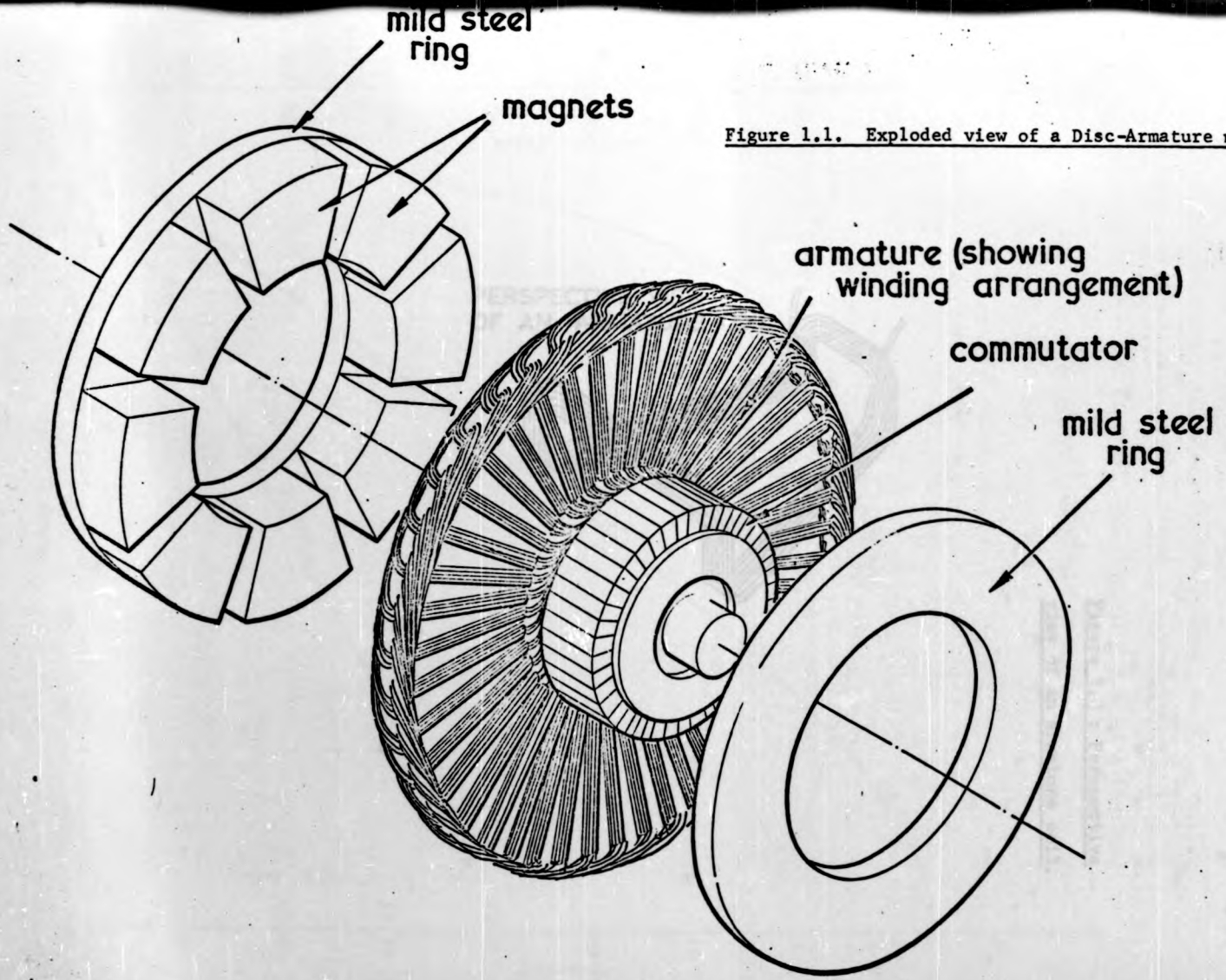

Figure 1.1. Exploded view of a Disc-Armature motor.

Figure 1.2 : Perspective view of an armature coil.

Figure 1.3: Performance curves of the 12V., 1.25 h.p. Disc-Armature motor.

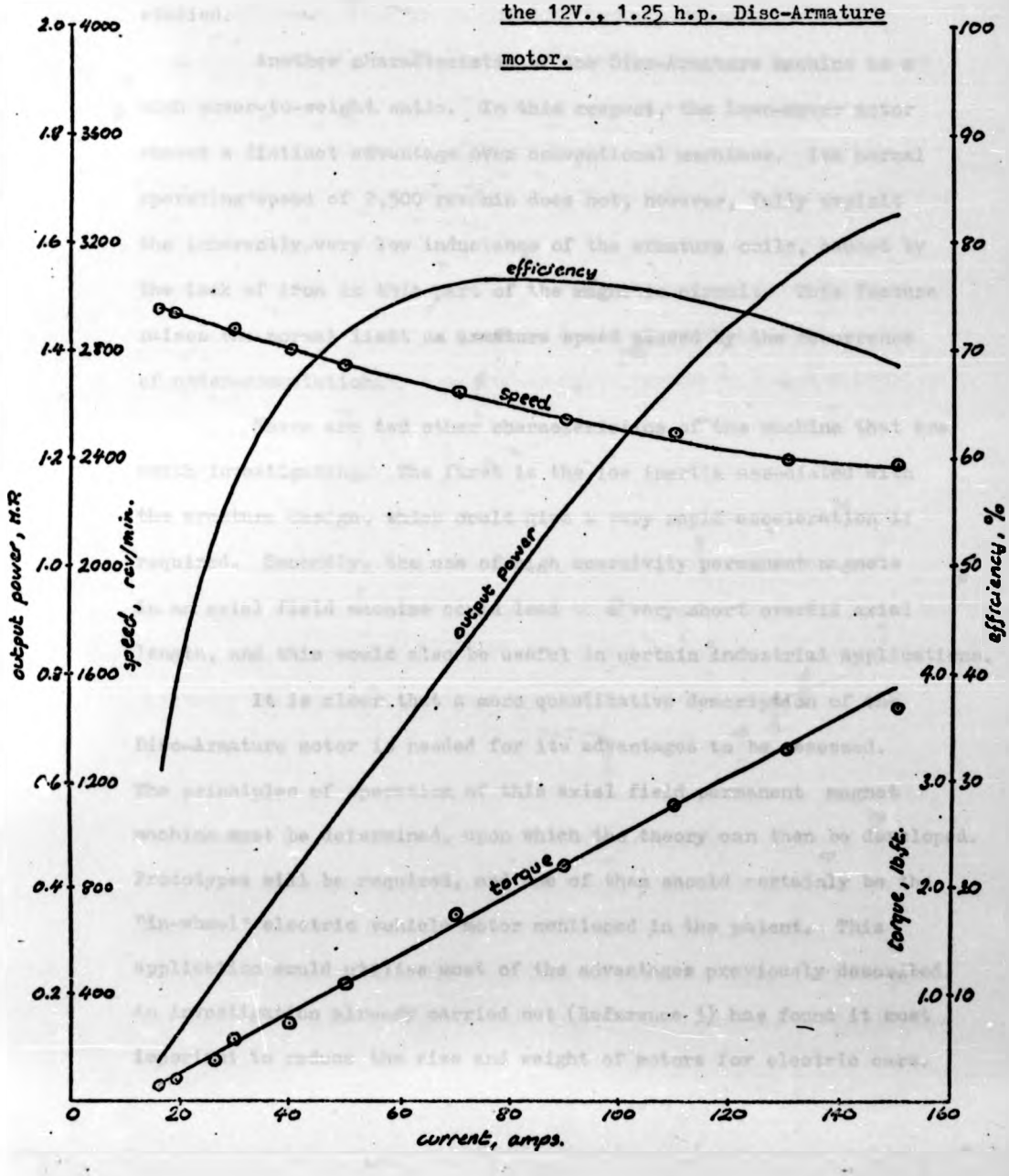

armature is free from iron, eliminating eddy-current and hysteresis losses. These features should therefore have given the motor a much higher efficiency, and so the method of design must be carefully studied.

Another characteristic of the Disc-Armature machine is a high power-to-weight ratio. In this respect, the lawn-mower motor showed a distinct advantage over conventional machines. Its normal operating speed of 2,500 rev/min does not, however, fully exploit the inherently very low inductance of the armature coils, caused by the lack of iron in this part of the magnetic circuit. This feature raises the normal limit on armature speed caused by the occurrence of under-commutation.

There are two other characteristics of the machine that are worth investigating. The first is the low inertia associated with the armature design, which could give a very rapid acceleration if required. Secondly, the use of high coercivity permanent magnets in an axial field machine could lead to a very short overall axial length, and this would also be useful in certain industrial applications.

It is clear that a more quantitative description of the Disc-Armature motor is needed for its advantages to be assessed. The principles of operation of this axial field permanent magnet machine must be determined, upon which the theory can then be developed. Prototypes will be required, and one of them should certainly be the "in-wheel" electric vehicle motor mentioned in the patent. This application would utilise most of the advantages previously described. An investigation already carried out (Reference 3) has found it most important to reduce the size and weight of motors for electric cars.

Although there are clear advantages in applying the Disc-Armature machine as an "in-wheel" motor, this is, however, a rather specialised application. There may be more immediate uses to which such a machine could be put. It has two particular characteristics that have already been mentioned, and are not fully exploited in the wheel motor. These are a low armature inertia and a short axial length, both of which are also achieved in the printed circuit type of motor. In fact, because of this existing coverage of these areas, it may be wondered whether there is any merit in investigating the Disc-Armature machine as a competitor.

Users of printed circuit motors have found that there is an inherent unreliability in this type of machine. This is due to a large armature heating loss, which is also detremental to the efficiency. It was felt, therefore, that the more conventional winding of the Disc-Armature machine would give an improved performance. The machine chosen for further study was to drive an automotive radiator cooling fan, a common application of the printed circuit motor.

Two different machines, the wheel motor and the fan motor, are therefore used to illustrate the characteristics of the Disc-Armature machine, and to verify the theory that will be developed for it. Each was designed by conventional methods, so that they would be available to yield experimental evidence at an early stage. More detailed descriptions of them are given in the following chapter.

CHAPTER 2: PRINCIPLES OF THE MACHINE.

2.1: Principles of the Magnetic Circuit.

The Disc-Armature motor was chosen to be a permanent magnet machine, the reason for which will shortly become clear. One advantage this field system has over electro-magnets is that, while the machine is running, no power is expended in producing a field. This leads to a greater overall machine efficiency, for any given power rating. This advantage is increased further by the absence of any iron in the armature, thus eliminating the associated eddy-current and hysteresis losses. A stationary flux return circuit on the remote side of the armature is therefore required if this gain is to be maintained. This is very difficult to achieve, in all but the smallest motors, unless an axial field arrangement is adopted. The machine now has a very large air-gap, comprising the armature thickness and running clearance on either side of it.

$$H_m . l_m = (\text{loss factor}) . H_g . l_g \qquad (2.1)$$

where l_m, l_g are the magnet and air-gap lengths,

H_m, H_g are the magnet and air-gap magnetising forces, respectively.

By equation 2.1, air-gap length, l_g, directly affects magnet length, l_m, and magnetising force, H_m. One of these quantities must therefore increase greatly to accomodate such a large l_g. So that machine weight did not become too large, permanent magnets with high coercivities were chosen to provide the field. This choice is clearly not as straightforward as equation 2.1 or the ensuing thoughts would suggest, though it does indicate the correct

CHAPTER 2: PRINCIPLES OF THE MACHINE.

2.1: Principles of the Magnetic Circuit.

The Disc-Armature motor was chosen to be a permanent magnet machine, the reason for which will shortly become clear. One advantage this field system has over electro-magnets is that, while the machine is running, no power is expended in producing a field. This leads to a greater overall machine efficiency, for any given power rating. This advantage is increased further by the absence of any iron in the armature, thus eliminating the associated eddy-current and hysteresis losses. A stationary flux return circuit on the remote side of the armature is therefore required if this gain is to be maintained. This is very difficult to achieve, in all but the smallest motors, unless an axial field arrangement is adopted. The machine now has a very large air-gap, comprising the armature thickness and running clearance on either side of it.

$$H_m . l_m = (\text{loss factor}) . H_g . l_g \qquad (2.1)$$

where l_m, l_g are the magnet and air-gap lengths,

H_m, H_g are the magnet and air-gap magnetising forces, respectively.

By equation 2.1, air-gap length, l_g, directly affects magnet length, l_m, and magnetising force, H_m. One of these quantities must therefore increase greatly to accomodate such a large l_g. So that machine weight did not become too large, permanent magnets with high coercivities were chosen to provide the field. This choice is clearly not as straightforward as equation 2.1 or the ensuing thoughts would suggest, though it does indicate the correct

class of material required.

The type of magnet material eventually chosen is determined largely by the application of the motor. For example, ceramic magnets, which are sintered from barium ferrite powder, have a comparatively high magnetising force, H_m, and low flux density, B_m. For a given flux per pole and air-gap length, they will therefore have a comparatively large pole face area but short length. Output power of the machine is determined by both the magnetic and the electric circuits, and the low value of B_m will impose a greater requirement on the armature winding design. Such magnets are, however, comparatively cheap and low in density. The high coercivity means that, on open circuit, they are still working on the straight portion of the B-H characteristic. Recoil does not move the operating point onto a minor loop, therefore, and magnetising windings do not have to be included in the machine itself.

If opposite conditions to these are required, they can mostly be supplied by alloy magnets, with a much higher B_m, but correspondingly lower H_m. A major consideration can be the need to magnetise these in the assembled magnetic circuit, to avoid recoil onto a minor B-H loop. This does not apply, however, to one new alloy, Hycomax IV, which can produce about twice the flux density of the ceramics, while having a high enough coercivity to permit magnetisation before assembly.

There are, then, three main types of permanent magnet material suitable for consideration in the design of Disc-Armature motors (rare earth magnets are, of course, highly desirable, but as yet their high cost precludes them). An application that requires two types will be described later, but it will be useful to record their B-H characteristics (Figure 2.1) now. Feroba III is the

Figure 2.1: Permanent magnet characteristics.

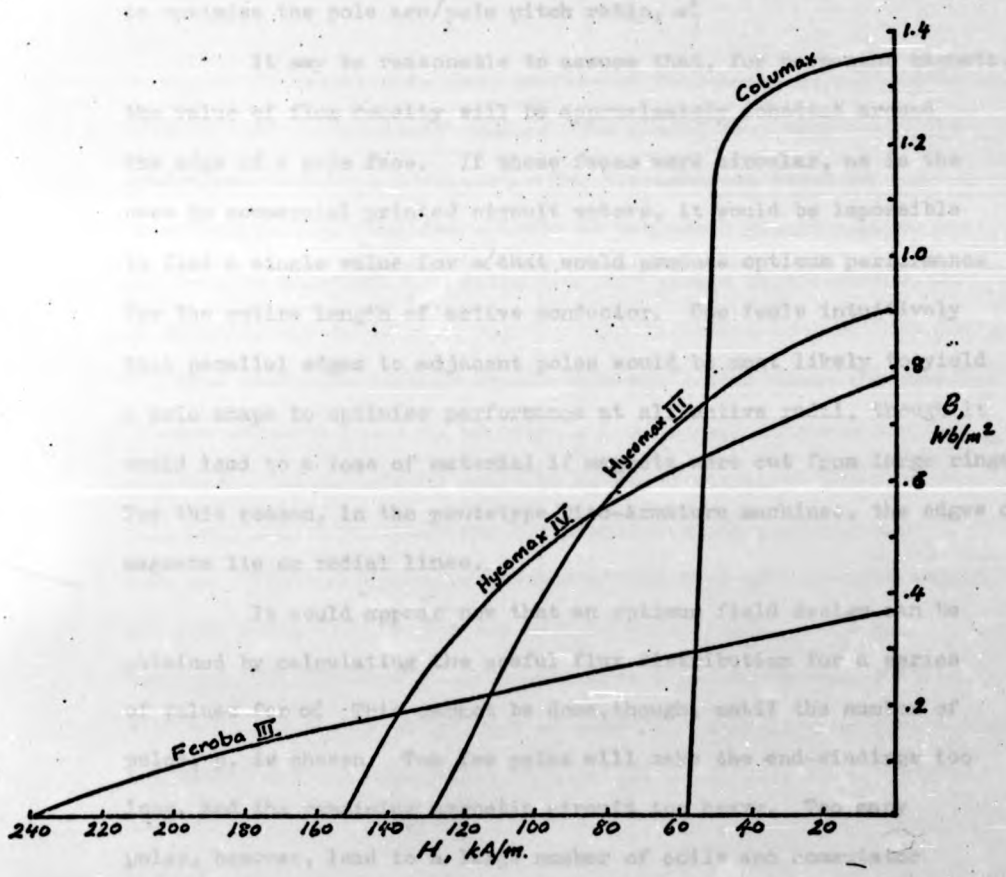

ceramic material that will be used, and Columax is the high remanence alloy. The choice of magnet material is only the start of the design, for it is the flux distribution cutting the armature conductors perpendicular to their direction of travel that determines motor performance. For a given operating flux density, B_m, this 'useful' flux will become greater as leakage flux between adjacent magnets is reduced. However, this is not consistent with the desire to increase the total flux per pole, and so there is clearly a need to optimise the pole arc/pole pitch ratio, α'.

It may be reasonable to assume that, for permanent magnets, the value of flux density will be approximately constant around the edge of a pole face. If these faces were circular, as is the case in commercial printed circuit motors, it would be impossible to find a single value for α' that would produce optimum performance for the entire length of active conductor. One feels intuitively that parallel edges to adjacent poles would be most likely to yield a pole shape to optimise performance at all active radii, though it would lead to a loss of material if magnets were cut from large rings. For this reason, in the prototype Disc-Armature machines, the edges of magnets lie on radial lines.

It would appear now that an optimum field design can be obtained by calculating the useful flux distribution for a series of values for α'. This cannot be done, though, until the number of poles, p, is chosen. Too few poles will make the end-windings too long, and the remaining magnetic circuit too heavy. Too many poles, however, lead to a large number of coils and commutator segments, making the brushes too thin. Fortunately, for the sizes of Disc-Armature motor considered, the selection of p can be done by intuition.

ceramic material that will be used, and Columax is the high remanence alloy. The choice of magnet material is only the start of the design, for it is the flux distribution cutting the armature conductors perpendicular to their direction of travel that determines motor performance. For a given operating flux density, B_m, this 'useful' flux will become greater as leakage flux between adjacent magnets is reduced. However, this is not consistent with the desire to increase the total flux per pole, and so there is clearly a need to optimise the pole arc/pole pitch ratio, α'.

It may be reasonable to assume that, for permanent magnets, the value of flux density will be approximately constant around the edge of a pole face. If these faces were circular, as is the case in commercial printed circuit motors, it would be impossible to find a single value for α' that would produce optimum performance for the entire length of active conductor. One feels intuitively that parallel edges to adjacent poles would be most likely to yield a pole shape to optimise performance at all active radii, though it would lead to a loss of material if magnets were cut from large rings. For this reason, in the prototype Disc-Armature machines, the edges of magnets lie on radial lines.

It would appear now that an optimum field design can be obtained by calculating the useful flux distribution for a series of values for α'. This cannot be done, though, until the number of poles, p, is chosen. Too few poles will make the end-windings too long, and the remaining magnetic circuit too heavy. Too many poles, however, lead to a large number of coils and commutator segments, making the brushes too thin. Fortunately, for the sizes of Disc-Armature motor considered, the selection of p can be done by intuition.

It has already been mentioned that the flux return circuit is stationary, on the remote side of the armature disc. This eliminates any need for a laminated material, so that a solid mild steel ring can now be used. An alternative arrangement is to have a duplicate set of magnets on the remote side of the disc, the total magnet volume being the same as in the former case. The magnetomotive force in the air-gap would therefore be supplied by two magnets, each of length $\frac{1}{2}l_m$, instead of one magnet of length l_m.

It has already been postulated (Reference 2) that this "double set" system would produce more useful flux than would the equivalent "single set" system. The argument was based on the amount of leakage flux there would be between adjacent magnets, for each arrangement. In going from the single to the double set of magnets, one individual magnet would be halved in length, halving the area producing leakage flux. This would also cause the m.m.f. between adjacent poles to be halved, but as each pole now has a duplicate, the net effect would be to halve the total leakage flux. This qualitative analysis has oversimplified the problem, and does not, for example, take account of the type of permanent magnet material being used, which may well be anisotropic. It does, however, indicate that a motor will have a greater useful flux with a double than a single set of magnets. Depending on the application, the extra cost and magnetisation involved might have to be weighed against this.

2.2: The Experimental motors.

2.2.1: The Electric Vehicle Traction Motor.

The electric vehicle traction motor is incorporated in the road wheel, and so adds to the unsprung weight. This means that,

for a battery powered vehicle, both efficiency and power-to-weight ratio must be maximised in the motor design. A double set of magnets was therefore used, the material being Hycomax III. This has a similar B-H characteristic to Hycomax IV, with a slightly higher remanence and lower coercivity. It would have been preferable to use Hycomax IV in this design, but it was not available when the prototype was manufactured. The "wheel motor" therefore has a quite small pole face area, without an excessively long magnet length. The full motor specification is given in Table 2.1.

It has already been mentioned that such a magnetic material can give the motor the required power-to-weight ratio advantage, without producing too low a value of flux density. The importance of this for battery electric vehicles can be seen by comparing the flux density produced by ferrite magnets. For a given machine design and performance, this is about one half that of Hycomax III or IV, and so the electric loading in the armature would have to be doubled. This could be achieved by increasing the number of conductors, or reducing the number of parallel paths, both of which would increase the armature resistance and generate greater heat losses. This, of course, is undesirable as battery power would be needed to overcome these extra losses in some way.

The choice of magnet material thus affects the armature winding design. This is used together with armature current and current density to select the conductor diameter, and is again used with the latter to find the thickness of the disc. Allowances are made for wire insulation and for complete encapsulation of the winding by epoxy resin. In the wheel motor, for example, a disc thickness of 3.0 mm. results from four layers of 0.63 mm. diameter conductors. The addition of running clearance gives a total air-gap

Table 2.1: Electric vehicle traction motor design specification.

Output power	1860 W.
Supply voltage	36 V.
Speed	10,500 rev/min
Outer active diameter	142 mm.
Inner active diameter	82 mm.
Number of poles	10
Pole arc/pole pitch ratio	0.78
Magnetic circuit:	
Material	Hycomax IV (later Hycomax III)
Magnet flux density	0.54 Wb/m^2
Magnet magnetising force	8.75×10^4 A/m.
Estimated useful flux/pole	3.51×10^{-4} Wb.
Magnet length (per stator half)	8.5 mm.
Air gap length	4.5 mm.
Electric circuit:	
Number of parallel paths	20
Number of layers	4
Number of coils	80
Number of turns/coil	7
Wire diameter (copper)	0.63 mm.
Current density	11.0 A/mm^2

of 4.5 mm. and magnet length of 17 mm. (because there is a double set of magnets, the individual length is 8.5 mm.).

A double-layer winding is the most efficient arrangement for conductors in a disc-armature. More than one such winding can be employed, though, if a greater number of conductors is required within a certain diameter. In the wheel motor, the four layers comprise two double-layer lap windings, assembled back-to-back (Figure 2.2). This does not become duplex lap, however, because they are connected in parallel. Each pair of adjacent commutator segments therefore has two coils connected in parallel across them. The advantage of this arrangement over a single double-layer winding is that twice the armature current is accommodated within a given diameter, without significantly altering either induced e.m.f. or speed. The reason for this is that both the number of conductors and the number of parallel paths have been doubled.

The absence of any iron in the armature of the machine implies that the armature inductance will be very small, and that armature reaction will be negligible. These two factors will reduce the static and dynamic e.m.f.s respectively, in a coil undergoing commutation, provided that the brushes are in the magnetic neutral position. It should therefore be possible to run such a machine at much higher speeds than normal. To investigate the effect of this on commutation, an operating speed of 10,500 rev/min was chosen for the wheel motor.

For a given output power from a motor, any increase in operating speed will reduce the torque developed. Although the size and weight of the motor would be very much reduced, those of the gearbox would be increased. At such high speeds, however, a two-stage reduction gearbox would almost invariably be used (Figure 2.3). It will be seen that a drum-type commutator is used for compactness,

Figure 2.2: Wheel motor armature winding and commutator.

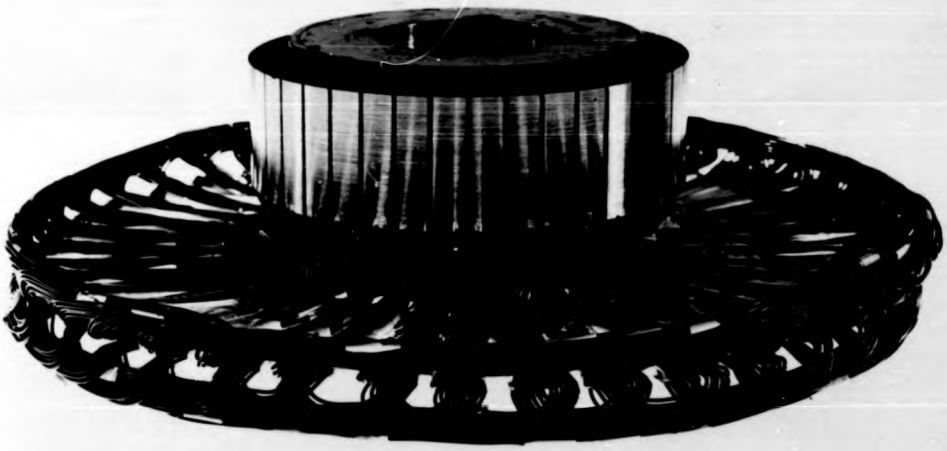

Figure 2.3 ELECTRIC VEHICLE TRACTION MOTOR

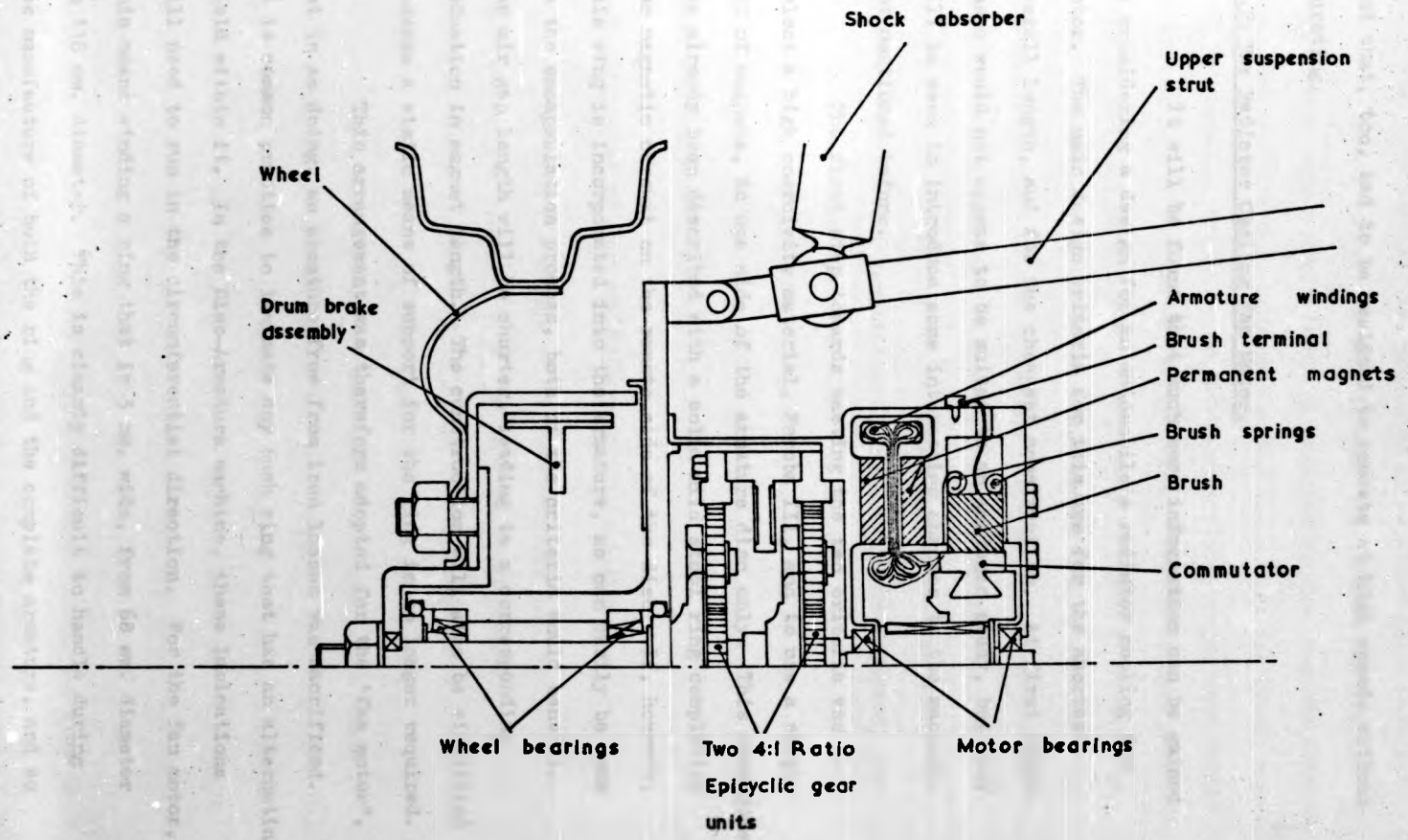

and that, too, had to be designed to operate at high speeds without bursting.

2.2.2: The Radiator Cooling Fan Motor.

It will be found that much more information can be gained by considering a design for an automobile's radiator cooling fan motor. The main design criteria for this are for the shortest overall length, and for the cheapest construction. At first sight, these would not appear to be suited to an academic study, but they will be seen to introduce some interesting changes to the machine, not mentioned before.

The first step towards meeting the two criteria was to select a high coercivity material, Feroba III, and to use a single set of magnets, to one side of the armature disc only. This arrangement has already been described with a solid mild steel ring completing the magnetic circuit on the remote side of the disc. If, however, this ring is incorporated into the armature, as can easily be done in the encapsulation process, both of the criteria would benefit. The air gap length will be shorter, leading to a corresponding reduction in magnet length. The construction will also be simplified because a static means of support for the ring is no longer required.

This arrangement was therefore adopted for the "fan motor", but in so doing, an armature free from iron losses was sacrificed. It is common practice to laminate any such ring that has an alternating field within it. In the Disc-Armature machine, these laminations will need to run in the circumferential direction. For the fan motor, this means winding a ring that is 3 mm. wide, from 68 mm. diameter to 118 mm. diameter. This is clearly difficult to handle during the manufacture of both the ring and the complete armature, and so

compressed iron powders were evaluated as an alternative material.

Having decided on some form of laminated structure, an even shorter magnet length would be required if the ring was slotted, occupying the full disc thickness at the teeth. It was found, however, that at present, neither a laminated nor an iron powder ring could be slotted to fit an armature of this size. The motor design is shown in Figure 2.4, and its specification is given in Table 2.2.

The armature coils are connected as a wave winding, thus minimising the cost of the brushgear. This motor was originally designed with a face-type commutator, but the brushholders were found to protrude well beyond the limits of the machine's magnetic circuit. The present commutator shape was therefore adopted, such that the brushes are housed between the magnets. This represents a shift of half a pole pitch from their normal positions, which must be accompanied by a similar shift in the connections between coils and the commutator.

2.3: Principles of Machine Performance Calculations.

As with the design of any conventional d.c. motor, there are only a discrete number of winding arrangements. An attempt should be made, though, to fill up the available space at the inner radius of the active length of conductors, R_1 in Figure 2.5. This demonstrates a disadvantage of the axial field machine, because there will always be some wasted armature volume at radii greater than R_1. This is wasted in the sense that it is not filled with current carrying conductor producing torque in the available magnetic field. To completely fill the radius R_1 does not take account of the end-windings, which must exist at radii less than R_1. The shape of the coils is such that the end-windings are stacked behind the line of the pole faces. Their location must therefore be made as close to

compressed iron powders were evaluated as an alternative material.

Having decided on some form of laminated structure, an even shorter magnet length would be required if the ring was slotted, occupying the full disc thickness at the teeth. It was found, however, that at present, neither a laminated nor an iron powder ring could be slotted to fit an armature of this size. The motor design is shown in Figure 2.4, and its specification is given in Table 2.2.

The armature coils are connected as a wave winding, thus minimising the cost of the brushgear. This motor was originally designed with a face-type commutator, but the brushholders were found to protrude well beyond the limits of the machine's magnetic circuit. The present commutator shape was therefore adopted, such that the brushes are housed between the magnets. This represents a shift of half a pole pitch from their normal positions, which must be accompanied by a similar shift in the connections between coils and the commutator.

2.3: Principles of Machine Performance Calculations.

As with the design of any conventional d.c. motor, there are only a discrete number of winding arrangements. An attempt should be made, though, to fill up the available space at the inner radius of the active length of conductors, R_1 in Figure 2.5. This demonstrates a disadvantage of the axial field machine, because there will always be some wasted armature volume at radii greater than R_1. This is wasted in the sense that it is not filled with current carrying conductor producing torque in the available magnetic field. To completely fill the radius R_1 does not take account of the end-windings, which must exist at radii less than R_1. The shape of the coils is such that the end-windings are stacked behind the line of the pole faces. Their location must therefore be made as close to

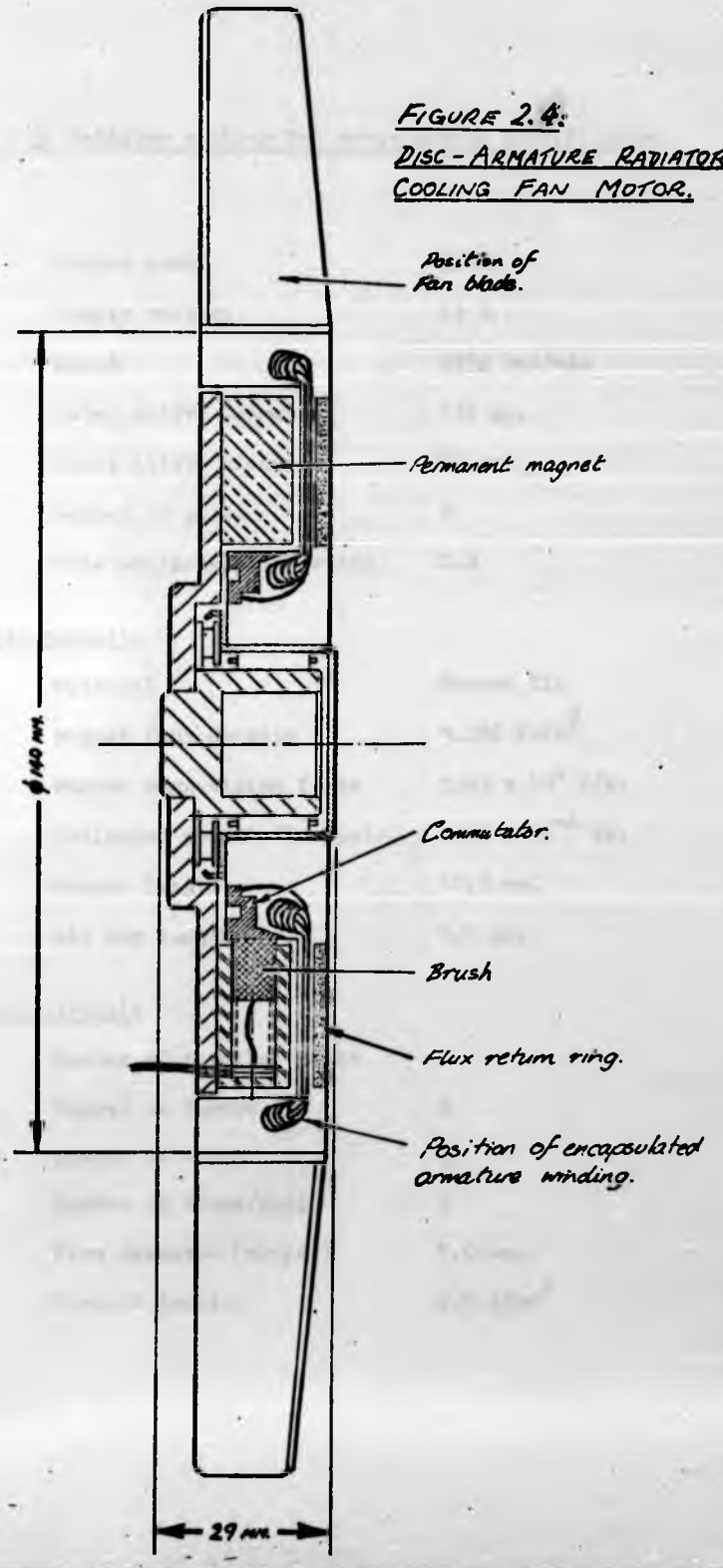

FIGURE 2.4:
DISC-ARMATURE RADIATOR
COOLING FAN MOTOR.

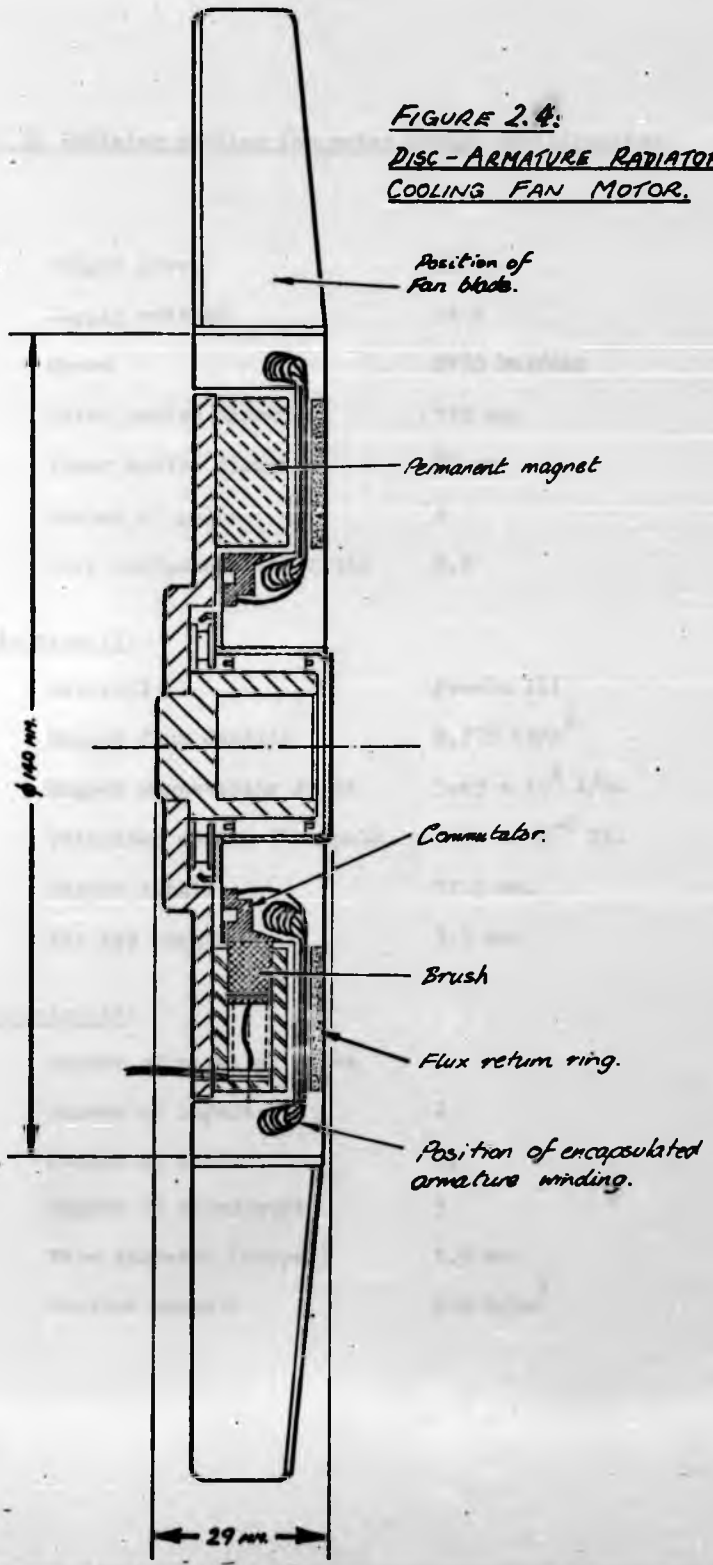

FIGURE 2.4:
DISC-ARMATURE RADIATOR
COOLING FAN MOTOR.

Table 2.2: Radiator cooling fan motor design specification.

Output power	90 W.
Supply voltage	14 V.
Speed	2730 rev/min
Outer active diameter	118 mm.
Inner active diameter	68 mm.
Number of poles	8
Pole arc/pole pitch ratio	0.8

Magnetic circuit:

Material	Feroba III
Magnet flux density	0.286 Wb/m^2
Magnet magnetising force	5.05×10^4 A/m.
Estimated useful flux/pole	1.64×10^{-4} Wb.
Magnet length	12.5 mm.
Air gap length	3.5 mm.

Electric circuit:

Number of parallel paths	2
Number of layers	2
Number of coils	39
Number of turns/coil	5
Wire diameter (copper)	1.0 mm.
Current density	6.0 A/mm^2

Table 2.2: Radiator cooling fan motor design specification.

Output power	90 W.
Supply voltage	14 V.
Speed	2730 rev/min
Outer active diameter	118 mm.
Inner active diameter	68 mm.
Number of poles	8
Pole arc/pole pitch ratio	0.8

Magnetic circuit:

Material	Feroba III
Magnet flux density	0.286 Wb/m^2
Magnet magnetising force	5.05×10^4 A/m.
Estimated useful flux/pole	1.64×10^{-4} Wb.
Magnet length	12.5 mm.
Air gap length	3.5 mm.

Electric circuit:

Number of parallel paths	2
Number of layers	2
Number of coils	39
Number of turns/coil	5
Wire diameter (copper)	1.0 mm.
Current density	6.0 A/mm^2

Figure 2.5: Element of an armature conductor.

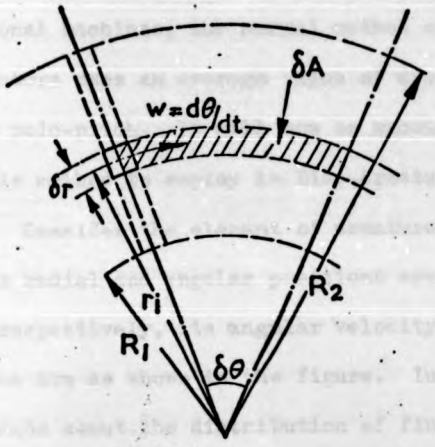

R_1 as possible, allowing a clearance (normally of about 1 mm.) between the armature and the bottoms of the magnets.

In the subsequent calculations it will be assumed that only the conductors lying between radii R_1 and R_2 (Figure 2.5) are producing useful torque. These dimensions are the inner and outer radii of the magnets. Any additional torque produced by stray fields in the end-windings will be assumed to be negligible. In conventional machines, the normal method of determining the e.m.f. in conductors uses an average value of useful flux density, calculated over one pole-pitch. It will now be shown that this is not a reasonable method to employ in Disc-Armature machines.

Consider the element of armature conductor shown in Figure 2.5. Its radial and angular positions are described by the subscripts i and j respectively, its angular velocity is w, and the remaining dimensions are as shown in the figure. Initially, no assumptions will be made about the distribution of flux, which will be described by the same subscripts. Thus, the flux cut by the element sweeping through area dA will be

$$d\phi_{i,j} = B_{i,j}.dA$$
$$= B_{i,j}.r_i.dr.d\theta$$

The e.m.f. in the element will then be given by

$$e_{i,j} = \frac{d\phi_{i,j}}{dt} = B_{i,j}.r_i.dr.\frac{d\theta}{dt}$$
$$= w.B_{i,j}.r_i.dr$$

$$e_j = w.\int_{r_1=R_1}^{R_2} B_{i,j}.r_i.dr \qquad (2.2)$$

e_j is the e.m.f. in the whole active conductor at angular position j. It would be convenient to remove the dependence of flux

density on radius, so that the integration can be performed. The use of such a flux density, $\underline{B}_j$, would only be valid if $\underline{B}_j$ itself was defined as an integration of $\underline{B}_{i,j}$ over radius. The expression for e.m.f. becomes

$$e_j = w.\underline{B}_j \int_{r_i=R_1}^{R_2} r_i.dr$$

$$e_j = \tfrac{1}{2}.w.\underline{B}_j.(R_2^2 - R_1^2) \qquad (2.3)$$

$\underline{B}_j$ must therefore be defined by

$$\tfrac{1}{2}.\underline{B}_j.(R_2^2 - R_1^2) = \int_{r_i=R_1}^{R_2} \underline{B}_{i,j}.r_i.dr$$

$$\underline{B}_j = \frac{2}{(R_2^2 - R_1^2)} \int_{r_i=R_1}^{R_2} \underline{B}_{i,j}.r_i.dr \qquad (2.4)$$

This expression is not the mean flux density at any given angular position. A similar calculation applied to a conventional machine shape is, however, identical to the determination of the mean. It will sometimes be found that the actual flux density distribution makes it difficult to perform the integration of Equation 2.4, and so it will be useful to state equivalent expressions for numerical integration. If the active conductor length is divided into n elements of length δr, then

$$e_j = \tfrac{1}{2}.w.n.\delta r.\underline{B}_j.(R_1 + R_2) \qquad (2.5)$$

$$\underline{B}_j = \frac{2}{n.(R_1 + R_2)} \sum_{r_i=R_1}^{R_2} \underline{B}_{i,j}.r_i \qquad (2.6)$$

Equation 2.4 indicates that the contribution of a given flux density to the e.m.f. of the conductor is proportional to that radius at which it is situated. This is because the linear velocity of the conductor is proportional to radius. It is therefore not surprising to find that the inverse of the multiplying constant in Equation 2.4 is the product of active conductor length, l, and

average radius. If the linear velocity, v, is calculated at this radius, Equation 2.3 then becomes the familiar expression

$$e_j = \underline{B}_j.l.v \qquad (2.7)$$

It is correct to use this for the Disc-Armature machine, provided that $\underline{B}_j$ is not calculated as the mean of $\underline{B}_{i,j}$.

The cause of the deviation from conventional d.c. machine calculations is the inseparability of $\underline{B}_{i,j}$ from r_i. This is overcome by defining a "moment of flux density", $\overline{P}_j$, such that

$$\overline{P}_j = \frac{1}{R_2 - R_1} \int_{r_i = R_1}^{R_2} \underline{B}_{i,j}.r_i.dr \qquad (2.8)$$

The bar over P_j indicates that the calculation is that of the mean of $\underline{B}_{i,j}.r_i$ over the active radius. The conductor e.m.f., which was given in Equation 2.2, now becomes

$$e_j = \overline{P}_j.l.w \qquad (2.9)$$

This same result is obtained by defining $\overline{P}_j$ also as

$$\overline{P}_j = \frac{1}{n} \sum_{r_i = R_1}^{R_2} \underline{B}_{i,j}.r_i \qquad (2.10)$$

These results show that the calculation of conductor e.m.f. in an axial field machine can be simplified by taking a suitable mean. However, this is not the mean of flux density, as is true for conventional machines, but the mean of flux density moment.

The e.m.f. calculated from Equation 2.9 is for a given angular position j, and from it can be found the average conductor e.m.f., E_c, for one complete armature revolution. For a d.c. machine, this is

$$E_c = \frac{p}{2\pi} \int_0^{2\pi/p} e_j.d\theta$$

$$= \frac{p.l.w}{2\pi} \int_0^{2\pi/p} \overline{P}_j.d\theta$$

The integration is performed over one pole pitch, p being the number

of poles per set of magnets. As the result of this is the mean of $\bar{P}_j$, another moment of flux density, $\bar{P}$, can be defined, that is not dependent on angular position.

$$\bar{P} = \frac{p}{2\pi} \int_0^{2\pi/p} \bar{P}_j . d\theta$$

$$\therefore \quad \bar{P} = \frac{p}{2\pi.(R_2 - R_1)} \int_0^{2\pi/p} \int_{r_i = R_1}^{R_2} \underline{B}_{i,j} . r_i . dr . d\theta \qquad (2.11)$$

Hence $$E_c = \bar{P}.l.w \qquad (2.12)$$

where $\bar{P}$ is the mean of $\underline{B}_{i,j}.r_i$ over the active area of a pole pitch. If there are Z_s conductors in series, the total armature e.m.f. will therefore become

$$E = \bar{P}.l.w.Z_s \qquad (2.13)$$

For the purpose of designing a machine, it is better to write this as

$$E = \frac{\pi.N.\bar{P}.(d_2 - d_1).Z}{a} \qquad (2.14)$$

where N rev/sec is the speed,

Z is the number of conductors,

a is the number of parallel armature paths,

d_1, d_2 are the diameters corresponding to R_1, R_2.

It is possible to calculate the total flux per pole, ϕ, for a Disc-Armature machine in a similar way. It is simplest to remember that

$$e_j = \frac{d\phi_j}{dt} = \bar{P}_j.l.\frac{d\theta}{dt}$$

Hence $$\phi = l. \int_0^{2\pi/p} \bar{P}_j . d\theta$$

$$\therefore \quad \phi = \frac{2\pi.l.\bar{P}}{p} \qquad (2.15)$$

The combination of Equations 2.13 and 2.15 yields the familiar expression for a d.c. machine,

$$E = \frac{\phi . N . p . Z}{a} \qquad (2.16)$$

The geometry of the field system has now been eliminated, and it need not appear in subsequent calculations of machine performance. The associated geometry of the armature winding will, however, have to occur in a calculation for armature resistance.

It has been shown that an important quantity in the theory of the Disc-Armature machine is the moment of flux density. Its mean value directly affects the armature e.m.f. and the flux per pole. This value itself depends upon the design of the field system, and so the effect of the latter upon machine performance must be carefully studied.

$$E = \frac{\emptyset.N.p.Z}{a} \qquad (2.16)$$

The geometry of the field system has now been eliminated, and it need not appear in subsequent calculations of machine performance. The associated geometry of the armature winding will, however, have to occur in a calculation for armature resistance.

It has been shown that an important quantity in the theory of the Disc-Armature machine is the moment of flux density. Its mean value directly affects the armature e.m.f. and the flux per pole. This value itself depends upon the design of the field system, and so the effect of the latter upon machine performance must be carefully studied.

3. MAGNETIC CIRCUIT.

The performance of an axial-field permanent magnet machine depends very much upon the design of the field system. The first step towards investigating this dependence is an accurate determination of the field distribution in the air-gap of the machine. This will lead, firstly, to an indication of the optimum pole shape, and then to a direct calculation of the e.m.f. induced in the armature conductors. There can be no approximation to a two-dimensional system, as no account could then be taken of the dependence of flux density upon radius.

3.1. Permeance of the air-gap.

An attempt has already been made to determine the useful flux density in the air-gap of a Disc-Armature motor (Reference 2). This was derived from the working point on the B-H characteristic, by subtracting the leakage flux to adjacent magnets. It was therefore necessary to define the paths of the leakage flux, and this was done by a well-known method (Reference 4). The product of the permeance of each path, and the magnetomotive force acting along it, yields the required value of flux.

Initially, four paths for leakage flux were considered (Figure 3.1). It was assumed that a path was either a straight line, an arc of a circle, or a combination of both. It was realised that flux would actually follow shorter paths than those assumed for the magnet tops and bottoms, paths (ii) and (iii). Accordingly, 20% was added to the permeance calculated for these. Conversely, it was felt that leakage flux at the magnet faces, path (iv), would follow longer paths, and so 20% less permeance was used. It is difficult, now,

Figure 3.1: Paths of leakage flux.

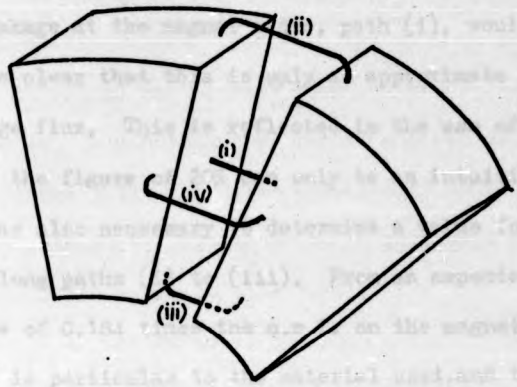

to see any justification for treating these differently, although the proximity of the remaining magnetic circuit to the latter path might provide an explanation. In fact, the shortness of the air-gap length was used to show that leakage along path (iv) very rarely occurred. A very high pole arc/pole pitch ratio was required for this, when direct leakage at the magnet sides, path (i), would be dominant.

It is clear that this is only an approximate model of the paths of leakage flux. This is reflected in the use of a correction factor, though the figure of 20% can only be an intuitive guess.

It was also necessary to determine a value for the m.m.f. driving flux along paths (i) to (iii). From an experiment on a single magnet, a value of 0.184 times the m.m.f. on the magnet face was deduced. This is particular to the material used, and the shape of the magnet, and could not therefore be used for any future designs. It is doubtful whether this value is the same when the magnet is assembled into a complete circuit.

A useful flux density was nevertheless arrived at, but not without making a further estimation of the loss of m.m.f. in the remaining magnetic circuit, defined as the 'loss factor' in Eqn. 2.1. This method is therefore not sufficiently accurate to be used in the determination of an optimum design of the machine. It is also doubtful whether it would accurately predict its performance. An alternative method of calculating the field in the air-gap will therefore be sought.

3.2. Direct solution of Laplace's Equation, and simplification of the boundary conditions.

A method that uses the Schwarz-Christoffel transformation was developed by F.W.Carter in 1900 (Reference5). Carter's derivation is extremely complicated, and is not suitable for such an array of

magnetic poles. The assumptions are made that the poles are infinitely long, and that the whole pole surface, including the sides, is at one potential. It is clearly not sufficiently accurate to assume these when the poles are high coercivity permanent magnets. The solution is in two-dimensions, and would become extremely difficult to handle in three-dimensions. However, the need to consider the third (radial) direction has already been indicated, and will be demonstrated later. A conclusion of Carter's paper is that the presence of adjacent poles will have practically no effect on the field under the main pole. Simple tests on permanent magnet blocks will show a noticeable error in this result.

It would be desirable to use such a direct calculation of the field, and yet the assumptions used by Carter will not be valid. It will be worthwhile attempting a direct solution without transforming the system into new co-ordinates, as the assumtions were originally made to ease this transformation. For the moment, though, it will be simpler to consider the two-dimensional problem at a given radius. This is shown in Figure 3.2, where OC and AB are the flux return ring surfaces, OA and CB are the neutral lines between adjacent magnets, and the magnet boundary is DEFG. The north and south pole faces are FG and ED respectively. If the potential distribution over the pole surface is known, it is possible to find the flux distribution in the air-gap as required. However, some important simplifications can be made for these permanent magnet poles.

The high coercivity materials used in Disc-Armature machines are homogeneous uniformly magnetised media. It will therefore be assumed that the direction of the intrinsic magnetisation, $\underline{J}$, is constant and in the axial x-direction. Within the permanent

Figure 3.2: Two-dimensional representation of magnet and air gap.

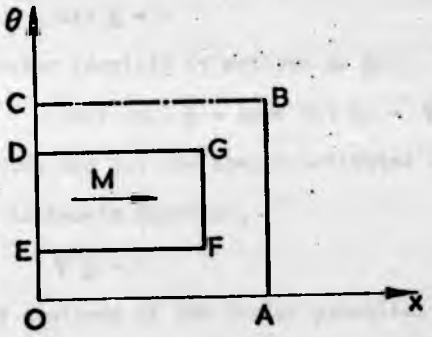

magnet material, the following expressions apply, their relationship being given in Appendix I.

$$\underline{B} = \mu_0(\underline{H} + \underline{M}) \qquad (3.1)$$

$$\text{div } \underline{B} = 0 \qquad (3.2)$$

$$\text{curl } \underline{H} = 0 \qquad (3.3)$$

Substituting Eqn. 3.1 into Eqn. 3.2, the magnetising force, $\underline{H}$, in the material will obey

$$\text{div } \underline{H} = - \text{ div } \underline{M} \qquad (3.4)$$

This type of permanent magnet can therefore be likened to an air-gap, since the assumption about $\underline{M}$ means that, within the material

$$\text{div } \underline{M} = 0 \qquad (3.5)$$

The following vector identity is written in $\underline{H}$:

$$\text{curl curl } \underline{H} = \text{grad div } \underline{H} - \nabla^2\underline{H}$$

Equations 3.3, 3.4, and 3.5 are then substituted into this, and $\underline{H}$ then reduces to Laplace's Equation,

$$\nabla^2\underline{H} = 0 \qquad (3.6)$$

Because $\underline{H}$ is the gradient of the scalar potential distribution already mentioned, it is possible to solve Laplace's Equation for either magnetising force or potential in such a material.

The exceptions to this rule are the faces of the magnet, where $\underline{M}$ terminates. However, there need be no boundary conditions on any other surfaces of the magnet, so that the sides DG and EF can be eliminated from Figure 3.2. Furthermore, the south pole, ED, is attached to a mild steel plate, and will be assumed to be at zero potential. This is true if the effect of the plate is to remove the south pole to an imaginary position behind the plate's surface, at a distance equal to the magnet's length. This would cause the flux density, $\underline{B}$, and the magnetising force, $\underline{H}$, to cross the magnet/mild steel boundary normally at all points. At any such boundary,

the normal component of B and the tangential component of H will be identical on either side. To ensure that H in the magnet is mostly normal to the boundary, while satisfying the continuity conditions, it will therefore be necessary for the permeability of the mild steel to be much greater than that of the magnet material. Most permanent magnets operate at permeabilities comparable with μ_0, and so the assumption will not introduce any significant error. Figure 3.2 can therefore be simplified to Figure 3.3, the whole boundary OABC being at zero potential. Upon the north pole, FG, there will be a source potential distribution, $\psi(\theta)$.

These boundary conditions do not hold for H, and so it will be simpler to solve Laplace's Equation for potential than for magnetising force. The solution of $\nabla^2\psi = 0$ is eased if the region is divided into two areas by the line HI, and if the definition of $\psi(\theta)$ is extended to the whole of this line. The separation of variables and application of the boundary conditions is straightforward, and this is given in Appendix II. The potential distributions in areas 1 and 2 are then given by :

$$\psi_1(x,\theta) = \frac{2}{C}\sum_{n=1}^{\infty}\left[\frac{1}{\sinh\left(\frac{n\pi H}{C}\right)}\int_0^C \psi(\theta).\sin\frac{n\pi\theta}{C}.d\theta\right]\sin\frac{n\pi\theta}{C}.\sinh\frac{n\pi x}{C} \qquad (3.7)$$

$$\psi_2(x,\theta) = \frac{2}{C}\sum_{n=1}^{\infty}\left[\frac{1}{\sinh\left(\frac{n\pi(A-H)}{C}\right)}\int_0^C \psi(\theta).\sin\frac{n\pi\theta}{C}.d\theta\right]\sin\frac{n\pi\theta}{C}.\sinh\frac{n\pi(A-x)}{C} \qquad (3.8)$$

The magnetising force crossing the lines GI and FH must be continuous. Considering the x-direction, this is expressed as

$$\left(\frac{\partial\psi_1}{\partial x}\right)_{x=H} = \left(\frac{\partial\psi_2}{\partial x}\right)_{x=H}$$

Figure 3.3: Two-dimensional representation with simplified magnet.

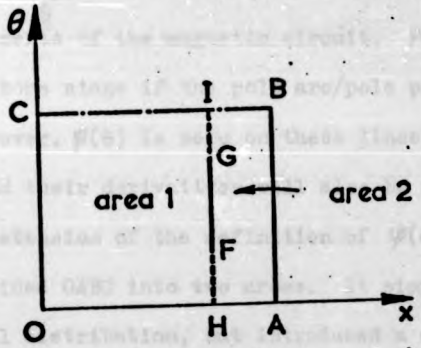

Differentiating Equations 3.7 and 3.8, this condition becomes

$$\coth \frac{n\pi H}{C} = -\coth \frac{n\pi(A-H)}{C} \qquad (3.9)$$

There is, however, no way in which Equation 3.9 can be realised, as A must always be greater than H. Continuity must therefore be achieved by the function $\psi(\theta)$ being zero along HF and GI. If the source potential on FG is given, there now exists a complete set of boundary conditions for the rectangle HABI. It will then be possible to find the field in the air-gap, area 2, without reference to area 1.

This direct solution has led to an erroneous result, because there must clearly be field lines crossing HF and GI for certain arrangements of the magnetic circuit. For example, this must happen at some stage if the pole arc/pole pitch ratio is steadily decreased. However, $\psi(\theta)$ is zero on these lines, and so Equations 3.7 and 3.8, and their derivatives will also be zero.

The extension of the definition of $\psi(\theta)$ to the whole of the line HI divided OABC into two areas. It simplified the solution of the potential distribution, but introduced a clear error in the result. It has, in fact, taken no account of the magnet length, which was originally stated to be of importance for high coercivity permanent magnets. A solution to $\nabla^2\psi = 0$ will now be sought that requires potential to be specified only on the magnet face within the boundary. An iterative method will easily allow a solution to the three-dimensional problem, which will subsequently be shown to be important.

3.7. Iterative solution of Laplace's Equation.

The geometry of this machine requires that Laplace's Equation be expressed in cylindrical co-ordinates as :

$$\frac{1}{r}\cdot\frac{\partial}{\partial r}\cdot\left(r\cdot\frac{\partial\psi}{\partial r}\right) + \frac{1}{r^2}\cdot\frac{\partial^2\psi}{\partial\theta^2} + \frac{\partial^2\psi}{\partial x^2} = 0 \qquad (3.10)$$

For an iterative solution, it is simpler to differentiate the first term with respect to r.

$$\frac{\partial^2\psi}{\partial r^2} + \frac{1}{r}\cdot\frac{\partial\psi}{\partial r} + \frac{1}{r^2}\cdot\frac{\partial^2\psi}{\partial\theta^2} + \frac{\partial^2\psi}{\partial x^2} = 0 \qquad (3.11)$$

The air-gap in the machine, including the regions between adjacent magnets, can be spanned by a three-dimensional grid. Each point in the grid will be denoted by the subscripts i, j, and k, these being integers describing the position of the point in the r, θ, and x directions respectively. Figure 3.4 shows the relationship of adjacent points to a point $Q_{i,j,k}$.

A solution of the field will be symmetrical about the centre-line of a magnet, and any iterative method need only be performed to one side of the radial plane defined by this line. Figure 3.5 shows the volume in which the calculation will be performed, ϵ being the pole pitch and α the pole arc. The origin is defined so that the increments in each direction can be related to the absolute distances by the integers i, j, and k. Thus:

$$r = i.(\delta r) \quad ; \quad \theta = j.(\delta\theta) \quad ; \quad x = k.(\delta x)$$

Finite difference formulae are used to express Equation 3.11 in terms of the grid shown in Figure 3.4. If the increments are related by a constant ν, such that $\delta x = \nu.\delta r$, the potential at the point Q can be expressed in terms of the potentials at adjacent points as

$$\psi_{i,j,k} = \frac{1}{2\left(1 + \frac{1}{i^2.\delta\theta^2} + \frac{1}{\nu^2}\right)}\left[\left(1 + \frac{1}{2i}\right)\psi_{i+1,j,k} + \left(1 - \frac{1}{2i}\right)\psi_{i-1,j,k}\right.$$
$$+ \frac{1}{i^2.\delta\theta^2}\left(\psi_{i,j+1,k} + \psi_{i,j-1,k}\right)$$
$$\left. + \frac{1}{\nu^2}\left(\psi_{i,j,k+1} + \psi_{i,j,k-1}\right)\right] \qquad (3.12)$$

Figure 3.4: Relationship of adjacent grid points.

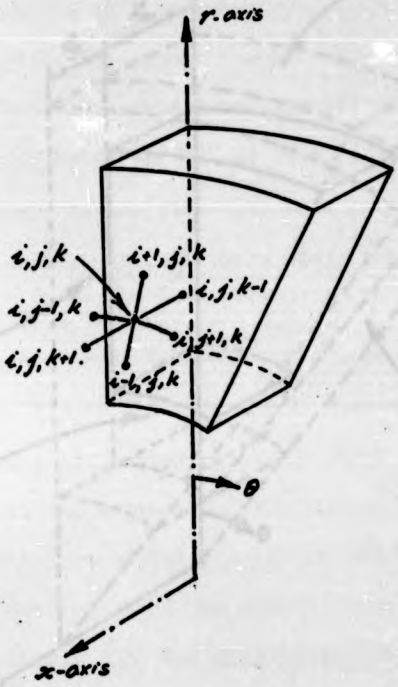

Figure 3.4: Relationship of adjacent grid points.

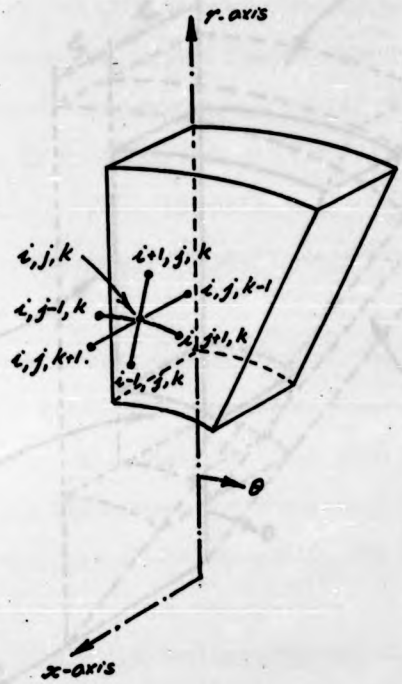

Figure 3.5: Air gap regions for half a pole pitch.

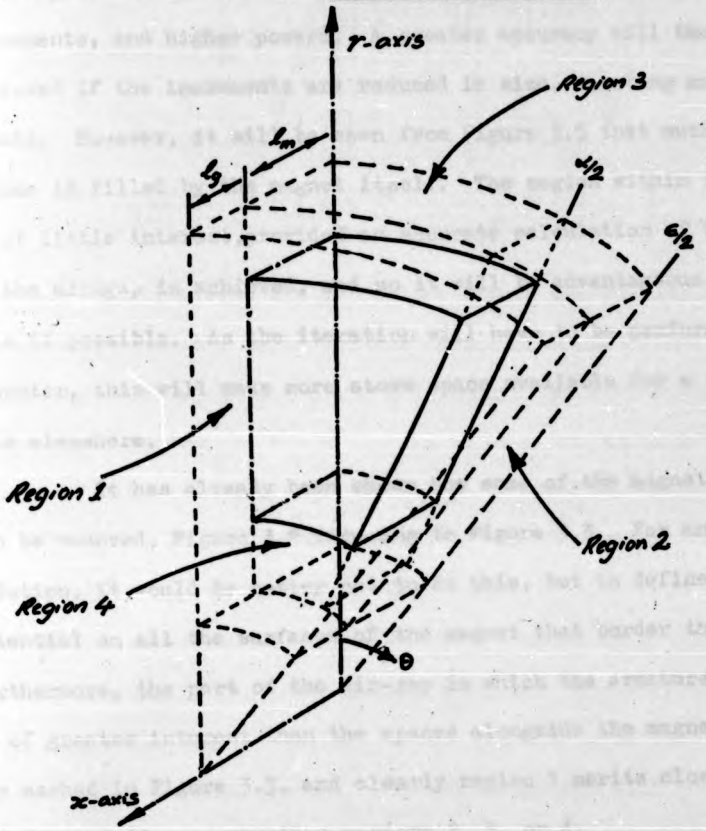

This expression ignores terms proportional to the square of the increments, and higher powers. A greater accuracy will therefore be achieved if the increments are reduced in size, creating more grid points. However, it will be seen from Figure 3.5 that much of the volume is filled by the magnet itself. The region within the magnet is of little interest, provided an accurate calculation of the field in the air-gap is achieved, and so it will be advantageous to exclude this if possible. As the iteration will have to be performed by computer, this will make more store space available for a finer grid elsewhere.

It has already been shown how some of the magnet boundaries can be removed, Figure 3.2 reducing to Figure 3.3. For an iterative solution, it would be better not to do this, but to define the source potential on all the surfaces of the magnet that border the air-gap. Furthermore, the part of the air-gap in which the armature lies is of greater interest than the spaces alongside the magnet. Regions are marked in Figure 3.5, and clearly region 1 merits closer attention, and hence a finer mesh, than regions 2, 3, or 4.

Equation 3.12 will therefore take on a different form for each of the four regions, and there will be unequal increments in the grid at the boundaries between them. In the θ-direction (Figure 3.5) a finer grid will be used for $\theta > \frac{1}{2}\alpha$ than for $0 < \theta < \frac{1}{2}\alpha$. There will also be a finer grid in the x-direction over the air-gap length than the magnet length. The ratio of the increments in the coarse and the fine grids will be η and ξ, for the θ- and x-directions respectively. Equation 3.12 should therefore be written in the more general form:

$$\psi_{i,j,k} = \frac{1}{2\left(1 + \frac{1}{\eta.i^2\delta\theta^2} + \frac{1}{\zeta\nu^2}\right)}\left[\left(1 + \frac{1}{2i}\right)\psi_{i+1,j,k} + \left(1 - \frac{1}{2i}\right)\psi_{i-1,j,k}\right.$$

$$+ \frac{2}{i^2\delta\theta^2\eta(1+\eta)}\psi_{i,j+1,k} + \frac{2}{i^2\delta\theta^2(1+\eta)}\psi_{i,j-1,k}$$

$$\left. + \frac{2}{\nu^2\zeta(1+\zeta)}\psi_{i,j,k+1} + \frac{2}{\nu^2(1+\zeta)}\psi_{i,j,k-1}\right] \qquad (3.13)$$

Equation 3.13 can be applied to all the boundaries between different grid sizes, by a suitable choice of η and ζ. It can be used within any grid by setting η and ζ to unity, and making the appropriate choice of $\delta\theta$ and ν.

It will be necessary to define boundaries, which will be at zero potential, in the radial direction. In the machine itself, there will clearly be an outer casing which, if made from mild steel, would be the outer radial boundary. A consideration of the commutator or shaft would give the inner radial boundary. However, as the field beyond the tops or bottoms of the magnets is of little significance in determining machine performance, the assumption will be made that these radial boundaries are only small distances beyond the magnets. This will benefit the calculation in the air-gap as more computer store will be available for the grid there.

Before any iteration can commence, all of the grid points must be given initial values. A linear extrapolation will be used along grid lines running normally from the magnet surface to the zero potential boundaries. The remaining regions will be initialised by similar extrapolations from grid points already valued. A successive over-relaxation method will be used (Ref. 6), Equation 3.13 providing the residual values at the grid points. The iteration will terminate when the maximum residual is reduced to a satisfactorily low value. It will then be possible to calculate the magnetising

$$\psi_{i,j,k} = \frac{1}{2\left(1 + \frac{1}{\eta i^2 \delta\theta^2} + \frac{1}{\zeta \nu^2}\right)}\left[\left(1 + \frac{1}{2i}\right)\psi_{i+1,j,k} + \left(1 - \frac{1}{2i}\right)\psi_{i-1,j,k}\right.$$

$$+ \frac{2}{i^2\delta\theta^2\eta(1+\eta)}\psi_{i,j+1,k} + \frac{2}{i^2\delta\theta^2(1+\eta)}\psi_{i,j-1,k}$$

$$\left. + \frac{2}{\nu^2\zeta(1+\zeta)}\psi_{i,j,k+1} + \frac{2}{\nu^2(1+\zeta)}\psi_{i,j,k-1}\right] \qquad (3.13)$$

Equation 3.13 can be applied to all the boundaries between different grid sizes, by a suitable choice of η and ζ. It can be used within any grid by setting η and ζ to unity, and making the appropriate choice of $\delta\theta$ and ν.

It will be necessary to define boundaries, which will be at zero potential, in the radial direction. In the machine itself, there will clearly be an outer casing which, if made from mild steel, would be the outer radial boundary. A consideration of the commutator or shaft would give the inner radial boundary. However, as the field beyond the tops or bottoms of the magnets is of little significance in determining machine performance, the assumption will be made that these radial boundaries are only small distances beyond the magnets. This will benefit the calculation in the air-gap as more computer store will be available for the grid there.

Before any iteration can commence, all of the grid points must be given initial values. A linear extrapolation will be used along grid lines running normally from the magnet surface to the zero potential boundaries. The remaining regions will be initialised by similar extrapolations from grid points already valued. A successive over-relaxation method will be used (Ref. 6), Equation 3.13 providing the residual values at the grid points. The iteration will terminate when the maximum residual is reduced to a satisfactorily low value. It will then be possible to calculate the magnetising

$$\psi_{i,j,k} = \frac{1}{2\left(1 + \frac{1}{\eta i^2 \delta\theta^2} + \frac{1}{\zeta \nu^2}\right)}\left[\left(1 + \frac{1}{2i}\right)\psi_{i+1,j,k} + \left(1 - \frac{1}{2i}\right)\psi_{i-1,j,k}\right.$$

$$+ \frac{2}{i^2\delta\theta^2\eta(1+\eta)}\psi_{i,j+1,k} + \frac{2}{i^2\delta\theta^2(1+\eta)}\psi_{i,j-1,k}$$

$$\left. + \frac{2}{\nu^2\zeta(1+\zeta)}\psi_{i,j,k+1} + \frac{2}{\nu^2(1+\zeta)}\psi_{i,j,k-1}\right] \qquad (3.13)$$

Equation 3.13 can be applied to all the boundaries between different grid sizes, by a suitable choice of η and ζ. It can be used within any grid by setting η and ζ to unity, and making the appropriate choice of $\delta\theta$ and ν.

It will be necessary to define boundaries, which will be at zero potential, in the radial direction. In the machine itself, there will clearly be an outer casing which, if made from mild steel, would be the outer radial boundary. A consideration of the commutator or shaft would give the inner radial boundary. However, as the field beyond the tops or bottoms of the magnets is of little significance in determining machine performance, the assumption will be made that these radial boundaries are only small distances beyond the magnets. This will benefit the calculation in the air-gap as more computer store will be available for the grid there.

Before any iteration can commence, all of the grid points must be given initial values. A linear extrapolation will be used along grid lines running normally from the magnet surface to the zero potential boundaries. The remaining regions will be initialised by similar extrapolations from grid points already valued. A successive over-relaxation method will be used (Ref. 6), Equation 3.13 providing the residual values at the grid points. The iteration will terminate when the maximum residual is reduced to a satisfactorily low value. It will then be possible to calculate the magnetising

force, and hence flux density in the air-gap, from the gradient of the grid potentials.

Of greatest interest is the magnetising force in the x-direction, which can be expressed at any of the grid points as:

$$H_{x_{i,j,k}} = \frac{\psi_{i,j,k+2} - 8\psi_{i,j,k+1} + 8\psi_{i,j,k-1} - \psi_{i,j,k-2}}{12.\nu.\delta r} \qquad (3.14)$$

The error in this equation is in the fourth and higher powers of the increments, this being additional to the original error in calculating the potentials. For grid points that are close to any of the boundaries, it will be necessary to use one of Equations 3.15 rather than Equation 3.14. In this case, the error is slightly greater, commencing in the square of the increments.

$$\left.\begin{aligned} H_{x_{i,j,k}} &= \frac{-\psi_{i,j,k-2} + 4\psi_{i,j,k-1} - 3\psi_{i,j,k}}{2.\nu.\delta r} \\ H_{x_{i,j,k}} &= \frac{\psi_{i,j,k+2} - 4\psi_{i,j,k+1} + 3\psi_{i,j,k}}{2.\nu.\delta r} \end{aligned}\right\} \qquad (3.15)$$

A program entitled "Fields" was written to calculate the air-gap field in this way, and its flow diagram is given in Figure 3.6. The grid is stored in four arrays, corresponding to the regions defined in Figure 3.5. It will, however, be noticed that unique calculations are required not only on the regional boundaries, by virtue of the unbalanced mesh, but at some points adjacent to these boundaries, because Equation 3.13 refers to more than one array. Region 1 is defined to include the magnet face, and region 2 the magnet side. Regions 3 and 4 will, therefore, not end on the planes defined by the extensions of these surfaces, but at distances of one increment behind the planes. The same applies to region 2 and the extension of the magnet face. A unique calculation will also be required

Figure 3.6: Flow diagram of the program "Fields".

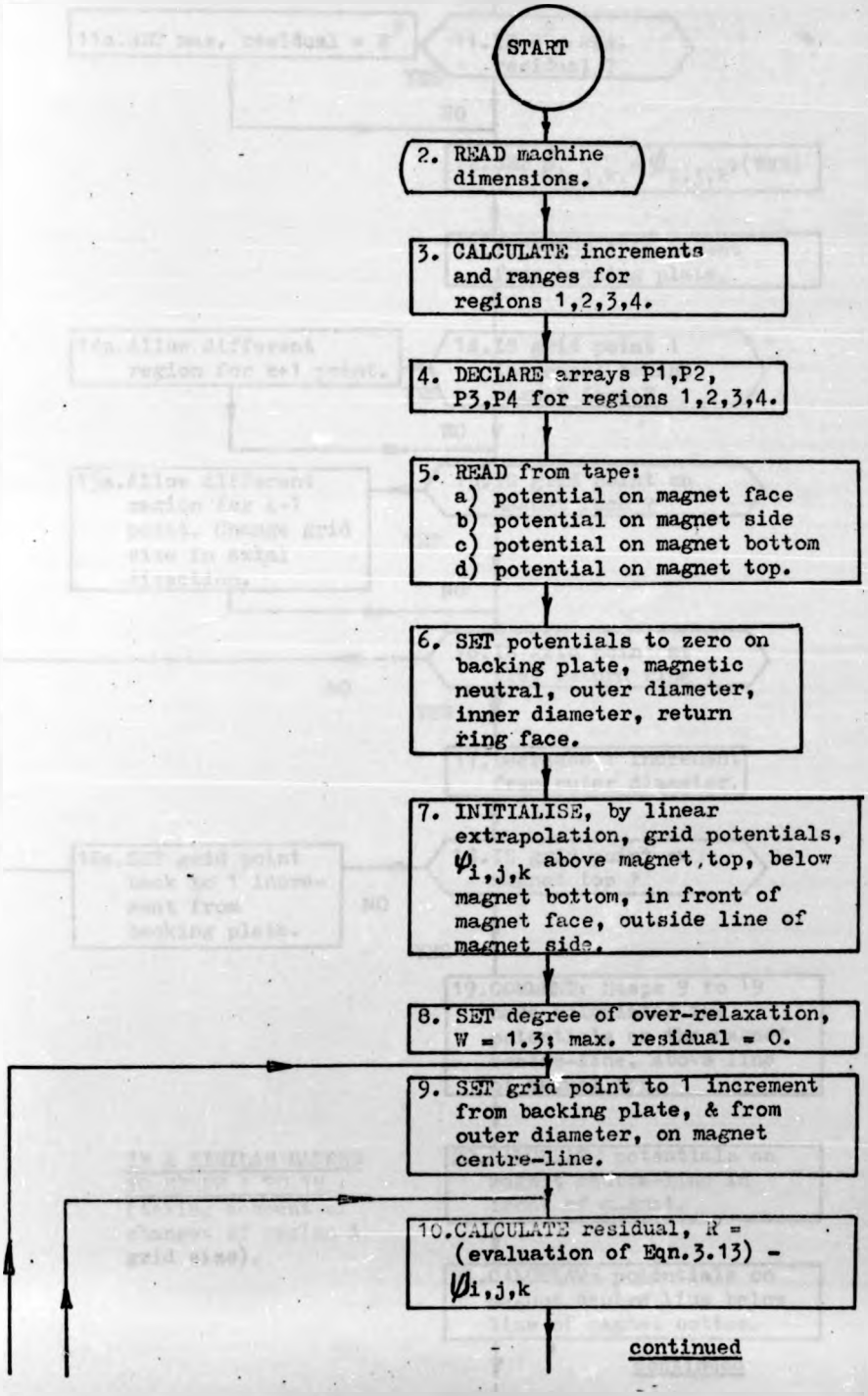

Figure 3.6 (continued)

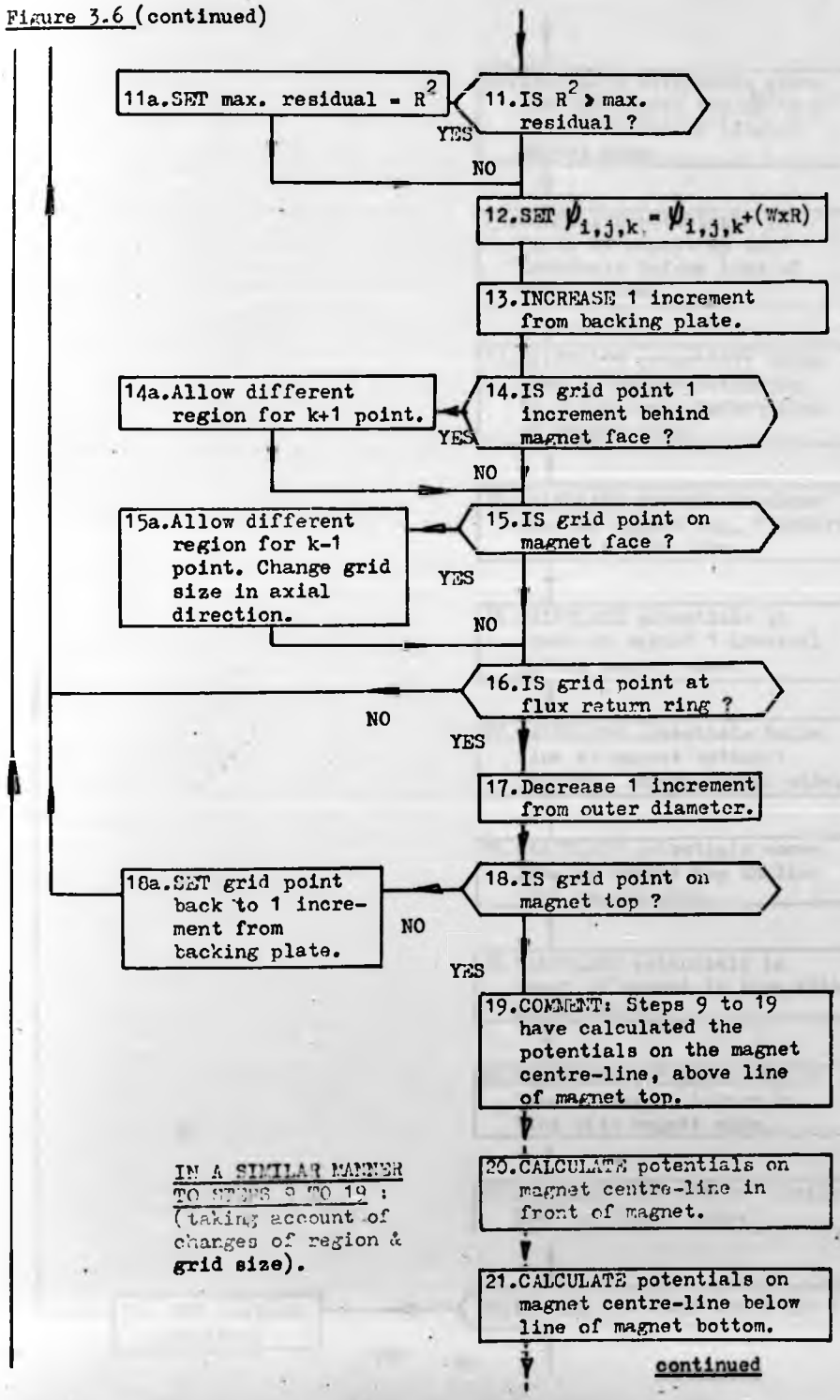

Figure 3.6 (continued)

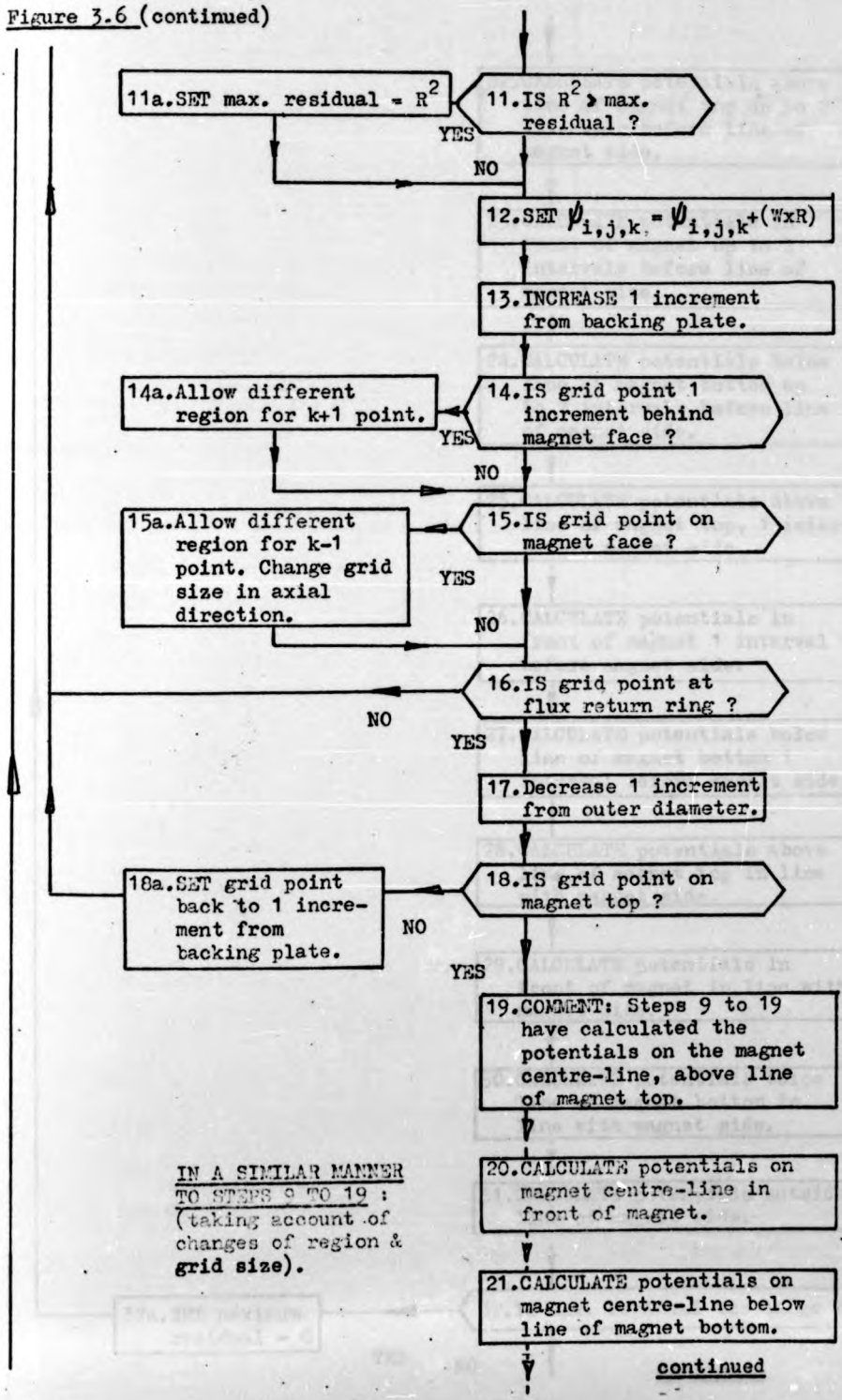

continued

Figure 3.6 (continued)

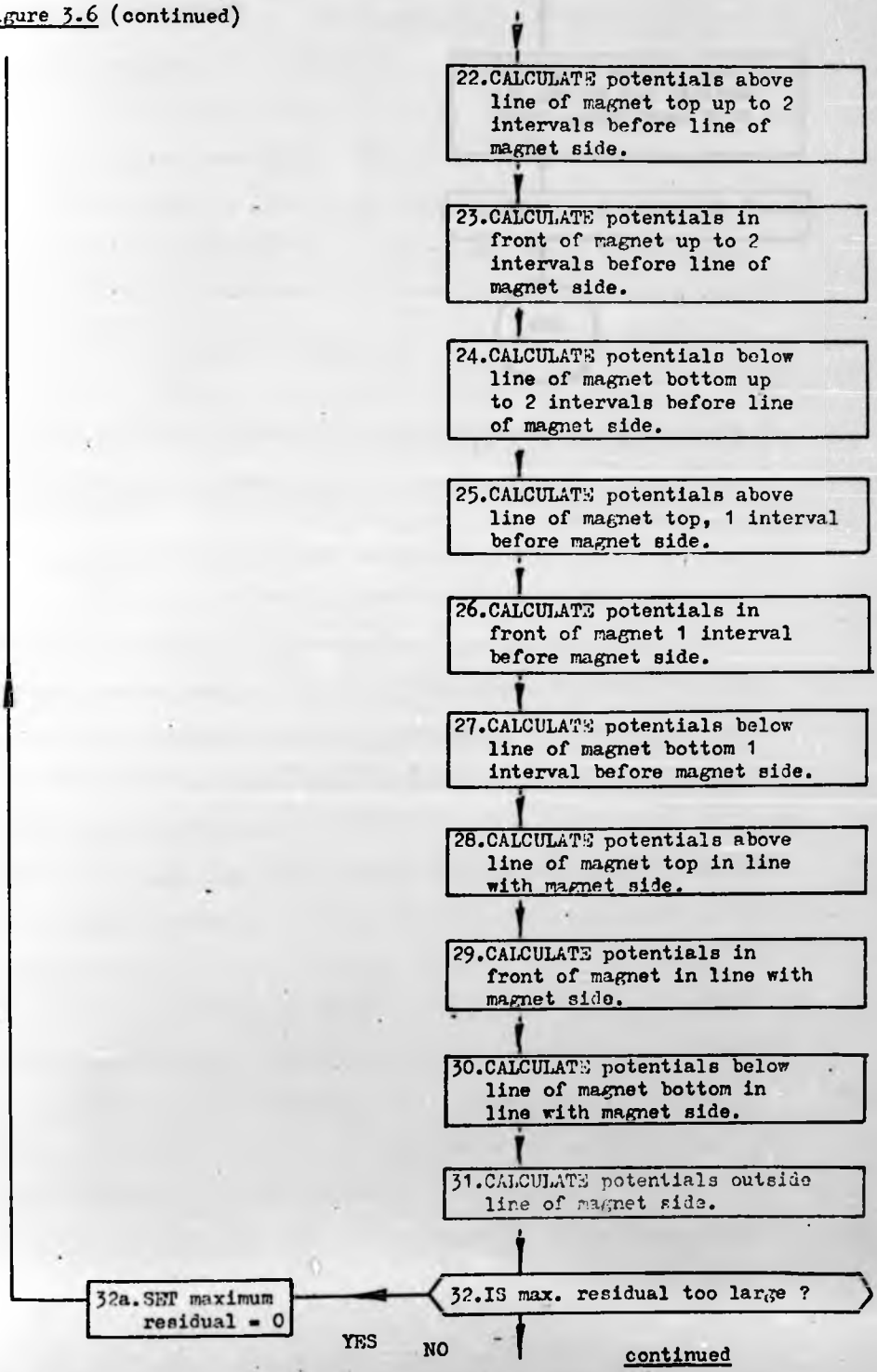

continued

Figure 3.6 (continued)

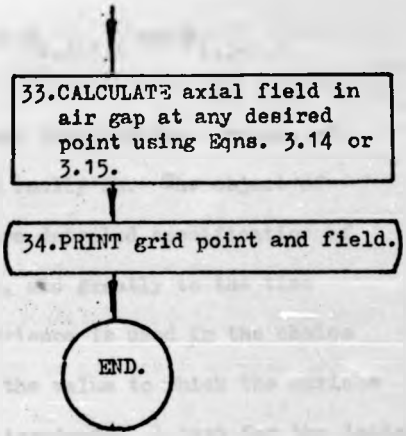

on the magnet centre-line plane, giving $\psi_{i,j+1,k}$ and $\psi_{i,j-1,k}$ identical values.

These unique calculations make the iteration process of Figure 3.6 appear more lengthy than it really is. The object of saving store space is achieved by a more detailed specification of the iteration. This does not, however, add greatly to the time taken to complete the solution. Experience is used in the choice of the degree of over-relaxation, and the value to which the maximum residual must fall for the process to terminate. A test for the latter is performed at the end of each complete scan of the grid, using the modulus of the residuals.

3.3.1. Potential on the magnet surface.

The input to this program also includes the potentials at the grid points on the magnet surface. It has been shown, for example, that a constant potential is an unsatisfactory assumption, and so a more accurate method of calculation must be sought. This must be capable of determining the potential on the magnet sides as well as on its face.

By combining $\underline{H} = -\text{grad}\,\psi$ and Equation 3.4, the general relationship between potential and intrinsic magnetisation can be written as

$$\nabla^2\psi = \text{div}\,\underline{M} \qquad (3.16)$$

At the magnet surface, $\underline{M}$ is discontinuous, and appears as a surface pole strength M_s. Using Equation 3.1, and equating the normal components of flux density on either side of the surface, the surface condition can be found as

$$\frac{\partial\psi}{\partial n} + \frac{\partial\psi}{\partial n'} = M_s \qquad (3.17)$$

where n and n' denote the normals to the surface pointing towards

opposite sides. If the potential becomes zero at infinity, Equations 3.16 and 3.17 can be combined to give a general solution (Reference 7) for the potential at any point Q (Figure 3.7):

$$4\pi\psi = \int \frac{\text{div } \underline{M}}{q} .dV + \int \frac{M_s}{q} .dA \qquad (3.18)$$

For a homogeneous uniformly magnetised medium, div $\underline{M} = 0$ and M_s only occurs on the pole faces. It will therefore be seen that the surface condition is needed in order to produce a non-trivial solution. Equation 3.18 can be reduced to Equation 3.19, and the normal direction becomes the x-direction in Figure 3.7.

$$\psi = \int \frac{M_s}{4\pi q} .dA \qquad (3.19)$$

It is now possible to calculate the potential at all points on the magnet surface, including its sides as required. However, since there is a singularity at $q = 0$, care will have to be taken to exclude this point from the integral in order to produce a finite result. Equation 3.19 could also be used to calculate the potential at each of the grid points directly, though it will be found much less time consuming to follow the iteration process already described. This is due mainly to the geometry of the magnet system, which makes it necessary to perform the integration in the angular direction by numerical means. The potential at the point Q is derived with the aid of standard integrals (Reference 8) from Equation 3.19 using Figure 3.7 as

$$\psi = \frac{M_s}{4\pi}\int_{-\beta}^{\alpha-\beta}\left[(x^2 + r^2 + s^2 - 2rs.\cos\theta)^{\frac{1}{2}} + s.\cos\theta.\sinh^{-1}\frac{r - s.\cos\theta}{(x^2 + s^2.\sin^2\theta)^{\frac{1}{2}}}\right]_{r=R_1}^{R_2} d\theta \qquad \ldots.(3.20)$$

This expression will clearly give a much more realistic variation in potential over the magnet surface, than that used by Carter for

Figure 3.7: Position of a point, Q, related to a magnet face.

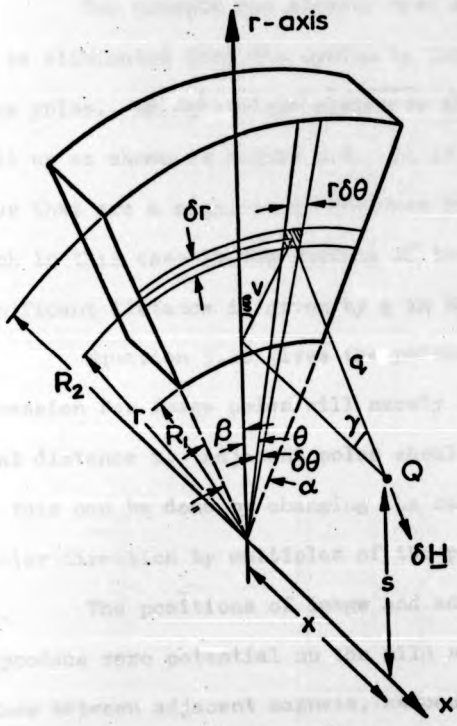

Figure 3.7: Position of a point, Q, related to a magnet face.

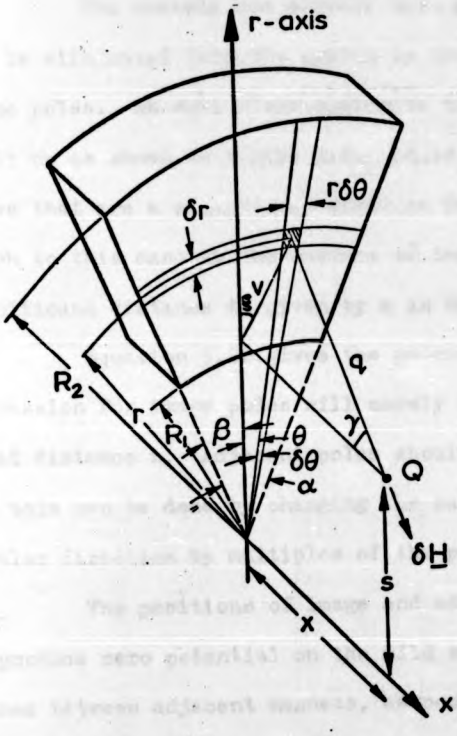

example. Furthermore, it can take account of the whole magnet system if necessary.

3.3.2. Allowance for neighbouring magnetic materials.

The example has already been given of how a mild steel plate can be eliminated from the system by the suitable positioning of image poles. An equivalent system to that in the machine can be built up as shown in Figure 3.8. It is only necessary to include poles that are a significant distance from the region of interest, which in this case is the surface of the original magnet. The significant distance is given by q in Equation 3.19.

Equation 3.20 gives the potential due to one pole, and the expression for image poles will merely require an alteration to the axial distance x. Adjacent poles should also be taken into account, and this can be done by changing the range of integration in the angular direction by multiples of the pole pitch.

The positions of image and adjacent poles should be such as to produce zero potential on the mild steel plates and the neutral planes between adjacent magnets, as occurred on the boundary OABC in Figure 3.2. The close proximity of these to the main pole will give rise to a greater potential gradient in the air-gap, as would be expected. In the calculation of potential distribution on the surface of the main pole, their presence will reduce this at all points since the dominant image and adjacent poles will be of opposite polarity to the main pole. This will moderate any increase in the field caused by a reduction of the air-gap.

A much better appreciation of these effects can be gained by considering the build-up of a magnet system. Tests were performed on small blocks of Feroba III, the material used in the radiator

Figure 3.8. Development of image poles

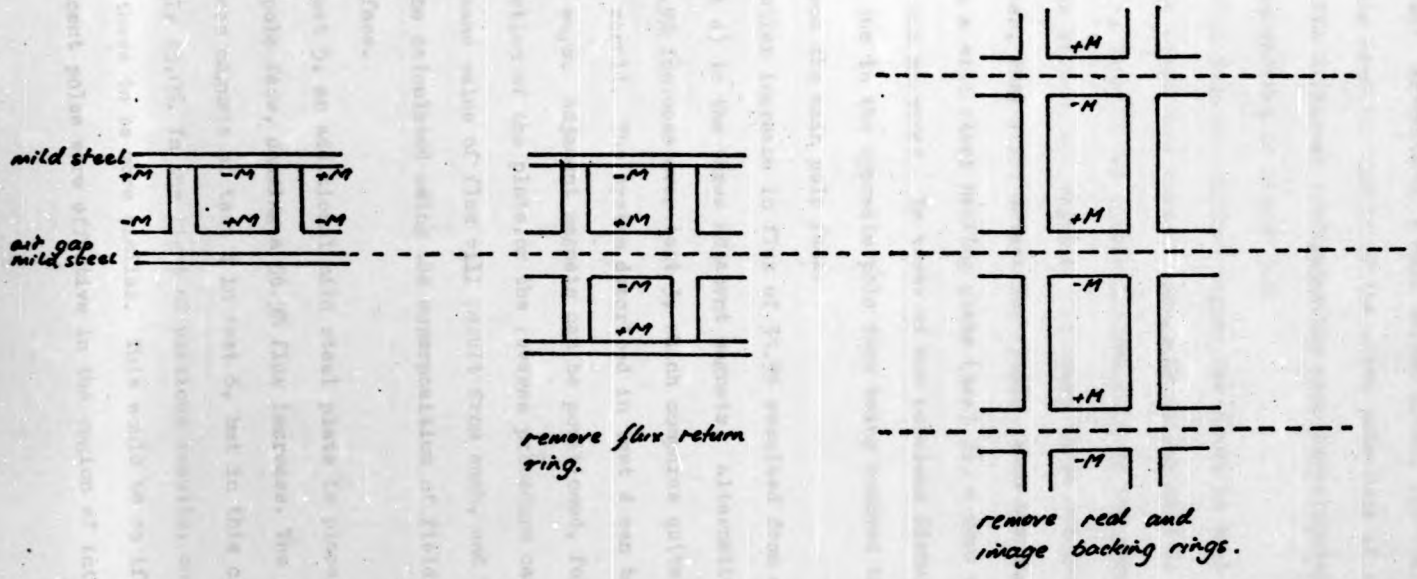

cooling fan motor. By means of a Hall Effect probe, the field emerging normally from the centre of the north pole face of one magnet was measured. Six different configurations were investigated, and these are summarised in Figure 3.9.

The flux from an isolated magnet was found in test 1, and two adjacent poles were brought alongside it for test 2. An 11.5% increase in flux is due to the introduction of the zero potential planes between the magnets. Although these are perpendicular to the pole faces, they still affect the field. When the magnet was attached to a mild steel backing plate (test 3), a more noticeable 32.7% increase was measured. In terms of the previous discussion, this is solely due to the opposite pole face being removed to twice the distance from the main pole face.

A similar increase in flux of 31.9% resulted from attaching the plate (test 4) to the three adjacent magnets. Alternatively, there was a 10.9% increase over test 3, which compares quite well with the first result. The system described in test 4 can be derived in two ways. Adjacent magnets can be positioned, followed by the introduction of the plate, or the reverse procedure can be adopted. The same value of flux will result from each, and this could clearly be calculated using the superposition of fields from a single pole face.

In test 5, an additional mild steel plate is placed 5 mm. from the main pole face, causing a 56.5% flux increase. The same is done to the three magnets of test 4 in test 6, but in this case the increase is only 45.0%. In the light of previous results, one would have expected these to be more similar. This would be so if all the image and adjacent poles were effective in the region of interest.

Figure 3.9: Tests on Feroba III magnet blocks.

TEST 1:

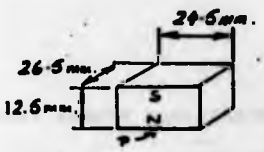

field at P = 1.04 Wb/m²

TEST 2:

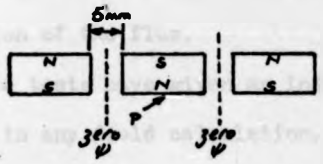

field at P = 1.16 Wb/m²

TEST 3:

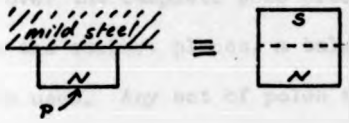

field at P = 1.38 Wb/m²

TEST 4:

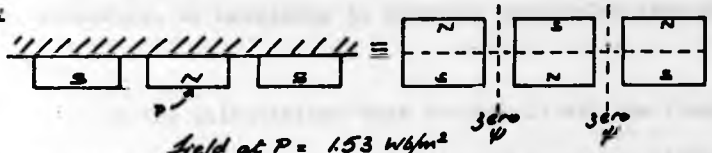

field at P = 1.53 Wb/m²

TEST 5:

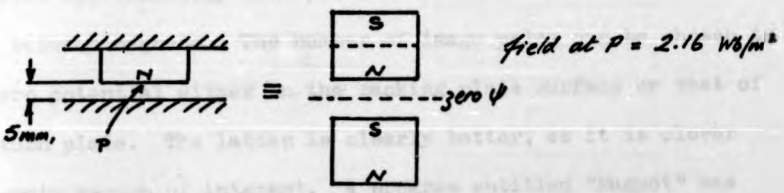

field at P = 2.16 Wb/m²

TEST 6:

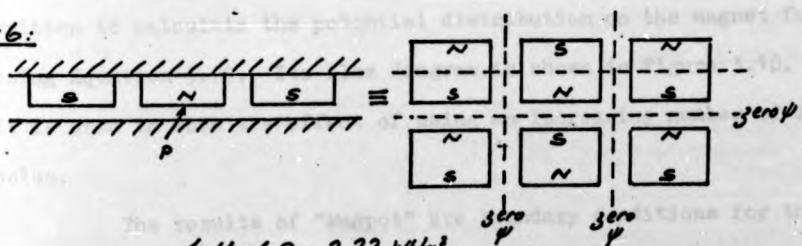

field at P = 2.22 Wb/m²

However, the most remote ones shown do not produce a significant field there, and it can be concluded that they would not be needed in a calculation of the flux.

These tests have given an indication of the poles that must be considered in any field calculation. It must be remembered, though, that the field in a machine is required across the active air-gap and over the complete pole pitch. In order to produce zero potential in the correct places, a balanced set of image and adjacent poles must be used. Any set of poles will only be evenly distributed about one point, and so there will always be a source of error. It may, therefore, be necessary to consider more poles than these tests suggest.

In the calculations that follow, it will be found that it is sufficient to take the nearest adjacent magnet on either side. This gives approximately zero potential on the magnetic neutral planes between magnets. The number of image poles can be chosen to give zero potential either on the backing plate surface or that of the return plate. The latter is clearly better, as it is closer to the main region of interest. A program entitled "Magpot" was written to calculate the potential distribution on the magnet face, using Equation 3.20. Its flow diagram is shown in Figure 3.10. It is used to show the effect of using an increasing number of image poles.

The results of "Magpot" are boundary conditions for the program "Fields",and so the grid over the magnet surface is identical in each. This grid is also used for the numerical integration in the angular direction, which makes it possible to overcome the singularity noted in Equation 3.19. The Gauss numerical integration method is employed (Reference 9), by which the potential is not evaluated

Figure 3.10: Flow diagram of the program "Magpot".

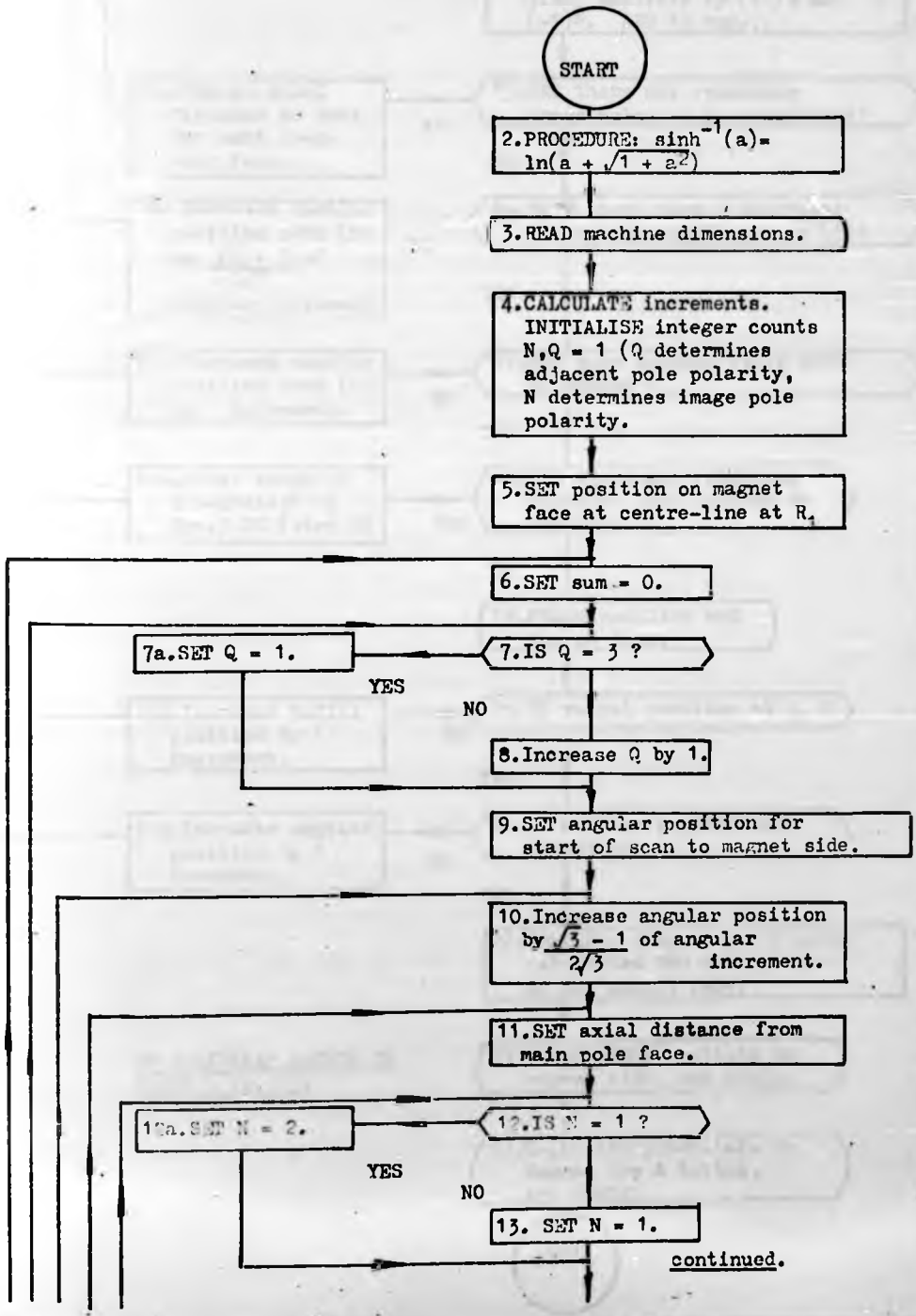

continued.

Figure 3.10 (continued)

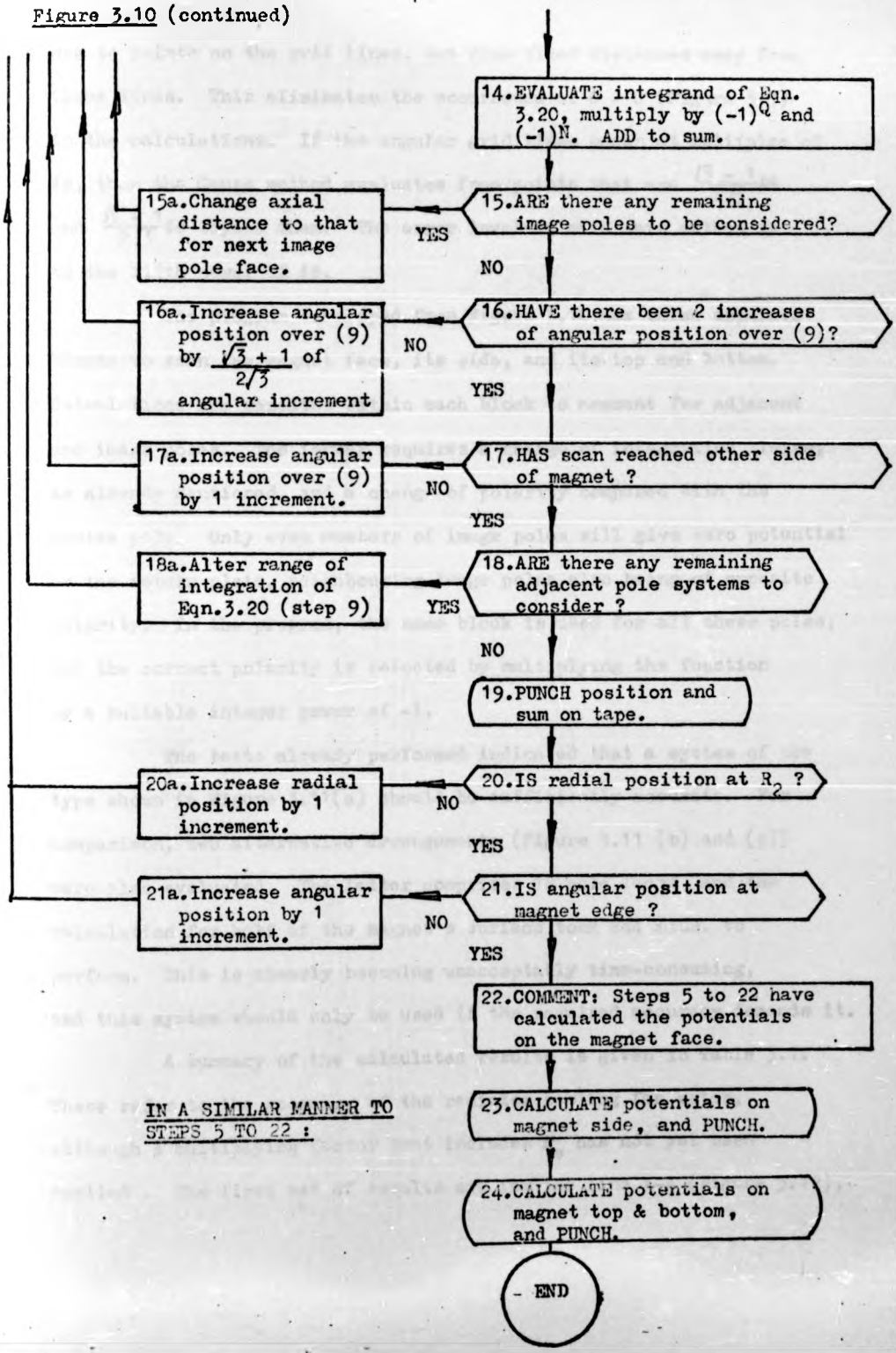

due to points on the grid lines, but from fixed distances away from those lines. This eliminates the occurrence of $\theta = 0$ (Figure 3.7) in the calculations. If the angular grid lines occur at multiples of $\delta\theta$, then the Gauss method evaluates from points that are $\frac{\sqrt{3}-1}{2\sqrt{3}}\delta\theta$ and $\frac{\sqrt{3}+1}{2\sqrt{3}}\delta\theta$ beyond them. The error involved with this method is to the fifth power of $\delta\theta$.

The program developed from Figure 3.10 has three separate blocks to scan the magnet face, its side, and its top and bottom. Calculations are repeated within each block to account for adjacent and image poles. The former requires a change of integration limits, as already mentioned, and a change of polarity compared with the centre pole. Only even numbers of image poles will give zero potential on the return plate, neighbouring image poles also being of opposite polarity. In the program, the same block is used for all these poles, and the correct polarity is selected by multiplying the function by a suitable integer power of -1.

The tests already performed indicated that a system of the type shown in Figure 3.11(a) should be sufficiently accurate. For comparison, two alternative arrangements (Figure 3.11 (b) and (c)) were also evaluated. The latter comprises 18 pole faces, and the calculation for half of the magnet's surface took 244 mins. to perform. This is clearly becoming unacceptably time-consuming, and this system should only be used if the required accuracy demands it.

A summary of the calculated results is given in Table 3.1. These refer to the geometry of the radiator cooling fan motor, although a multiplying factor that includes M_s has not yet been applied . The first set of results are for the line A-A (Figure 3.12),

Figure 3.11. Alternative systems using image poles.

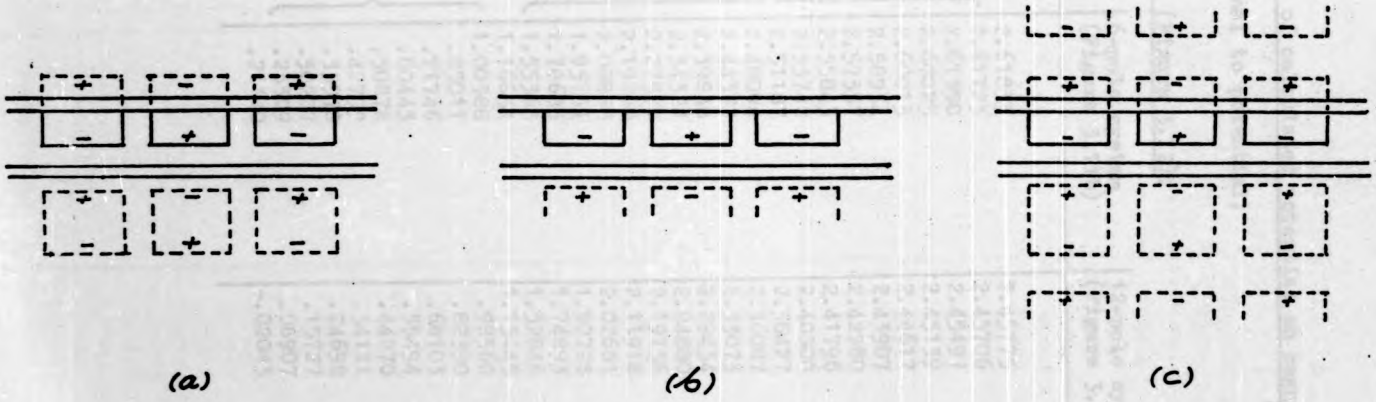

Table 3.1: Summary of calculated potential on magnet surface.

(figures proportional to potential)

(a) Along line A-A (Figure 3.12).

position	6-pole system (Figure 3.11b)	12-pole system (Figure 3.11a)	18-pole system (Figure 3.11c)
at magnet centre-line:	2.61833	2.45775	2.51218
at 20 equi-spaced increments along magnet face	2.61723	2.45706	2.51127
	2.61390	2.45497	2.50853
	2.60825	2.45139	2.50386
	2.60013	2.44617	2.49712
	2.58934	2.43907	2.48809
	2.57557	2.42980	2.47646
	2.55843	2.41796	2.46185
	2.53742	2.40300	2.44373
	2.51187	2.38427	2.42143
	2.48094	2.36087	2.39410
	2.44373	2.33073	2.36090
	2.39838	2.29434	2.31983
	2.34324	2.24880	2.26927
	2.27578	2.19156	2.20671
	2.19260	2.11918	2.12869
	2.08888	2.02681	2.03041
	1.95751	1.90728	1.90472
	1.78685	1.74893	1.73996
	1.55365	1.52846	1.51287
at magnet corner:	1.16654	1.15445	1.13203
at 10 equi-spaced increments along magnet side	1.00388	.98560	.95606
	.85011	.82390	.78807
	.71746	.68103	.63997
	.60443	.55494	.50997
	.50876	.44270	.39544
	.42799	.34111	.29350
	.35978	.24698	.20132
	.30207	.15727	.11625
	.25309	.06907	.03585
at backing plate:	.21140	-.02043	-.04218

continued

Table 3.1: Summary of calculated potential on magnet surface.

(figures proportional to potential)

(a) Along line A-A (Figure 3.12).

position	6-pole system (Figure 3.11b)	12-pole system (Figure 3.11a)	18-pole system (Figure 3.11c)
at magnet centre-line:	2.61833	2.45775	2.51218
at 20 equi-spaced increments along magnet face	2.61723	2.45706	2.51127
	2.61390	2.45497	2.50853
	2.60825	2.45139	2.50386
	2.60013	2.44617	2.49712
	2.58934	2.43907	2.48809
	2.57557	2.42980	2.47646
	2.55843	2.41796	2.46185
	2.53742	2.40300	2.44373
	2.51187	2.38427	2.42143
	2.48094	2.36087	2.39410
	2.44373	2.33073	2.36090
	2.39838	2.29434	2.31983
	2.34324	2.24880	2.26927
	2.27578	2.19156	2.20671
	2.19260	2.11918	2.12869
	2.08888	2.02681	2.03041
	1.95751	1.90728	1.90472
	1.78685	1.74893	1.73996
	1.55365	1.52846	1.51287
at magnet corner:	1.16654	1.15445	1.13203
at 10 equi-spaced increments along magnet side	1.00388	.98560	.95606
	.85011	.82390	.78807
	.71746	.68103	.63997
	.60443	.55494	.50997
	.50876	.44270	.39544
	.42799	.34111	.29350
	.35978	.24698	.20152
	.30207	.15727	.11625
	.25309	.06907	.03585
at backing plate:	.21140	-.02043	-.04218

continued

Table 3.1: Summary of calculated potential on magnet surface.

(figures proportional to potential)

(a) Along line A-A (Figure 3.12).

position	6-pole system (Figure 3.11b)	12-pole system (Figure 3.11a)	18-pole system (Figure 3.11c)
at magnet centre-line:	2.61833	2.45775	2.51218
at 20 equi-spaced increments along magnet face	2.61723	2.45706	2.51127
	2.61390	2.45497	2.50853
	2.60825	2.45139	2.50386
	2.60013	2.44617	2.49712
	2.58934	2.43907	2.48809
	2.57557	2.42980	2.47646
	2.55843	2.41796	2.46185
	2.53742	2.40300	2.44373
	2.51187	2.38427	2.42143
	2.48094	2.36087	2.39410
	2.44373	2.33073	2.36090
	2.39838	2.29434	2.31983
	2.34324	2.24880	2.26927
	2.27578	2.19156	2.20671
	2.19260	2.11918	2.12869
	2.08888	2.02681	2.03041
	1.95751	1.90728	1.90472
	1.78685	1.74893	1.73996
	1.55365	1.52846	1.51287
at magnet corner:	1.16654	1.15445	1.13203
at 10 equi-spaced increments along magnet side	1.00388	.98560	.95606
	.85011	.82390	.78807
	.71746	.68103	.63997
	.60443	.55494	.50997
	.50876	.44270	.39544
	.42799	.34111	.29350
	.35978	.24698	.20132
	.30207	.15727	.11625
	.25309	.06907	.03585
at backing plate:	.21140	-.02043	-.04218

continued

Table 3.1 (continued).

(b) Along line B-B (Figure 3.12).

position	6-pole system (Figure 3.11b)	12-pole system (Figure 3.11a)	18-pole system (Figure 3.11c)
at backing plate:	.37657	-.14416	-.04454
at 10 equi-spaced increments along magnet bottom	.43737	.00199	.07151
	.50584	.14378	.18930
	.58272	.28344	.31023
	.66865	.42300	.43564
	.76418	.56426	.56668
	.86961	.70868	.70422
	.98487	.85725	.84870
	1.10926	1.01024	.99993
	1.24110	1.16688	1.15667
at magnet corner:	1.36797	1.31561	1.30694
at 25 equi-spaced increments along magnet face	1.81310	1.75046	1.74731
	2.04808	1.97518	1.97757
	2.20588	2.12284	2.13075
	2.31846	2.22547	2.23885
	2.40137	2.29873	2.31748
	2.46366	2.35173	2.37573
	2.51101	2.39024	2.41932
	2.54709	2.41800	2.45179
	2.57432	2.43751	2.47614
	2.59429	2.45042	2.49345
	2.60798	2.45776	2.50491
	2.61593	2.46013	2.51108
	2.61833	2.45775	2.51218
	2.61506	2.45052	2.50807
	2.60565	2.43801	2.49833
	2.58931	2.41943	2.48215
	2.56480	2.39352	2.45827
	2.53028	2.35846	2.42485
	2.48310	2.31156	2.37923
	2.41939	2.24892	2.31750
	2.33339	2.16475	2.23388
	2.21612	2.05000	2.11934
	2.05239	1.88944	1.95866
	1.81122	1.65202	1.72081
at magnet corner:	1.36846	1.21327	1.28178
at 10 equi-spaced increments along magnet top	1.26650	1.05302	1.14721
	1.15675	.88172	1.00372
	1.05385	.71347	.86543
	.95766	.54724	.73181
	.86808	.38205	.60241
	.78502	.21686	.47674
	.70833	.05052	.35423
	.63778	-.11822	.23428
	.57312	-.29072	.11621
at backing plate:	.51402	-.46843	-.00070

Figure 3.12: Examples of potential on magnet face.

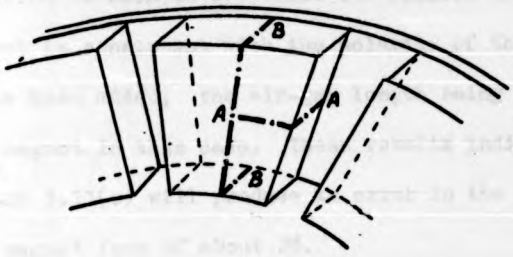

which is at a constant radius of 47 mm. The second set are for the magnet centre-line B-B, about which the potentials are symmetrical. The addition of a further six pole faces to the system brings the potentials closer to their correct values, though each subsequent calculation is seen to overshoot the correct value. The direction of overshoot is consistent with the polarity of the dominant pole face that has been added, the air-gap length being much less than that of the magnet in this case. These results indicate that the system of Figure 3.11(a) will produce an error in the calculated potentials on the magnet face of about 2%.

It is now possible to see the error incurred by assuming a constant potential over the whole magnet surface. The results for Figure 3.11(a) are shown graphically in Figure 3.13, and there is a noticeable decrease in potential as the edges of the pole face are approached. The need to consider the three-dimensional system is also clearly shown.

There now exists a complete method for solving the field in the air-gap of a machine having homogeneous uniformly magnetised poles. It can be as easily applied to the double-sided magnet arrangement as to the single-sided one described here. For the former, a zero-potential plane would occur halfway across the air-gap, and the closer proximity of this to the armature conductors would lead to slightly more accurate results.

In the radiator cooling fan motor, the flux return ring is incorporated in the armature. It was mentioned in Section 2.4 that a slotted ring would be desirable, but as yet could not be manufactured for that size of machine from the available materials.

Figure 3.13: Potential distribution on magnet surface.

(along the lines indicated on Figure 3.12).

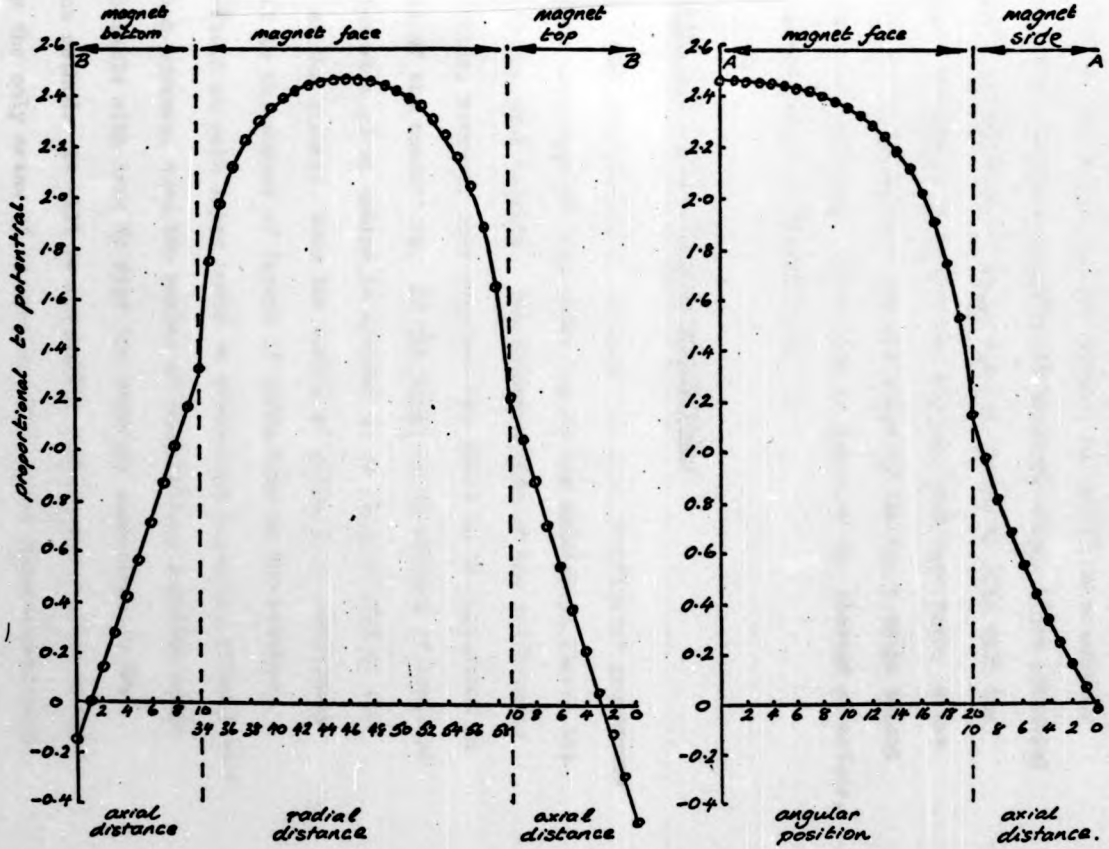

It is hoped, though, that future work might succeed in this, for larger diameter machines at least. This method of field calculation could then be adapted to the new system, to provide a reasonably accurate result within a complicated boundary shape. Zero potential would exist on the slotted ring, and the theory to cope with the additional changes in grid size has already been developed. A new problem would be to account for the shape of the image poles beyond the surface of the ring. These have to describe the slotted structure, in the manner shown in Figure 3.14.

3.4. Direct calculation of magnetising force.

The possibility of extension to more complicated geometries is a clear advantage of this model, as is its ability to survey the whole air-gap most quickly. The determination of the performance of a machine, however, only requires the field to be calculated in the path of the conductors. If the force on an element of armature conductor at a given radius is assumed to be concentrated at the centre of the element, then the number of paths to be considered is equal to the number of layers of conductors in the armature. If the field at each layer could be determined directly, without an iteration process, then the number of calculations involved would be comparable with that to find the boundary conditions in the previous method. It will be worthwhile considering further whether that is the only means of accurately solving the three-dimensional field problem.

In order to complete the boundary conditions on the magnet surface, Equation 3.19 was developed. The possibility of calculating the potential at the grid points directly from this has already been

It is hoped, though, that future work might succeed in this, for larger diameter machines at least. This method of field calculation could then be adapted to the new system, to provide a reasonably accurate result within a complicated boundary shape. Zero potential would exist on the slotted ring, and the theory to cope with the additional changes in grid size has already been developed. A new problem would be to account for the shape of the image poles beyond the surface of the ring. These have to describe the slotted structure, in the manner shown in Figure 3.14.

3.4. Direct calculation of magnetising force.

The possibility of extension to more complicated geometries is a clear advantage of this model, as is its ability to survey the whole air-gap most quickly. The determination of the performance of a machine, however, only requires the field to be calculated in the path of the conductors. If the force on an element of armature conductor at a given radius is assumed to be concentrated at the centre of the element, then the number of paths to be considered is equal to the number of layers of conductors in the armature. If the field at each layer could be determined directly, without an iteration process, then the number of calculations involved would be comparable with that to find the boundary conditions in the previous method. It will be worthwhile considering further whether that is the only means of accurately solving the three-dimensional field problem.

In order to complete the boundary conditions on the magnet surface, Equation 3.19 was developed. The possibility of calculating the potential at the grid points directly from this has already been

Figure 3.14: Image pole arrangement for a slotted return ring.

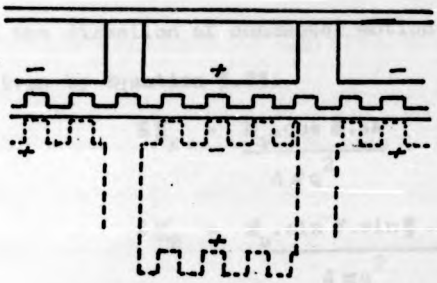

ruled out. However, the gradient of Equation 3.19 yields the magnetising force, $\delta \underline{H}$, at the point Q due to an element of the pole face, δA. $\delta \underline{H}$ is then given by

$$\delta \underline{H} = \frac{M_s . \underline{q} . \delta A}{4\pi |q|^3} \qquad (3.21)$$

The performance characteristics of the machine can be found from the axial component of $\delta \underline{H}$, given by Equation 3.22. If, however, the alternating axial forces on the disc are required, the component of $\delta \underline{H}$ in the direction of conductor motion will be relevant, and this is given by Equation 3.23.

$$\delta H_x = \frac{M_s . \cos \delta . \delta A}{4\pi q^2} \qquad (3.22)$$

$$\delta H_\theta = \frac{M_s . \sin \gamma . \sin \phi . \delta A}{4\pi q^2} \qquad (3.23)$$

Clearly, neither of Equations 3.22 or 3.23 are easier to solve than Equation 3.19, which illustrates how time consuming it would be to calculate the field in the whole air-gap directly. It has already been shown that Laplace's equation in $\underline{H}$ (Equation 3.6) is valid within these permanent magnets, as it also is in air. An iterative solution could therefore be found directly in $\underline{H}$, the boundary conditions being determined by Equations 3.22 and 3.23. However, not only the magnet surface, but all the boundaries would require their application. There would, therefore, appear to be no clear advantage of this method over either the direct calculation or the iteration of potential.

The magnetising force producing useful torque on an element of conductor, due to a pole face, is given by the integration of Equation 3.22 over that pole face. As with the evaluation of

ruled out. However, the gradient of Equation 3.19 yields the magnetising force, $\delta \underline{H}$, at the point Q due to an element of the pole face, δA. $\delta \underline{H}$ is then given by

$$\delta \underline{H} = \frac{M_s . q . \delta A}{4\pi |q|^3} \qquad (3.21)$$

The performance characteristics of the machine can be found from the axial component of $\delta \underline{H}$, given by Equation 3.22. If, however, the alternating axial forces on the disc are required, the component of $\delta \underline{H}$ in the direction of conductor motion will be relevant, and this is given by Equation 3.23.

$$\delta H_x = \frac{M_s . \cos \delta . \delta A}{4\pi q^2} \qquad (3.22)$$

$$\delta H_\theta = \frac{M_s . \sin \gamma . \sin \xi . \delta A}{4\pi q^2} \qquad (3.23)$$

Clearly, neither of Equations 3.22 or 3.23 are easier to solve than Equation 3.19, which illustrates how time consuming it would be to calculate the field in the whole air-gap directly. It has already been shown that Laplace's equation in $\underline{H}$ (Equation 3.6) is valid within these permanent magnets, as it also is in air. An iterative solution could therefore be found directly in $\underline{H}$, the boundary conditions being determined by Equations 3.22 and 3.23. However, not only the magnet surface, but all the boundaries would require their application. There would, therefore, appear to be no clear advantage of this method over either the direct calculation or the iteration of potential.

The magnetising force producing useful torque on an element of conductor, due to a pole face, is given by the integration of Equation 3.22 over that pole face. As with the evaluation of

potential, the effect of image and adjacent poles will have to be taken into account. The results of the magnet tests (Figure 3.9) and the subsequent calculations (Table 3.1) are still valid, since $\underline{H}$ decreases more rapidly with q than Φ does. In fact, because of this, it may be possible to use the six pole face system of Figure 3.11 (b) for the determination of $\underline{H}$ at the armature conductors. The accuracy of such a change can be gauged best by measurements in a motor, and these will show that the simplified system can be adopted for the evaluation of Equations 3.22.and 3.23.

Comparison has already been made in Section 2.1 between the pole shape of the Disc-Armature motor, and that of the printed circuit motor. Using Equation 3.22, the axial field distribution in the former could be compared with that produced by circular poles if desired.* Reference 8 is again used, and the field at a point Q due to a circular pole face (Figure 3.15) is given by Equation 3.24. Similarly, that due to a segment (Figure 3.7) is given by Equation 3.25.

$$H_x = \frac{M_s x}{4\pi}\int_0^{2\pi}\left[\frac{1}{(x^2 + s^2\sin^2\theta)}\left\{\frac{R.s.\cos\theta - x^2 - s^2}{(R^2 + x^2 + s^2 - 2.R.s.\cos\theta)^{\frac{1}{2}}} + (x^2 + s^2)^{\frac{1}{2}}\right\}\right]d\theta \qquad .....(3.24)$$

$$H_x = \frac{M_s x}{4\pi}\int_{-\beta}^{\alpha-\beta}\left[\frac{r.s.\cos\theta - x^2 - s^2}{(x^2 + s^2\sin^2\theta)(r^2 + x^2 + s^2 - 2.r.s.\cos\theta)^{\frac{1}{2}}}\right]_{r=R_1}^{R_2} d\theta \qquad .....(3.25)$$

For both of these expressions, the integration in the angular direction has to be performed by numerical means, and the Gauss method is employed for the same reasons as before. A program

* This has been done (Reference 31), and the results showed the segment shape to be preferable to the circular poles.

Figure 3.15: Position of a point, Q, related to a circular pole face.

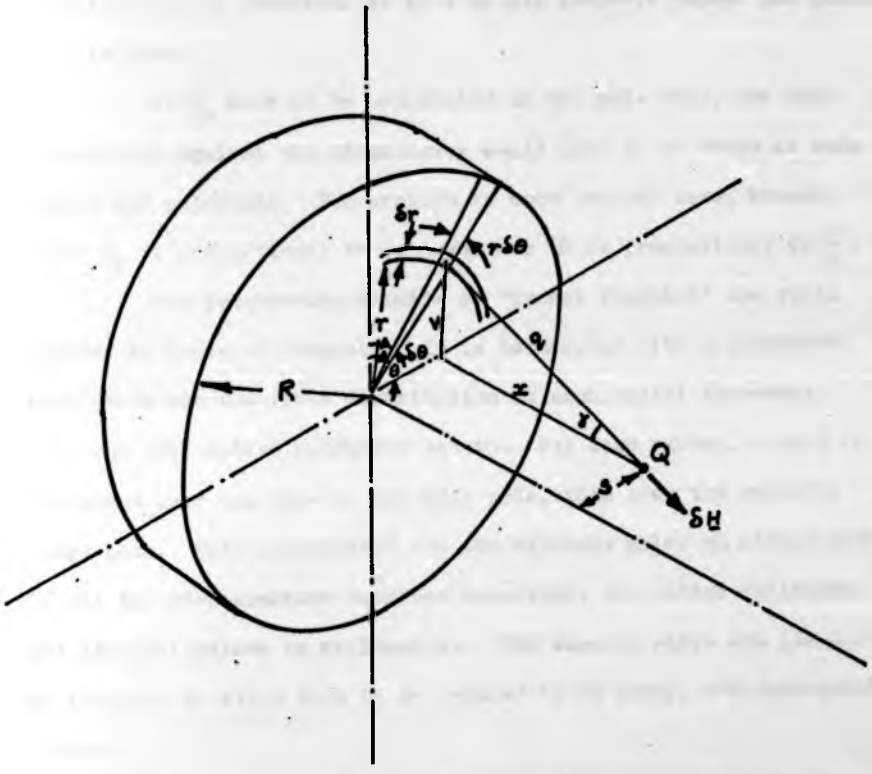

Figure 3.15: Position of a point, Q, related to a circular pole face.

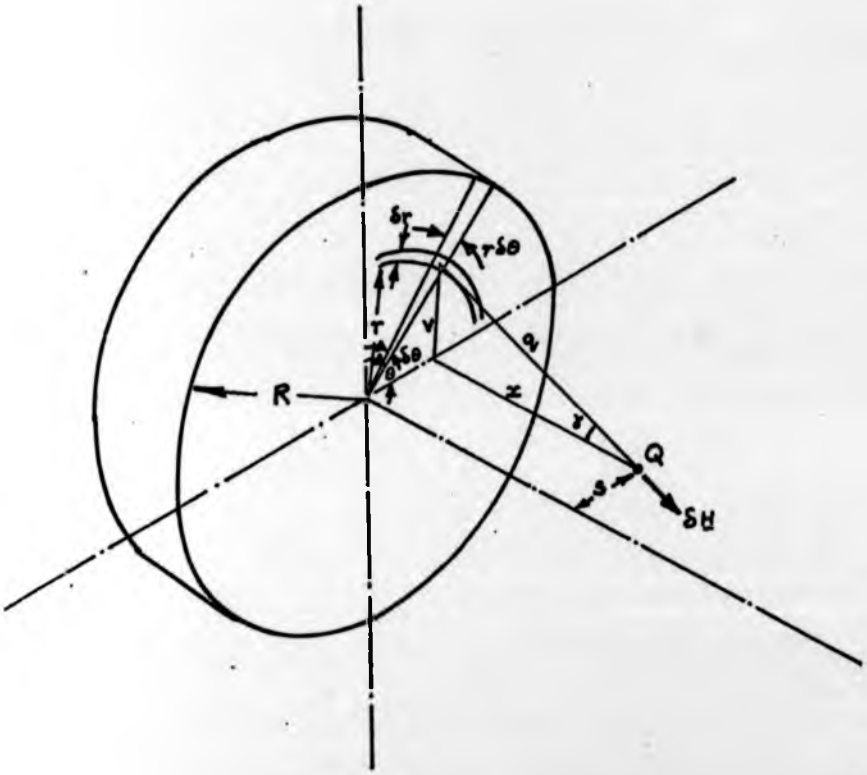

entitled "Normal Fluxplot" was written to evaluate Equation 3.25, and its flow diagram is shown in Figure 3.16. The program for Equation 3.24 is identical to this in all respects except the function that is used.

If H_x were to be calculated on the pole face, the same precautions against the singularity would have to be taken as were needed for potential. The problem is more serious here, though, since H_x is proportional to $\frac{1}{q^2}$, whereas ψ is proportional to $\frac{1}{q}$.

The programming details of "Normal Fluxplot" are quite similar to those of "Magpot". It is terminated with a procedure that plots out the field distribution at each radial increment, over the full active conductor length. For each radius, a scan is performed over the face of the main pole, then over the opposite image pole. This is repeated for the adjacent poles on either side. In all the Disc-Armature machines described, the radial distances are integral values in millimetres. The angular steps are identified by integers to allow them to be stored in an array, and subsequently plotted.

Figure 3.17 shows the field distribution calculated at a few radii for the radiator cooling fan motor. These examples indicate the importance of considering the three-dimensional system, because of the noticeable variation with radius. It will be more useful to study the field distribution along a conductor's length, and so the program was amended to "Normal Fluxplot 2". The only difference in this is that, for each angular position now, the scan is performed over the pole faces. Typical results that apply to the fan motor are shown in Figure 3.18. The plot on the neutral line between two adjacent magnets should be entirely zero, due to symmetry in

Figure 3.16: Flow diagram of the program "Normal Fluxplot".

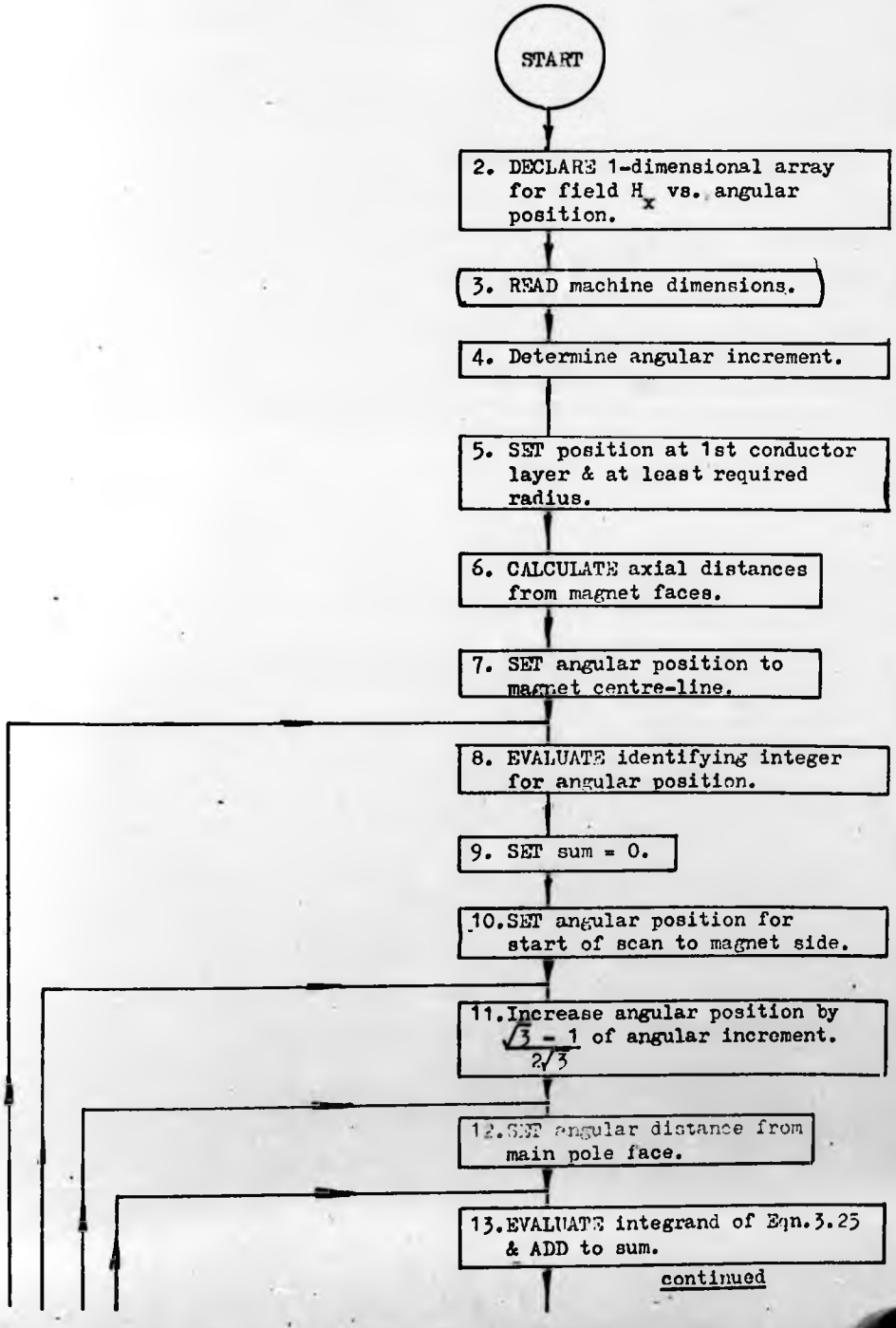

Figure 3.16 (continued)

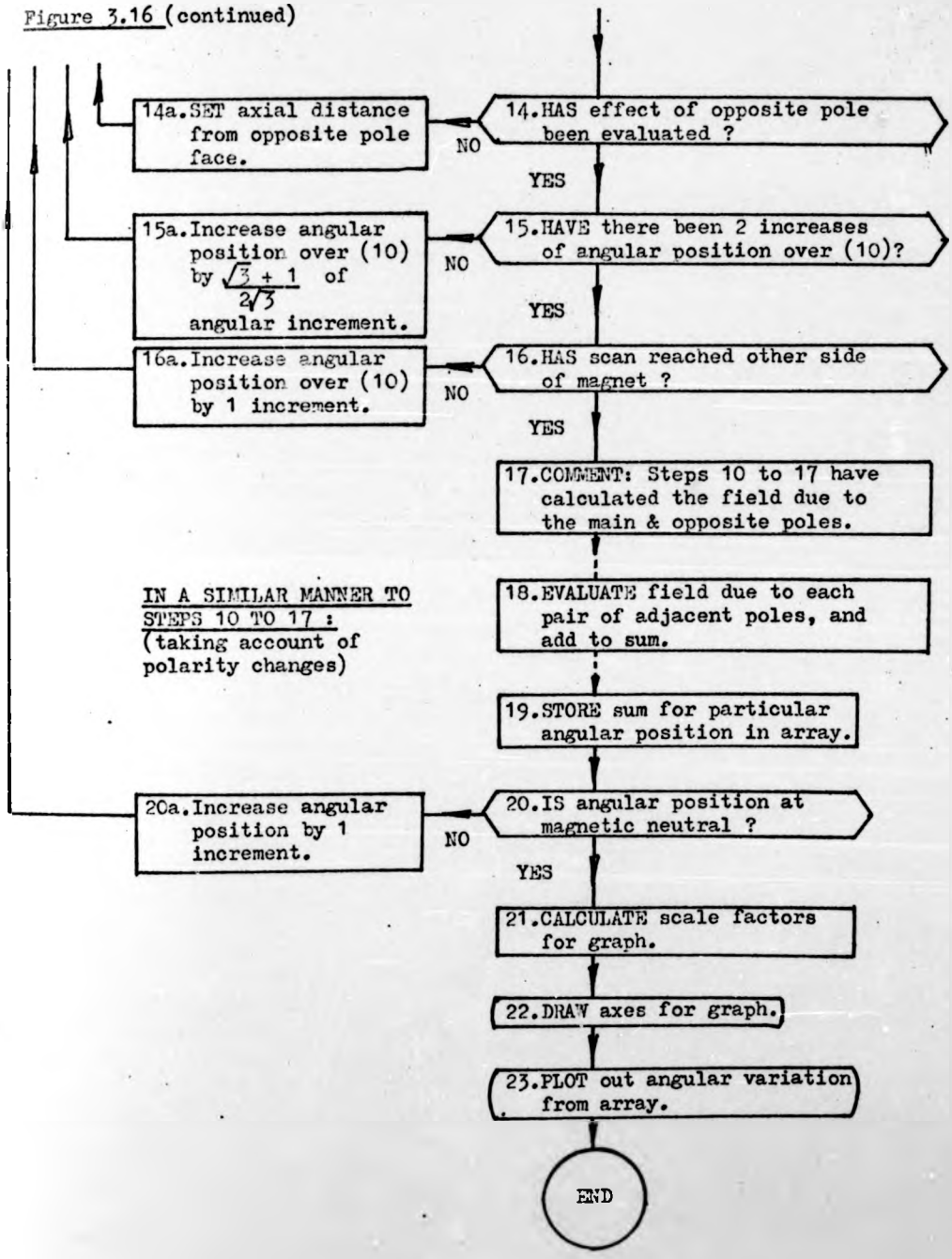

Figure 3.17: Angular field distribution at certain radii in the fan motor.

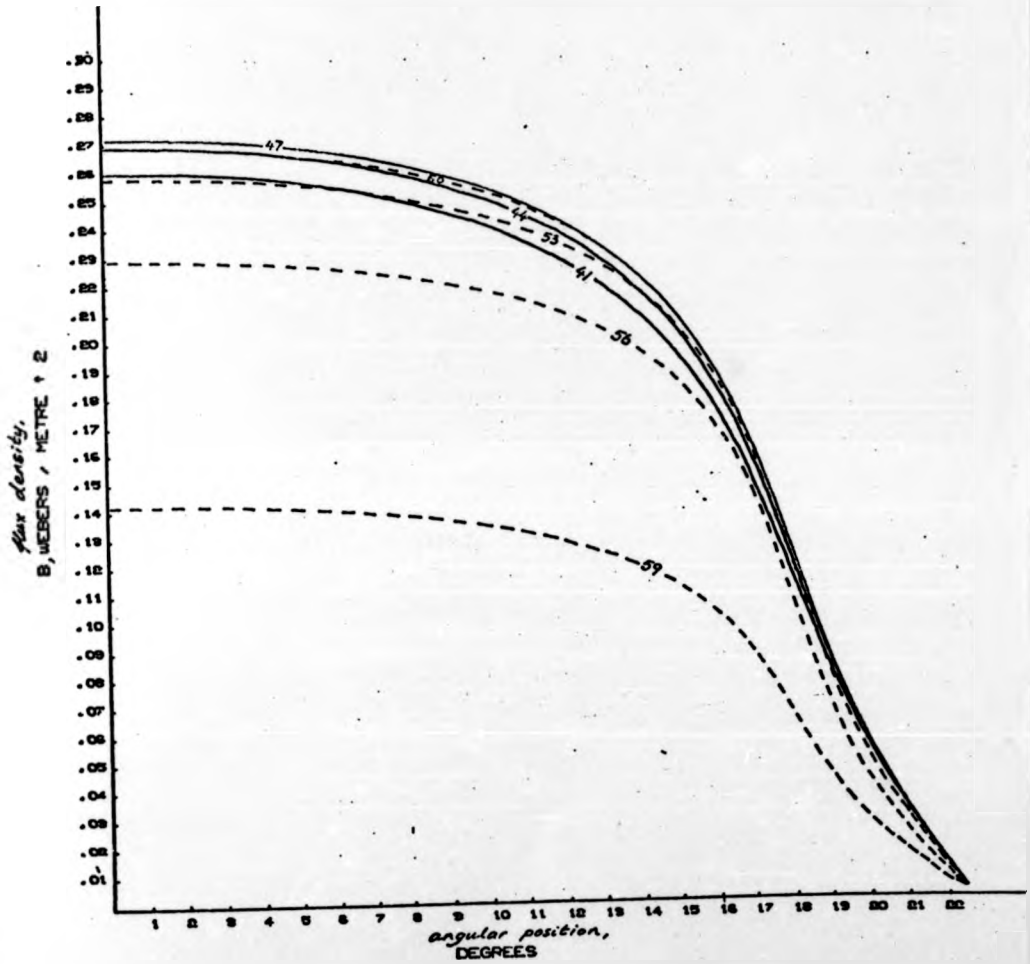

Figure 3.18. Radial field distributions in the fan motor.

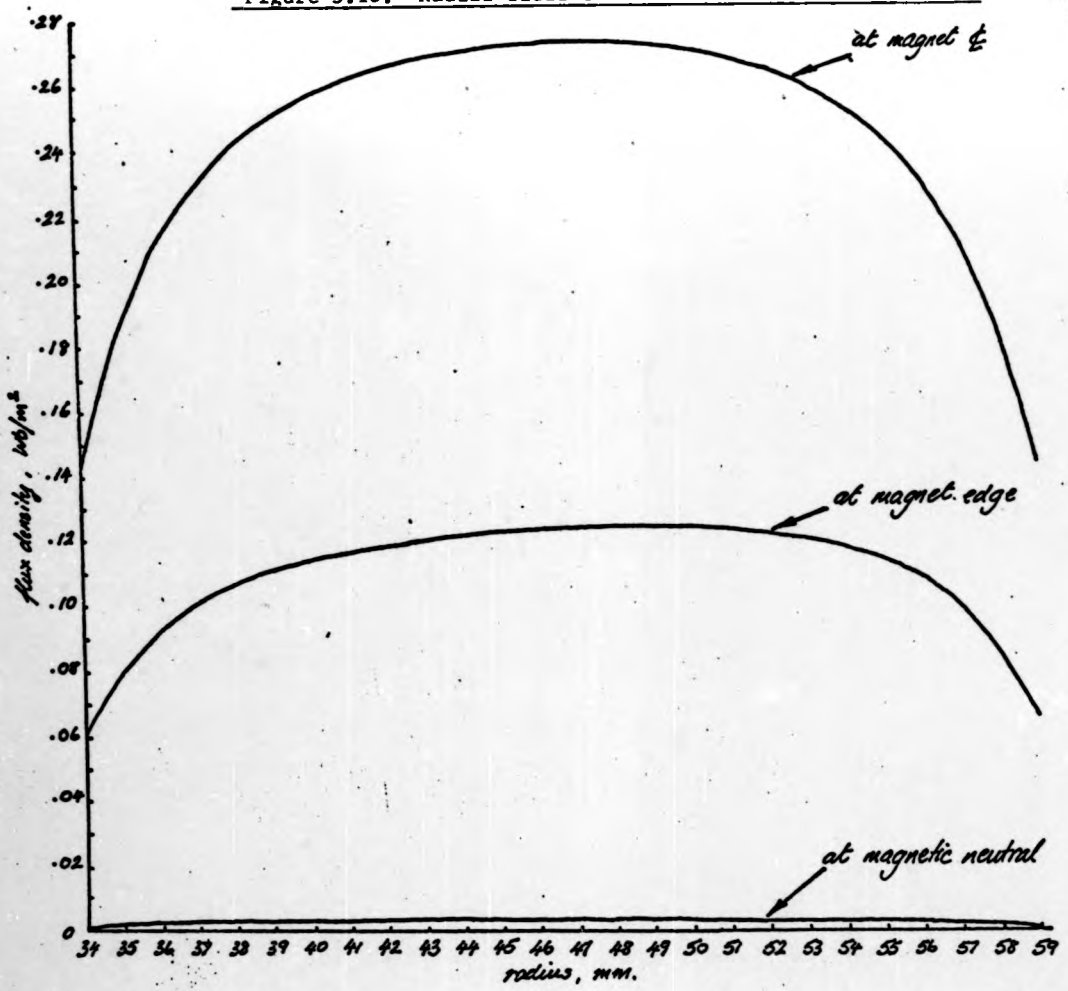

the complete machine. The error shown is caused by the use of only three adjacent magnets in the calculation, its maximum value being approximately 0.003 Wb/m^2.

3.4.1. Superposition, and the effect of neighbouring magnetic materials.

All of the programs so far described account for the presence of image and adjacent poles by the superposition of their effects at various axial and angular distances. The number of such poles required has been estimated by the tests of Figure 3.9., though it is being assumed that a six pole face system will suffice for the evaluation of Equation 3.25. This can be verified theoretically by calculating the field over a wide arc at various distances from a single pole face. This must be done for either H_x or H_θ, since the vector nature of $\underline{H}$ precludes a simple superposition of results. The former is the more significant, and it is evaluated for the radiator cooling fan motor at distances that will yield the axial field distribution entering the flux return ring. The fields of an isolated pole face at radii of 41 mm., 47 mm., and 53 mm. are given in Figure 3.19. By suitable additions of these results, the systems of Figure 3.11 can be built up (the direction of H_x is of opposite polarity due to pole faces on either side of the flux return ring surface). A comparison is then made between the three systems for each radius in Figure 3.20.

The closest approximation to zero axial field on the magnetic neutrals will be obtained from the simplest system, since the more remote pole faces contribute more to H_x in this region. Consider, for example, the maximum field at a radius of 47 mm., which occurs on the plane from the centre-line of the main pole.

Figure 3.19. Field distribution from an isolated pole face of the fan motor

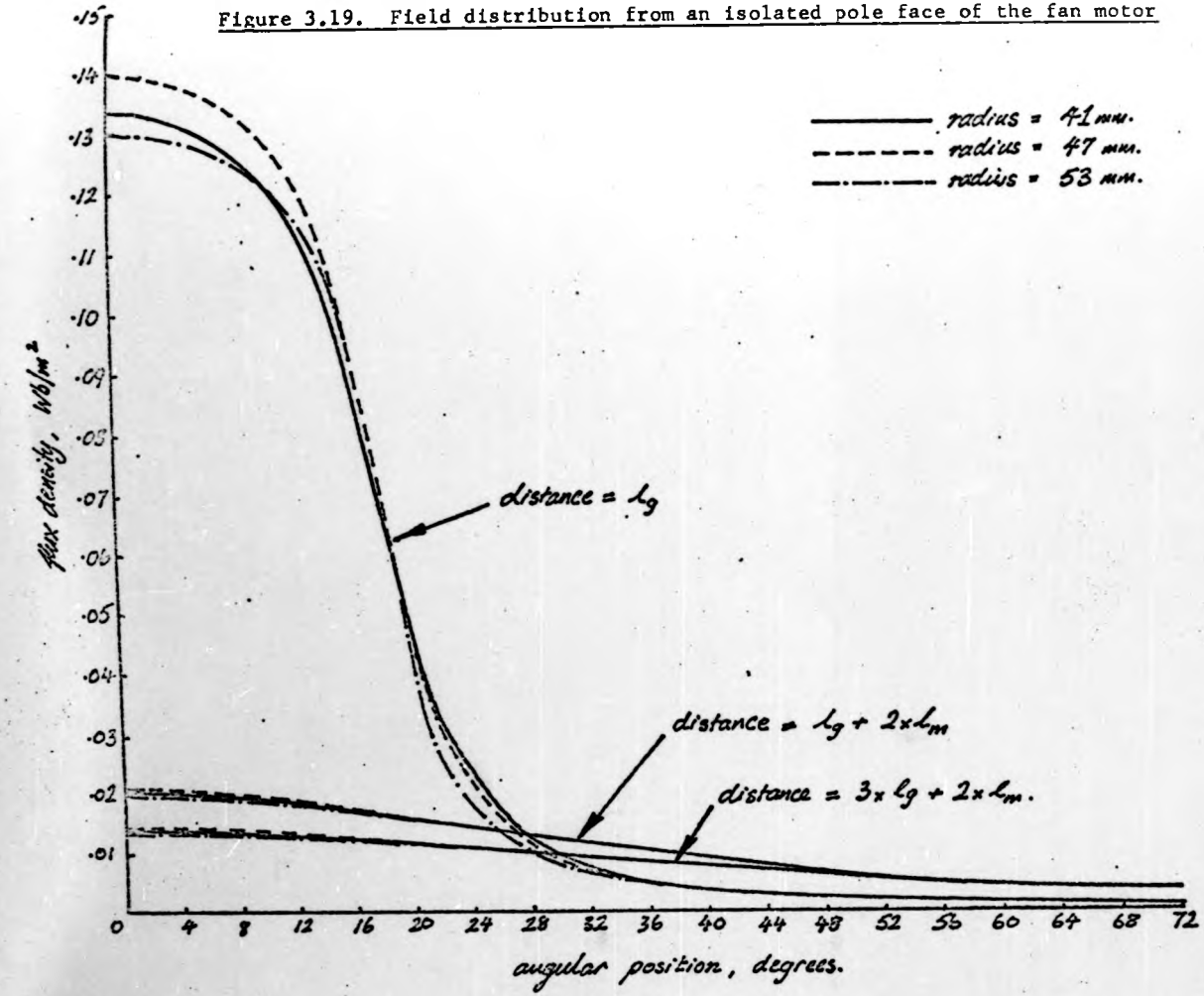

Figure 3.20. Superposition of field distributions for the fan motor.

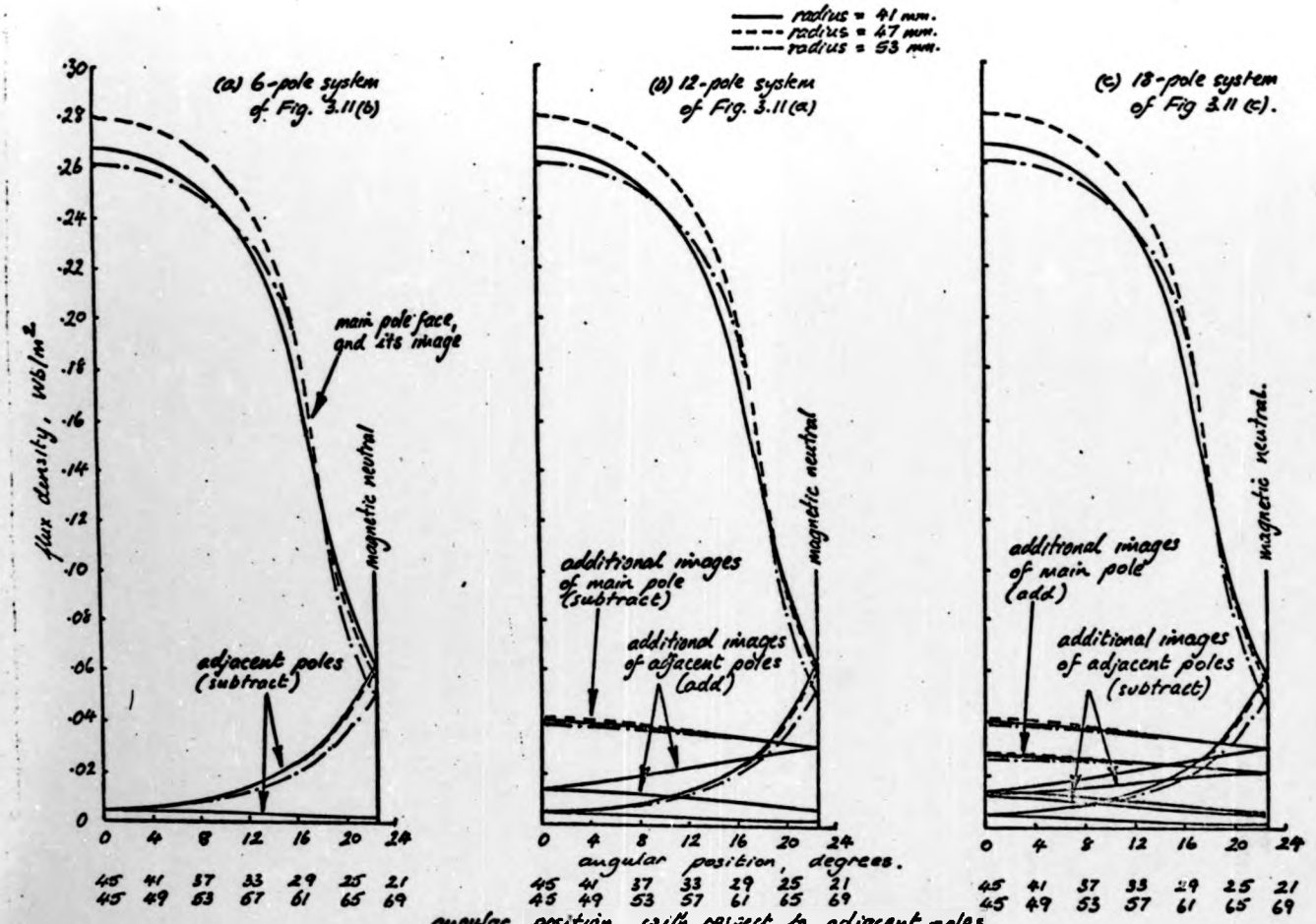

The effect of adding more poles to the system is summarised in Table 3.2. There is a noticeable discrepancy in the result from 12 poles, whereas the use of 6 poles yields a field very similar to that from 18 poles. This supports the use of the simplest system for these calculations, and close agreement will be found with experimental results.

The main consideration in developing the theory of the magnetic circuit has been the eventual determination of machine performance. It will be clear that the angular field distribution could be developed from Equation 3.23 in an identical manner to that of the axial field. H_x and H_ρ can be combined to give a magnitude and direction to the field throughout the system, including the magnet's interior if required. Of particular relevance to machine design would be the magnet's operating point on open circuit. It is quite likely that this would not be a unique point, but a short band on the B-H characteristic. Its position would indicate whether the magnets must be magnetised after assembly into the machine.

Two alternative methods of calculating the useful field in the air-gap have been developed. A complicated geometry, for example the existence of slots in the flux return ring to house the conductors, would require an iterative solution to Laplace's equation in potential, followed by the use of $\underline{H} = -\text{grad}\,\psi$. For the simpler geometries that allow an easy substitution of image poles, a direct calculation of the field is quicker, provided it is only required over a limited region. In order to derive machine performance, these methods must be related to the design of

the armature and the arrangement of the conductors within it.

Table 3.2: Calculated field normal to magnet face, on its centre-line at 47mm. radius.

	Field, Wb/m^2
6-pole system (Figure 3.11(b)):	0.271
12-pole system (Figure 3.11(a)):	0.265
18-pole system (Figure 3.11(c)):	0.271

4. ARMATURE WINDINGS.

4.1. E.M.F. and Torque of an armature conductor in the fan motor.

A direct method of calculating the magnetising force, and hence the flux density, has been developed for the Disc-Armature machine. It is only economical to use, though, if the number of calculations is restricted, for example, to the positions of the conductors. These positions must now be related to the magnet systems described in Chapter 3.

The shape of an individual armature coil has already been described (Figure 1.2). Its sides, which contain the active lengths of conductor, lie approximately in the radial direction in the machine. The coils are connected together as a double layer winding in the radiator cooling fan motor, and as two such windings in parallel in the electric vehicle traction motor. The former will be used as an example in this chapter, and a portion of the winding arrangement is shown in Figure 4.1.

Although the moulding of the armature winding in epoxy resin does not assure this, it will be assumed that each layer lies at a unique distance from the main pole face. It will further be assumed that the complete layer of epoxy resin separating the conductor layers, and those between each conductor layer and its respective armature surface, are of equal thickness. In practice, the armature thickness is only slightly greater than twice the overall conductor diameter in such a winding. The separating and covering layers of epoxy resin are therefore very thin, and even if the last assumption were invalid, this would be of little significance.

Figure 4.1. A double-layer winding arrangement.

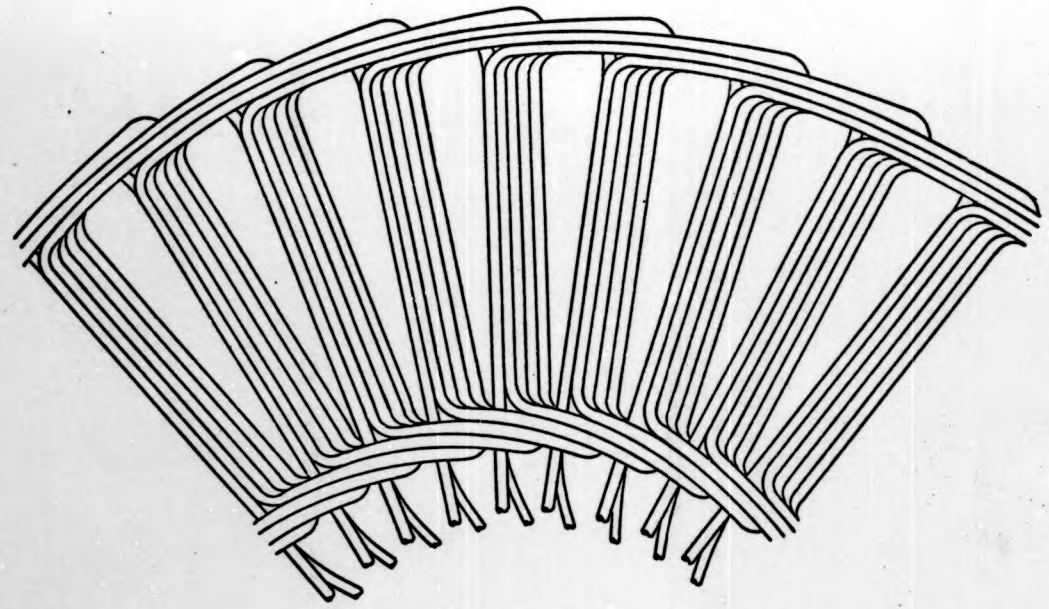

Figure 4.2 shows the double layer winding positioned in the air-gap of machines with a single and a double set of magnets. In order to minimise the number of calculations, the finite conductor diameter will be ignored for the purpose of determining conductor e.m.f., and each layer will be assumed to lie in a single plane passing through the centres of the active lengths. The distance of the $m^{th.}$ layer from the main pole face is given by Equation 4.1, and this can be used for any number of layers, n.

$$x = \frac{m(t - n.d)}{n + 1} + \frac{(2m - 1)d}{2} + c \qquad (4.1)$$

where t = thickness of the armature disc,

d = overall conductor diameter,

c = clearance between armature and main pole face.

This distance, x, is identical to x in Equations 3.24 and 3.25.

Equation 3.25 gives the magnetising force, H_x, giving angular motion to any element of conductor along its active length. The flux density associated with H_x is $B_{i,j}$, which produces an induced e.m.f. in the element. The summation of these elemental e.m.f.s over the whole active length will give the conductor e.m.f. at a particular angular position. However, this summation must be performed in accordance with Equations 2.8. and 2.9, since the radius of the element, r_i, is inseparable from $B_{i,j}$. In order that the winding design may be studied, there will be no use made in this chapter of the total armature e.m.f., given by Equations 2.11 and 2.13.

The evaluation of Equation 3.25 requires a numerical integration in the angular direction, and produces discrete results along a conductor. The conductor is therefore divided into elements of length δr, and the function evaluated at the junction of these

Figure 4.2 shows the double layer winding positioned in the air-gap of machines with a single and a double set of magnets. In order to minimise the number of calculations, the finite conductor diameter will be ignored for the purpose of determining conductor e.m.f., and each layer will be assumed to lie in a single plane passing through the centres of the active lengths. The distance of the $m^{th.}$ layer from the main pole face is given by Equation 4.1, and this can be used for any number of layers, n.

$$x = \frac{m(t - n.d)}{n + 1} + \frac{(2m - 1)d}{2} + c \qquad (4.1)$$

where t = thickness of the armature disc,

d = overall conductor diameter,

c = clearance between armature and main pole face.

This distance, x, is identical to x in Equations 3.24 and 3.25.

Equation 3.25 gives the magnetising force, H_x, giving angular motion to any element of conductor along its active length. The flux density associated with H_x is $B_{i,j}$, which produces an induced e.m.f. in the element. The summation of these elemental e.m.f.s over the whole active length will give the conductor e.m.f. at a particular angular position. However, this summation must be performed in accordance with Equations 2.8. and 2.9, since the radius of the element, r_i, is inseparable from $B_{i,j}$. In order that the winding design may be studied, there will be no use made in this chapter of the total armature e.m.f., given by Equations 2.11 and 2.13.

The evaluation of Equation 3.25 requires a numerical integration in the angular direction, and produces discrete results along a conductor. The conductor is therefore divided into elements of length δr, and the function evaluated at the junction of these

Figure 4.2. Position of a double-layer winding in the air gap.

(a) single set of magnets.

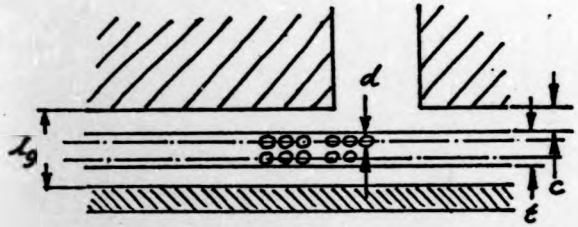

(b) double set of magnets.

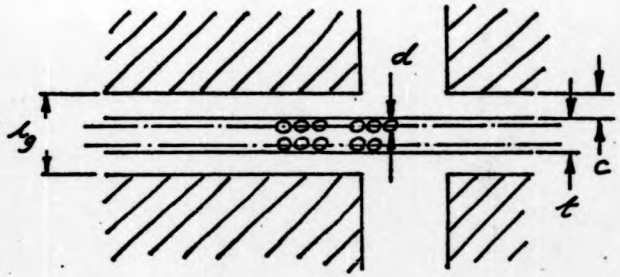

elements. This was the reason for defining $\bar{P}_j$ alternatively by Equation 2.10, which must be used here instead of Equation 2.8. A direct measure of conductor e.m.f will be more helpful here than the moment of flux density. Since $l = n.\delta r$, Equations 2.9.and 2.10 can be combined to produce Equation 4.2.

$$e_j = w.\delta r \sum_{r_i=R_1}^{R_2} \underline{B}_{i,j}.r_i \qquad (4.2)$$

Consideration of the power in the conductor yields an expression for the torque, T_j, at angular position j as

$$T_j = I_c.\delta r \sum_{r_i=R_1}^{R_2} \underline{B}_{i,j}.r_i \qquad (4.3)$$

where I_c = current in the conductor.

The summation of Equations 4.2.and 4.3 is performed in the manner of the Romberg numerical integration method (Reference 9). Unlike the Gauss method, this calculates the function at the boundaries of each interval, and thus uses fewer calculations for any given interval size. It is more straighforward for a simple summation of this kind, although the error is proportional to the cube of δr. Figure 4.3 shows how the Romberg method would be applied to a field distribution similar to those given in Figure 3.18. The function is calculated at the points shown, the values at R_1 and R_2 being given half weight. Equations 4.2.and 4.3 will therefore be evaluated as Equations 4.4 and 4.5 respectively.

$$e_j = w.\delta r \left(\tfrac{1}{2}.B_{0,j}.r_0 + B_{1,j}.r_1 + \ldots\ldots + \tfrac{1}{2}.B_{n,j}.r_n\right) \qquad (4.4)$$

$$T_j = I_c.\delta r \left(\tfrac{1}{2}.B_{0,j}.r_0 + B_{1,j}.r_1 + \ldots\ldots + \tfrac{1}{2}.B_{n,j}.r_n\right) \qquad (4.5)$$

Figure 4.3. Romberg summation of a radial field distribution.

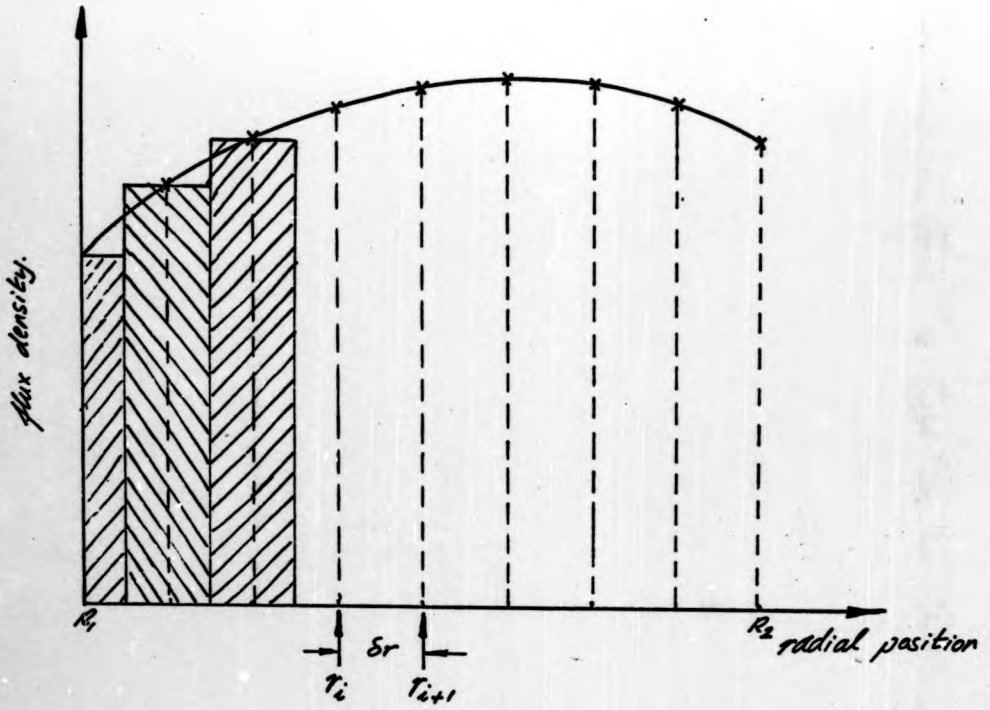

The program "Normal Fluxplot 2" already produces a radial field distribution, with a step size in this direction of one millimetre. The calculations this program performs are restricted by the inclusion of Equation 4.1, and in fact the results of Figures 3.17 and 3.18 were at the conductor layer nearest to the main pole face in the fan motor. The field distribution plot is now replaced by the summation of Equations 4.4 and 4.5, with δr equal to 1 mm.. As an example, Equation 4.4 is evaluated at the same conductor layer at the normal operating speed of the motor, and Figure 4.4 shows the variation of conductor e.m.f. over half a pole pitch.

4.2. Consideration of true conductor positions.

In practice, not all the conductors in the coils are exactly radial in the machine. The sides of each coil are bound together before the winding is assembled, the final arrangement being that of Figure 4.1. Certain conductors will therefore lie along lines that are displaced by small angles, δ, from radial lines. It will therefore be necessary to investigate what effect this has on the e.m.f. generated in a conductor, since the results of "Normal Fluxplot 2" cannot be accurate for every conductor in the machine.

It will be assumed that the same spacing exists between all conductors at the radius R_1. A machine is usually designed for the closest possible packing of conductors at this radius, and so any error in this assumption would be of little significance. All the conductors in one side of a coil will be assumed to lie parallel to the centre-line of that side, which would be the central conductor for an odd number of turns per coil. The number of

The program "Normal Fluxplot 2" already produces a radial field distribution, with a step size in this direction of one millimetre. The calculations this program performs are restricted by the inclusion of Equation 4.1, and in fact the results of Figures 3.17 and 3.18 were at the conductor layer nearest to the main pole face in the fan motor. The field distribution plot is now replaced by the summation of Equations 4.4 and 4.5, with δr equal to 1 mm.. As an example, Equation 4.4 is evaluated at the same conductor layer at the normal operating speed of the motor, and Figure 4.4 shows the variation of conductor e.m.f. over half a pole pitch.

4.2. Consideration of true conductor positions.

In practice, not all the conductors in the coils are exactly radial in the machine. The sides of each coil are bound together before the winding is assembled, the final arrangement being that of Figure 4.1. Certain conductors will therefore lie along lines that are displaced by small angles, δ, from radial lines. It will therefore be necessary to investigate what effect this has on the e.m.f. generated in a conductor, since the results of "Normal Fluxplot 2" cannot be accurate for every conductor in the machine.

It will be assumed that the same spacing exists between all conductors at the radius R_1. A machine is usually designed for the closest possible packing of conductors at this radius, and so any error in this assumption would be of little significance. All the conductors in one side of a coil will be assumed to lie parallel to the centre-line of that side, which would be the central conductor for an odd number of turns per coil. The number of

Figure 4.4: Variation of conductor e.m.f., e_j, in fan motor, at layer nearest to magnets.

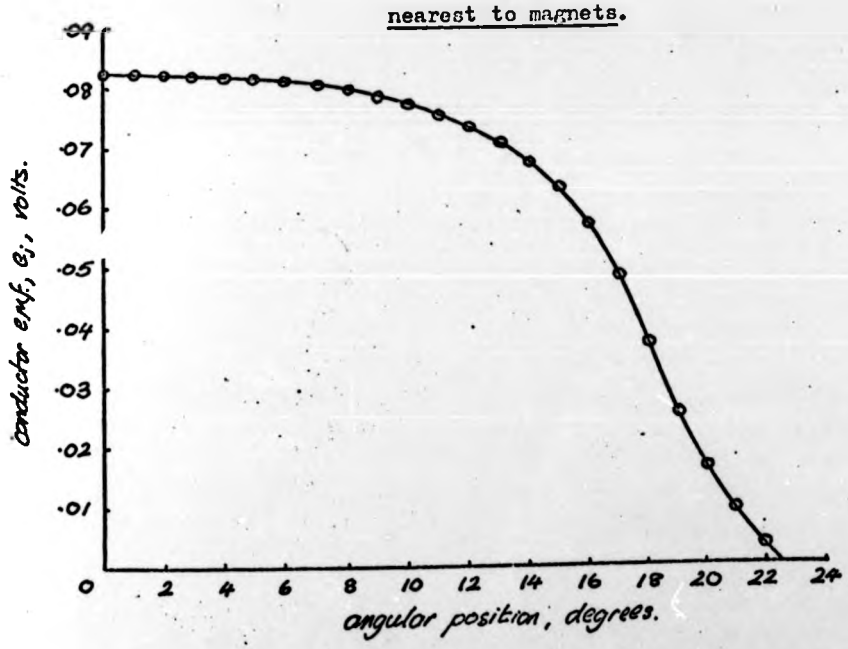

conductors per layer, C_1, is given by Equation 4.6, and this is used in Equation 4.7 to calculate the clearance between conductors in a coil side, S_c.

$$C_1 = \frac{2.(\text{turns/coil}).(\text{number of coils})}{\text{number of layers}} \qquad (4.6)$$

$$S_c = \frac{(2.\pi.R_1) - (C_1.d)}{C_1} \qquad (4.7)$$

where d = overall conductor diameter.

It will be remembered that the calculations are being performed along the conductors' centre-lines, where distances from the coil centre-line will lead to values for δ. If the number of turns per coil is written as N_{tc}, these distances, S_n, will be given by the series

$$S_n = (d + S_c).\left[\left(\frac{N_{tc}-1}{2}\right), \left(\frac{N_{tc}-1}{2}\right)-1, \left(\frac{N_{tc}-1}{2}\right)-2, \ldots, 0\right] \qquad (4.8)$$

Provided that it is small, δ will have values calculated from Equations 4.8 and 4.9.

$$\delta = \frac{S_n}{R_1} \qquad (4.9)$$

The calculations performed by "Normal Fluxplot 2" are for $\delta = 0$. They are executed along a line running through a point Q (Figure 3.7), parallel to the r-axis, from R_1 to R_2. The variation described in Figure 4.4 is achieved by incremental changes in β. However, the centre-lines of conductors displaced by angles δ do not pass through the origin in Figure 3.7, and a scan over the main pole face will not be described by θ varying from $-\beta$ to $\alpha-\beta$. The new situation viewed in the -x direction is shown in Figure 4.5.

Figure 4.5: Position of a point, Q, on a displaced conductor.

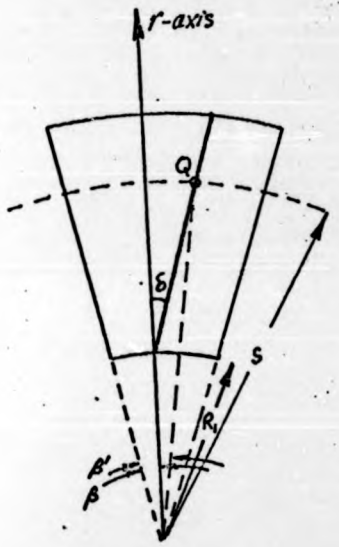

It is clear that the required scan will now be performed if β is replaced by β'. Provided $(\beta'-\beta)$ and δ are small angles, β' can be calculated from Equation 4.9 and Figure 4.5 as :

$$\beta' = \beta + \left(\frac{s - R_1}{s}\right).\delta \qquad (4.10)$$

A program called "Skewflux" was written to take account of finite values of δ in the calculation of conductor e.m.f.. Its flow diagram is essentially the same as that for "Normal Fluxplot 2", except that it evaluates Equations 4.6 to 4.10, and uses the result in the angular scan of the pole faces. The calculated values for δ in the radiator cooling fan motor and the wheel motor are given in Table 4.1.

"Skewflux" was used with the former to compare the variation of conductor e.m.f. with the results of Figure 4.4. The results are given, together with those of Figure 4.4, in Figure 4.6, which shows a complete pole pitch. For each δ curve, there will clearly be another, identical to it, but transposed about the magnet centre-line. This represents the equivalent conductor that is displaced in the opposite direction.

It is to be expected that displacement over the magnet centre-line will have little effect on the induced e.m.f., and there is very little difference between the curves in this region. The e.m.f. in a conductor in line (at radius R_1) with the magnet side shows a much greater variation,,though, particularly if it is displaced away from the main pole. The calculated values at this point are given in Table 4.2.

Consideration of the true positions of the armature

Table 4.1: Conductor's displacement angles, δ, in fan and wheel motors.

Fan motor: (5 turns/coil)

δ(radians) =
-.06450
-.03223
0
.03223
.06450

Wheel motor: (7 turns/coil)

δ(radians) =	
-.06738	
-.04490	Values given for reference (these are comparable with those for the fan motor).
-.02244	
0	
.02244	
.04490	
.06738	

Table 4.2: e.m.f. in a conductor that is in line (at radius R_1) with a magnet side in the fan motor.

Displacement angle, δ rad.	Conductor e.m.f., e_j, V.
.06450	.04363
.03223	.03757
0	.03735
-.03223	.03099
-.06450	.02556

Figure 4.6. Variation of conductor e.m.f. in the fan motor (at layer nearest to magnets), for different conductor displacements.

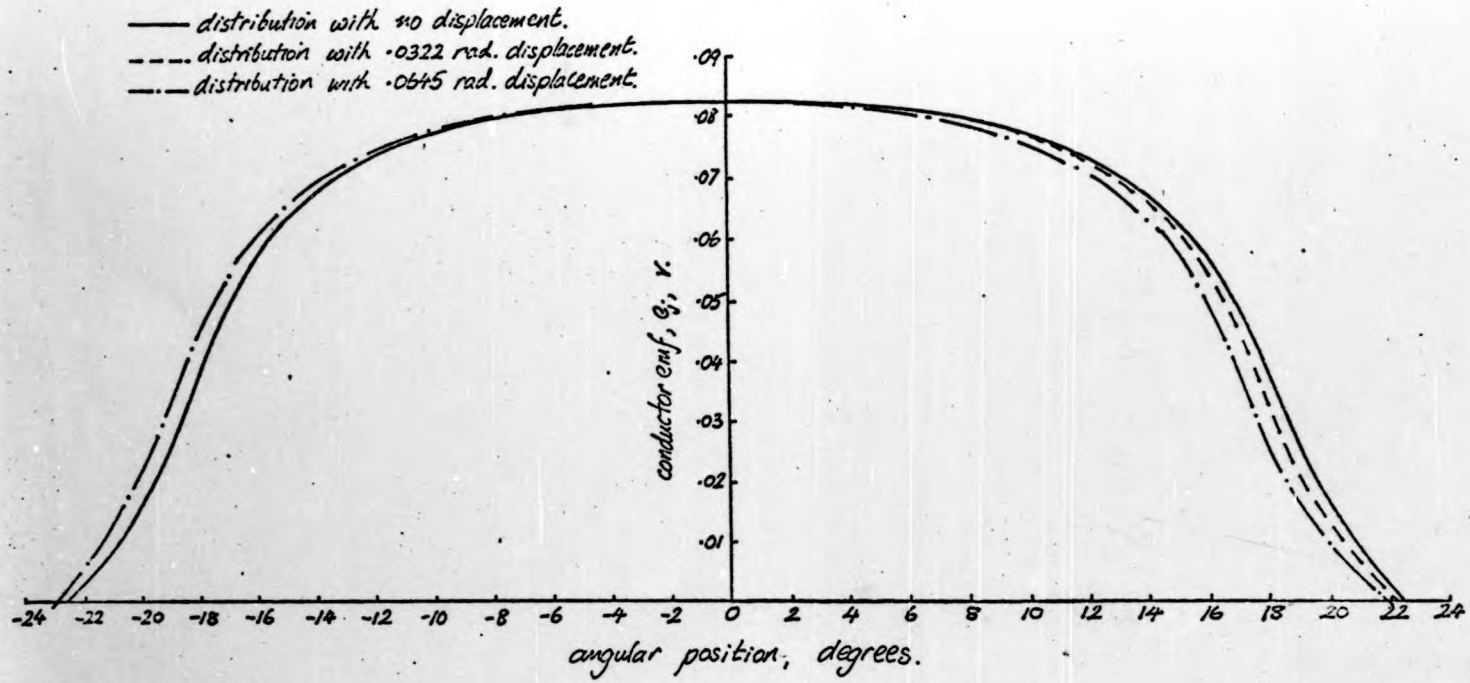

conductors is clearly important at certain angular locations. Their significance cannot be gauged, though, without a knowledge of the winding arrangement. This will show whether conductors with large displacements lie in the most sensitive regions, and therefore have a noticeable effect on the total induced e.m.f.. As the armature is rotated, the situation will change, and the error caused by approximating the conductors' positions to radial lines will alter. A method of performing this rotation will be described, that can take account of the true positions, and can then be amended for the approximate solution. More important than an indication of this error will be the eventual summation of the individual e.m.f.s in the correct manner. This will give information about the variation of armature e.m.f. in the real system.

4.3. Winding arrangements.

The calculations and results so far have all related to the fan motor. A program that places all the conductors in their correct positions will have to suit all types of winding arrangement. In fact, the fan motor has a wave winding, which is more awkward to deal with than the lap winding in the wheel motor. This is because the former does not have an integral number of coils per pole, and so there will be no symmetry of results over each pole pitch. For the wave winding, therefore, there must be a calculation of the conductor e.m.f.s around the whole armature.

For the armature in a given position, an e.m.f. will be calculated for each conductor in turn, and the results stored in

an array for subsequent addition in the correct manner. The conductor layer is already identified by the integer m in Equation 4.1. As occurred in the original program "Normal Fluxplot", the angular steps must also be identified by integers, the increments in this direction now being $\frac{2\pi}{C_1}$ radians. An integer count can then be established, starting at zero on the centre-line of the main pole, and progressing clockwise around the armature until $(C_1 - 1)$ is reached. From this count can be derived a number to identify the relevant value of δ to any conductor, and a sign to give the direction of this displacement.

The program "Series" was written to generate these numbers and signs, and it will appear as a block in the final program. The flow diagram of "Series" is given in Figure 4.7. The coil side conductor number is derived from the angular integral count by successively subtracting N_{tc} until the range 0 to N_{tc} is reached. This new number increases up to the coil side centre-line, beyond which it is decreased in a similar way. The change in the direction of displacement past this line is registered by multiplication by a suitable power of -1. Examples of the numbers generated by "Series" are given in Table 4.3, for different values of N_{tc}. For odd numbers of turns per coil, the highest number represents $\delta = 0$, and so the negative sign has no effect.

The e.m.f. induced in each conductor in its correct position can be calculated and identified using the programs "Skewflux" and "Series". These are combined into a new program, "Fluxcalc", whose flow diagram is given in Figure 4.8. The calculations so far have been based on three adjacent poles, and their images. A progression from one conductor to the next, clockwise around the

Figure 4.7: Flow diagram of the program "Series".

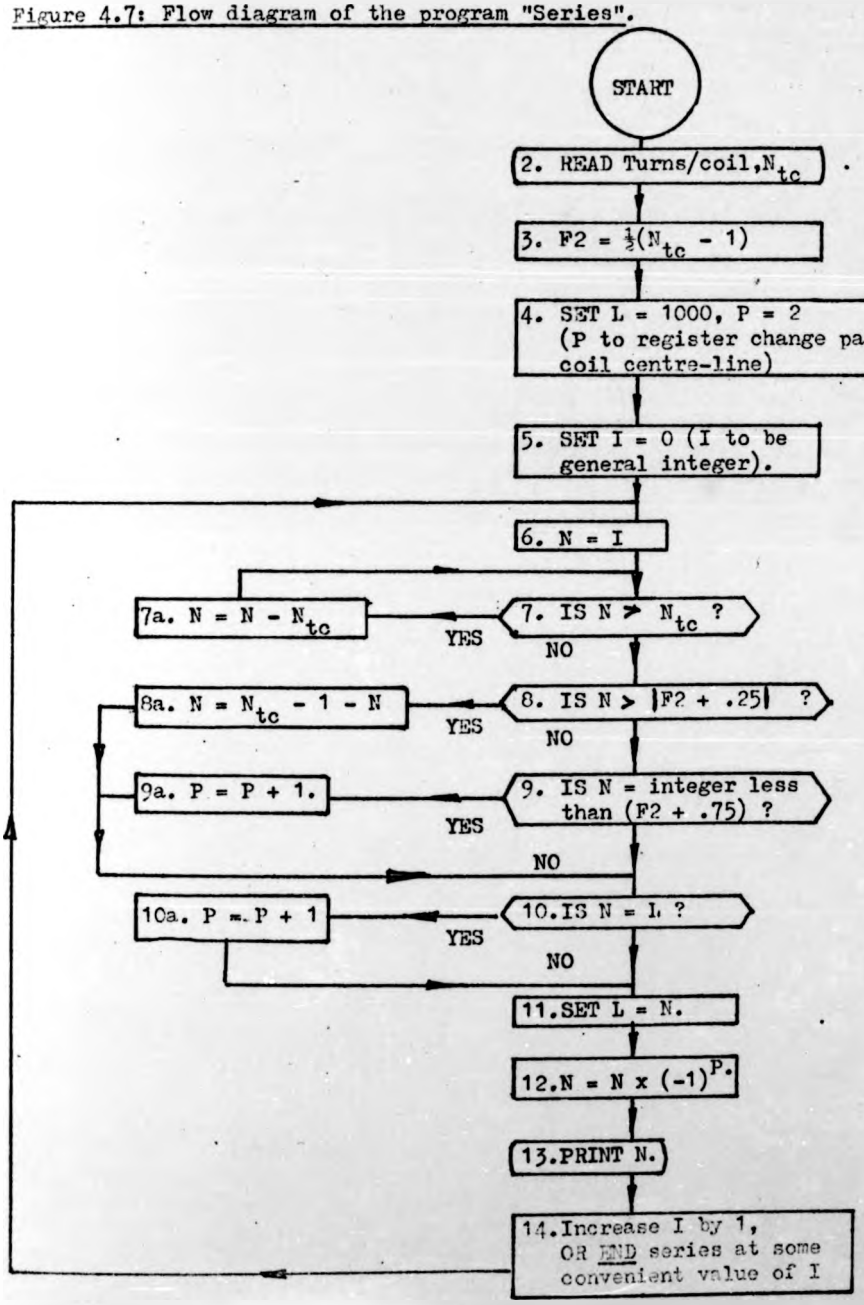

Table 4.3: Numbers generated by 'Series' for conductor identification.

Turns/coil, N_{tc}	$F2 = \frac{N_{tc}-1}{2}$	F2 + .25	$\lfloor F2 + .75 \rfloor$	Generated integers.
7	3	3.25	3	0, 1, 2, -3, -2, -1, -0,...
6	$2\frac{1}{2}$	2.75	3	0, 1, 2, -2, -1, -0,....
5	2	2.25	2	0, 1, -2, -1, -0.....
4	$1\frac{1}{2}$	1.75	2	0, 1, -1, -0,...
3	1	1.25	1	0, -1, -0,....

Figure 4.8: Flow diagram of the program "Fluxcalc".

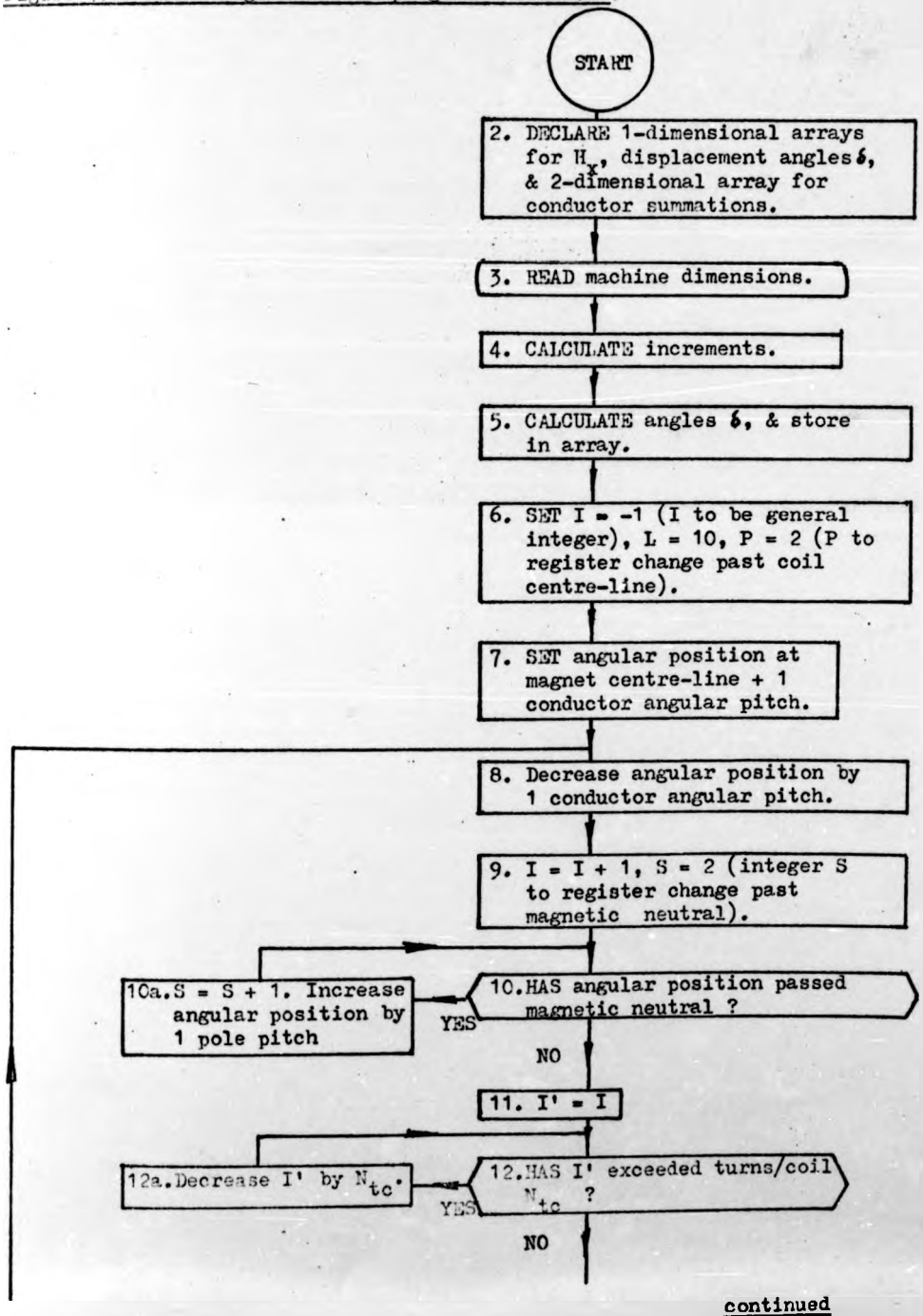

continued

Figure 4.8: Flow diagram of the program "Fluxcalc".

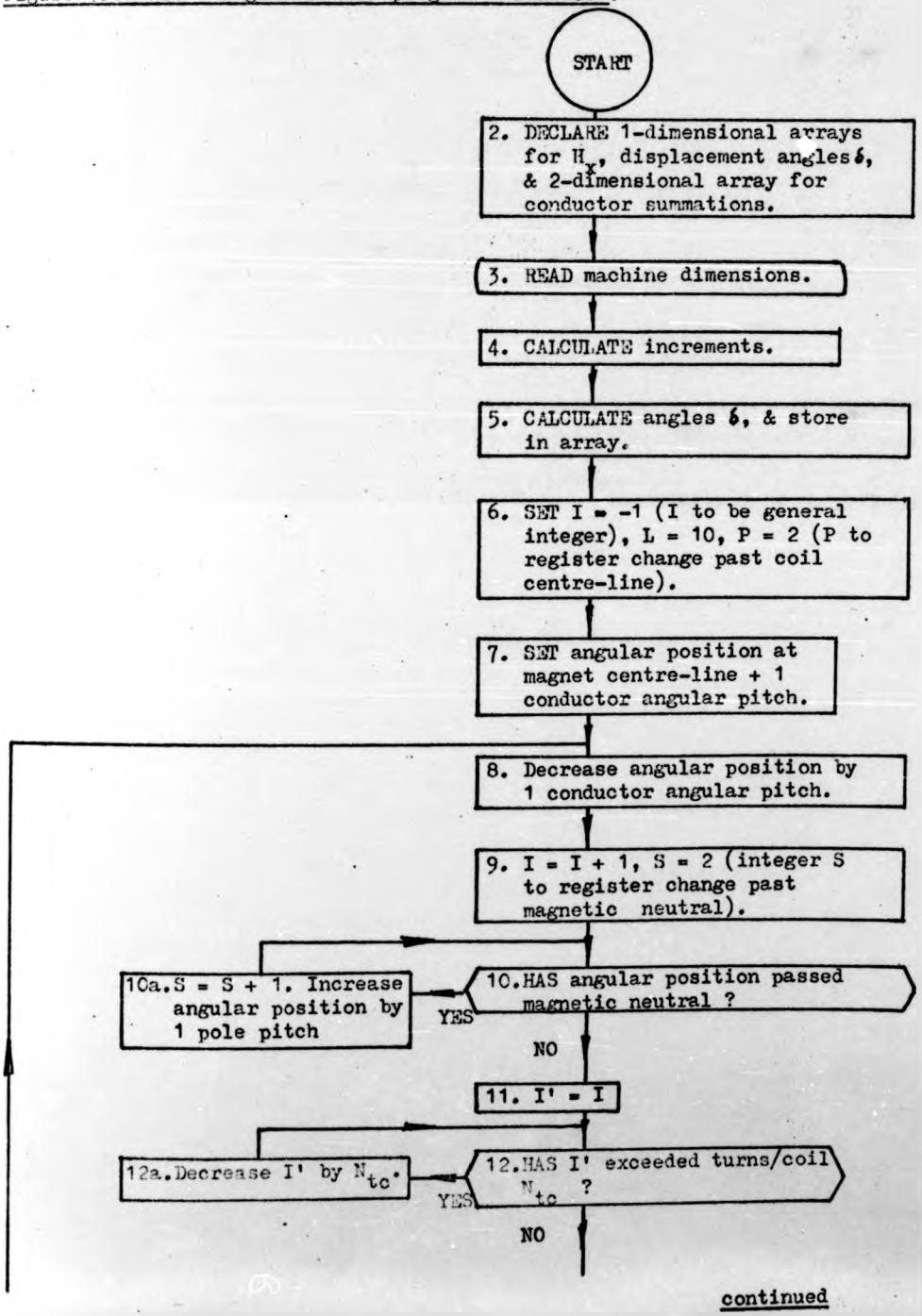

continued

Figure 4.8 (continued)

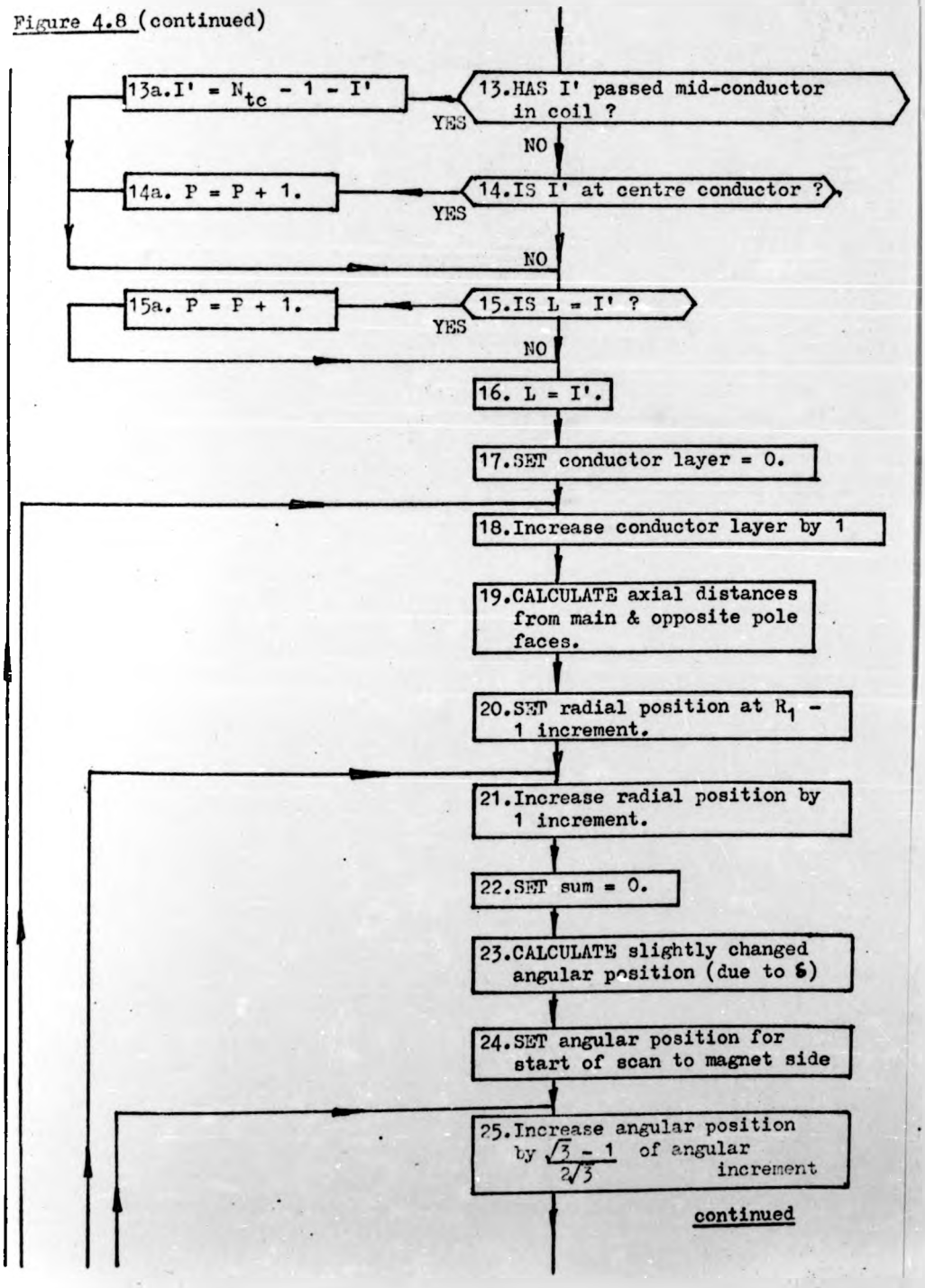

continued

Figure 4.8 (continued)

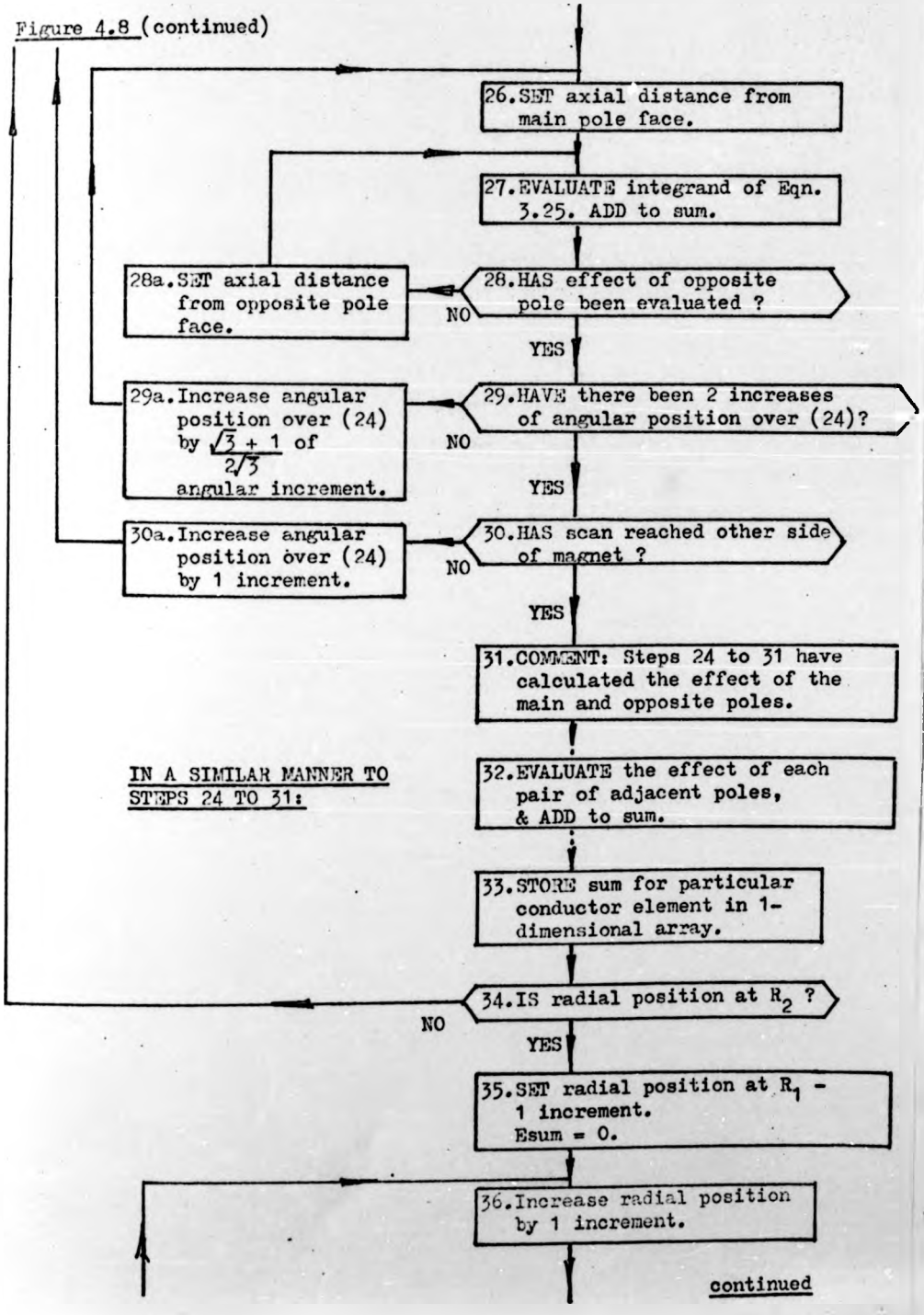

Figure 4.8 (continued)

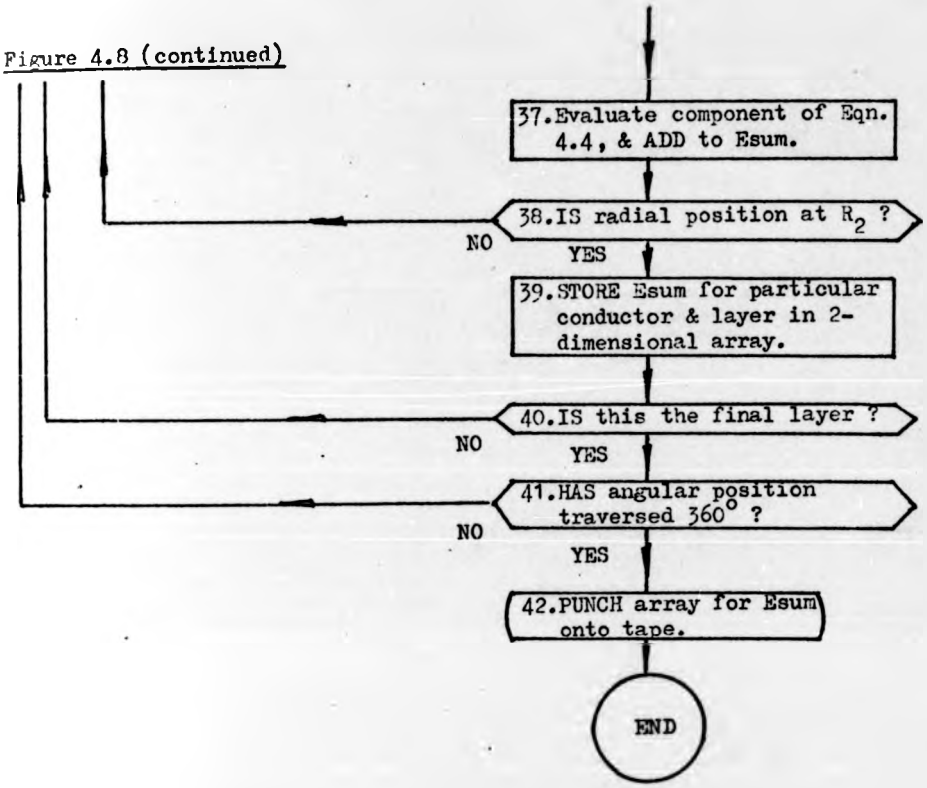

armature, will gradually move away from this system. In "Fluxcalc", therefore, whenever β is increased past a magnetic neutral between adjacent magnets, it will be returned to an equivalent position in front of the main pole face. This requires the subtraction of a pole pitch, and a change in the direction of the e.m.f.. The results of this program are stored in a two-dimensional array, representing the conductor layer and its angular position, for addition by a subsequent program.

The calculation of conductor e.m.f. in any position involves two numerical integrations. One is along the conductor's length, the radial increment being δr. The other is that of Equation 3.25, where θ scans the pole arc and the Gauss method is used. Because of the similarity between the angular and radial dimensions of a pole face, it is felt that the same number of increments could be employed in each direction. Upon this one number, then, will depend the accuracy of the complete calculation. However, the requirements of an accurate and a rapid calculation are not consistent. It is now possible, though, to investigate how the number of increments affects each of these, and to arrive at the most suitable value for it. The program "Fluxcalc" was therefore written with this facility included.

A maximum time of 10 mins. was allowed for the program to complete the 390 calculations for the fan motor. Table 4.4 compares the number of increments with the number of calculations actually completed. The accuracy can be gauged from Figure 4.9, which shows the summations in Equations 4.4 and 4.5 over a small angular distance, at the layer nearest to the main pole face.

Table 4.4: Number of calculations completed by 'Fluxcalc' for fan motor in 10 mins.

Number of increments.	Number of calculations completed.
5	390
10	136
15	62
20	36
30	16
40	9
60	2

Figure 4.9. Conductor calculations for various numbers of increments.

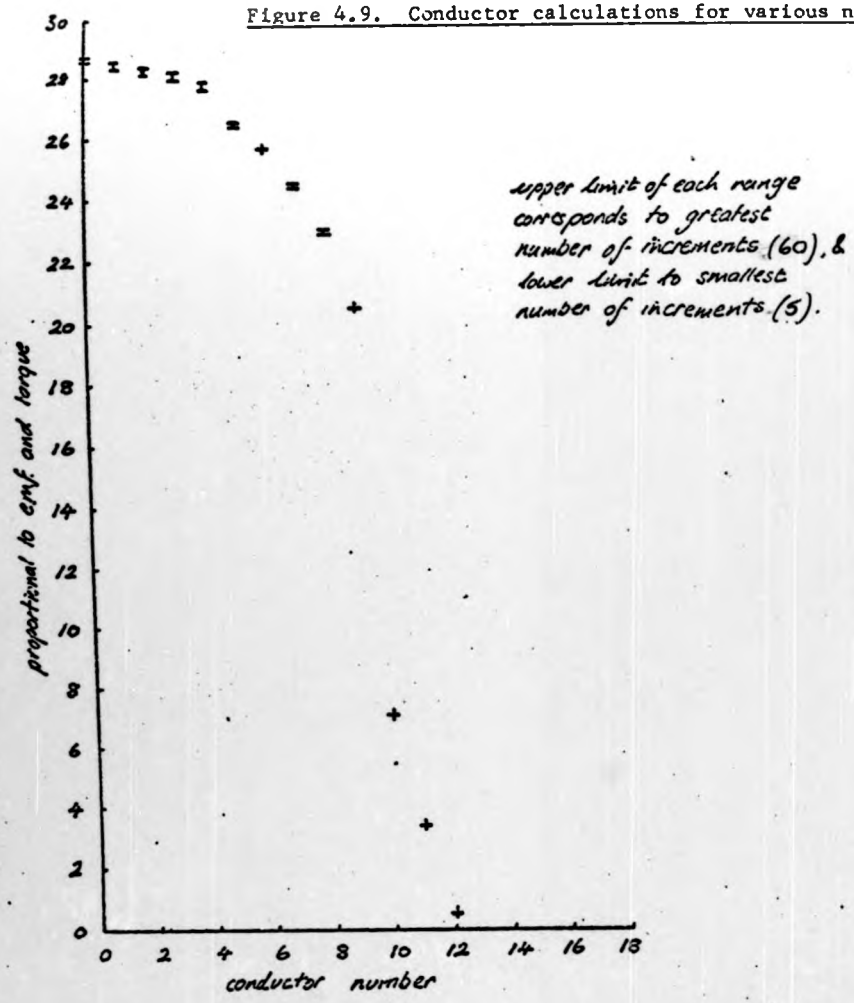

A comparison of Table 4.4 with Figure 4.9 indicates that 20 increments should be used in each direction, being a reasonable compromise between the two criteria. The difference between the values calculated with 20 and 60 increments is less than 0.2%.

The correct addition of the individual conductor e.m.f.s is dependent upon the type of winding and the number of conductor layers, and these will be specific to the program that performs the addition. The program to be described here is for a double-layer wave winding, as is used in the radiator cooling fan motor.

It will be assumed that the separation between adjacent commutator segments is negligible, so that the angular pitch of one segment, S_w, is

$$S_w = \frac{2\pi}{(\text{number of coils})} \quad \text{radians} \qquad (4.11)$$

The angular pitch of a brush, B_w, is calculated from the brush width assuming contact is made over the whole of its face with the drum-shaped commutator.

It will be helpful if the program can deduce as much as possible about the winding for itself. If C_p is the number of coils per pole, the nearest integer to this will usually give the number of commutator segments spanned by each coil. Furthermore, if the difference between C_p and its integral part is less than one half, the winding is retrogressive, and if this is greater than one half, it will be progressive. The program that decides this, and performs the subsequent additions is called "Tlwave", and its flow diagram is given in Figure 4.10. The input data to "Tlwave" consists of some machine parameters, and the conductor e.m.f.s evaluated by "Fluxcalc".

A comparison of Table 4.4 with Figure 4.9 indicates that 20 increments should be used in each direction, being a reasonable compromise between the two criteria. The difference between the values calculated with 20 and 60 increments is less than 0.2%.

The correct addition of the individual conductor e.m.f.s is dependent upon the type of winding and the number of conductor layers, and these will be specific to the program that performs the addition. The program to be described here is for a double-layer wave winding, as is used in the radiator cooling fan motor.

It will be assumed that the separation between adjacent commutator segments is negligible, so that the angular pitch of one segment, S_w, is

$$S_w = \frac{2\pi}{(\text{number of coils})} \quad \text{radians} \qquad (4.11)$$

The angular pitch of a brush, B_w, is calculated from the brush width assuming contact is made over the whole of its face with the drum-shaped commutator.

It will be helpful if the program can deduce as much as possible about the winding for itself. If C_p is the number of coils per pole, the nearest integer to this will usually give the number of commutator segments spanned by each coil. Furthermore, if the difference between C_p and its integral part is less than one half, the winding is retrogressive, and if this is greater than one half, it will be progressive. The program that decides this, and performs the subsequent additions is called "Tlwave", and its flow diagram is given in Figure 4.10. The input data to "Tlwave" consists of some machine parameters, and the conductor e.m.f.s evaluated by "Fluxcalc".

Figure 4.10: Flow diagram of the program "Tlwave".

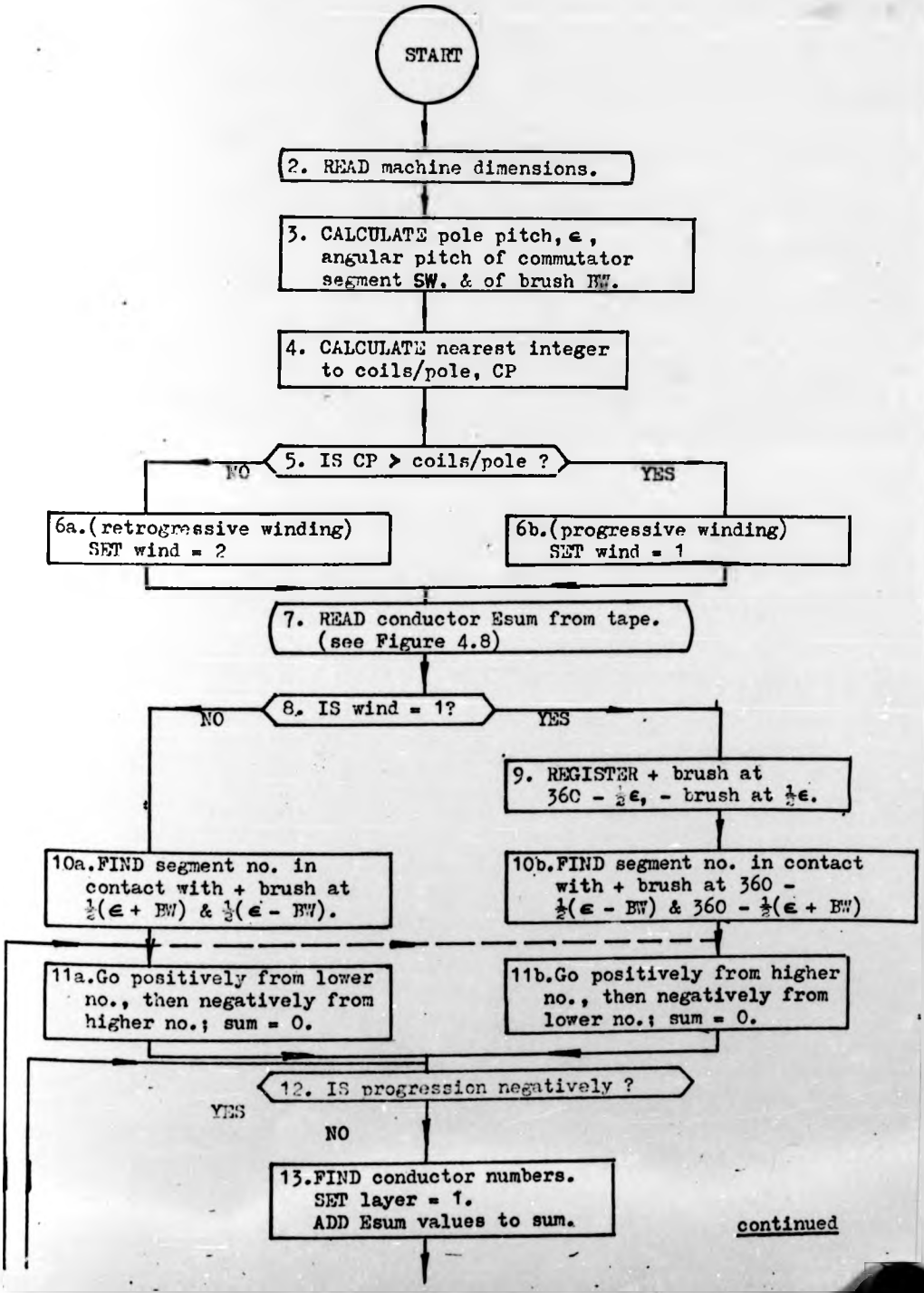

continued

Figure 4.10 (continued)

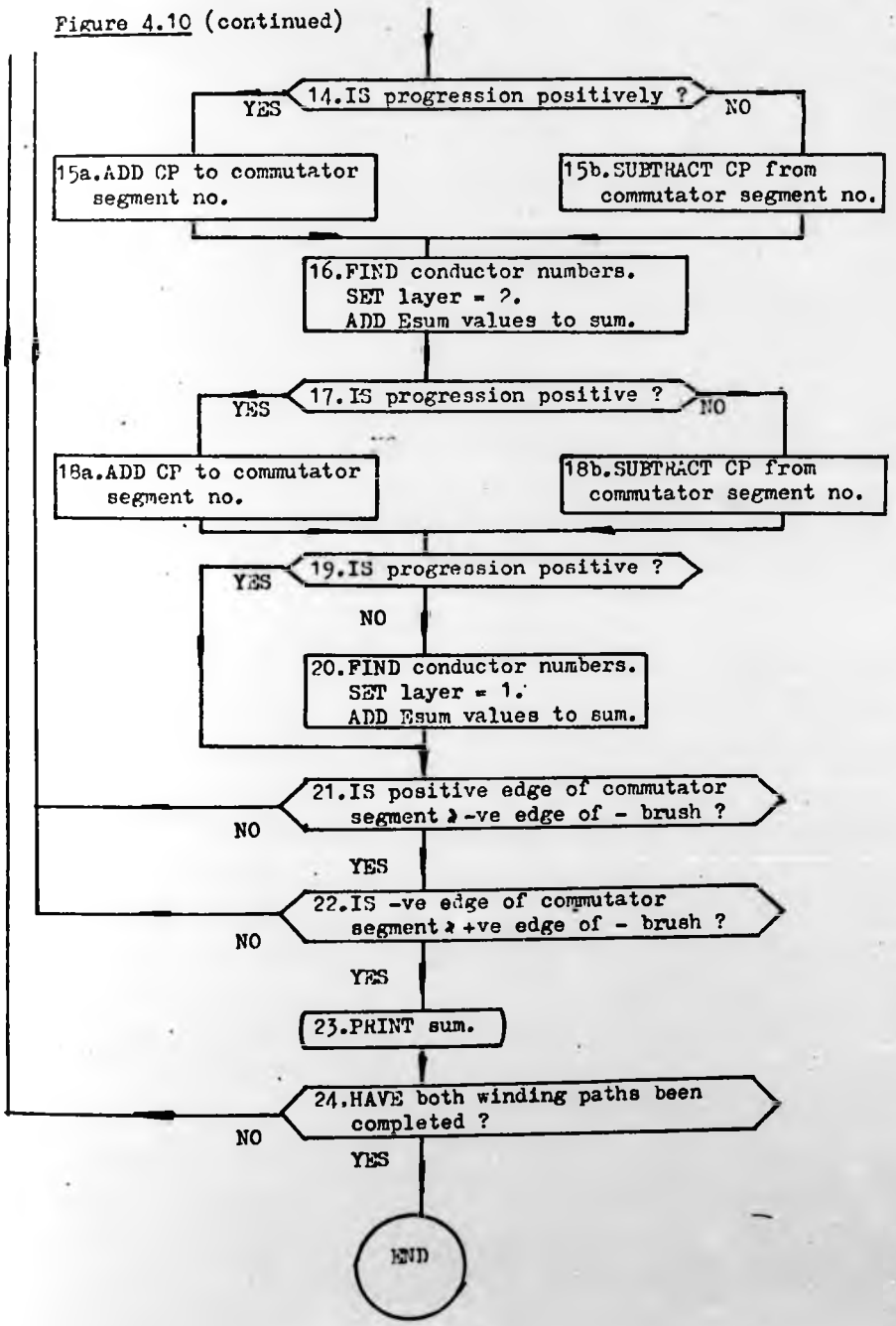

It was mentioned in Section 2.2.2 that the brushes in the fan motor are located between the magnets. It must be remembered here that this required the connections between the coils and the commutator to be displaced from their normal positions by half a pole pitch. A connection diagram of part of the winding is shown in Figure 4.11. The centre-lines of a north pole and commutator segment number 1 are coincident.

A clockwise progression around the winding from the positive brush will involve addition of e.m.f.s due to north poles, and subtraction of those due to south poles. Since the input data takes account of these polarities, a net positive e.m.f. will result for this path. The same applies to an anti-clockwise progression for the other path. Figure 4.11 shows a progressive winding, although "Tlwave" can adjust the addition to suit a retrogressive winding in the following manner.

Firstly, it positions the positive brush half a pole pitch anti-clockwise of the centre-line through segment 1, and the negative brush the same distance clockwise of it. It then determines which commutator segment number is in contact with the entering and leaving edges of each brush. The action the program will take depends upon the identification it has made of the winding. If it is progressive, the clockwise path will be from the leaving edge of the positive brush to the entering edge of the negative brush. For a retrogressive winding, the reverse happens, and it is the anti-clockwise path that terminates at these edges.

In determining the segment number in contact with any edge, allowance is made for the position of the centre-line.

Figure 4.11. Connection diagram of fan motor winding.

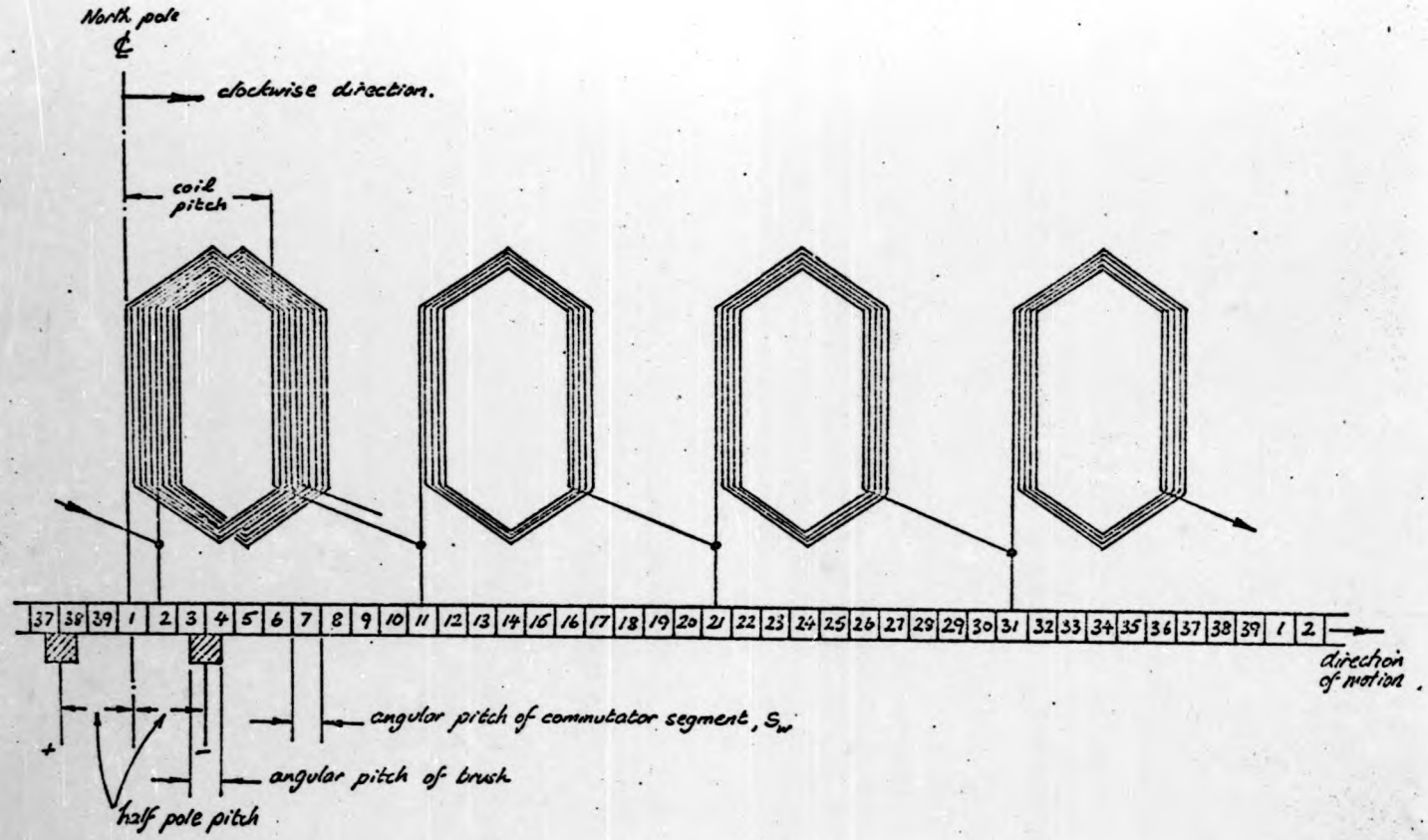

The angular position is divided by S_w, and the integral part is taken as the segment number. However, Figure 4.11 shows that 1.5 segments must be subtracted before the integer gives the correct number.

The block in the program that adds the conductor e.m.f.s is run twice, for the clockwise and anti-clockwise progressions. The procedure is to repeatedly add, or subtract, the coil pitch, then to find the new commutator segment number. If the negative brush edge has not been reached, the conductor numbers and layer associated with that coil side are found, and the e.m.f.s are read from the input data. The condition for the path being completed is that the entering edge of the segment is clockwise of the entering edge of the negative brush, and also that the segment's leaving edge is anti-clockwise of that brush's. The subtraction of 1.5 segments is again required.

4.4. Angular position of the armature.

Rotation of the armature by a given amount is achieved by moving the magnets and the brushes anti-clockwise by the same amount in "Fluxcalc" and "Tlwave" respectively. A new set of results from the former is required for each angular increment. However, these will repeat themselves more often if the conductors are assumed to lie on radial lines, than if their true positions are used. For example, if an angular increment of $\frac{1}{4}C_1$ is employed in the fan motor, four sets of calculations will be required from the approximate system. As there are five turns per coil, twenty

sets are needed for the exact arrangement.

Figure 4.12 shows the results of "Fluxcalc" for each of the systems in this example. The summations of Equations 4.2 and 4.3, which have to be multiplied by the appropriate factors to give e.m.f. and torque, are plotted against conductor number. The graphs compare these values for the conductors in one layer over a small angular range, the angular position of the armature increasing by $\frac{1}{4}C_1$ in each successive graph. The points describing the exact conductor positions are joined, for clarity, to produce a continuous curve, as are those for the approximate conductor positions.

The results of Figure 4.12 indicate again that the greatest errors will occur if displaced conductors are assumed to run radially in the regions between adjacent magnets. The magnitudes of these errors will alter, however, as the armature is rotated. When the greatest displacements are in this region, the errors will be largest. When the conductors are added in "Tlwave", the errors could cancel at certain armature positions, but this is unlikely in a wave winding. This total error would also vary as the armature is rotated. Since the allowance for the exact conductor positions in the programs is not very time-consuming, the approximate arrangement will no longer be used.

4.4.1. Brush arrangements and Commutation.

The full set of exact values, some of which appeared in Figure 4.12, have been found for rotation of the fan motor's armature over $5.C_1$. Added in "Tlwave", these give the complete variations in each winding path, and are shown in Figure 4.13. This gives some interesting information about a wave winding, and about the

Figure 4.12: Conductor calculations for rotation of armature.

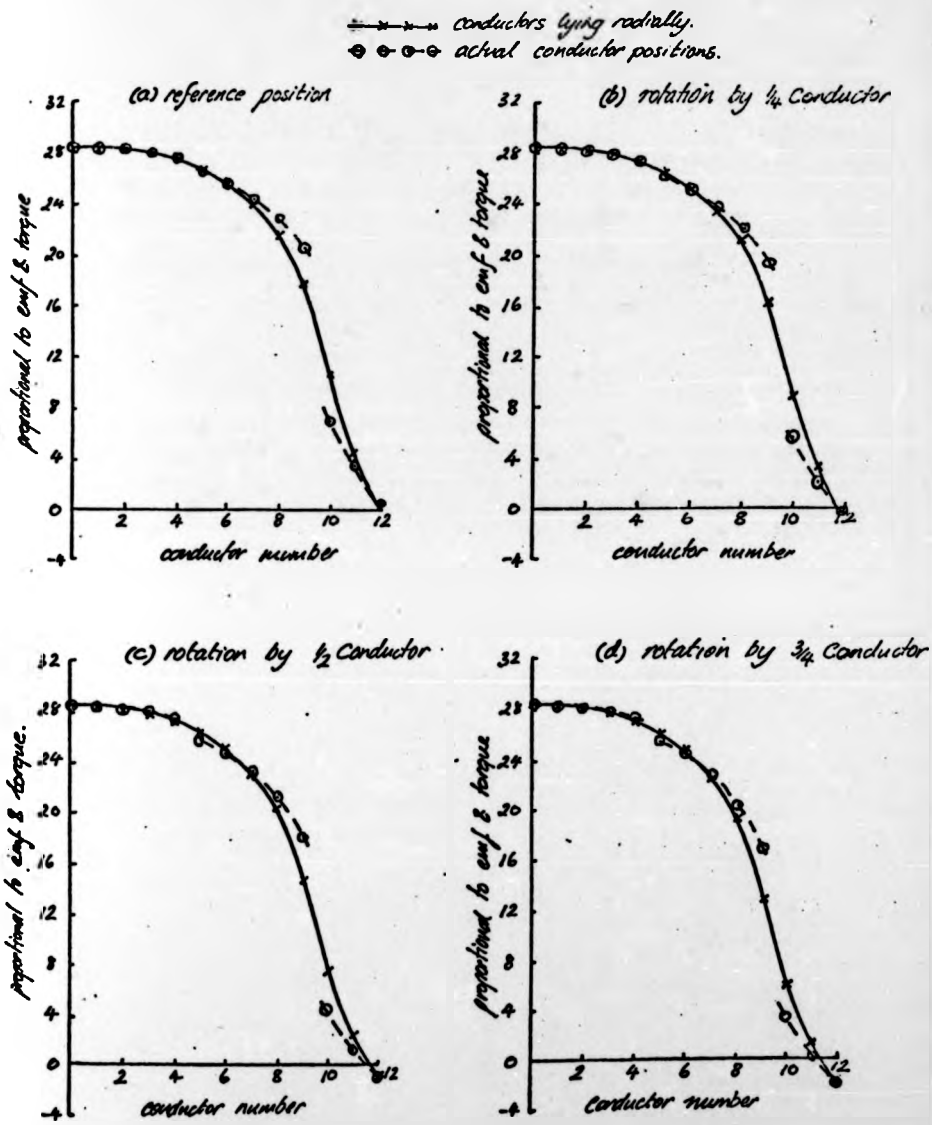

continued

Figure 4.12 (continued)

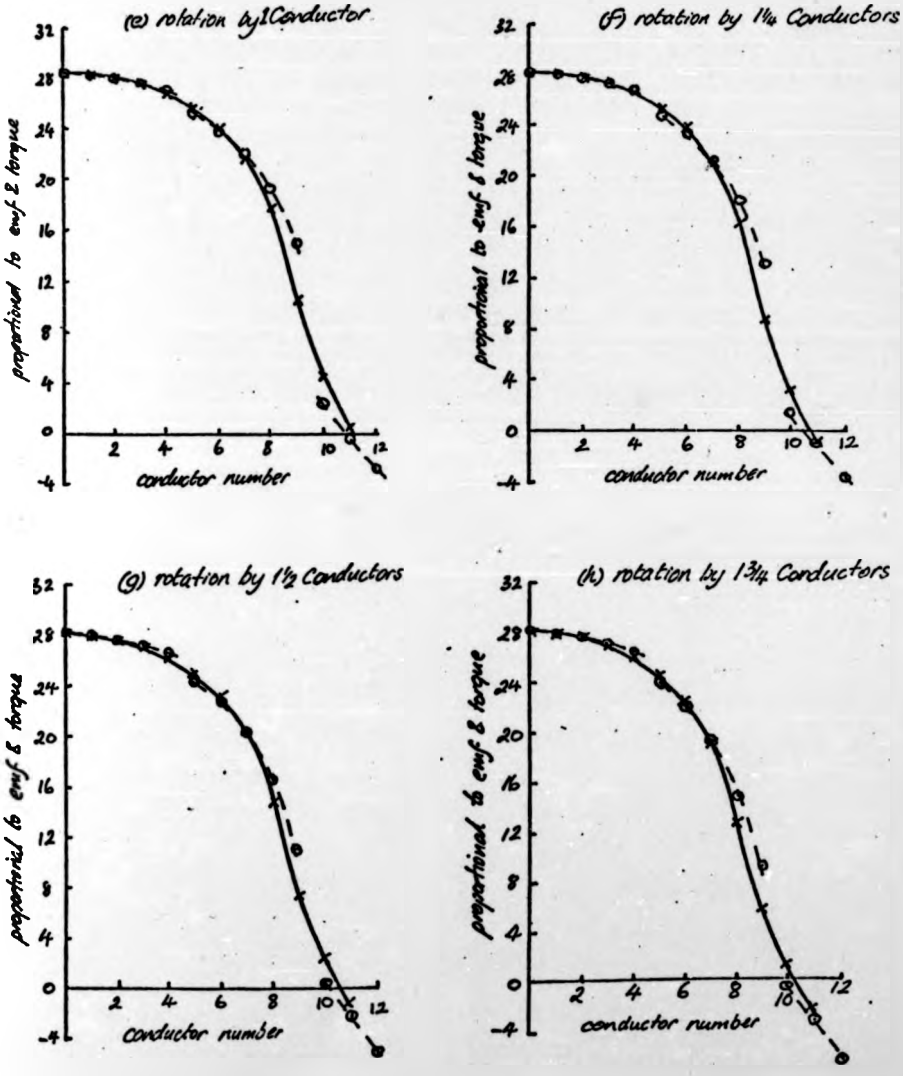

continued

Figure 4.12 (continued)

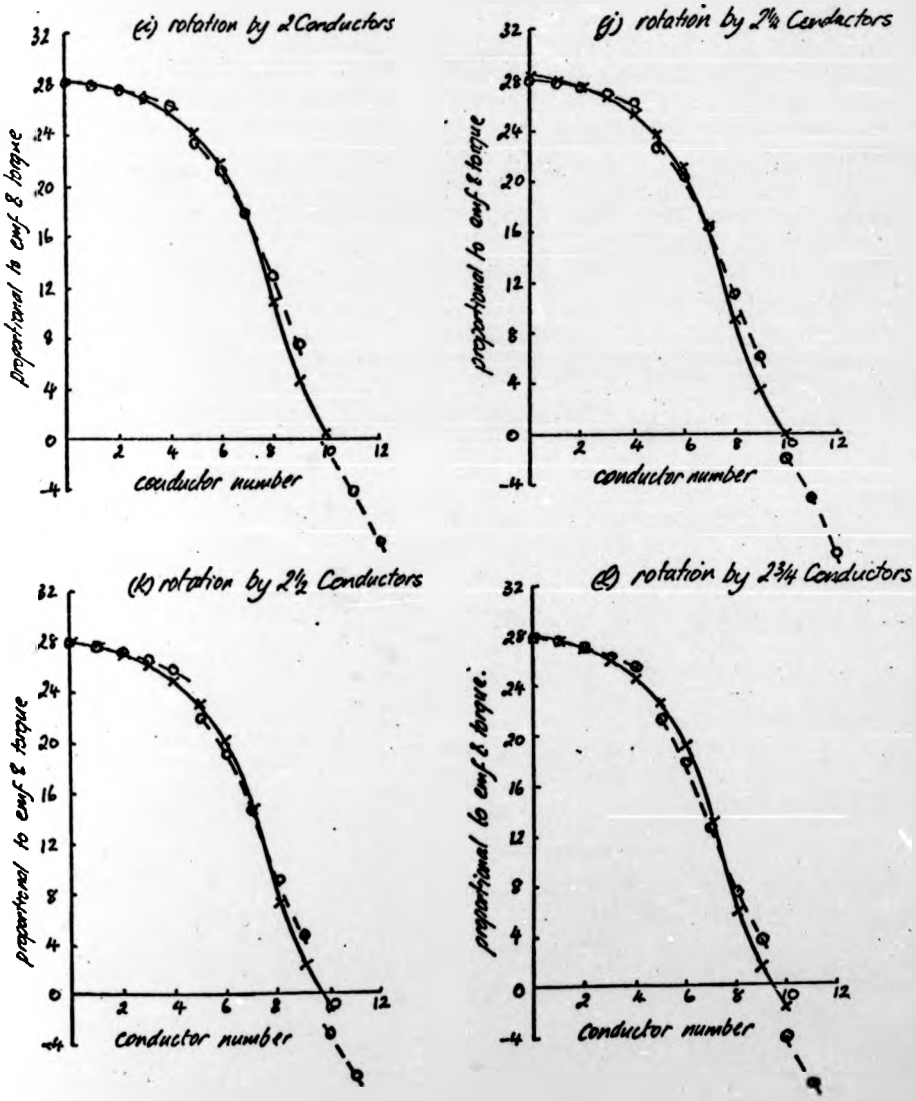

continued

Figure 4.12 (continued)

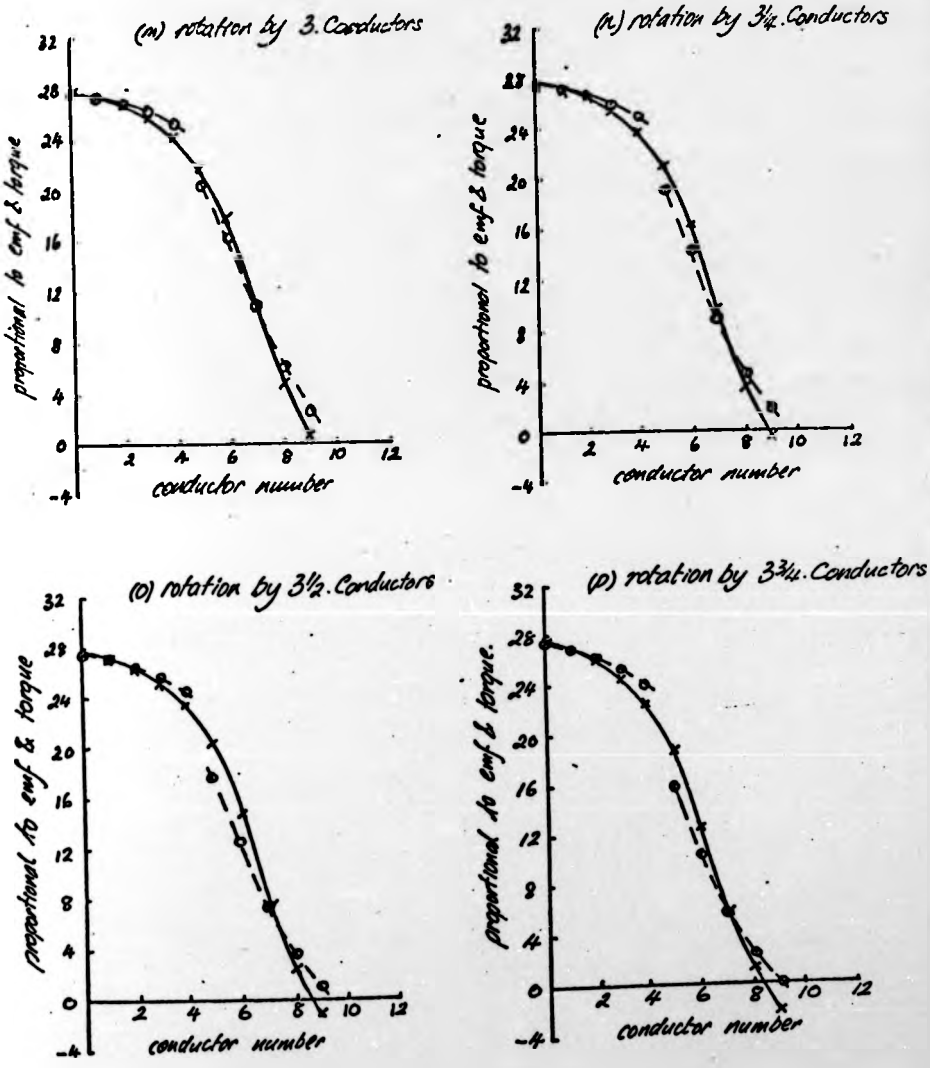

continued

Figure 4.12 (continued)

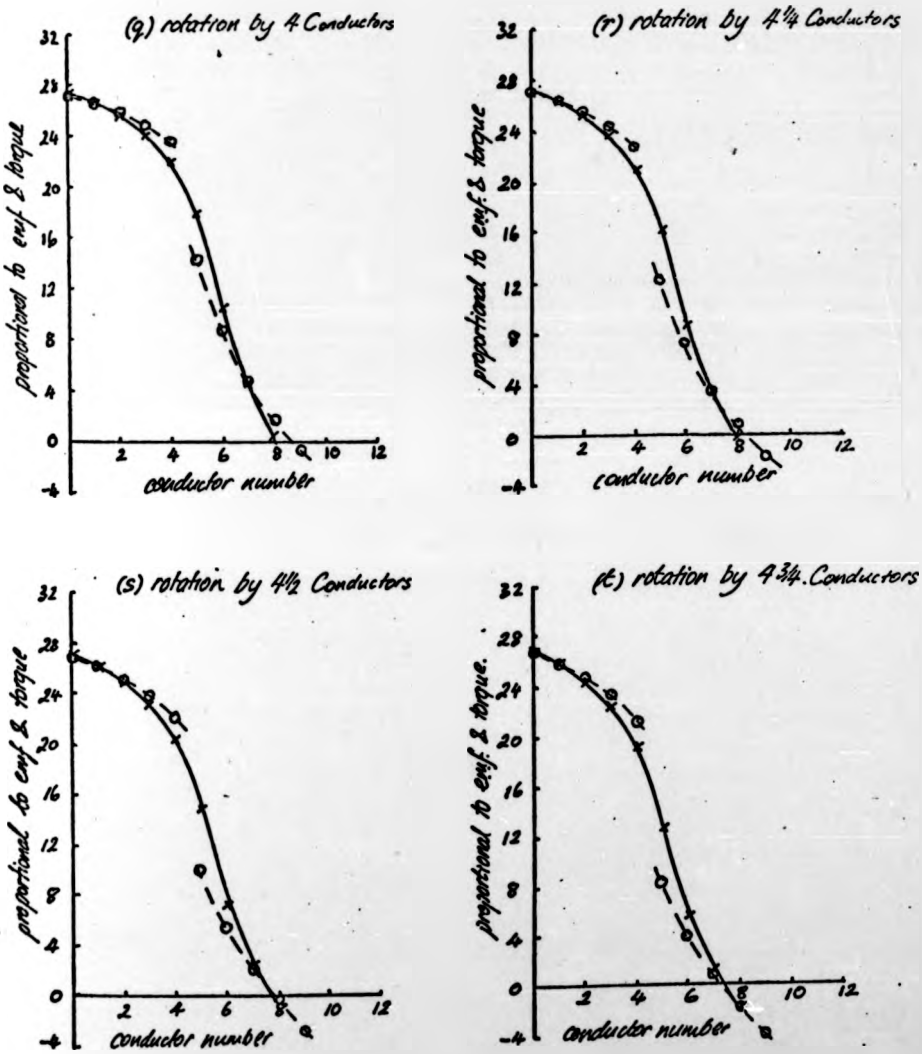

Figure 4.13: Variation of fan motor e.m.f. as armature is rotated.

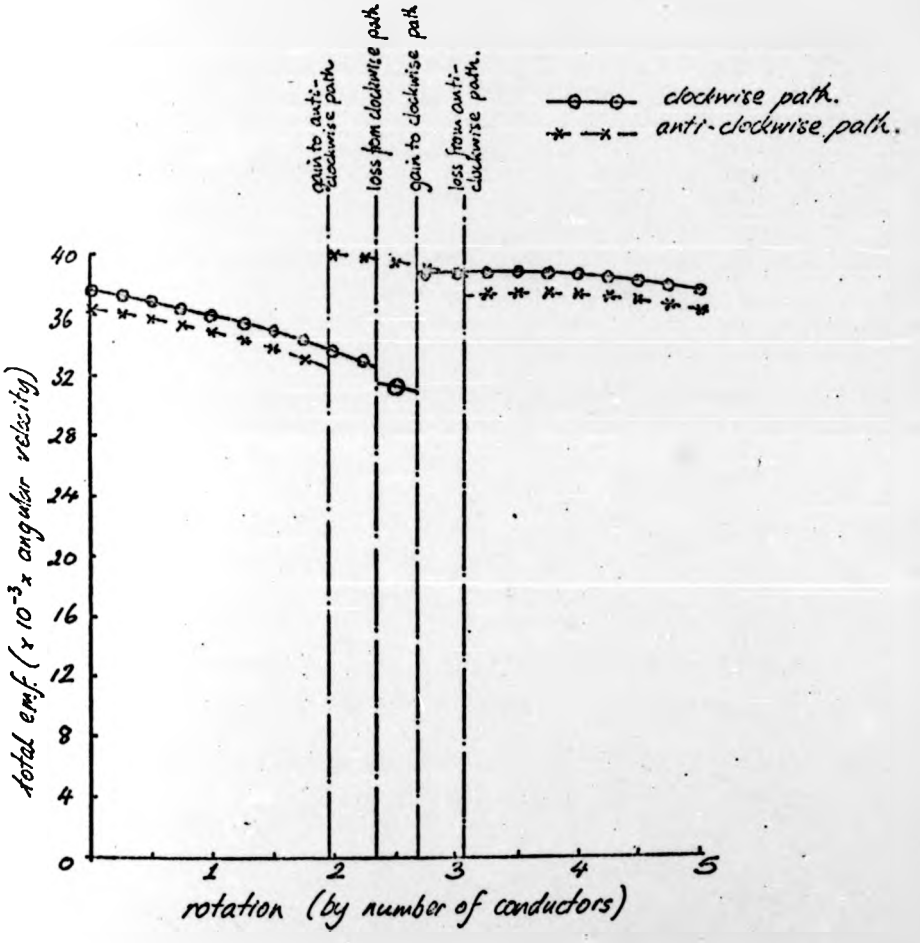

connections in the fan motor in particular. The angular pitch of a brush in this machine is slightly less than that of a commutator segment, so that commutation at one brush is the alternate short-circuiting of a number of coils, then no coils. These pitches are used to calculate at what angular positions coils are gained, and then lost, from each parallel path, and these positions are marked on Figure 4.13.

It will be noticed that the addition of coils gives rise to a significant rise in the e.m.f. in either path. However, their loss has very little effect. No account is taken of the inductance of the coils, which will be shown to be negligibly small. The effect of this would be to limit the rate of change of current calculated from these results. The relative positions of the armature conductors and the commutator segments, shown in Figure 4.11, are identical to those in the motor. There is, therefore, a slight error in these, since the centre of a coil side, and not the outermost conductor, should be in line with the centre of a segment. This error is half the angular pitch of a segment.

Considering the direction of rotation shown, it can be seen that the short-circuiting of coils at a brush occurs when those coils are approximately in the magnetic neutral positions. When they are subsequently reconnected into a path, they are well under the influence of the pole faces they are approaching. Although the connections in the fan motor were made in this way, excessive brush losses were not found to occur. These results show, however, the effect on the e.m.f. and torque developed in each armature path, due to a slight error in the alignment of the winding and

the commutator. When there is no such error, the gain and loss of coils to a path will lead to an equal rise and fall of e.m.f. and torque.

The winding described is a wave-type. For a progressive lap winding, however, there would be a certain amount of symmetry in such results as those of Figure 4.13. The gain of a coil to a clockwise path would coincide with the gain of one to an anti-clockwise path, since these occur at the leaving edges of a positive and a negative brush respectively. There would be similar coincidences in the loss of coils, and for retrogressive lap windings.

The effect of the fan motor's peculiar coil connections is again noticed when the relative positions of the two brushes were altered. A simple amendment to the program "Tlwave" moves the negative brush, for example, any number of pole pitches in the clockwise direction , there being four possible positions in this machine. By producing a graph of the type of Figure 4.13 for each combination, it would be possible to select the most suitable arrangement. All that is attempted here is a direct comparison of each path for the four positions of the negative brush, when the armature is in the position indicated in Figure 4.11.

"Tlwave" was also made to print out the commutator segment numbers in each path, from which the number of coils was deduced. These, together with the summations of Equations 4.2 and 4.3 are given in Table 4.5. One result, for the clockwise path and the brush moved two pole pitches, again shows that some coils are being more strongly influenced by a magnet of the wrong polarity. In the fan motor, coils are added to and subtracted from the winding paths four at a time. There is little significance, therefore, in the difference

Table 4.5: Effect of brush positions on summation of 'Tlwave' for fan motor.

Distance of negative brush from positive brush.	Clockwise winding path.		Anti-clockwise winding path.	
	Summation.	No. of coils in path.	Summation.	No. of coils in path.
1 pole pitch:	.0376	16	.0364	15
2 pole pitches:	.0373	17	.0341	14
3 pole pitches:	.0359	14	.0397	17
4 pole pitches:	.0371	15	.0383	16

of three coils between the paths, that occurs for brush displacements of two and four pole pitches.

Graphs of the type of Figure 4.13 can also be produced for various brush widths, again by a simple alteration to "Tlwave". Figure 4.14 shows the effect of increasing the brush width for the armature again located as in Figure 4.11. The brushes are in adjacent gaps between magnets. Since there are 39 coils in this wave winding, the clockwise path loses eight coils before the anti-clockwise path loses a similar number. The effect on the e.m.f. and torque will be quite considerable.

Examples have been given of how the position and width of the brushes can be studied. The number of brushes to be used could also be investigated, and this method can be applied to any winding and connection arrangement. Performing the calculations in two parts, the programs "Fluxcalc" and "Tlwave", allows all these features of the machine's design to be studied quickly and most easily. A closer examination of the brush design will not be performed here, since there is no facility for checking these results in the fan motor itself.

4.5. Conductor currents and Armature reaction.

The main objective in developing the programs already described was to provide a method of evaluating various magnet arrangements, and this will be considered in later chapters. This method calculates the torque and induced e.m.f. in the winding paths, though, from Equations 4.2 and 4.3. The current in each path could then be found if the corresponding resistances were known. Taking the end-windings into account, an approximate length per conductor is:

Figure 4.14: Variation of fan motor e.m.f. with brush width.

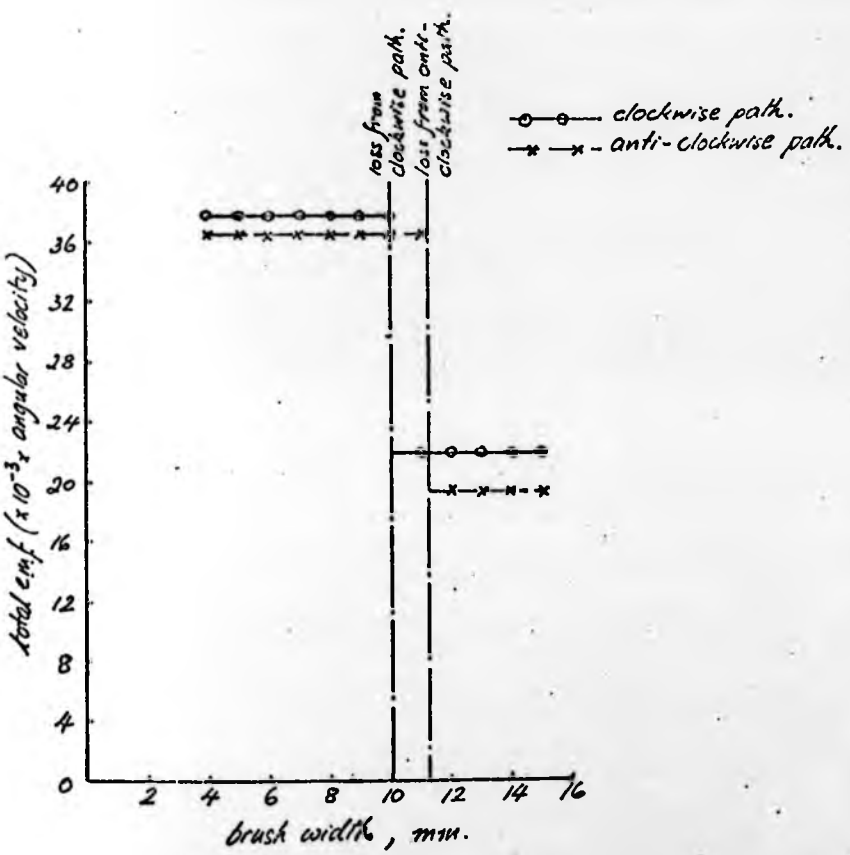

$$(R_2 - R_1) + \frac{\pi}{p}.(R_2 + R_1) \ ,$$

where p is the number of poles. It has already been possible to deduce the number of coils in a path from "Tlwave", and so the number of conductors, Z_p, could be similarly found. The resistance of each winding path would then be given by:

$$\text{path resistance} = \frac{4.\rho.Z_p}{\pi.d_c^{\,2}}.\left[(R_2 - R_1) + \frac{\pi}{p}.(R_2 + R_1) + C_1\right] \quad (4.12)$$

where ρ = resistivity of copper,

d_c = diameter of the copper ($< d$)

C_1 = additional length, to allow for connections between coils, and the actual shape of the coil corners.

Just as Figure 4.13 indicates the variation of e.m.f. and torque as the armature is rotated, a combination of Equation 4.12 and "Tlwave" could show the variation of current. This would be more relevant than e.m.f. to the calculation of the electrical power losses in the machine.

Throughout the calculation of magnetic fields, it has been assumed that armature reaction is negligible. It has also been suggested that the self-inductance of a coil, and the mutual inductance between coils is negligible. The latter will be true if the field experienced by a conductor due to its neighbours is negligibly small. Since adjacent conductors are closer together than to the nearest magnet face, this will be a sufficient condition for the former to be true also.

Consider a point P in the same layer as a conductor carrying current i (Figure 4.15). It can easily be shown that the axial field at P due to i is given by :

Figure 4.15: Position of a point, P, on an adjacent conductor.

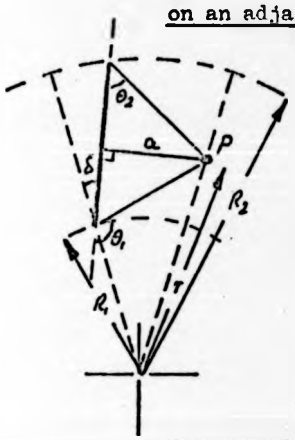

Figure 4.16: Variation of axial flux density due to a conductor in the fan motor, at radius 47 mm., carrying a current of 9.5 A.

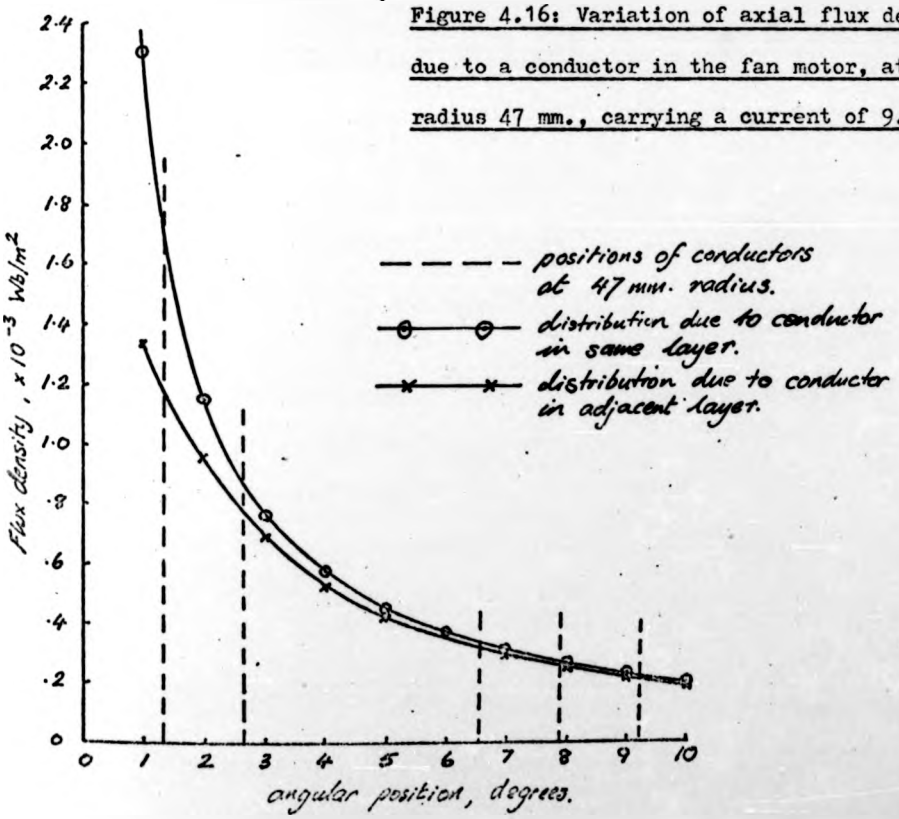

$$B_x = \frac{\mu_0 . i . (\cos \theta_2 - \cos \theta_1)}{4\pi a} \qquad (4.13)$$

There is a similar result for the field due to conductors in adjacent layers. As an example, the field experienced by a point at a radius of 47 mm. on the centre conductor of a coil side in the fan motor is calculated. Figure 4.16 shows the axial field due to a conductor in the same layer and one in the adjacent layer, for the motor's normal operating current of 9.5 A.. Allowing for the correct displacements of conductors in the winding, the positions of the adjacent conductors at that radius are marked.

A net axial field at this point will be most significant due to one neighbouring coil side, when the other neighbour is short-circuited during commutation. This field can be estimated from Figure 4.16 as approximately 0.002 Wb/m^2. Compared with the field calculated from the permanent magnets at this radius (Figure 3.17), this value is very small. It will therefore continue to be assumed that self-inductance and mutual inductance of coils, and armature reaction can be neglected. If it was ever to be found that the demagnetising field due to armature reaction was not negligible, it could be calculated in this way, and its effect on the permanent magnets taken into account using the B-H characteristic of the material (Reference 10).

4.6. Armature Inductance and Commutation.

It was originally postulated that the negligible armature inductance raises the operating speed of the machine by virtue of the consequential reduction in the static and dynamic e.m.f.s in the commutated coil. It is the static e.m.f. that is due to the

self-inductance of the commutated coil and the mutual inductance from other coils, and which opposes changes of current in the commutated coil. The dynamic e.m.f. is normally due to armature reaction, and is reduced either by the use of interpoles or by off-setting the brushes from the magnetic neutral positions. It is these causes of the respective types of e.m.f. that commonly occur in conventional d.c. machines, but are not significant in the Disc-Armature type. This is the reason for supposing that the latter can operate at higher speeds than normal, but there will be an additional source of dynamic e.m.f. that may also need consideration.

A coil is commutated over a finite arc, centred on a magnetic neutral, during which time it is short-circuited through the brush. At the onset of commutation, the coil is still under the influence of the pole it is leaving. If, as a result of the low coil inductance, the induced e.m.f. can change very rapidly, a reverse current will be generated in the coil until the magnetic neutral is reached. From this point until the end of commutation, the reverse will happen, as summarised in Figure 4.17. The most harmful effect could be that a voltage is generated across the segments to which the commutated coil is connected.

This is clearly a situation where a small amount of coil inductance would reduce the rate of change of current in a coil, and aid the commutation. The amount required will depend upon the operating speed, the brush width, and the commutator design. It will not be worthwhile calculating this effect in the wheel motor, for instance, since any errors in the pole arc or conductor positions will be important. It will be much better to observe the voltage developed across two adjacent commutator segments

Figure 4.17: Variation of coil current during commutation.

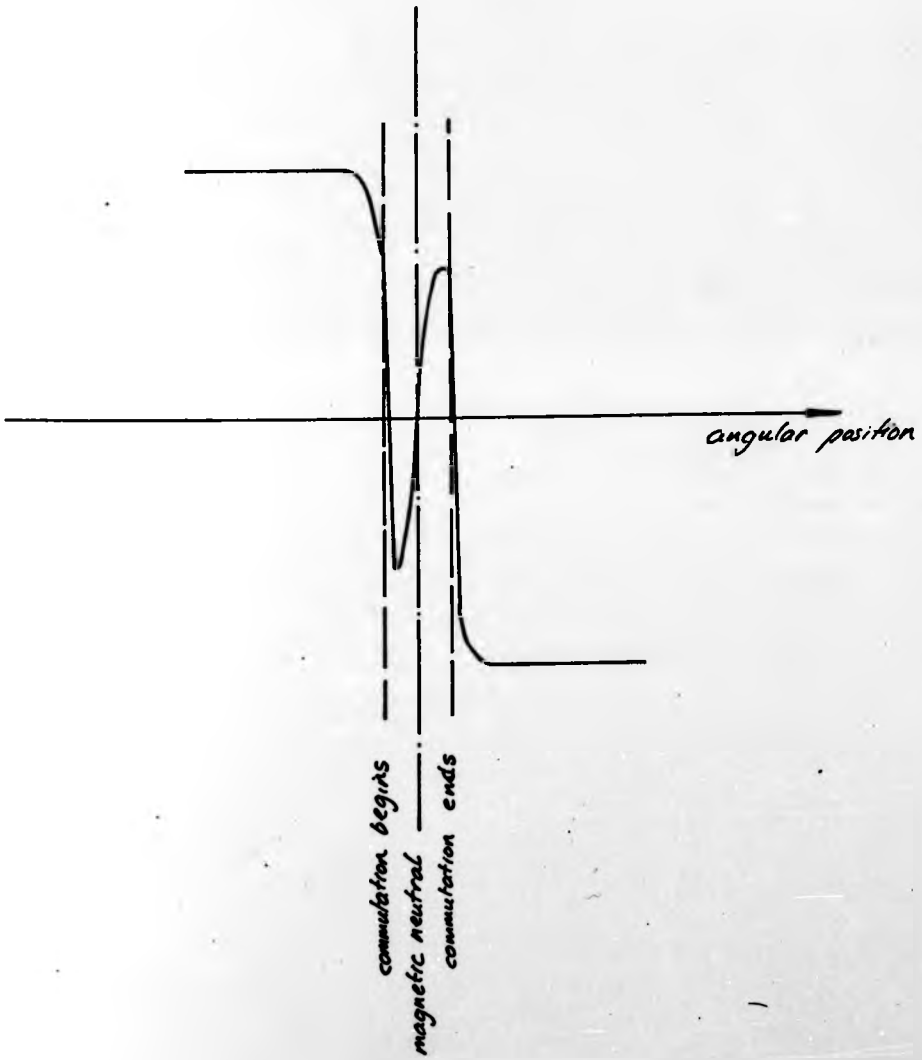

on an oscilloscope. Connections can be made in the machine (Reference 11) and brought out through slip-rings to give a continuous record.

5. PERFORMANCE OF THE MAGNETIC CIRCUIT.

5.1: Operating points on the B-H characteristic.

In order to verify the theory already developed, it will firstly be necessary to ensure that the operating characteristic of the magnets is known. For instance, they may be operating on a minor B-H loop, if not fully magnetised, or on a recoil loop.

Figure 5.1: Examples of magnet operating characteristics.

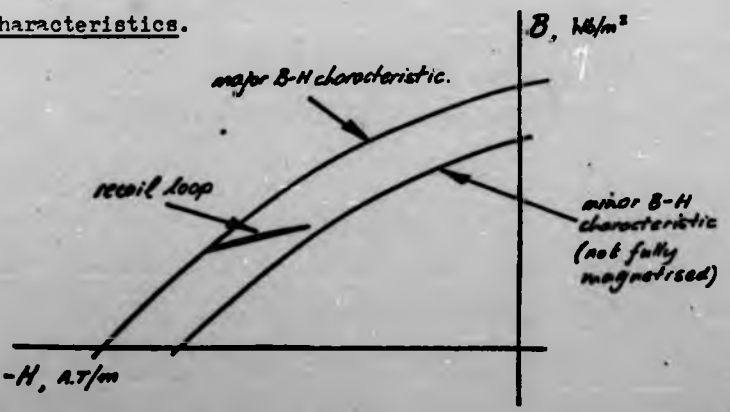

Examples of these are shown in Figure 5.1. It will be assumed throughout that recoil loops can be approximated by straight lines, the slopes of which are the recoil permeability.

The theory of the magnetic circuit developed in Chapter 3 assumed that the intrinsic magnetisation, M, was of constant magnitude and in the axial direction throughout the volume of the magnets. This was because the materials used are homogeneous uniformly

magnetised media. It was explained in Section 3.2 that, for some values of pole arc/pole pitch ratio, flux must pass from the magnet faces back alongside the poles. However, the theory developed there was unable to predict this, and it continued to use the original assumption. This therefore neglects the existence of pole sources on the magnet sides, being the only means of altering that theory and the field distribution. It will, however, be shown in this chapter that the difference between the calculated and the measured fields in the air gap of the fan motor is not great.

A magnet will not, therefore, have a unique value of $\underline{M}$ throughout its volume, though it will be reasonable to assume it is so for ceramic ferrites at least. In general, a small range of $\underline{M}$ will actually exist, and this will correspond to a small range of $\underline{B}$ on the B-H characteristic.

In Section 2.1, the significance of operating on the straight portion of the B-H characteristic to the initial magnetisation procedure was briefly mentioned. With any permanent magnet machine, it is undesirable that operation should be on a recoil line within the major B-H loop, for this represents a loss of potentially available energy. Recoil operation will not occur provided that the lowest flux density the magnet yields after magnetisation is on a reasonably straight portion of the B-H characteristic, and that the slope of this portion is approximately equal to the recoil permeability of the material. If magnetisation takes place prior to assembly of the machine, the lowest point will be for open circuit operation of the magnets.

A straight portion on the B-H characteristic will exist for two situations. Firstly, if $\underline{M}$ is constant, then Equation 3.1

holds, and the slope of the curve is μ_0. However, $\underline{M}$ could also be a linear function of $\underline{H}$, given by

$$\underline{M} = M_0 + k.\underline{H} \qquad (5.1)$$

where M_0 and k are constants.

The slope of the curve is now found from Equations 3.1 and 5.1 to be $\mu_0(1 + k)$, which is also a constant.

The recoil permeability will be less than or equal to the slope of the major curve in the region of interest. The manufacturer's literature (Reference 12) gives the operating point that has to be reached before recoil operation will become significant. At flux densities on the major curve greater than at this point, therefore, the gradient of the major curve will be approximately equal to the recoil permeability, which is also given by the manufacturer. The constant (1 + k) is then identical to the relative recoil permeability. This is best illustrated by considering the three materials whose B-H characteristics were given in Figure 2.1. The relevant details from Reference 12 are reproduced in Table 5.1.

For the radiator cooling fan motor, the field from an isolated Feroba III pole face was calculated at a distance equal to the air gap length, and at some typical radii. These results were given in Figure 3.19. The flux densities in line with the magnet sides at 41 mm., 47 mm., and 53 mm. radius were found to be 0.071 Wb/m^2, 0.073 Wb/m^2, and 0.068 Wb/m^2 respectively. Without calculating the field emitting from the magnet, it will be clear from these results that all of the magnet face is producing a field in excess of the critical value, 0.05 Wb/m^2, given in Table 5.1. An accurate assessment of the range of $\underline{B}$ on open circuit could be gained by

Table 5.1: Properties of permanent magnet materials,

(from Reference 12).

	Relative recoil permeability.	Conditions for recoil working. B_o, Wb/m^2.	H_o, kA/m.
Columax:	1.8	1.14	52
Hycomax IV	2.0	0.34	120
Feroba III	1.05	0.05	220

evaluating H_x and H_θ over the pole face. As before, this would require the exclusion of the singularity at the point of evaluation. The vector sum of H_x and H_θ would then yield the required field.

However, the existing calculations for the fan motor indicate that recoil operation does not occur. Also from the table, the value of the constant k is found to be 0.05. This is sufficiently small in Equation 5.1 for the assumption that $\underline{M}$ is constant to be quite accurate. It is therefore expected that the field calculations for the fan motor will be realistic.

The alloy, Columax, has a critical value for recoil operation at a much lower value of magnetising force. The flux density is only 0.03 Wb/m^2 below the manufacturer's optimum value for static working, and so it will be inevitable that recoil will result from Columax being magnetised before assembly of the machine. Assuming that the recoil permeability is constant for the whole of that quadrant of the B-H characteristic, k will be 0.8. However, the value of M_0 will have to be deduced from the recoil line now, instead of from the major loop. This makes it difficult to accurately determine the open circuit point, because $\underline{M}$ is needed in these calculations, and yet it varies with $\underline{H}$ through k and sometimes M_0 also. The field calculations will be much more accurate if magnetisation occurs after assembly, though this will be limited again by the large value of k.

It was stated in Section 2.1 that Hycomax IV would not operate in recoil if magnetised prior to assembly. Table 5.1 shows the critical point to be well down the major curve, its remanence being 0.78 Wb/m^2. Furthermore, the manufacturer's optimum static

working point occurs at 0.45 Wb/m^2, 0.11 Wb/m^2 above the critical point. There is a reasonable margin for increasing the air gap after magnetisation, though it will be difficult to calculate the open circuit point accurately. This is because the value of k = 1.0 is again quite high. If, however, $\underline{M}$ at remanence was used initially, a succession of field calculations and re-valuations of $\underline{M}$ could lead to greater accuracy. This is not felt to be worthwhile here, since there exists the fan motor using Feroba III to investigate the theoretical principles of the Disc-Armature machine already discussed.

5.2. Field in the air gap of the fan motor.

The conventional method of reducing eddy-current and hysteresis losses in a rotating ring, such as that in the fan motor, is to use a laminated construction. A return ring was therefore made with the laminations running circumferentially. This ring was difficult to handle, as it was only 3mm. thick, and so some iron powder compacts (Reference 13) were investigated as an alternative material. Carbonyl and electrolytic iron powders were studied, and the latter was found to have the better mechanical strength. These return rings are described in Appendix III.

The low values of field in the fan motor allowed the assembly of the magnetised magnets onto the backing plate without any great difficulty. In view of the discussion in the previous section, it was decided initially to check that saturation could be achieved when magnetising the individual Feroba III magnets. The manufacturers produced a B-H characteristic for the material supplied, and that is shown in Figure 5.2 (C.G.S. units are used). The remanence and coercivity are 3630 G and 3180 Oe respectively, which are quite close to the typical values of 3700 G and 3000 Oe given in Reference 12.

Figure 5.2: B-H and M-H characteristics of Feroba III magnet.

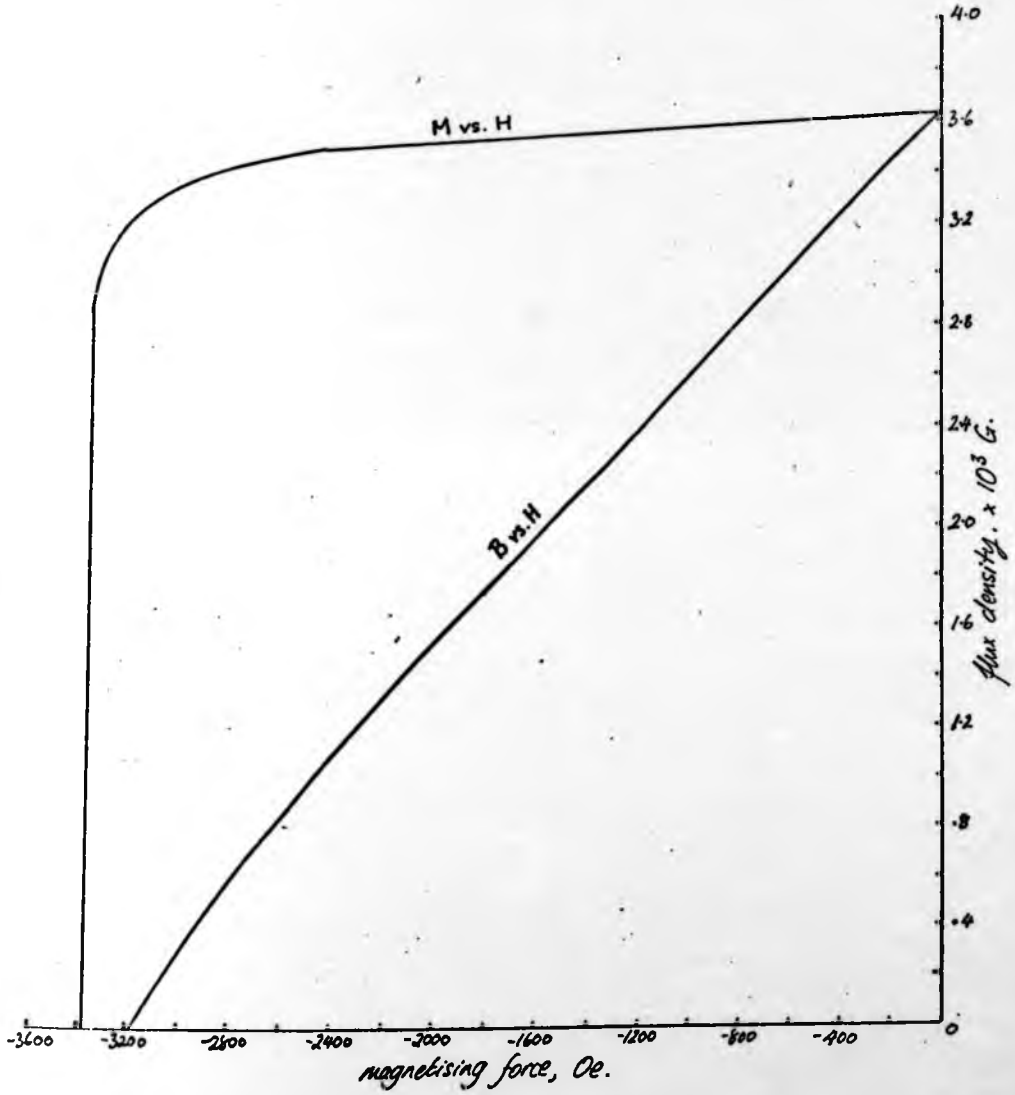

Figure 5.2: B-H and M-H characteristics of Feroba III magnet.

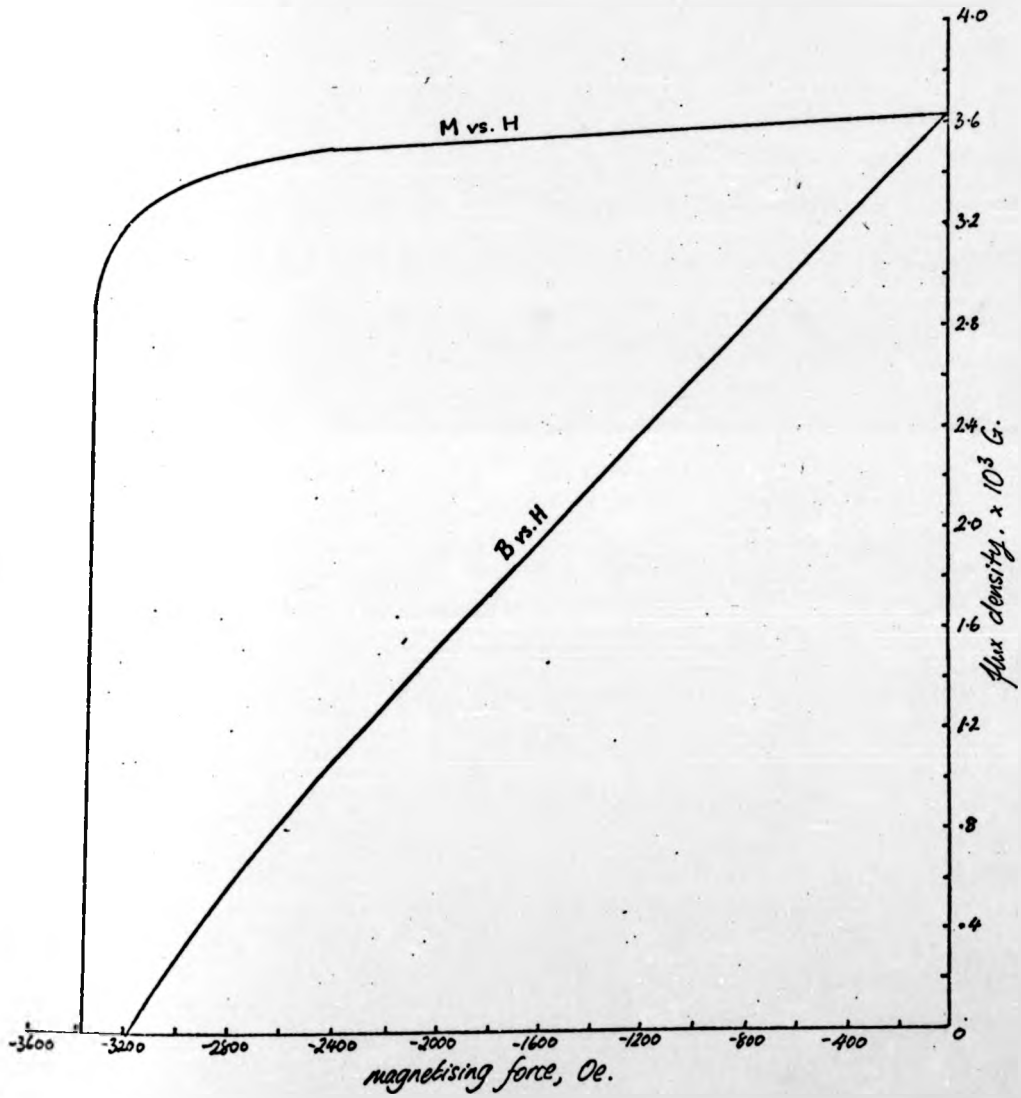

A small mild steel jig was used for the magnetisation of the individual magnets, but the coil was not calibrated with the magnetiser. Reference 14 gives the minimum magnetising force to saturate Feroba III as 8.7×10^5 A.T/m, but observations of the remanence resulting from various magnetiser voltages had to be used to verify that saturation had been achieved. After one pulse of a set voltage, a search coil around the centre of the magnet measured the remanence, and the values recorded are given in Table 5.2. All of these are quite close to the manufacturers' measured value of 0.363 Wb/m^2, and so it can be concluded that, even with the lowest set voltage on the magnetiser of 200 V, these magnets are fully magnetised.

Equation 5.1 gave an expression for the intrinsic magnetisation $\underline{M}$, and it was shown that, for Feroba III, this was approximately independent of $\underline{H}$ for the range encountered by these magnets. $\underline{M}$ will therefore be equal to the constant term, M_0, which will be given by μ_0 times the remanence, 0.363 Wb/m^2. This is the value of $\underline{M}$ that has been used in all the calculations of the fan motor's field.

5.3. Field entering fan motor flux return rings.

Having obtained an experimental value for M_s, it will be possible to calculate and measure the field entering the flux return ring of the fan motor. This will show how realistic Equation 3.25 is, and whether the image and adjacent poles have the desired effect upon the calculated field. In particular, the way in which the image poles were used assumed that the permeability of the flux return ring material was much greater than that of air. In fact, it was assumed to be infinite, so that the field entered the ring normally at all points. With certain materials, notably the iron powder

Table 5.2: Remanence achieved after 1 magnetising pulse to fan motor magnet.

Magnetiser set voltage, V.	Remanence, Wb/m^2
200	0.363
300	0.360
400	0.360
500	0.369
600	0.368
700	0.365

mixtures described in Appendix 3, this may not be wholly true, and the experimental results will reveal any such discrepancies.

Before the motor was constructed as shown in Figure 2.4, some initial tests were performed, the main objective of which was to compare the two types of iron powder ring, and to select the more suitable one. The permanent magnet poles were made from bars of Feroba III, that were the correct thickness, but which had to be cut to approximate the correct pole shape. This was achieved by joining two pieces along the centre-lines of the poles (Figure 5.3 i). A spare armature was slightly modified so that a Hall effect element could be positioned at various radii in the air gap, against the flux return ring face, and facing the magnets across the gap. The various return rings could be located in their correct positions with respect to the magnets. The dimensions of the Hall element were approximately 2.0 mm. square by 0.32 mm. thick, so that it gave a reasonably accurate measure of the flux density entering the ring at any point. The radial position of the element was set by locating it in one of several slots, each extending to a particular radial distance. The angular position was recorded by attaching a dial to the stator and a pointer to the armature.

The field distributions in the various rings at a radius of 41 mm. are shown in Figure 5.4. The use of these approximate pole shapes in the motor itself would clearly be unwise. The slight variations in the poles' arcs leads to different peak flux densities. More serious is the noticeable effect on the distribution of the join along the poles' centre-lines. This is caused by a slightly ragged edge that always occurs when these brittle ceramic ferrites

Figure 5.3.: Approximate shape of magnets for fan motor.

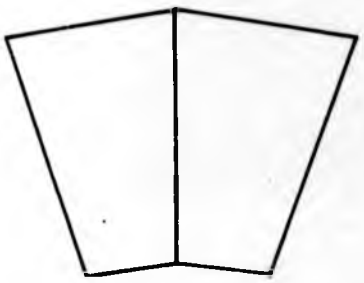

Figure 5.4. Flux distribution in fanmotor entering return ring normally at a radius of 41 mm.

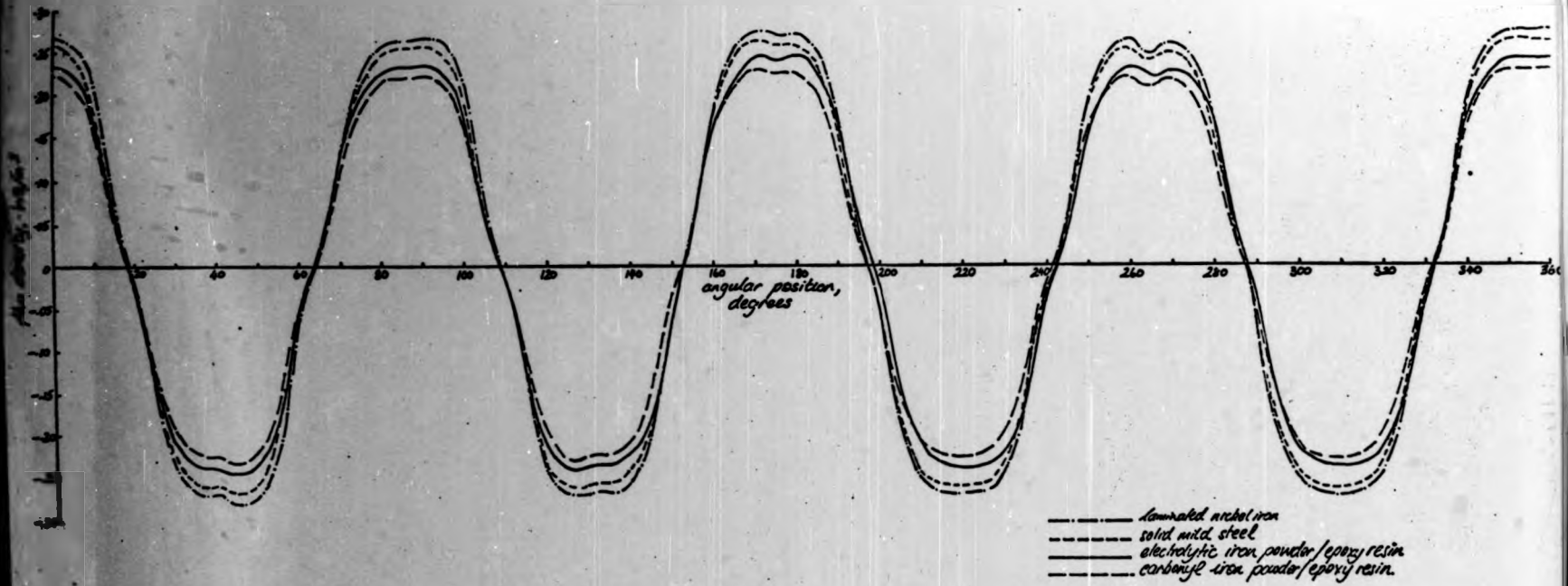

are cut. However, this does not prevent a comparison being made between these materials, and since armature reaction is negligible in a Disc-Armature machine, these distributions would be realistic at any speed if this stator were used in a motor.

All of the rings tested were of the same thickness, since the operating flux density has been shown to be less than the saturation value in each material (see Appendix 3[8]). The laminated ring, made from nickel iron strip, carries more flux than a solid mild steel one. The former has the greater permeability, and this difference indicates that, whereas mild steel has been used as an example so far having approximately infinite permeability, it would be more appropriate to use nickel iron in this context. The laminated ring should therefore be used to test the calculations using image poles.

One of the iron powder rings will actually be used in the motor, and it can be seen that both carry less flux than either the mild steel or the laminated rings. It is therefore expected that the calculated field distribution for the fan motor will be greater than that actually occurring. The relationships between the distributions given in Figure 5.4 are maintained at other radii, and the carbonyl iron powder ring carries less flux than the electrolytic one. This makes the latter preferable to use in the motor. Of course, the eddy-current and hysteresis losses in each type will be an additional criterion for this choice, though it will be shown that there is little difference between the two types in this respect. Thus, from these tests, the electrolytic iron powder ring was preferred to the carbonyl type, and it should also be remembered that the former was found to have the greater mechanical strength.

These initial tests gave a good appreciation of the relative merits of the different materials. It would not be possible, though, to determine the effect on the motor's performance, since the test rig's magnets were not as designed. When the motor was completed, with correctly shaped magnets, the modified armature was attached to its stator so that more realistic measurements could be taken.

5.3.1. Field with no flux return ring.

The first measurements were intended to indicate the accuracy with which Equation 3.25 calculates the field. The same axial position was used as in the other tests, that being the plane of the return ring face. However, it was decided to investigate the effect of adjacent poles alone firstly, so that any errors in the image poles' effect due to the return ring material would be separated. Thus, no return ring was used in this experiment, and the field was calculated using the programs "Normal Fluxplot" and "Normal Fluxplot 2", with no image poles present.

It was possible to measure the flux density at radial increments of 3 mm., from R_2 (59 mm.) to a radius of 41 mm.. It was not possible to penetrate any nearer to R_1, due to the length of the Hall effect probe. As an example, the flux distribution around the machine at 47 mm. radius is given in Figure 5.5 . It will be noticed that the peaks are of slightly different magnitudes, and it must again be concluded that the ragged edges are reducing the effective pole face areas, and hence also the field. This problem did not occur with the wheel motor since Hycomax III is not brittle, and the magnets were cut from toroids of the correct diameter. There would be no such problem either with mass production of Feroba III, since

Figure 5.5. Fan motor field distribution at 47 mm. radius at entry point to return ring but with no ring present.

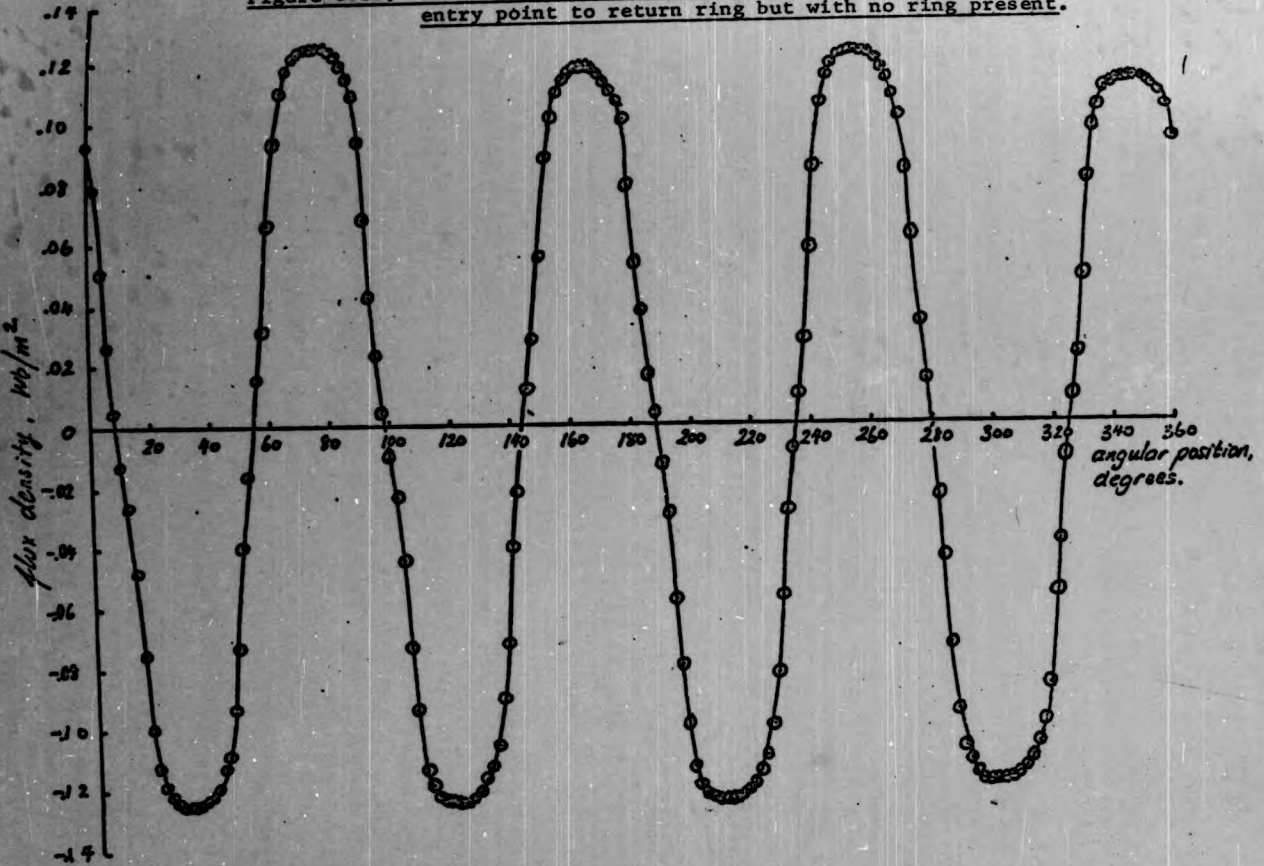

the desired shapes could be made individually, or a complete toroid could be magnetised in regions.

The poles whose face areas are reduced least are those centred at 31° and 76°. For comparison with the calculated field distributions, the latter will be considered from its centre-line to the magnetic neutral at 98.5°. Examples of the calculated and experimental distributions in the angular direction are given in Figures 5.6 to 5.9 . On the magnet centre-line, it is found that the greatest reduction in practice from the predicted field is approximately 7.5%. Of course, some of this difference may be due to the evaluated distributions being too great. However, there are indications in the experimental results that the ragged pole edges are having a definite effect. In Figures 5.6 , 5.7 and 5.9 , the difference becomes greater between about 16° and 18°, that is, in the region of the pole edge. The way in which this changes the distribution is very similar to that when the pole arc/pole pitch ratio is reduced.

The tops and bottoms of the magnets were ground to the required curvature, and performed carefully, this produced better defined edges than the straight cuts for the magnets' sides. It was noticed that at distances away from the sides, the measured flux density at R_2 was very close to its predicted value. An example is given in Figure 5.10, for the radial distribution along the magnet's centre-line. Towards the centre of the magnet, the effect of the poor edges again predominates. Figure 5.9, shows that, at R_2, this close agreement is maintained until about 3° from the magnet's edge.

Figure 5.6 : Fan motor flux distribution at 41mm. radius, at entry point to return ring but with no ring present.

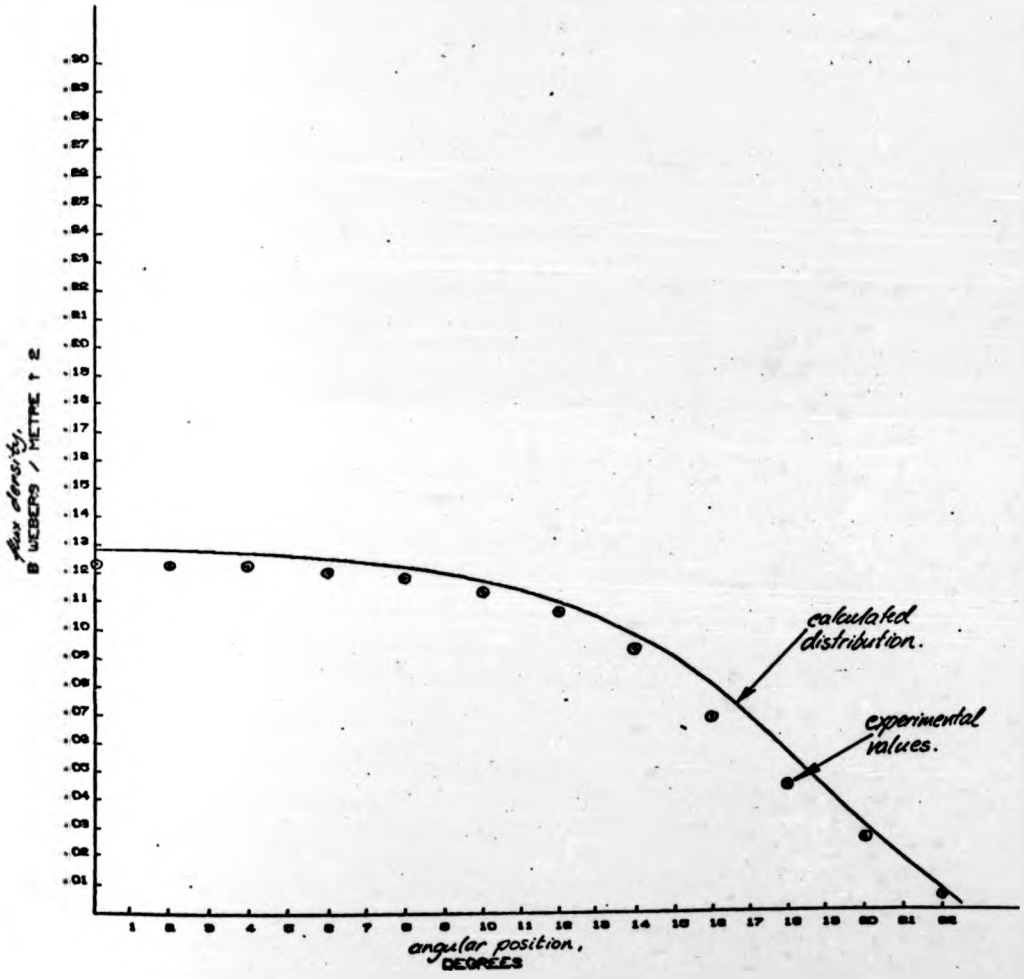

Figure 5.7 : Fan motor flux distribution at 47mm. radius, at entry point to return ring but with no ring present.

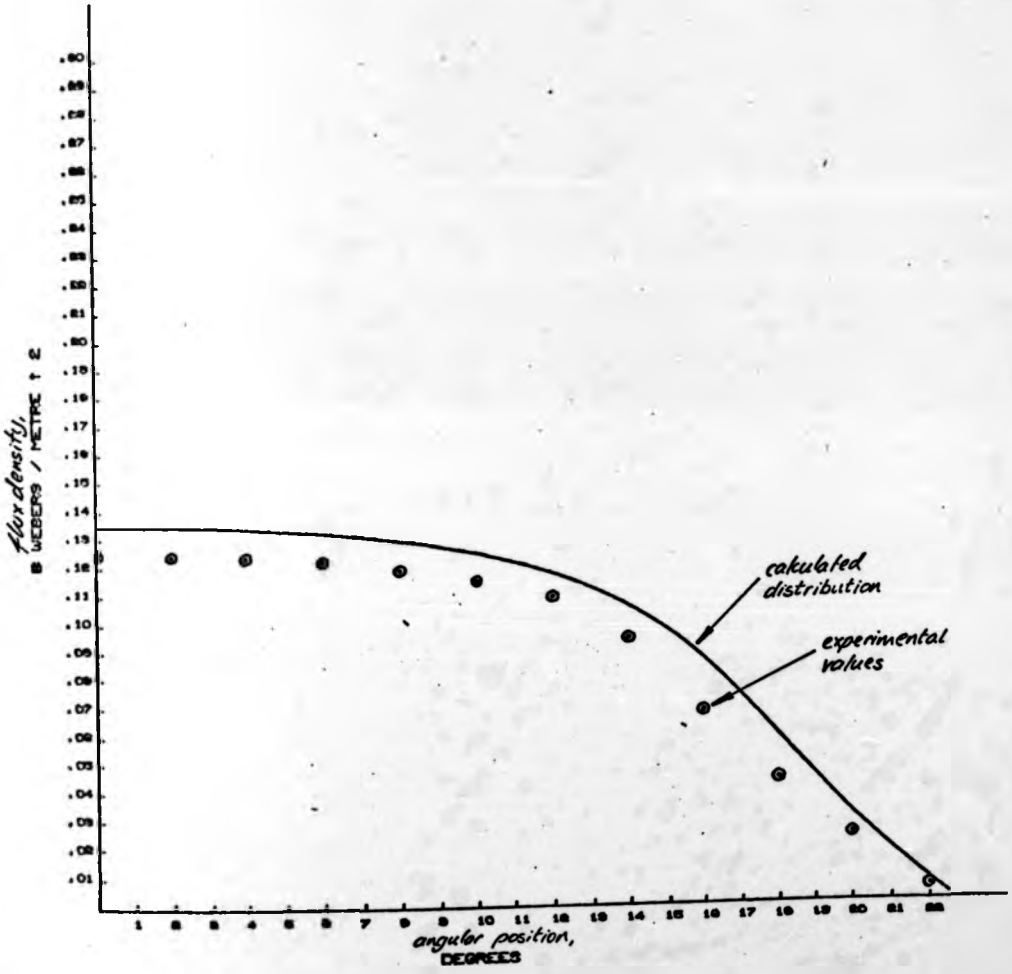

Figure 5.8 : Fan motor flux distribution at 53mm. radius, at entry point to return ring but with no ring present.

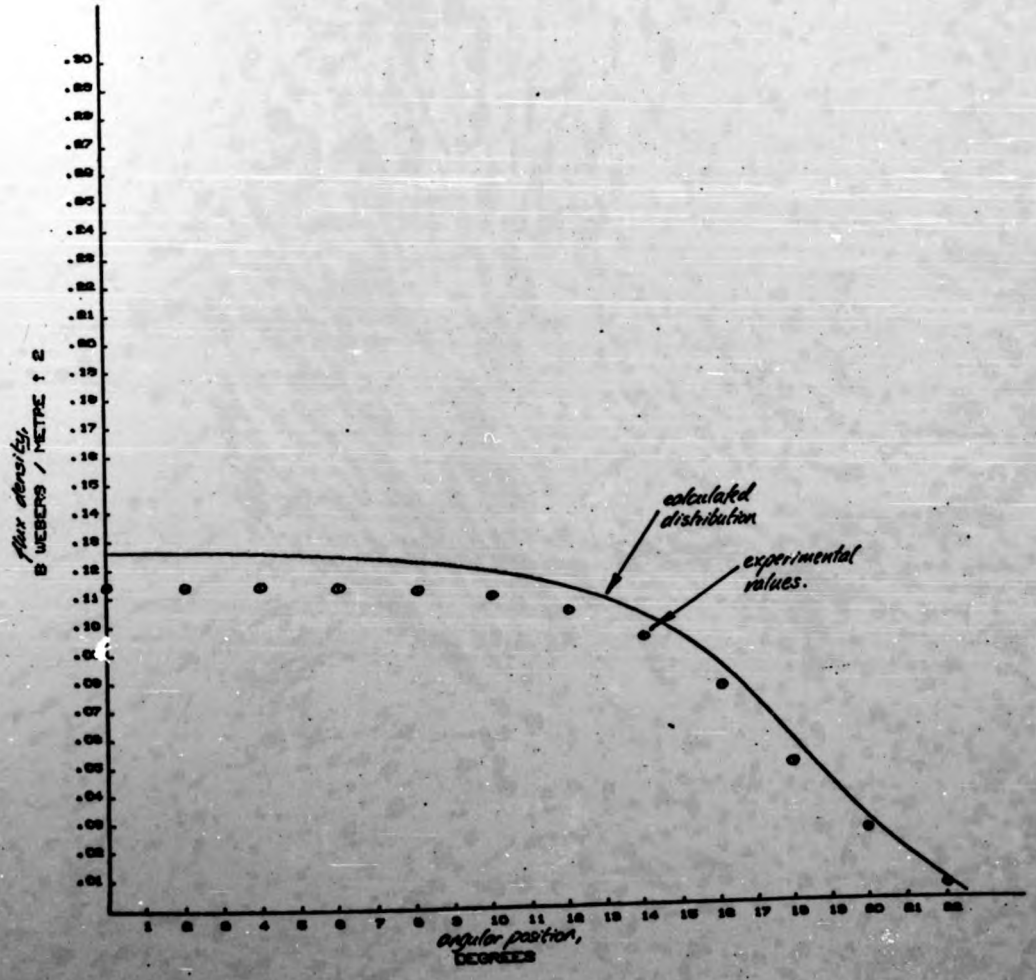

Figure 5.9 : Fan motor flux distribution at 59mm. radius, at entry point to return ring but with no ring present.

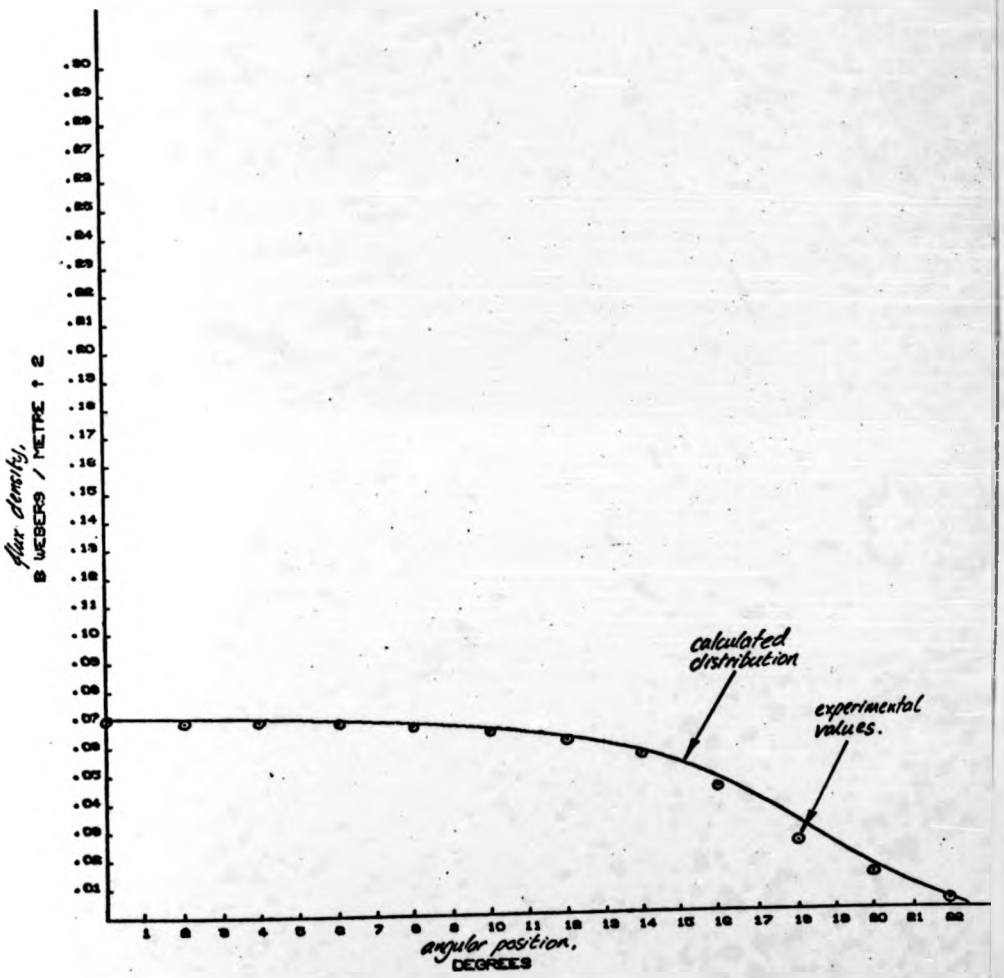

Figure 5.10: Fan motor flux distribution along magnet's centre-line, at entry point to return ring but with no ring present.

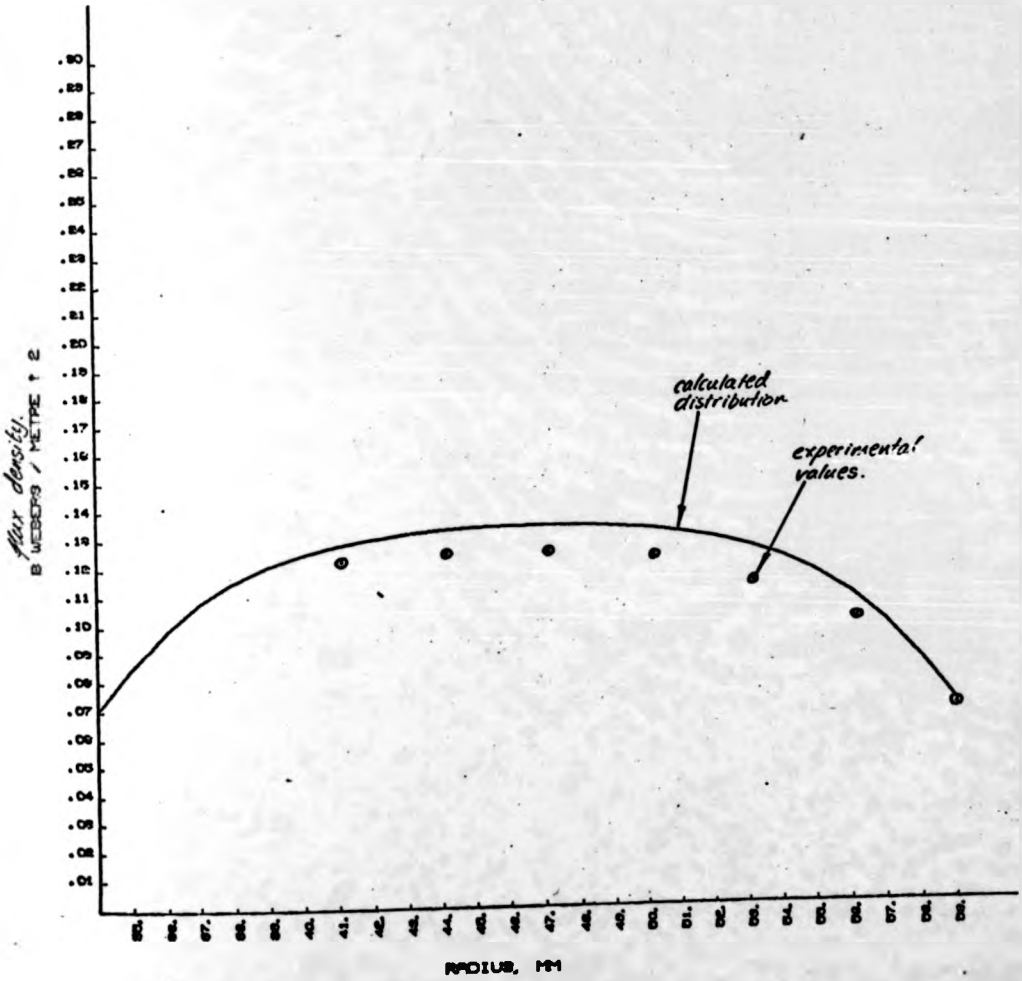

It is therefore felt that there is no reason to suppose that there is any significant error in the calculation of field, but that any reductions in the expected values are caused by the ragged magnet edges.

5.3.2. Field with laminated and mild steel flux return rings.

It has already been shown that the laminated ring has a higher permeability than mild steel, and should therefore be used as an approximation to the assumption of infinite permeability from which the image poles were derived. However, it was mentioned in Section 5.1 that there was considerable difficulty in handling a laminated ring of these dimensions, and it was not possible to maintain flat surfaces on the ring up to the time it was assembled in the modified armature.

The flux distribution was plotted in the radial direction at various angular positions in front of the same pole face that was used in the previous section. These curves are shown in Figure 5.11, and there appears to be a discontinuity at about 48.5 mm. radius, which was also found to occur in front of all the other poles. This was due to the uneven surface of the flux return ring , which was closer to the magnets at radii greater than about 48.5 mm. than it was at radii less than this. There was, therefore, an abrupt change in the air gap length as each of these curves was plotted. It was not possible to press the ring to obtain a flat surface, because the nickel iron strip was only 1 thou thick, and it was wound quite tightly. Neither was it possible to slacken the laminations to facilitate this, as the annealing had already been performed and

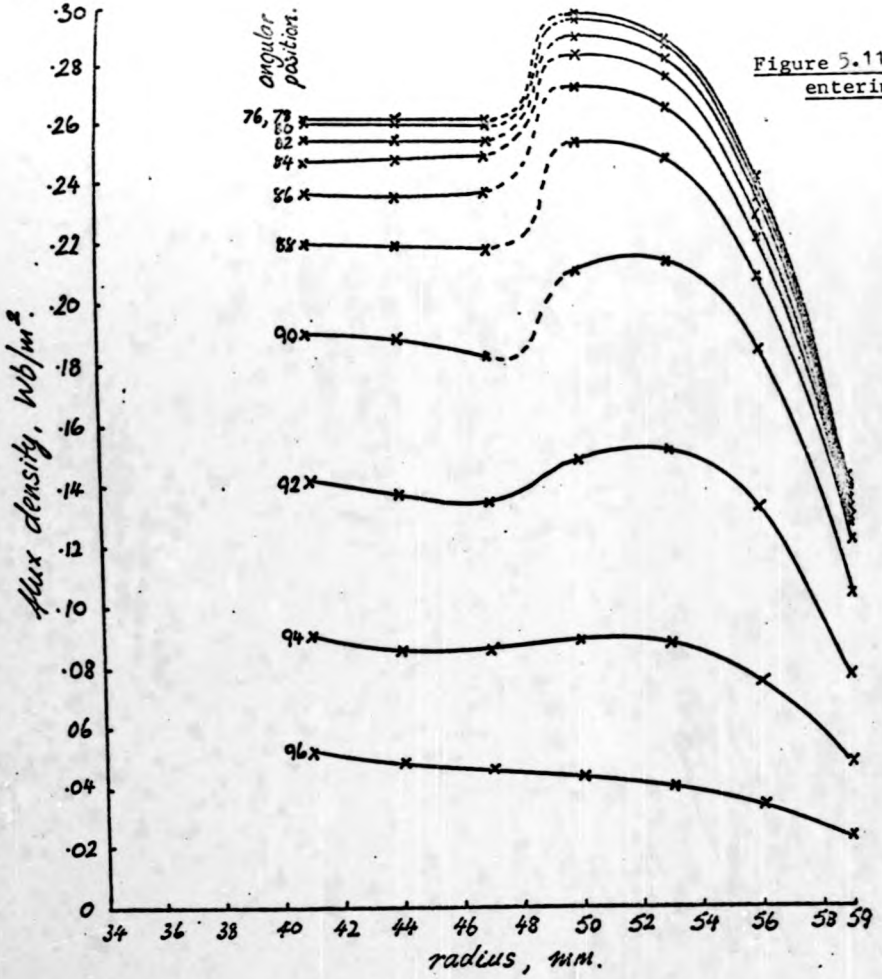

Figure 5.11. Fan motor flux distribution entering laminated return ring.

an outer steel band shrunk on. Although a laminated ring can be wound so that its surfaces are flat, there was no way of ensuring that they remained so during annealing and subsequent handling (It should be noted that this might also make any test results non-repeatable). The results of Figure 5.11 must therefore be treated as an illustration of the effect of a slight change in the air gap length on the flux distribution.

In this case, there is a step decrease in the air gap length, which leads to a sudden increase in flux density. At some distance from the discontinuity, the flux density approaches its predicted value, and Figure 5.12 shows that this occurs at R_2. It will be remembered that this was the situation that occurred with no flux return ring present, as described by Figure 5.10 . The calculated and measured flux distributions at R_2 for the laminated ring are given in Figure 5.13, which again shows that this close agreement is true except near the magnet's edge. As described in the previous section, this discrepancy is due to these edges having a ragged finish, which reduces the flux density at certain places from that calculated. It must therefore be concluded from the measured points on Figure 5.12, that the profile of this laminated ring contains other complications than the abrupt change already mentioned. These need only be quite small variations from a perfectly flat surface, and are not apparent in the photograph of the ring, Figure AIII.1. It should also be remembered that, whereas the ring is constrained at R_2 by a mild steel band, the laminations were wound onto a stainless band whose inner radius was R_1. This was necessary for the annealing process, but clearly this return ring is sacrificing some of the

Figure 5.12 : Fan motor flux distribution along magnet's centre-line, entering return ring.

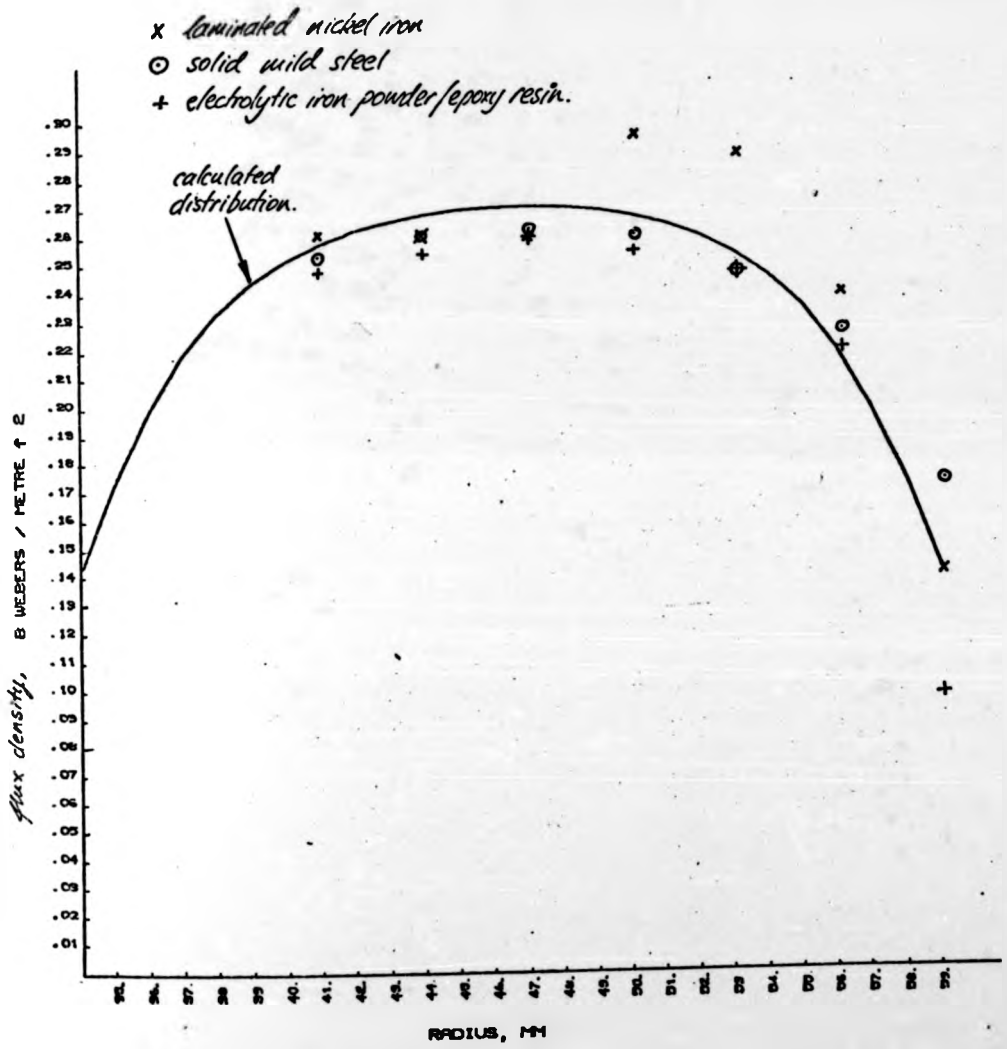

active length in this region.

Although it has been said that the laminated ring would be the most appropriate for confirming the calculations using image poles, these difficulties will prevent this, and the solid mild steel ring will have to be used instead. On Figure 5.12 is also marked the flux distribution entering the mild steel ring opposite to the centre-line of a pole. The shape of this curve is much closer to that calculated, though it gives slightly lower values towards the middle of the active region, and slightly higher values towards R_2 and presumably R_1 also. This graph should be compared with that for no flux return ring present (Figure 5.10), so that the accuracy of using image poles for the return ring can be studied.

To agree with the theory and the discussion in the previous section, this flux distribution for mild steel should coincide with the calculated curve at R_2 and R_1, and show a maximum reduction from it of about 7.5%. In fact, the measured values at all radii are greater than these. It would therefore seem that the direct superposition of a set of image poles, as described in Section 3.4.1, does not exactly account for the presence of a flux return ring. This discrepancy can best be explained by considering the magnet system before and after the image poles are added.

The importance of the recoil permeability as a guide to the accuracy of the calculations was described in Section 5.1. For Peroba III, this gave a value for k in Equation 5.1 of 0.05, which was assumed to be negligible. The measured B-H characteristic of this material was given in Figure 5.2, onto which the M-H curve is also plotted. From this can be judged the accuracy of assuming that μ is equal to the constant μ_0.

In the case of the results of Figure 5.10, the error due to this cause will be compounded with that caused by the ragged magnet edges. The calculated field is directly proportional to M_s for this type of material (Equation 3.25), and the deviation of this from M_0 becomes greater as the demagnetisation is increased. It is not possible to re-draw the calculated flux distributions, since they do not relate to the field emitting from the pole face. However, by taking the maximum calculated value on the magnet centre-line as being typical of this, an estimate of the error in M_s can be made. Thus, the calculated distribution of Figure 5.10 is approximately 3.3% too great, and that of Figure 5.12 is about 1.1% too great. It should be stressed that these are only estimates, that will become less certain towards the edges of the pole face. However, they show, as does the M-H characteristic, that the error is greatest with no return ring present.

The measured flux distribution in the radial direction is therefore slightly "flatter" than the calculated one. However, Figure 5.12 shows that the total flux measured through a narrow strip in front of the magnet's centre-line will be quite similar to that calculated. This is true also at angular positions away from the centre-line, and an example is shown in Figure 5.14. The dip in the curve, that was noticed with no ring present, due to the ragged magnet edges, extends over a greater arc with a flux return ring in place. The distribution for a position 6° away from the edge, towards the magnet, exhibits this effect (Figure 5.15). The results plotted in the angular direction show this better, and Figure 5.16 can be compared with Figure 5.7 .

It can therefore be concluded that, once again, the poorly

Figure 5.14: Fan motor flux distribution 6° from magnet's centre-line, entering return ring.

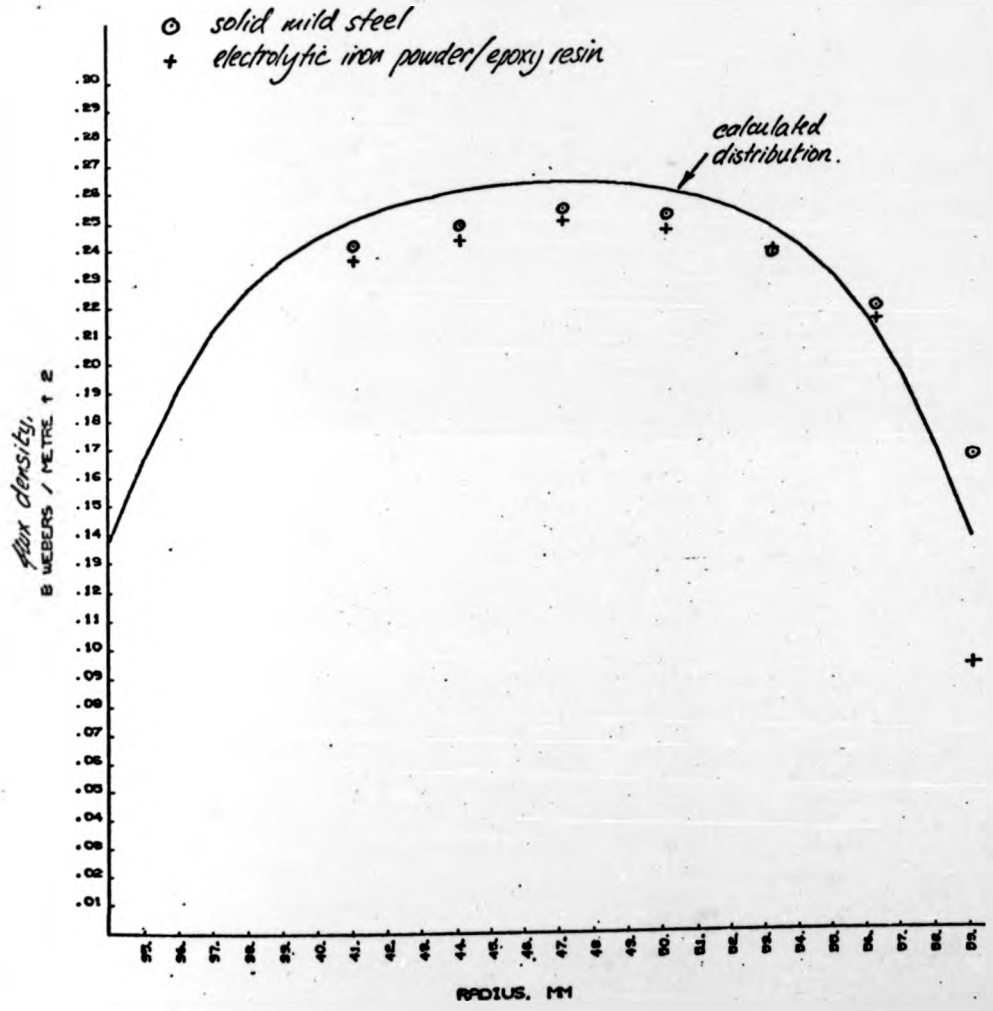

Figure 5.16: Fan motor flux distribution at 47mm. radius entering return ring.

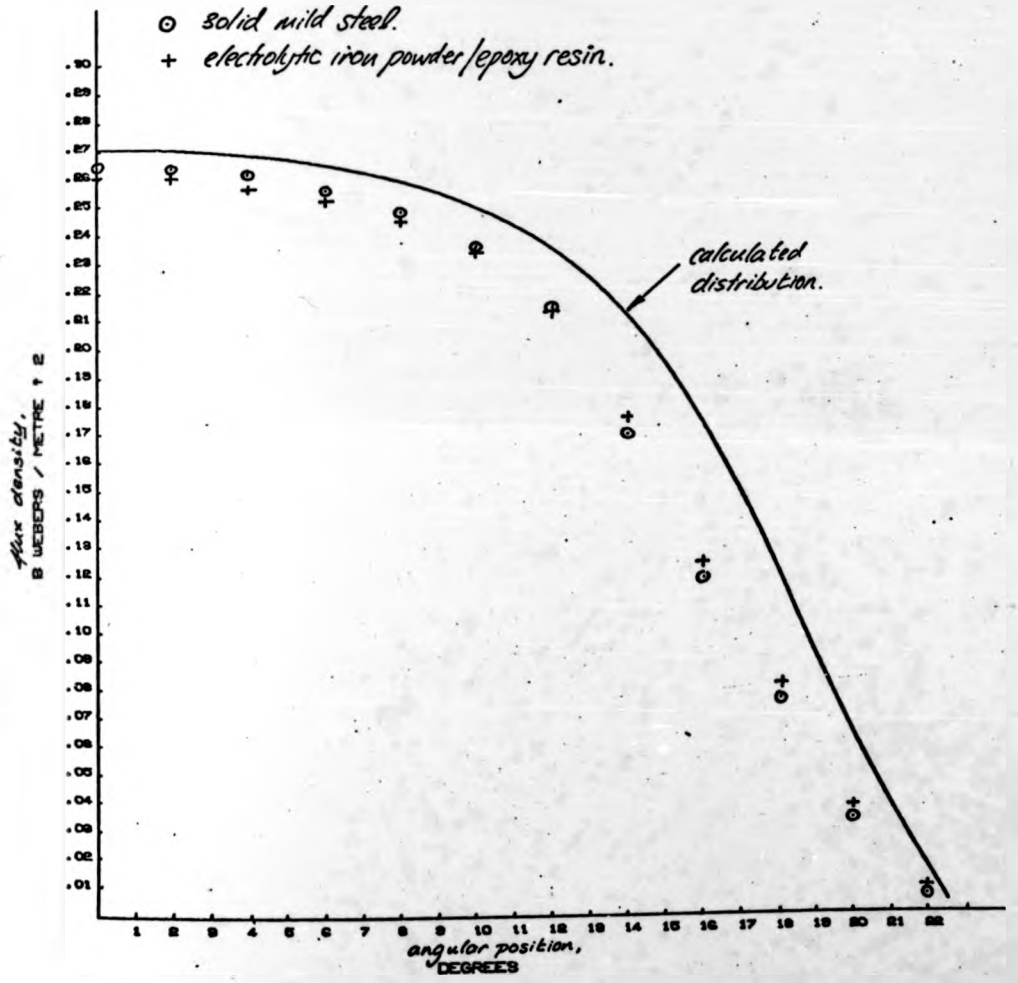

defined pole edges are leading to a discrepancy between the measured and calculated flux distributions. At angular positions where this effect is minimal, the system of image and adjacent produces quite a good model of the radial distribution, and this was based on the assumption that the mild steel ring had infinite permeability. The measured curves in this direction are slightly "flatter" than those calculated, though this would not greatly affect the calculation of induced e.m.f. in a radial-lying conductor.

5.3.3. Field with iron powder flux return ring.

For the operation of the radiator cooling fan motor, the performance of the iron powder flux return ring is important. The electrolytic iron powder has already been preferred to the carbonyl type, and so this section will only refer to the former.

The flux distribution entering the electrolytic ring was compared with that for the laminated and mild steel rings on the approximate test rig, and those results were given in Figure 5.4.. They refer to a particular radius, and it has since been shown that the distribution for the laminated ring may be non-repeatable, and will therefore not be used for comparison. The results for the mild steel agree quite well with the theory, however, although this is limited by the accuracy of manufacturing the required magnet shape. A comparison should therefore be made between the field entering the iron powder ring and that into the mild steel ring, to give an indication of the reduction of flux caused by using the powder material. The former can also be compared with the calculated field, to determine the accuracy of the theory for this case.

In Figure 5.4., the flux density entering the electrolytic

iron powder ring was found to be approximately 7.5% less than that into the mild steel ring. These distributions were repeated using the stator from the motor, at the same radius, and the difference was somewhat smaller (Figure 5.17). A similar result was found nearer to the centre of the active region, at a radius of 47 mm. in the machine (Figure 5.18). The variation of the heights of the peaks in Figure 5.18 corresponds to that in Figure 5.5, and has the same cause. As before, a better appreciation of the shapes of the distributions can be gained by considering the region from the pole centre-line at 76° to the magnetic neutral at 98.5°.

The results for this ring are also shown, therefore, in Figure 5.16. Compared with the mild steel ring, the distribution in the angular direction is slightly "flatter" in shape, though there is quite close agreement between these two. The distributions in the radial direction also show good agreement, and the iron powder ring's results are shown in Figures 5.12, 5.14, and 5.15. These three figures show that a discrepancy with the mild steel's curves occurs near the radius R_2, and so may also happen near R_1. When examined closely, it was found that the iron powder ring had been damaged in the same way as the magnets. The edges at R_1 and R_2 were not straight, but the corners with its two faces had become rounded during its manufacture. This probably occurred when the ring was extracted from the die, after the compaction process. The graphs show that the drop in flux density towards R_2 is quite abrupt, which indicates that the extent of this damage is not very great.

It can therefore be concluded that the iron powder ring tested compares very well with a mild steel ring of the same dimensions, in terms of the flux entering this component in the radiator cooling

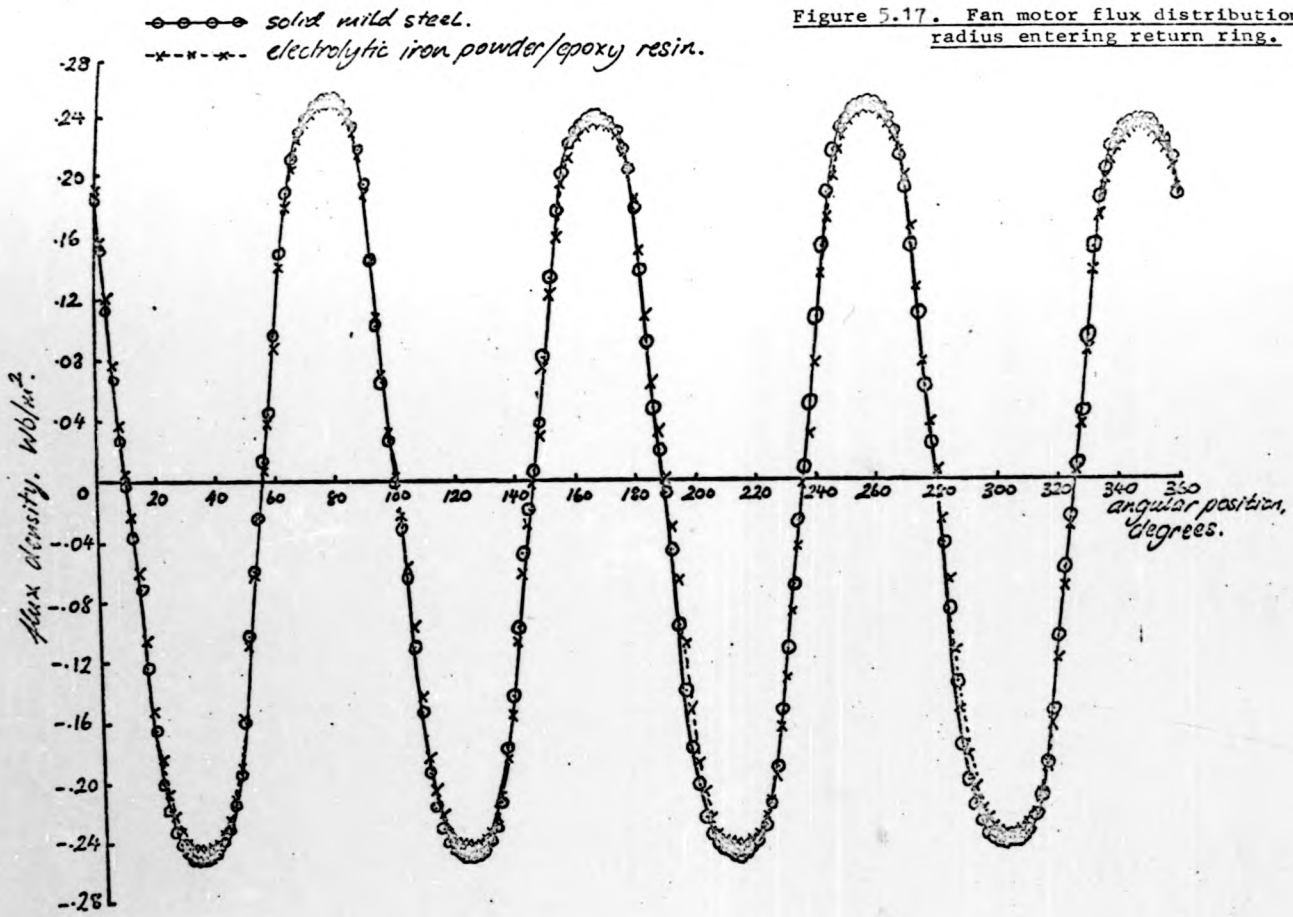

Figure 5.17. Fan motor flux distribution at 41mm. radius entering return ring.

Figure 5.18. Fan motor flux distribution at 47mm. radius entering return ring.

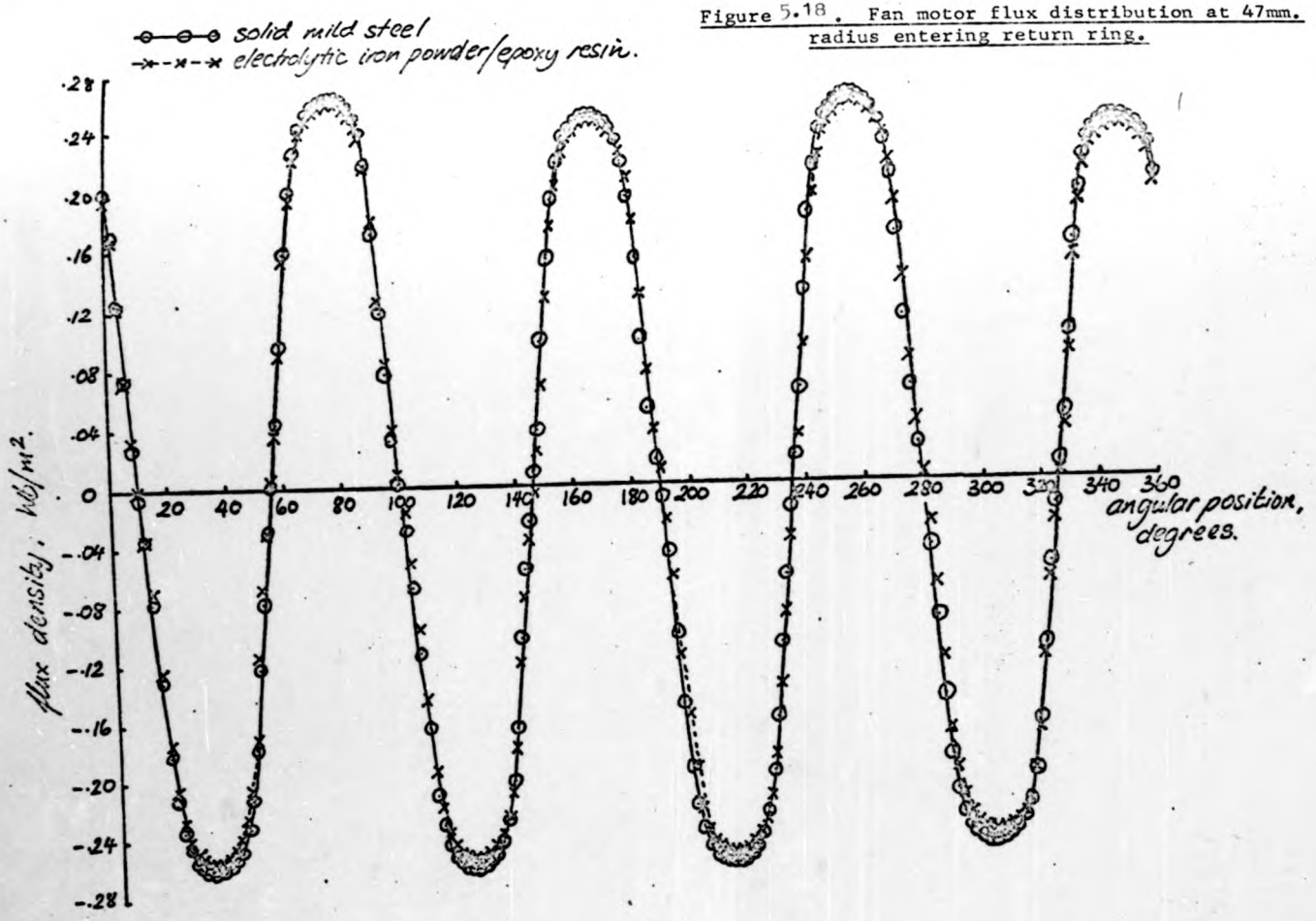

fan motor. There is no reason to suppose that the theory derived to calculate the magnetic field is not applicable to each type with reasonable accuracy, although the errors in the manufacture of the magnets and the iron powder ring have led to some discrepancies with this machine. It remains to be demonstrated that the iron powder ring has much lower losses, due to its rotation in this field, than even the laminated ring has.

5.4. Power losses in the flux return rings.

It is possible to analyse the power losses in a d.c. machine, such as the fan motor, by performing various tests after it has been constructed. However, it was desired to gain some appreciation of the relative magnitudes of the losses in the various flux return rings, in order to select the most suitable for incorporation into the machine. An approximate stator was described in Section 5.3, and it was also used for this purpose.

The arrangement of the test rig is shown in Figure 5.19. A phosphor bronze bearing, which was used in the first prototype fan motor, is included, attached to which is a tufnol carrier, which holds the ring in position with the correct air gap length. The method employed for determining the variation of these losses with speed was to drive the rig with another motor, and to deduce the required power from the input power to that machine. Clearly, the drive motor itself would have losses, and it was important that these (with the exception of its I^2R losses) did not depend upon the load applied. This condition is met by a machine that has no iron in the rotor, such as the Disc-Armature electric vehicle

fan motor. There is no reason to suppose that the theory derived to calculate the magnetic field is not applicable to each type with reasonable accuracy, although the errors in the manufacture of the magnets and the iron powder ring have led to some discrepancies with this machine. It remains to be demonstrated that the iron powder ring has much lower losses, due to its rotation in this field, than even the laminated ring has.

5.4. Power losses in the flux return rings.

It is possible to analyse the power losses in a d.c. machine, such as the fan motor, by performing various tests after it has been constructed. However, it was desired to gain some appreciation of the relative magnitudes of the losses in the various flux return rings, in order to select the most suitable for incorporation into the machine. An approximate stator was described in Section 5.3, and it was also used for this purpose.

The arrangement of the test rig is shown in Figure 5.19. A phosphor bronze bearing, which was used in the first prototype fan motor, is included, attached to which is a tufnol carrier, which holds the ring in position with the correct air gap length. The method employed for determining the variation of these losses with speed was to drive the rig with another motor, and to deduce the required power from the input power to that machine. Clearly, the drive motor itself would have losses, and it was important that these (with the exception of its I^2R losses) did not depend upon the load applied. This condition is met by a machine that has no iron in the rotor, such as the Disc-Armature electric vehicle

traction motor, or the printed circuit motor. In fact the latter was used here.

It was found necessary to apply forced cooling to the printed circuit motor's casing for some of the measurements, so all were taken with this in operation, and the locked rotor test produced the curve shown in Figure 5.20. The system was run with all the components of Figure 5.19 except a flux return ring, to determine the mechanical losses in the drive motor, those in the sleeve bearing, and the windage loss. The variation with speed of the total of these, with the motor's I^2R power subtracted, is shown in Figure 5.21. The additional losses due to incorporating the return ring in the rotor can be found with the aid of Figures 5.20 and 5.21, and the procedure is demonstrated for the laminated ring in Figure 5.22.

From the input power to the drive motor is subtracted the I^2R power. The mechanical power found in Figure 5.21 is then subtracted, leaving the variation with speed of the power due to eddy-currents, hysteresis, and the thrust force between rotor and stator. The latter is also caused by the new position of the return ring, though the magnitude of this loss depends upon the type of bearing used, phosphor bronze having quite high losses.

This last curve is repeated in Figure 5.23, together with those found for the electrolytic and carbonyl iron powder rings, and the mild steel ring. The speed range over which these could be determined was restricted somewhat by speed fluctuations at lower values, caused by variable losses in the phosphor bronze thrust bearing. Other problems developed with this component, and its performance will be mentioned in Chapter 6.

Figure 5.20 : Printed circuit motor I^2R losses, with applied cooling.

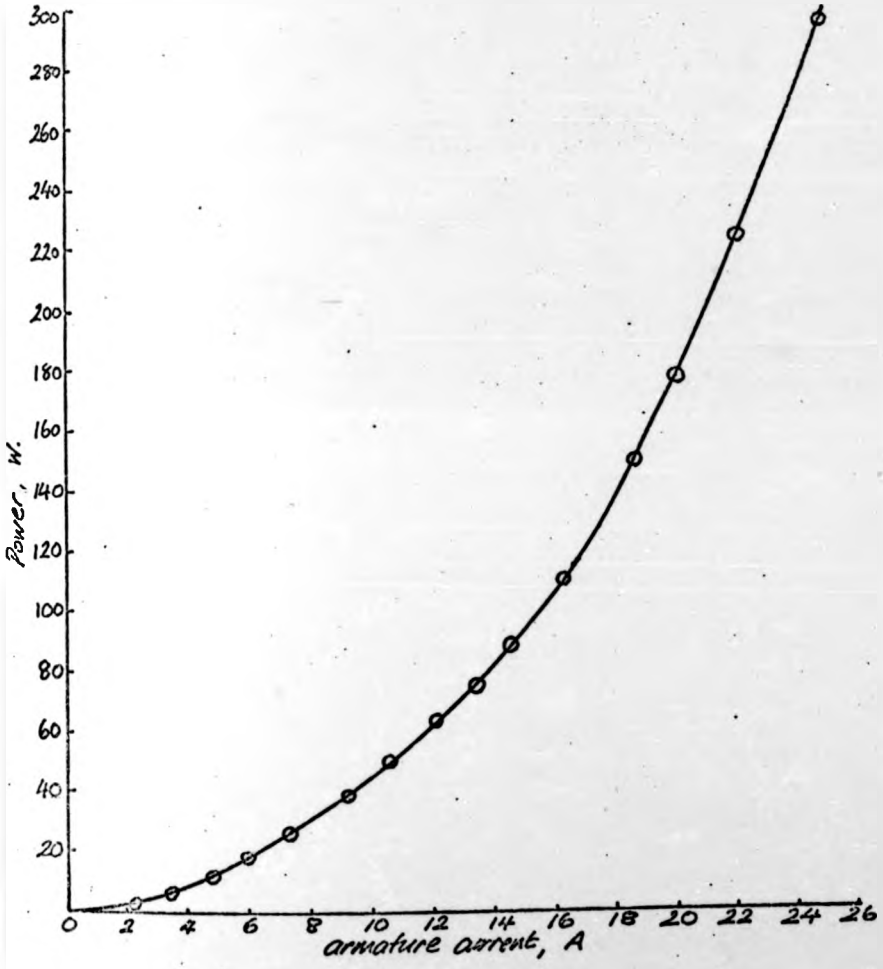

Figure 5.21 : Power losses in return ring test rig.

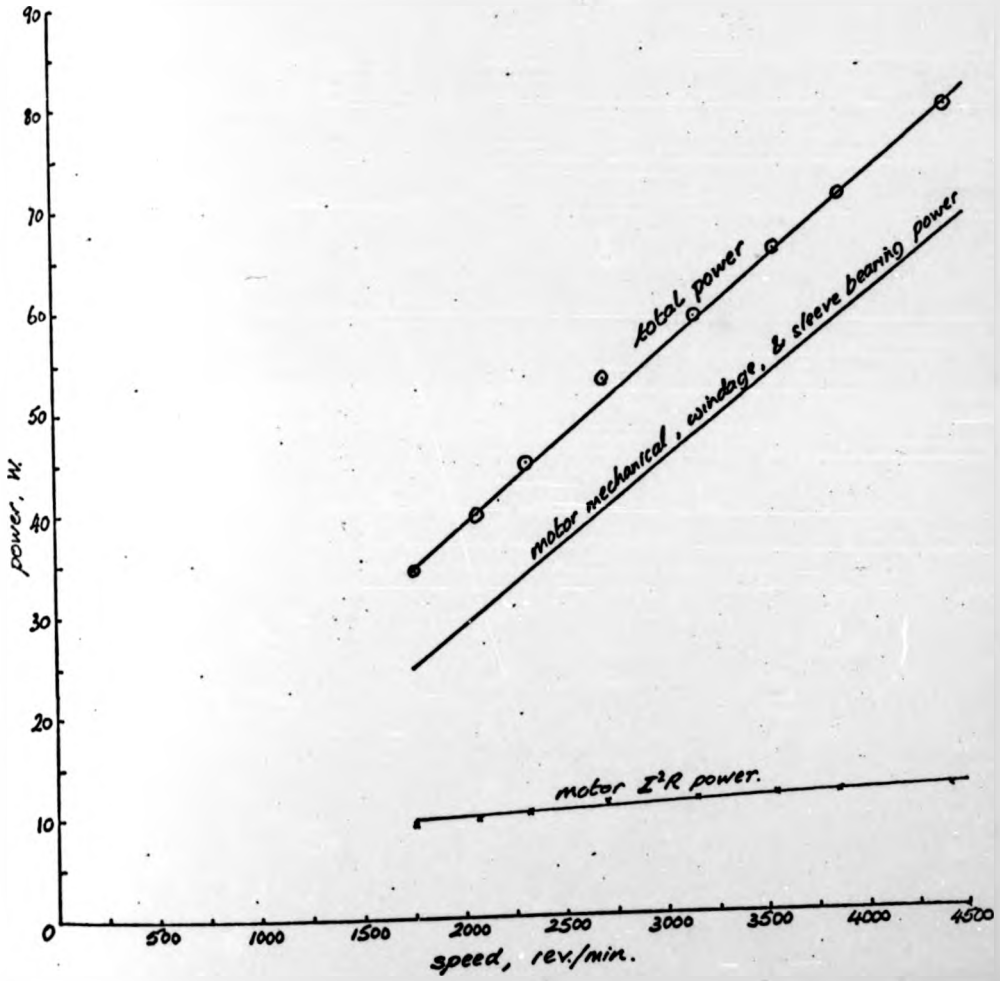

Figure 5.22 : Determination of power losses in rotating laminated flux return ring.

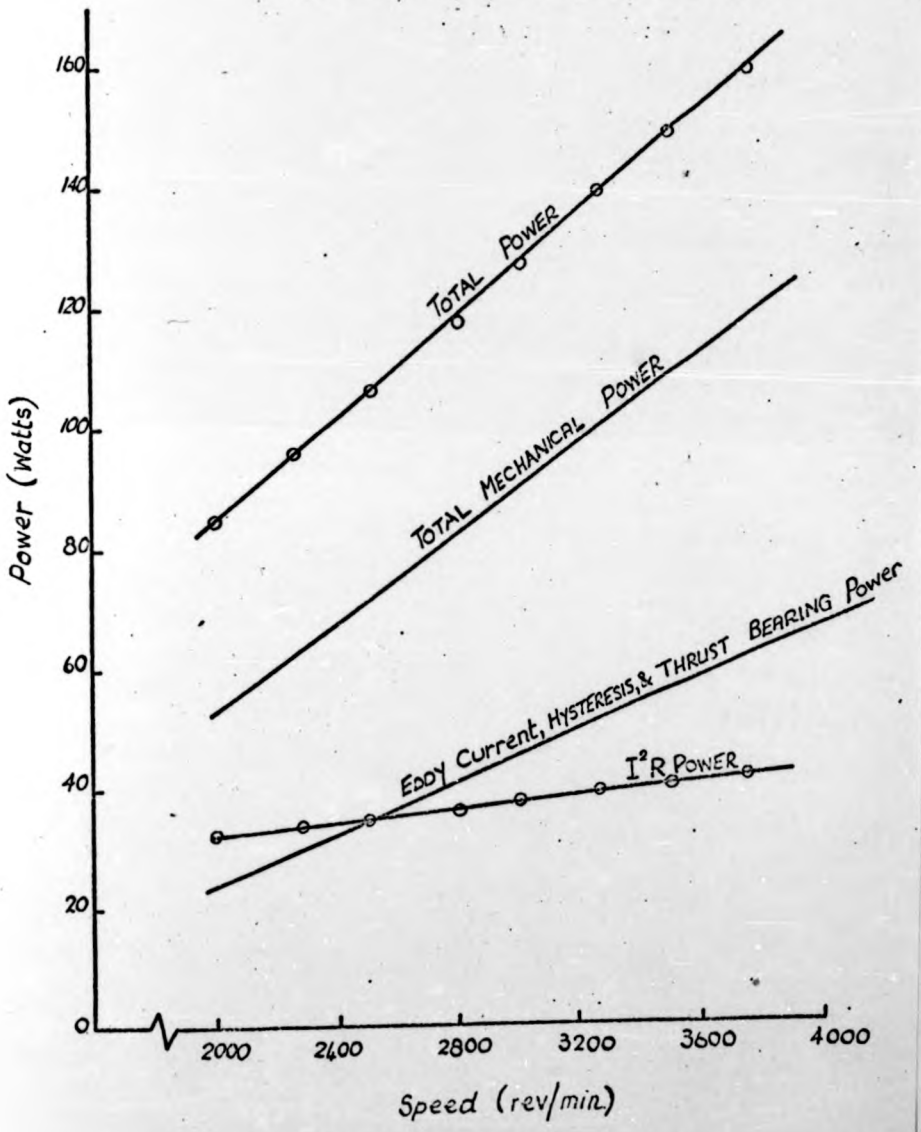

Figure 5.23: Power loss in fan motor return ring and thrust bearing.

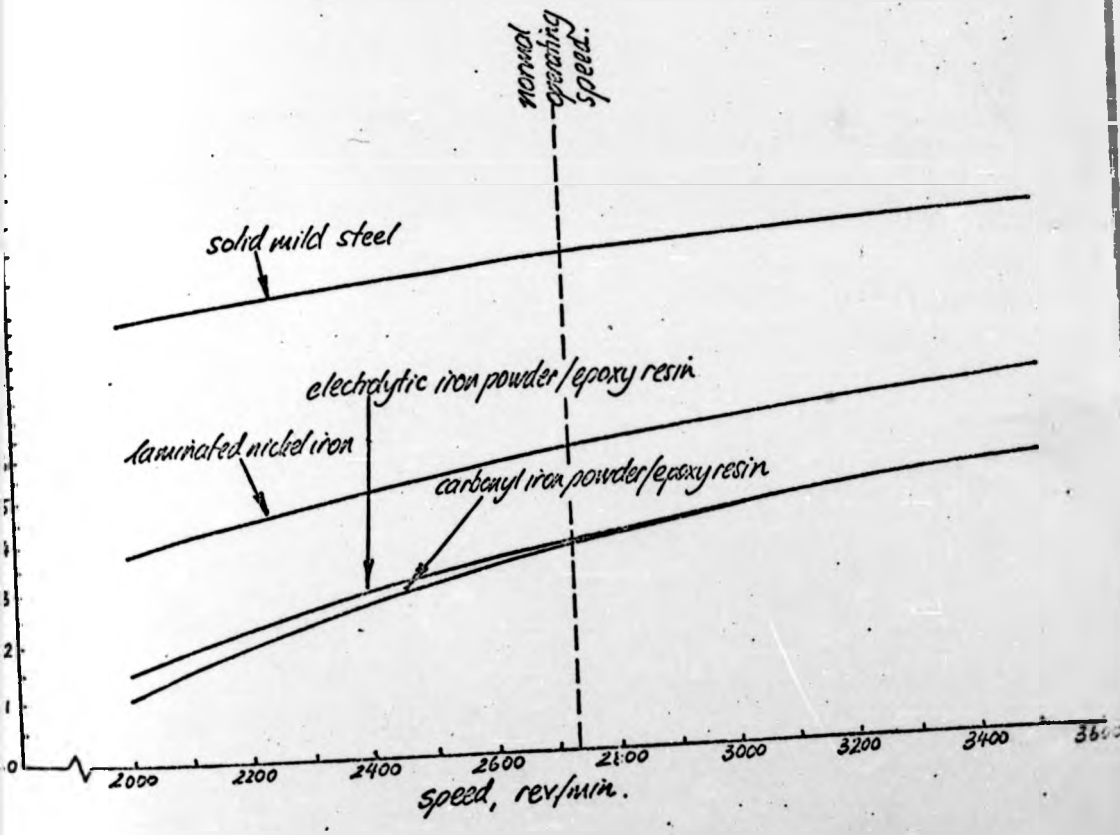

These results show, not surprisingly, that solid mild steel has extremely high losses in the rotating member, these being 180 W at the fan motor's normal operating speed. For this reason, it is not a suitable material in this situation.

More interesting is a comparison between the losses for the laminated ring, and those for the iron powder ring. The former is nearly twice as large as the other two, though there are limitations in this comparison. Firstly, it will be remembered that the laminated ring has an uncertain profile, and may be carrying a greater flux density than the others. However, it will be shown in Chapter 6 that the thrust bearing friction loss is a significant part of each of the totals, although this too is dependent upon the flux distribution entering the return ring. It is unfortunate that, with this simple test rig, it is not possible to separate this loss from the eddy-current and hysteresis losses. Of course, tests performed in a drum-shaped machine would achieve this. It must be remembered, though, that the purpose of these initial tests was to select a suitable material for the fan motor, and either iron powder ring appears from Figure 5.23 to be preferable to the laminated ring.

The electrolytic iron powder ring has slightly higher losses than the carbonyl iron powder. However, the difference at the motor's normal operating speed is only 0.4 W, and so the advantage might alter if the greater field entering the former type was taken into account. It has been shown, then, that the selection of the electrolytic iron powder ring for use in the fan motor, made in Section 5.3, was quite justified. Chapter 6 will describe tests on this machine that indicate the true magnitude of the eddy-current and hysteresis losses.

5.5. Field in the air gap of the wheel motor.

The electric vehicle traction motor was designed to use Hycomax IV permanent magnets to produce the field. However, as was mentioned in Section 2.2, this material was not available when the prototype was manufactured, and so Hycomax III was used instead. Each set of magnets was magnetised in the manner described in Appendix IV, although that was intended for Hycomax IV. It was therefore decided to encapsulate some search coils in the armature of the wheel motor, with which to measure the field.

Two types of search coil were used, and each is shown in Figure 5.24. One spanned one pole pitch, and the other was much narrower, though it also extended over the whole active radial length. Both of these were located in the middle of the armature, between the two double-layer windings. Since armature reaction is negligible, the armature could be rotated by hand, and a field distribution for normal operating conditions would be produced. The leads from the ends of the coils come out of the machine through the centre of the shaft, and a hole was left in the centre of the mould (Figure AIV.5) for them to protrude through during encapsulation. A dial was attached around the shaft to indicate the angular position of the armature.

The flux distribution for the small search coil is plotted in Figure 5.25, its area being 120 mm^2. This approximates to the flux cut by a conductor, as it performs a revolution in the machine. A calculation of a similar distribution to this was given in Figure

Figure 5.24 Search coils used in the wheel motor.

(a) Pole-pitch coil:

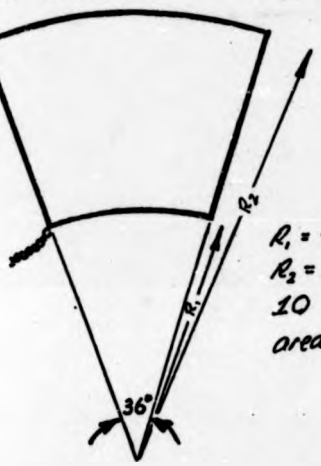

R_1 = 41 mm
R_2 = 71 mm
10 turns.
area = 1057 mm^2

(b) Small coil:

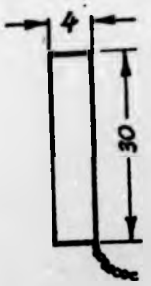

10 turns.
area = 120 mm^2

Figure 5.25 Field distribution in the wheel motor measured with small search coil.

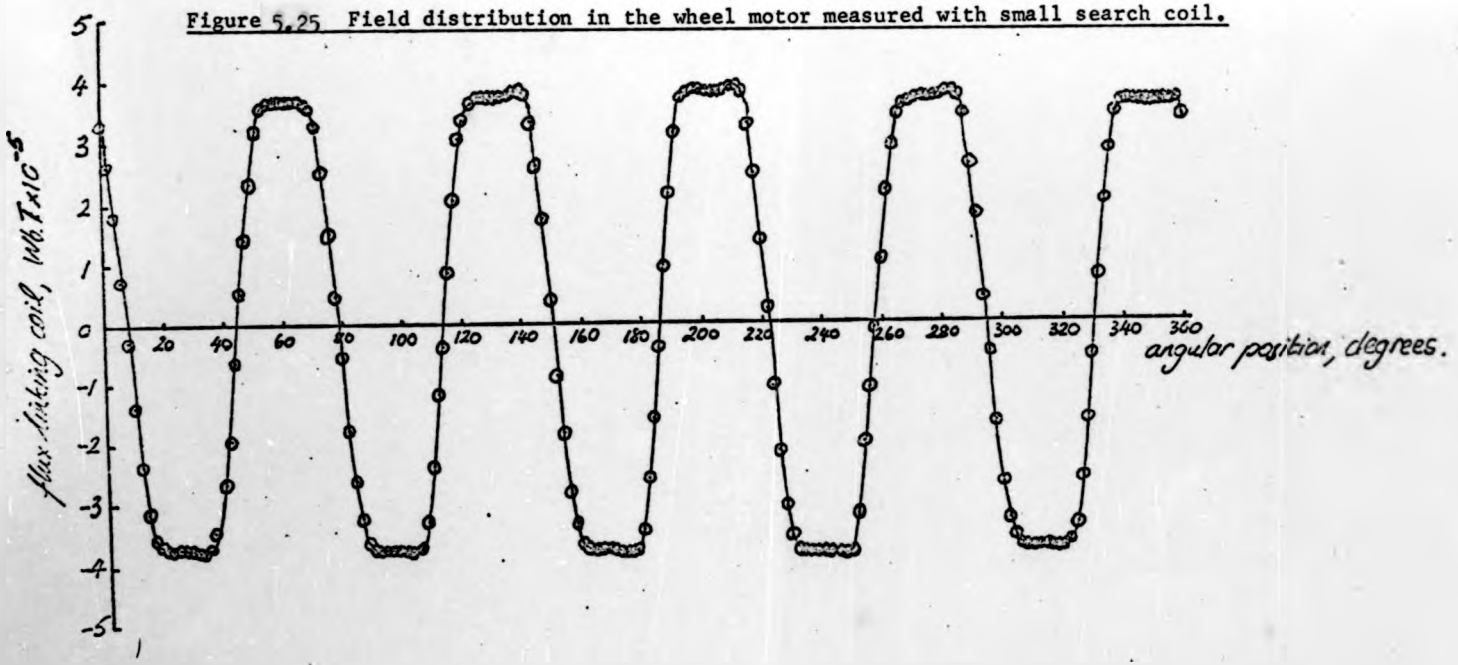

3.17 for the fan motor. A comparison of the shapes of the two distributions shows that the wheel motor's is uncharacteristic in that a slight reduction in flux is detectable over the centre of each pole. This raises doubts about the validity of the theoretical approach for this magnet material.

The peaks in the flux distribution for the pole pitch coil can be used to determine the useful flux from each pole. That distribution is shown in Figure 5.26 and the area of the coil is 1057 mm^2. There is a slight variation in the heights of the peaks, due to small errors in the dimensions and locations of the magnets. The useful flux densities from the poles will therefore be within a range, which is found to be 0.172 Wb/m^2 to 0.185 Wb/m^2. The densities at the magnet faces will be greater than these, but will nevertheless be much smaller than the designed values. An approximate method will be used initially, to show that these magnets are working on a recoil line.

First of all, it was felt advisable to check the B-H characteristic of this particular material with that quoted by the manufacturers for Hycomax III. A sample was therefore returned to them, and they produced the characteristic (in C.G.S. units) shown in Figure 5.27. The remanence and coercivity quoted in Reference 12 are 9000 G and 1600 Oe respectively, which are quite close to the values of 9480 G and 1590 Oe found for the sample.

The useful flux densities found in the air gap are equivalent to the magnetising force, H_g, in Equation 2.1, being directly related to it by the constant μ_0. The equivalent range of flux density, B_m, produced at the magnet face will be greater than these due to the

Figure 5.26 Field distribution in the wheelmotor measured with pole pitch search coil.

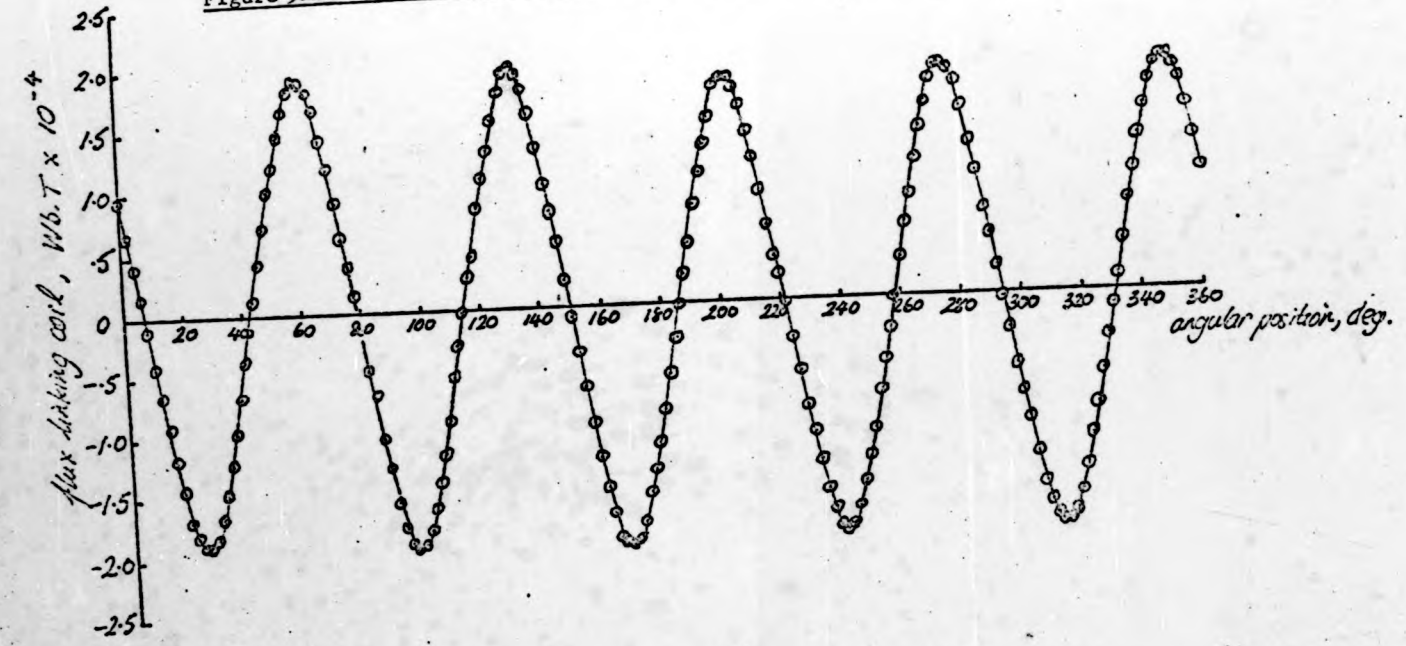

Figure 5.27 B-H characteristics of Hycomax III magnet.

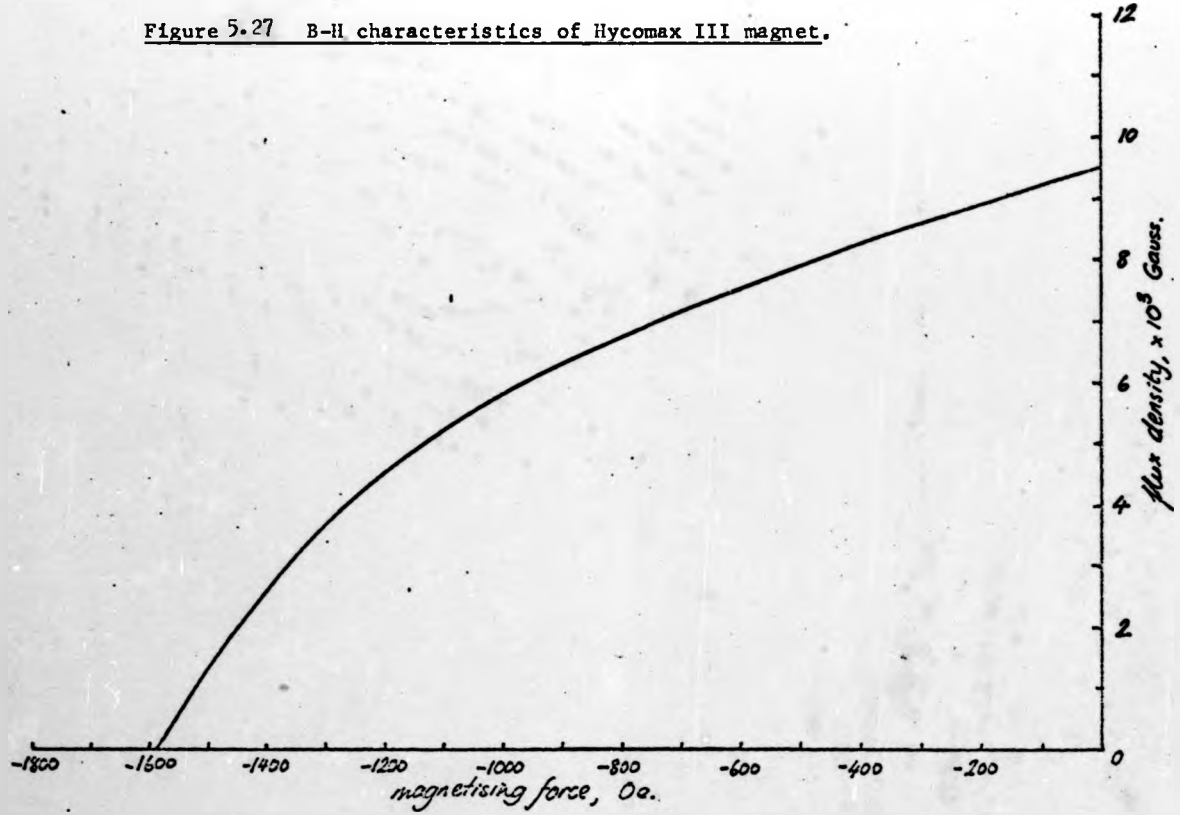

pole arc being less than the pole pitch, and the existence of leakage flux to adjacent magnets. For the wheel motor, the pole arc/pole pitch ratio is 0.78, and it will be estimated that the magnet flux is reduced by 20% due to leakage. This means that B_m is within the range 0.276 Wb/m^2 to 0.296 Wb/m^2. Furthermore, if it is estimated that 20% of the magnet m.m.f. does not appear in the air gap, Equation 2.1 can be used to plot an air gap load line on the B-H characteristic. From the axial dimensions in Table 2.1, it can be found that

$$B_m = 4.85.\mu_0.H_m$$

The B-H characteristic is repeated in Figure 5.28, with the load line and operating range inserted on it. The relative recoil permeability of Hycomax III is 2.4, and this is used to plot the equivalent operating range of these magnets on open circuit. This is clearly well beyond the critical field for recoil working, given by the manufacturers as 0.41 Wb/m^2. This critical point is marked on the curve, as is that for Hycomax IV, whose characteristic is included for reference. It will not be possible, though, to make a direct comparison between the two materials, since their intrinsic magnetisations are not the same, and that for Hycomax III does not even obey the relationship of Equation 5.1 in this region.

5.5.1. Magnetisation of the wheel motor's poles.

A more accurate determination of the operating point of the magnets can be achieved by taking measurements during the magnetisation process. The jig that is used for each stator half in turn is described in Appendix IV. This is connected

Figure 5.28 B-H characteristics of Hycomax III and IV magnets, and operating points.

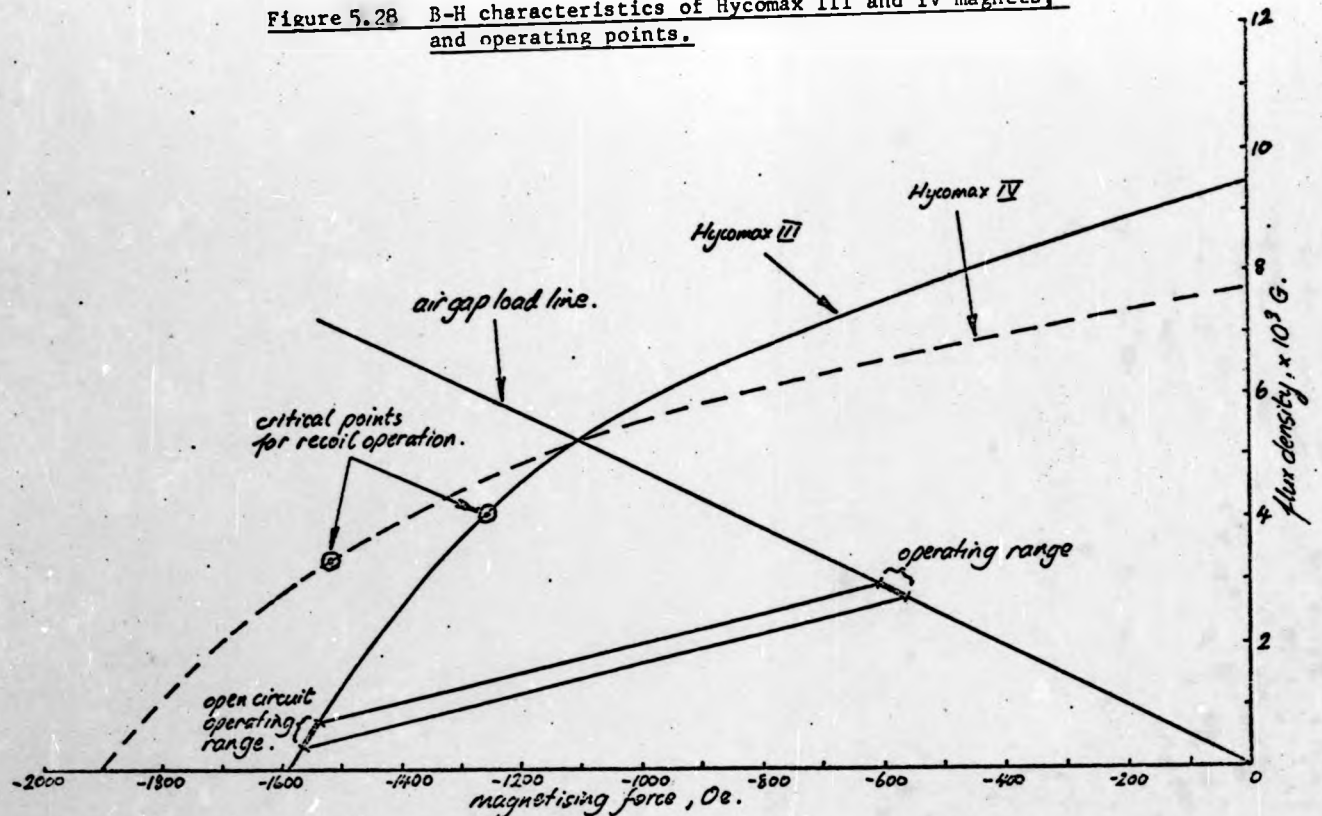

to a capacitor impulse magnetiser, through the circuit shown in Figure 5.29.

The voltage to be delivered to the magnetising coil is set on the magnetiser, so that the current drawn will be dependent on the total load impedance. The circuit had to allow the current to be altered, because the magnetiser used could not supply less than about 180 V. A low resistance coil of quite thick conductor, R1, is shunted across the source to produce a high current range, and a high resistance coil, R2, is connected in series with the magnetising coil to give a low range.

The magnetising current is passed through a shunt, connected to the Y-plates of a storage oscilloscope. The voltage displayed will be proportional to the ampere turns developed in the magnetising coil. A calibration curve between this and the set voltage can therefore be prepared for each range, and these are given in Figure 5.30. These curves apply to demagnetisation also, which is achieved by the four reversing contactors shown in Figure 5.29. When the set voltage on the capacitor magnetiser is released into the circuit, the current rises sharply, and then decays, in the manner shown in Figure 5.31. The shape of this pulse is determined by the voltage and the circuit connections.

The manufacturers' literature (Reference 14) states that the minimum magnetising force to take Hycomax III to its saturation flux density is 4.0×10^5 A.T/m. Applied to the ten magnets in one stator half, this is equivalent to a set voltage of 210 V. Below this minimum value, the flux density reached is reduced quite sharply. The flux density in one pole was recorded using an integrating fluxmeter.

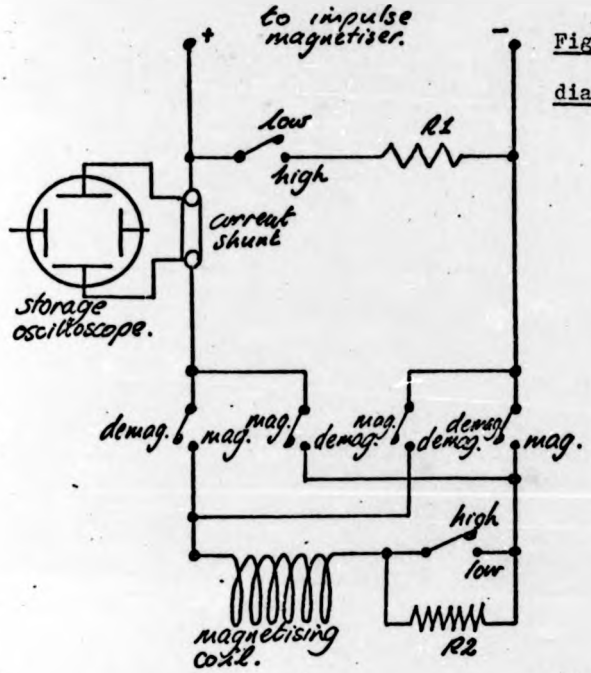

Figure 5.29 Circuit diagram for magnetisation.

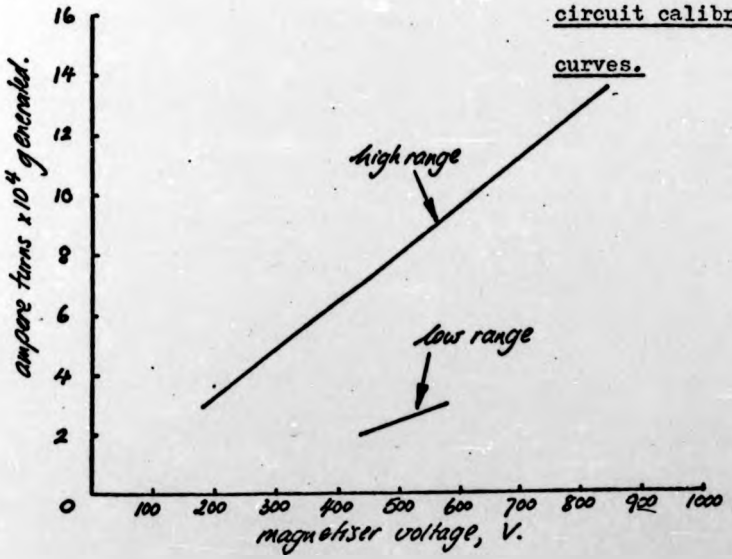

Figure 5.30 Magnetisation circuit calibration curves.

Figure 5.31 Current pulse from impulse magnetiser.

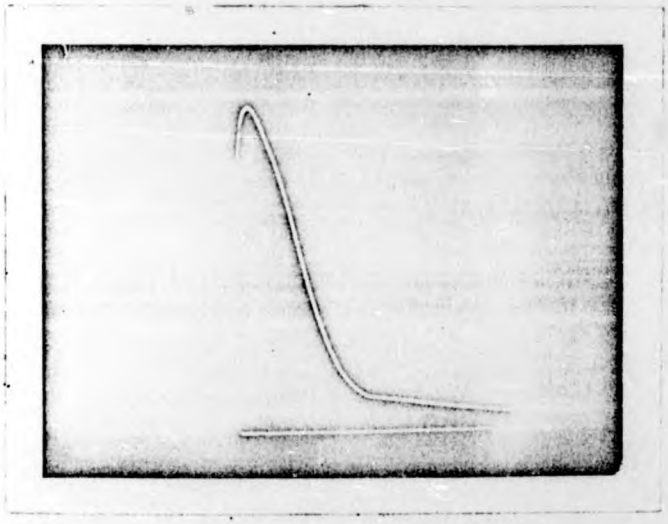

The search coil was located at the root of the magnet, where it is attached to the mild steel backing plate. This plane through the magnet is the most remote from the magnetising coil, and so it will record the lowest value of flux density.

The conditions to produce a magnetising force of 4.0×10^5 A.T/m were set up, and this was repeatedly applied to the magnets, producing the increasing flux density shown in Figure 5.32. This by no means reaches saturation after one pulse, and after 13 has only risen to 0.58 Wb/m^2. It was then decided to apply 13 pulses at higher values of magnetising force, and the fields reached are given in Table 5.3 . These results are too erratic to be plotted as a curve, but they do show that the remanence of 0.948 Wb/m^2 has not yet been achieved.

The most likely explanation of this is that there is excessive leakage between adjacent magnetising coils, so that the field in the magnets is considerably reduced. The conductors forming adjacent coils are quite close together, since the gap between adjacent magnets is also quite small. As the magnets are to be of alternate polarity, these adjacent conductors carry current in the same direction, and this gives rise to the high leakage flux. These results have therefore revealed an unforseen difficulty in magnetising a complete set of magnets at once. It will be seen, though, thatthe approximate prediction of the operating point was quite accurate.

One set of magnets was magnetised by gradually increasing the applied voltage up to the maximum, which was repeated for two further pulses. The flux density rose to the same value it achieved after 13 pulses of the maximum voltage, thus showing again the

Figure 5.32 Magnetisation of wheel motor stator half with 4×10^5 A/m.

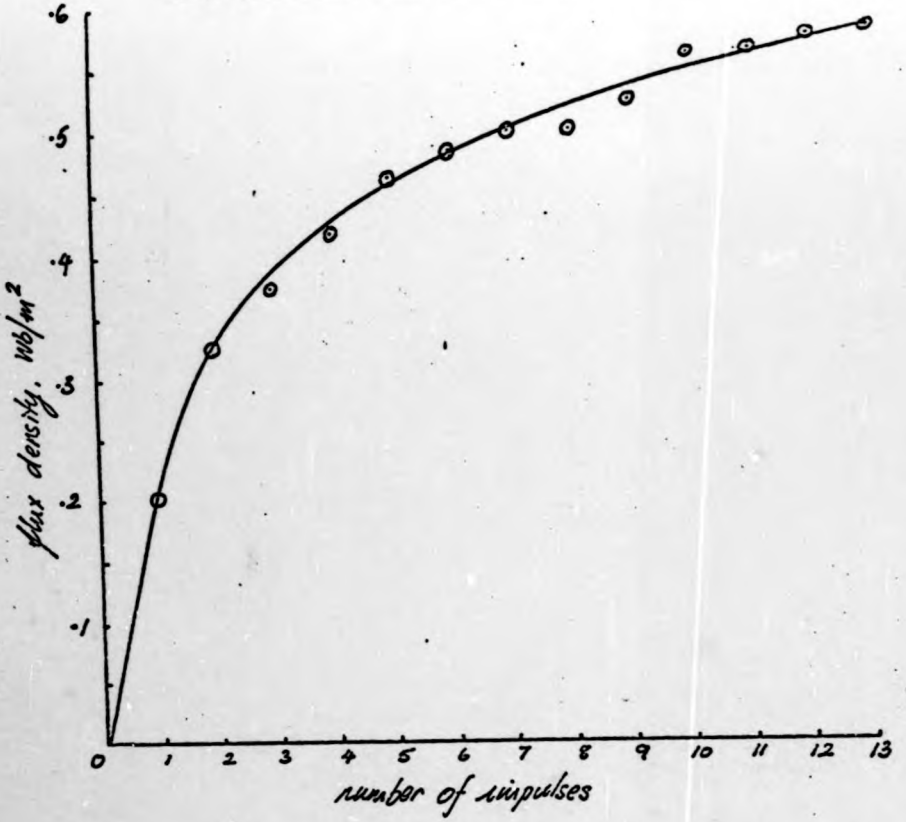

Table 5.3: Remanence achieved after 13 pulses of given field strength to wheel motor stator half.

Applied field, A/m x 10^4	Remanence, Wb/m^2
40	0.58
71	0.61
108	0.77
138	0.82
158	0.88

unpredictability of the results. This rise to 0.88 Wb/m^2 is shown in Figure 5.33. The magnetising jig was then removed, and the field at the root of the magnet fell to 0.242 Wb/m^2. However, the field at the face of the magnet will give a better indication of the useful flux density available, and this was found to be 0.154 Wb/m^2.

The assembly of this stator half into the machine was then simulated by placing a mild steel ring at half the air gap length from the pole faces. This was preferable to assembling the whole machine, as the change in field could be measured more quickly. The flux densities at the root and face rose to 0.346 Wb/m^2 and 0.275 Wb/m^2 respectively. The latter value falls within the operating range already predicted in Figure 5.28. This point, and the load line, are transferred to Figure 5.34., and the relative recoil permeability is used to locate the open circuit operating point on the magnet face.

These two points on Figure 5.34 are the first to be plotted in this series of tests, that can be relied upon to be realistic. They show that these magnets are clearly operating on a minor B-H loop during magnetisation, and also that the remanence of 0.88 Wb/m^2 seems an unlikely value. For the tests relating to Figures 5.32 and 5.33 and Table 5.3, it was not possible to remove the search coil between successive pulses. Each reading after the first was, therefore, not absolute, but the increase of its predecessor. This was a problem caused by the closed magnetic circuit. If, between pulses, the flux density settled to a lower value than the recorded change had indicated, then there would be cumulative error making the predicted value too high. This might be caused by a strong field perpendicular to the anisotropic direction, that gradually rotated

Figure 5.33). Magnetisation of wheel motor stator half by an increasing force.

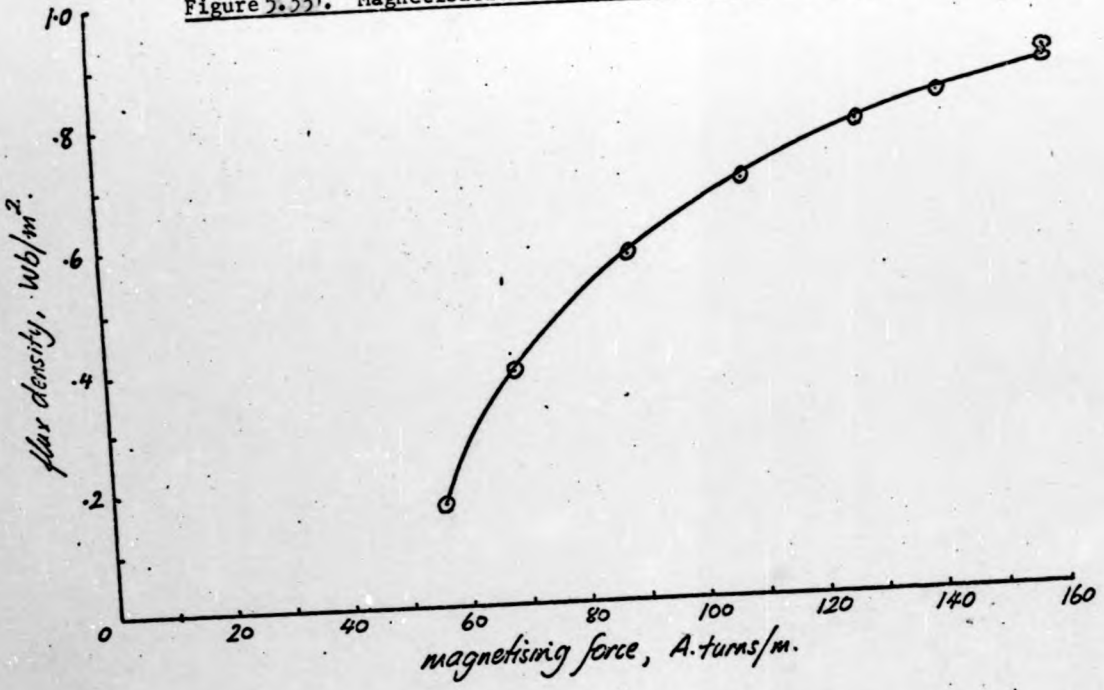

Figure 5.34. Hycomax III B-H characteristics, and minor loop operating points.

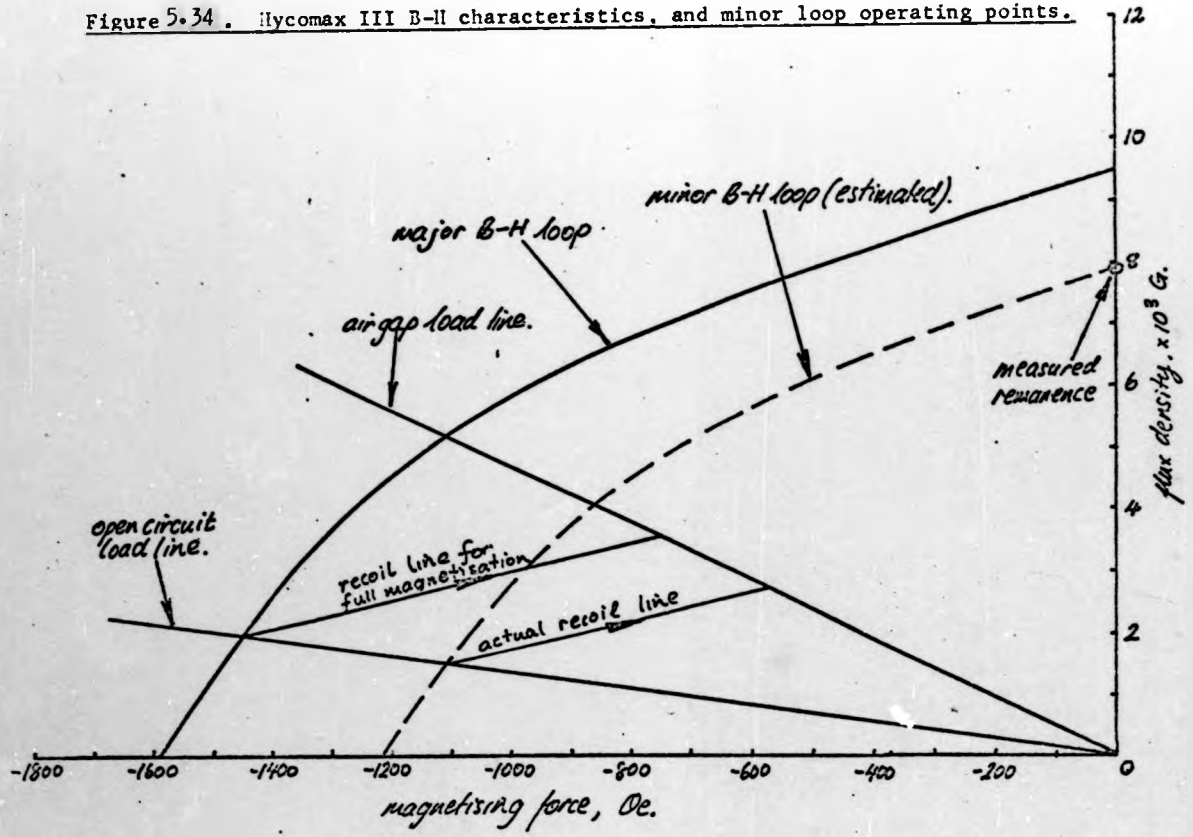

the magnetic domains. Such a field would result from excessive leakage flux, as has already been shown to exist.

An experiment was therefore devised from which the remanence could be found with only absolute readings of flux density. The maximum magnetising force was applied several times, to achieve the saturation condition. The direction of current flow through the magnetising coil was then reversed, a selected demagnetising voltage was applied, and the decrease in flux density was measured. With the magnetising jig removed, the flux density on open circuit was recorded. If this was zero, then the decrease would have been equal to the remanence, for the closed circuit and open circuit operating points after demagnetisation must both have been at the origin.

These measurements were made at the face of the magnet, and the experiment was repeated until the desired results were found. Table 5.4 shows that the magnetising force was gradually increased, through the value that completely demagnetised the stator half. The remanence was therefore deduced to be 0.791 Wb/m^2. This value is marked on Figure 5.34 in preference to the previously determined 0.88 Wb/m^2, and an estimated minor B-H loop that these magnets are operating on is plotted.

An open circuit line can be drawn on Figure 5.34 as shown . The intersection of this with the major B-H characteristic indicates the operating point of these magnets, had they been fully magnetised. The relative recoil permeability and the load line are then used to show that, even if this had happened, recoil operation would still have occurred, and the magnet flux density would have been 0.36 Wb/m^2.

The substitution of Hycomax III for Hycomax IV in the wheel

Table 5.4: Demagnetisation of wheel motor stator half from remanence.

Applied demagnetising force, A.turns.	Reduction in flux density, Wb/m^2	Absolute flux density on open circuit, Wb/m^2
24500	0.754	0.025
25900	0.775	0.012
27400	0.791	0.000
28800	0.820	-0.012
30200	0.832	-0.025

motor was therefore not successful, for two reasons. Firstly, it has been shown that fully magnetised magnets of the former type will operate in recoil, due to the shape of its B-H characteristic. Secondly, the decision to magnetise a complete stator half at the same time has led to operation on a minor B-H loop, due to saturation not being achieved. Consider the demagnetising forces given in Table 5.4. The value of 27,400 A.T. is equivalent to 322 kA.T/m, and yet the coercivity of Hycomax III is only 126 kA.T/m. A large proportion of the magnetising force is therefore supplying leakage flux, because of the close proximity of adjacent poles. This could be overcome by magnetising each magnet individually before assembling it onto the backing plate, but even so, operation on a minor B-H loop would occur in the complete machine.

6. MOTOR PERFORMANCE.

6.1. The Radiator Cooling Fan Motor.

The first prototype of the fan motor had a parallel-surface thrust bearing, with phosphor bronze on the rotor and mild steel on the stator. This combination was also used for the sleeve bearing. When the tests to find the losses due to the rotating flux return rings were performed using this bearing, speed fluctuations were noticed at certain values. These were due to variable power losses in the bearing, that occurred despite a circumferential groove that retained a layer of lubricant.

This motor was tested, with a dummy shaft fitted for it to drive the dynamometer. It was found necessary to correct the reading on the dynamometer, for its own losses were not insignificant. This correction was determined using the second prototype fan motor, and will be described presently. The performance curves of this machine are shownin Figure 6.1, and because this correction has already been applied, no experimental points are shown for torque, output power, or efficiency.

This motor has a very disappointing efficiency, and, once again, considerable fluctuations in the speed are noticed, that are reflected by the plotted points. The operation of the thrust bearing is the cause of this problem, for, although there was always a thin oil film present when the motor was disassembled, it was clearly not sufficient to sustain reasonably low and steady losses throughout

Figure 6.1 : First fan motor's performance curves.

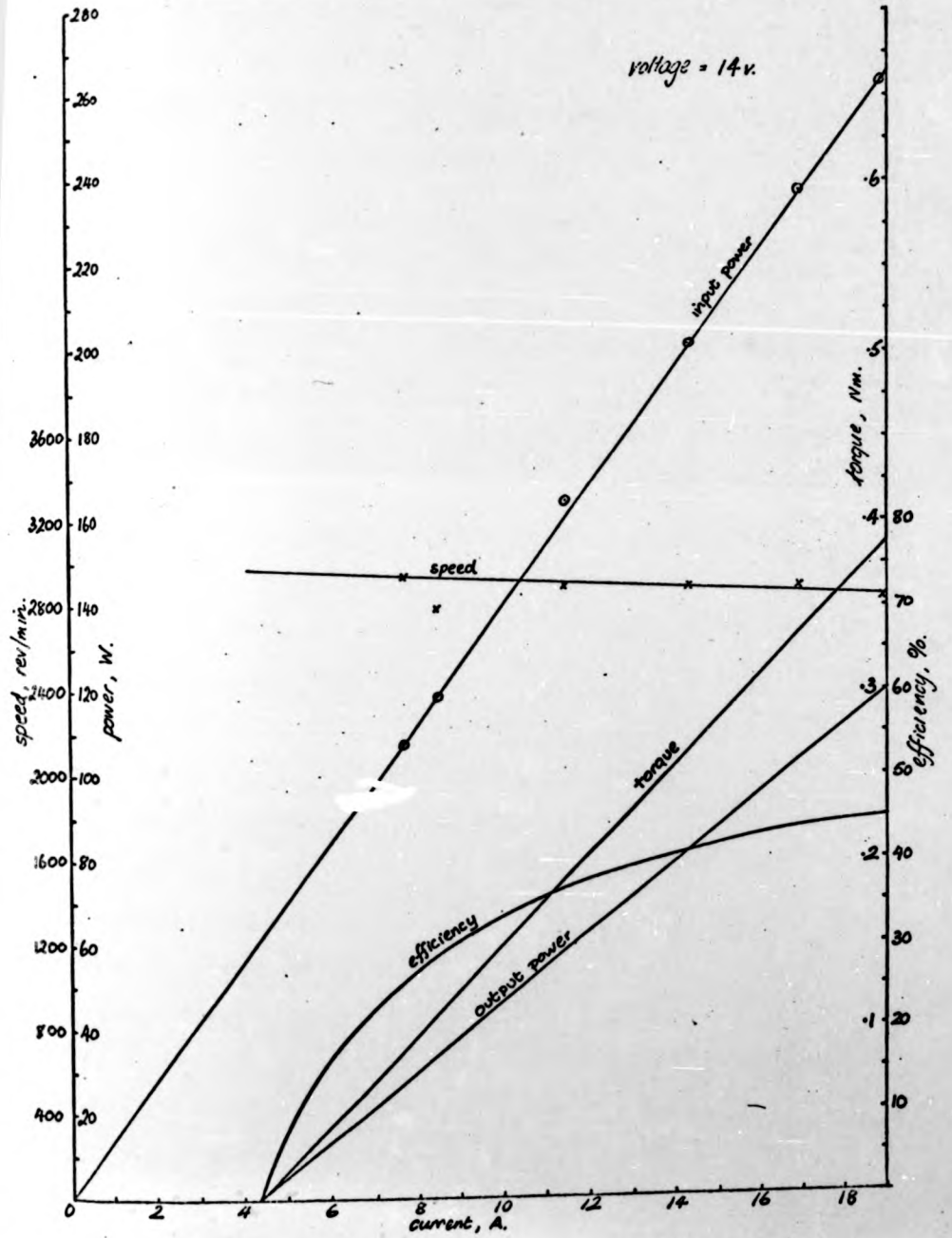

these lengthy tests. It is not within the scope of this thesis to undertake a particular study of the mechanism of these losses, though the following observations will be made. It is clear from the curves of Figure 6.1 that the losses due to incorporating the flux return ring in the armature are somewhat larger than those predicted in Figure 5.23 for the electrolytic iron powder sample. However, those earlier tests were performed with much shorter durations and with no I^2R heating present in the region of the bearing. These performance curves were plotted after the motor had "warmed up", and so there would be greater heating at the bearing surface, leading to different values for the losses from this source.

It appears, then, that the inclusion of this simple bearing to reduce the cost of the machine was not successful. It was therefore replaced by a combined roller bearing, although it may not actually have been necessary to discard the original sleeve bearing. The armature and stator of this second prototype fan motor are shown in Figure 6.2. It is possible to see, over the active region of the armature surface, the tapes holding individual coil sides together. The conductors themselves are just visible there, and also at the periphery. This indicates that very little of the machine's axial length is wasted, and there is only a very thin layer of epoxy resin between the conductors and the surface. On the stator, some of the magnets can be seen to have ragged edges, as already described in the previous chapter.

A locked rotor test was performed firstly on this motor, to determine the magnitude of the I^2R losses. This was performed

Figure 6.2 Second fan motor's armature (left) and stator (right).

after the motor had been run for some time and had attained its normal operating temperature. It should be noted that the resistance part of these losses is not only the armature winding resistance, but that at the brush contacts with the rotor stationary. The variation with current is shown in Figure 6.3, which is considerably less than that for the printed circuit motor. When it is also considered that the Disc-Armature machine has a greater armature volume, it is clear that the printed circuit motor operates at a much higher temperature, a factor that led to the failure of the armature when the latter was tested.

The motor was then run with no load to determine the magnitude of its mechanical losses. The I^2R power is subtracted from the measured value, to give the required variation as shown in Figure 6.4. In fact, this mechanical loss curve will be slightly in error, because the brush contact resistance will have increased due to armature rotation. However, the values of current involved are small, and this error will not be very great. Included in the mechanical power losses are eddy-currents and hysteresis in the flux return ring, friction in the combined bearing, brush friction, and windage.

Brush friction can be calculated over the speed range of interest using Reference 15 , and has been found to be 1.56 W. at 2730 rev/min.. This loss is subtracted from the total mechanical power loss in Figure 6.4. If it is assumed that the remaining losses are in the return ring and the thrust bearing, then the magnitude of these is somewhat less than that given in Figure 5.23. This is mainly due to the design of the thrust bearing, that has developed

Figure 6.3 Second fan motor's I^2R power losses.

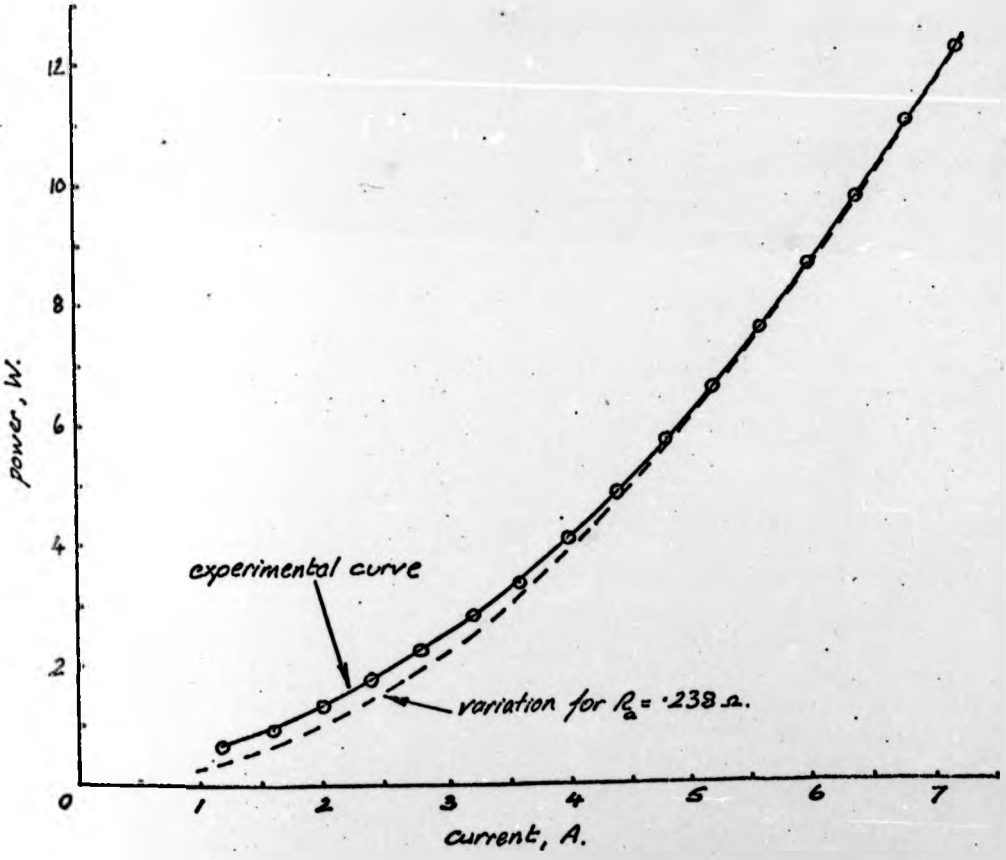

Figure 6.4 Second fan motor's performance with no load.

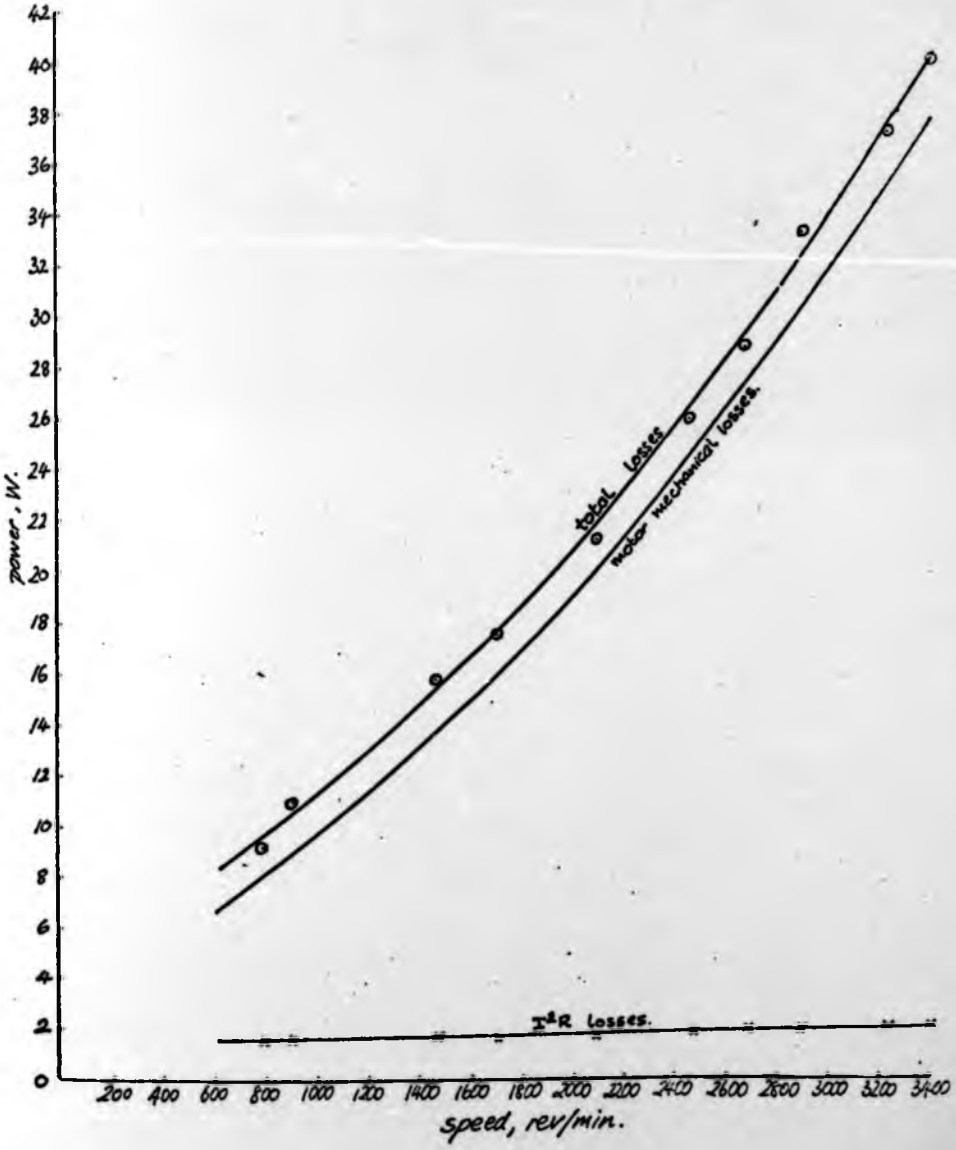

from the phosphor bronze type, which caused these losses to increase noticeably during lengthy tests, to the roller type. Both were lubricated with oil in the same way, but the latter has reduced the losses below those originally found for the well-lubricated parallel-plate bearing. Now, the total mechanical loss at 2730 rev/min is 28.20 W., or 26.64 W. with brush friction subtracted. Further tests on this motor will show that much of this is in the thrust bearing, so that the losses in the iron powder ring are quite small.

As has already been mentioned, this machine was used to determine the mechanical losses in the dynamometer. The latter was driven by the motor, with no load applied, and the variation with speed of the total mechanical losses in both machines was found as for the motor alone. This is shown in Figure 6.5, and the component in the dynamometer is found by subtracting the motor's mechanical losses (Figure 6.4). This last curve was used to plot the correct outputs from the two fan motors. The performance curves for the second prototype fan motor, that shown in Figure 6.2, are given in Figure 6.6. It will be noticed that these, like the curves for the other machine, are for a terminal voltage of 14 V. This is equivalent to a 12 V automobile starter battery, that is assumed to be being charged.

In Chapter 4, the method of calculating the variation of conductor e.m.f. and torque with angular position was described. This was developed into an evaluation of the equivalent quantities in each winding path for the fan motor, and the variation with angular position was shown in Figure 4.13. Those results were either e.m.f. per unit of angular velocity, or the torque per unit of conductor current. The average values, found from Figure 4.13, are 0.03668 for the clockwise path, and 0.03719 for the anti-clockwise path. The accuracy of the calculation can therefore

Figure 6.5 Second fan motor's performance with dynamometer load.

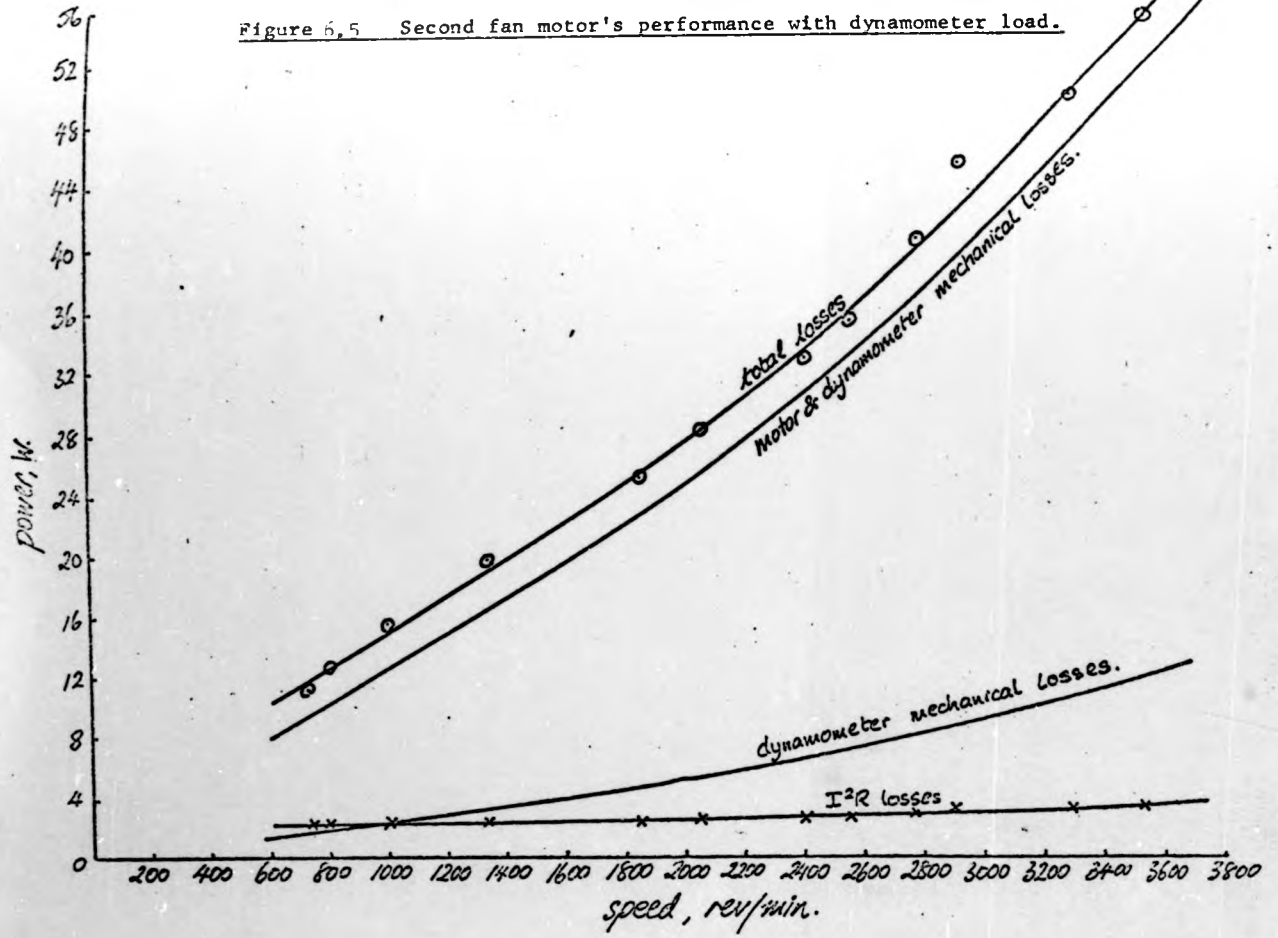

Figure 6.6

Performance Curves of the 2nd Fan motor (14v. supply)

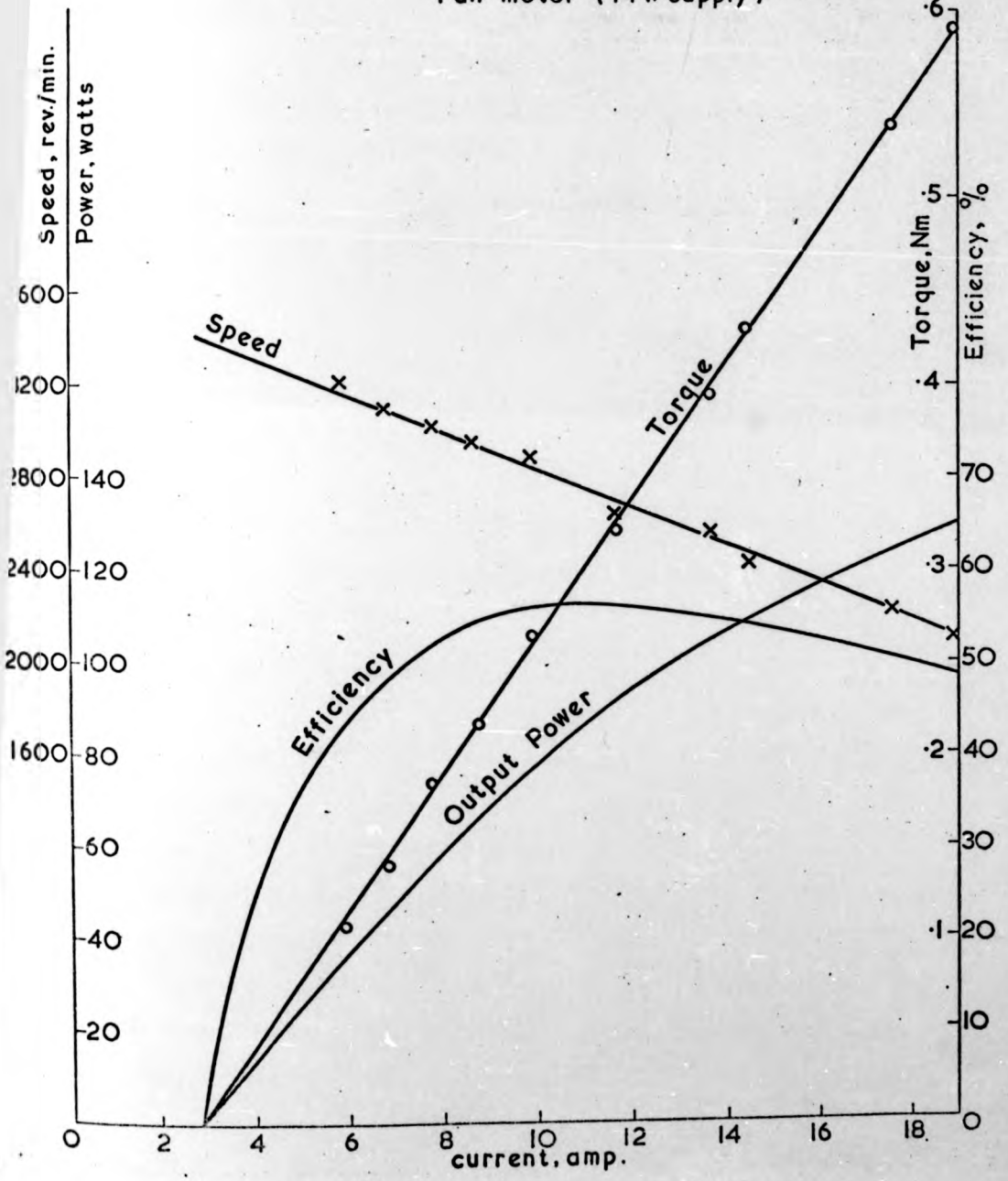

be checked from the experimental results of Figure 6.6, and it will be simpler to consider torque than e.m.f.

The calculated torque is equivalent to the armature torque, T, rather than the output torque, T', which is that plotted in Figure 6.6. The difference between T and T' is accounted for by a no load current , but this can be overcome by considering the slope of the experimental curve. It will be assumed that each winding path carries half the total current, so that although the torques for each path should be added, the values found from Figure 4.13 can be compared directly with the slope. This has a measured value of 0.0366, which is almost identical to the calculation for the clockwise path, and 1.6% below that for the anti-clockwise path. This agreement between the theory and the motor's performance is very good, and it should be remembered that the predicted values were found using the direct calculation of the axial field cutting the conductors.

The variations with speed of the various power losses in this fan motor are shown together in Figure 6.7. From the total losses, found from Figure 6.6, are subtracted the I^2R losses and the mechanical losses. The remainder is the curve labelled "brush drop loss". It has already been mentioned in connection with Figure 6.4 that the I^2R losses do not include an allowance for the relative motion between the commutator and the brushes. This factor is represented by the brush drop loss curve, which has a similar shape to the I^2R loss curve.

Figure 6.7 Second fan motor's power losses

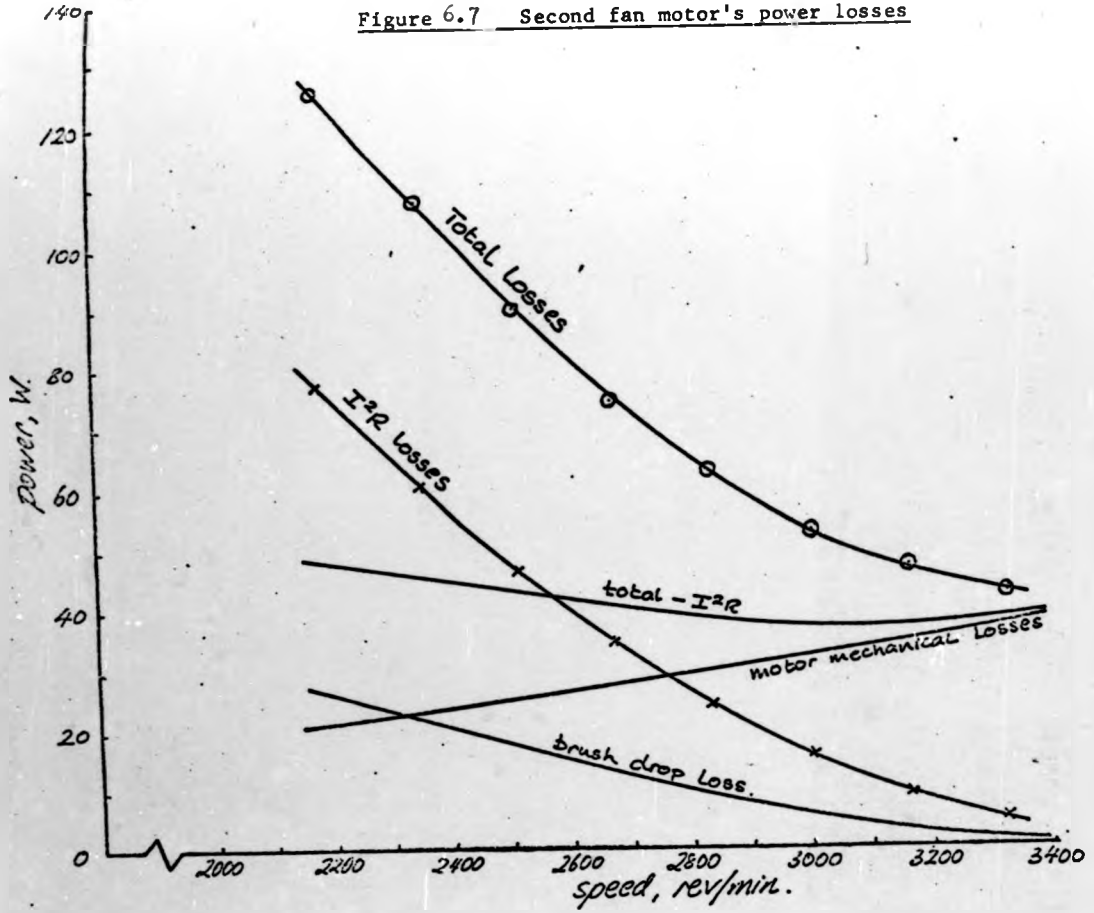

It might be assumed, for a steady-state analysis, that all the losses in the machine are either independent of, or proportional to the square of the armature current. It should therefore be possible to represent the brush drop loss by a constant resistance, part of a total resistance. The experimental values for this loss were therefore plotted against current, and the resulting curve is shown in Figure 6.8. A calculated curve for a resistance of 0.081 ohms is also shown, and the two are in quite good agreement.

The same procedure was adopted with Figure 6.3, and a resistance of 0.238 ohms is seen to be a good approximation to the I^2R losses. The additional resistance due to rotation is therefore most significant, and this should always be added to the static armature resistance used. The value of the total can be found from the stall current, which was estimated as 45.0 A., and the terminal voltage of 14 V.. The resulting resistance is 0.311 ohms. This is very close to the total of the resistances used in Figures 6.3 and 6.8, that being 0.319 ohms.

It should be noted that it is possible to calculate the resistance in a winding path using Equation 4.12. However, this cannot be expected to agree well with the measured value unless the constant C_1 is found accurately. If suitable tests were performed on the armature alone, without the brush contacts, the procedure described here could then be used to determine quite accurately the variation of the static and dynamic brush drop losses with speed.

It might be assumed, for a steady-state analysis, that all the losses in the machine are either independent of, or proportional to the square of the armature current. It should therefore be possible to represent the brush drop loss by a constant resistance, part of a total resistance. The experimental values for this loss were therefore plotted against current, and the resulting curve is shown in Figure 6.8. A calculated curve for a resistance of 0.081 ohms is also shown, and the two are in quite good agreement.

The same procedure was adopted with Figure 6.3, and a resistance of 0.238 ohms is seen to be a good approximation to the I^2R losses. The additional resistance due to rotation is therefore most significant, and this should always be added to the static armature resistance used. The value of the total can be found from the stall current, which was estimated as 45.0 A., and the terminal voltage of 14 V.. The resulting resistance is 0.311 ohms. This is very close to the total of the resistances used in Figures 6.3 and 6.8, that being 0.319 ohms.

It should be noted that it is possible to calculate the resistance in a winding path using Equation 4.12. However, this cannot be expected to agree well with the measured value unless the constant C_1 is found accurately. If suitable tests were performed on the armature alone, without the brush contacts, the procedure described here could then be used to determine quite accurately the variation of the static and dynamic brush drop losses with speed.

Figure 6.8 Second fan motor's brush drop losses

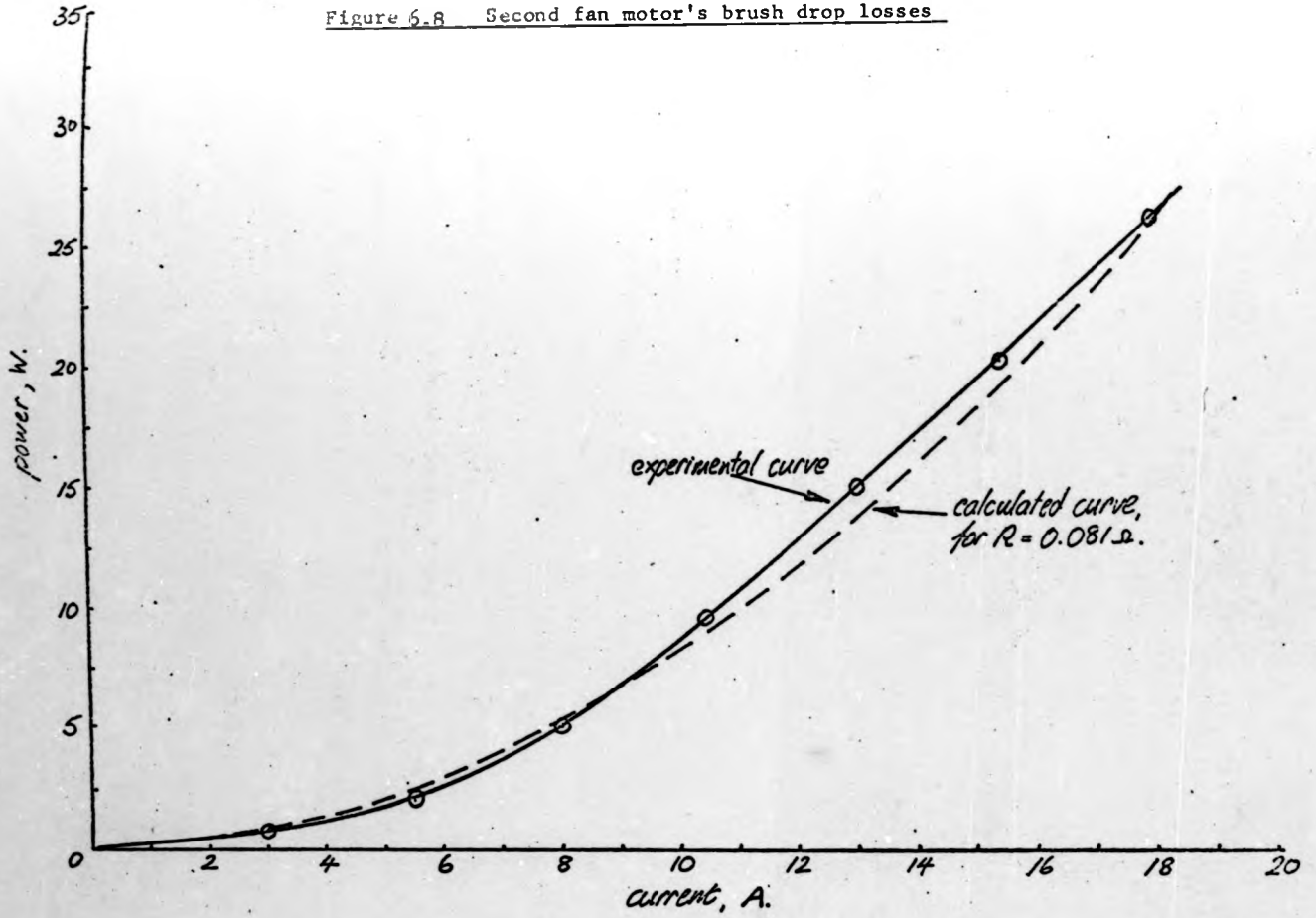

Finally, it was decided to test this motor with a fan load. It will be remembered that the intention is to attach fan blades to the periphery of this machine, but for this test, the fan used with a printed circuit motor was fixed to a dummy shaft as shown in Figure 6.9. At the normal supply voltage, a current of 9.5 A. was drawn at a speed of 2730 rev/min.. It will be noticed from the performance curves of Figure6 .6 that this point does not fall near the speed vs. current characteristic. It might be expected that the fan is blowing air over the motor to cool it, and thus alter the heating losses. However, most of the blades extend over radii greater than R_2, and so it is not likely that this effect would be the cause of such a large discrepancy. The performance curves predict a current of 11.2 A. at this operating speed.

In this machine design, the only force holding the rotor on the stator is that due to the attraction of the flux return ring to the magnets. There are no mechanical restraints such as bolts. The direction of rotation of this fan was such that air was blown past the motor, and the reaction force between rotor and stator was opposed to the magnetic attraction. Thus, operation with the fan load relieved the load on the thrust bearing, and reduced the losses associated with this.

A reduced input power can be calculated at this new current, which gives an operating efficiency of 65.8%. This can be compared with 56.2% without the fan effect, and is an additional advantage of this design over the printed circuit motor. The total power losses are 45.5 W., from which the mechanical losses can be found. At this current, the static I^2R losses are 21.5 W., and the dynamic brush drop loss is 7.3 W.. The fan effect has therefore reduced

Figure 6.9 Second fan motor with shaft mounted fan.

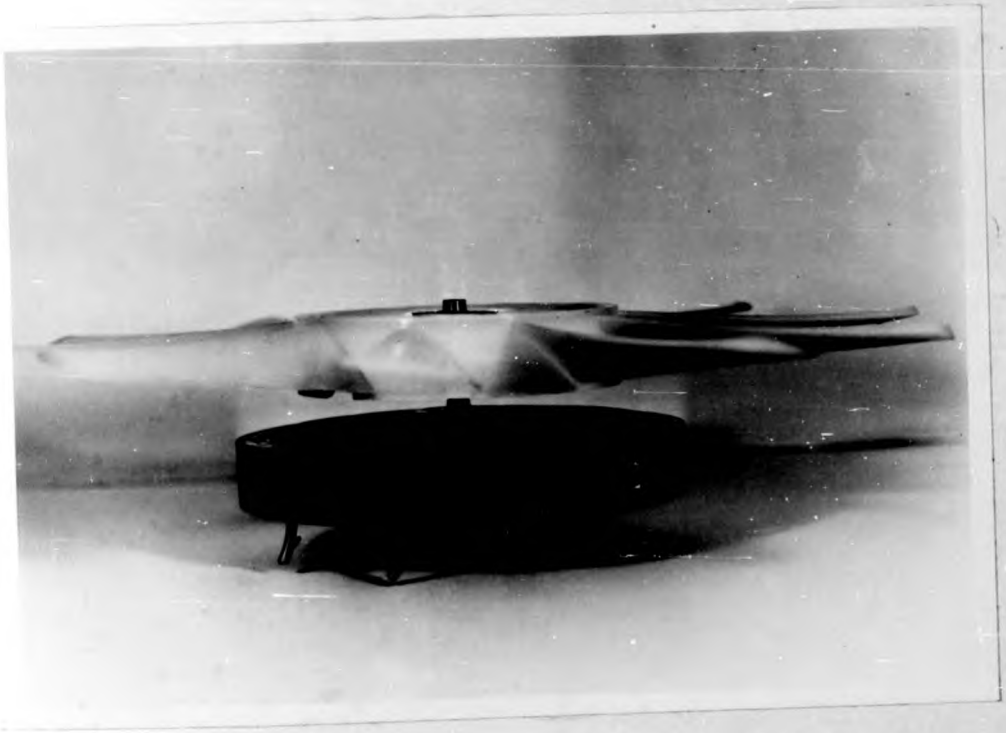

the mechanical losses from 28.0 W. to 16.7 W.. This reduction of 11.3 W. at this speed must have come off the thrust bearing losses alone, since the air gap length did not alter. Taking the calculated brush friction loss into account, the eddy-current and hysteresis losses in the iron powder flux return ring are seen to be no greaterthan 15 W. at 2730 rev/min.. Clearly some of this 15 W. is accounted for by the thrust bearing, since the armature did not come away from the stator at this speed. It can therefore be concluded that the rotational losses in the iron powder material alone may well be less than this figure, and that the major problem with incorporating the return ring into the rotor is the inherent thrust force.

6.2. The electric vehicle traction motor.

In Section 4.6, it wasdescribed how the negligible armature inductance in the wheel motor could lead to an unusual variation of voltage across a coil, while it was being commutated. To observe this effect in the first prototype wheel motor, wires were connected to two adjacent commutator segments. These were brought out of the machine via silver slip-rings and silver graphite brushes, and connected to an oscilloscope. These connections were made before the armature was moulded, in a similar way to the search coils already mentioned. The resulting trace can be used to observe the variation of flux density from each pole, and to verify that armature reaction is negligible. If sparking occurs, voltage peaks will indicate this as the coil passes under the brushes (In fact, it will be remembered that the wheel motor has two lap windings in

parallel, and there will be two coils connected across adjacent commutator segments).

It is usual in lap-wound machines to include equalising rings, to ensure that any circulating currents do not flow through the brushes. These may be caused by there being slight variations in the shapes of the poles or the armature coils. Although it would be desirable to have equalisers in the wheel motor, they would confuse the measurement of the one coil's bar-to-bar voltage. As they rotate with the armature, and the brushes are stationary, other coils would be continually connected in parallel to this coil, and then disconnected. Equalisers were therefore not included in this machine, though the field distribution of Figure 5.26indicates a need for them.

When this motor was initially run, a very satisfactory trace was observed, that indicated the existence of some sparking during commutation. Unfortunately, the connecting wires from the segments repeatedly became disconnected from the slip-rings after only a short operating time, and it was not possible to photograph any of the traces. This was due to heat being transmitted along these wires, the source of which will be subsequently explained.

The initial test performed on this motor was to find its losses, without the gearbox attached, and with no load applied. These are shown in Figure 6.10. The total losses are somewhat greater than expected, and some of the components were evaluated individually. The power lost due to brush friction can be calculated using Reference 15, and has been found to be 79 W. at a speed of 10,500 rev/min.. This varies linearly with speed as shown in the figure. The resistance of one of the parallel paths in the armature

Figure 6.10. First wheel motor's performance with no load

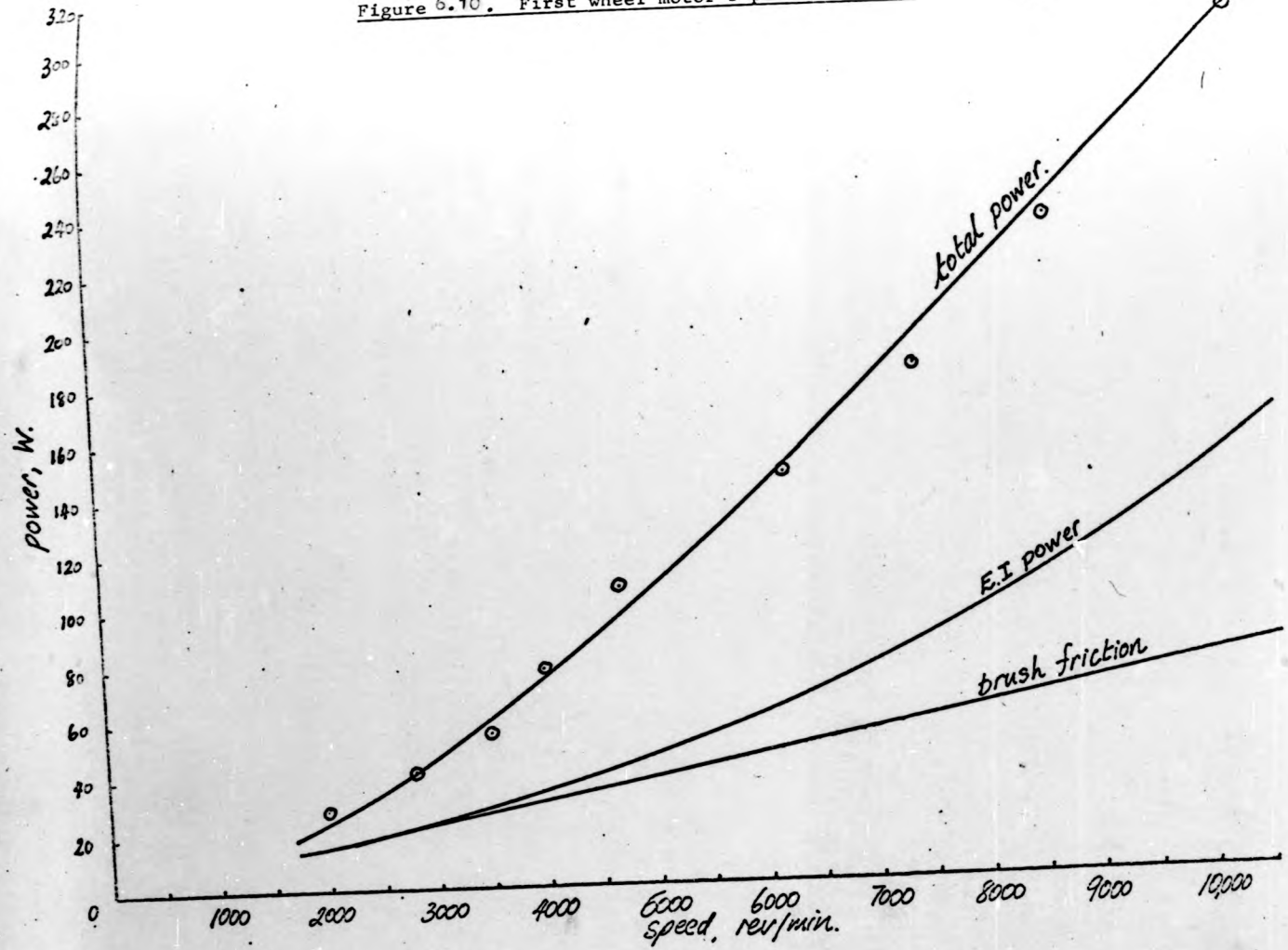

can be found from Equation 4.12. The total winding resistance, R_a, is then calculated as 0.01375 ohms, allowing a 20% addition for heating. Even so, the maximum I^2R_a power over the experimental range is only approximately 1 W.. It is therefore expected that the armature power, EI, should be approximately equal to the total power at any speed in Figure 6.10.

It is possible to evaluate the armature e.m.f., E, using Equation 2.14 and the values for $\bar{B}$ given in Section 5.5. The latter was in the range 0.172 Wb/m^2 to 0.185 Wb/m^2, and so the average flux density is used to give the variation of EI with speed that is shown in the figure. The difference between this curve and that for brush friction is the combined windage and bearing power losses. The bearings in this machine were designed to operate up to 20,000 rev/min., and it is not expected that they constitute the major part of this combined loss. It would be quite difficult to calculate the windage for this complicated armature shape, so this method gives some appreciation of its magnitude without this being necessary. It is not surprising that it has reached a significant value at speeds in excess of about 4,500 rev/min..

If the I^2R_a power loss is no greater than 1 W., then there must be an additional voltage drop in the electrical circuit to account for the large difference between the total power and the calculated armature power. The maximum current recorded during this test was 8.5 A., and this corresponds to a brush contact voltage drop of approximately 0.1 V. per brush, found from the manufacturers' data. This clearly does not account for the power difference, which is 156 W. at 10,500 rev/min.. The type

of commutation occurring in this machine must therefore be very different from that in the tests from which the manufacturers derived their data.

This effect strongly supports the description of the commutation given in Section 4.6. There will be a voltage generated across the segments to which the coil being commutated is attached. This voltage will cause a current to flow through the short-circuited coil, the segments, and the brush that completes the circuit. Furthermore, the current will change direction three times during the short-circuit. It would be very difficult to determine the magnitude of this current at each moment, since the current density through each brush/segment contact is continually changing, and the brush contact voltage drop does not vary linearly with this. It would, in fact, be difficult to obtain an accurate relationship that could be used for this situation.

The resistance of one coil is calculated as 0.069 ohms, and this would assist quite a high short-circuit current, and hence heating loss, from a modest value of induced voltage in the commutated coil. If the coil's self-inductance is assumed to be zero, the maximum value of this e.m.f. can be calculated from the brush and segment dimensions, and the field distribution of Figure 5.26. It is estimated that commutation commences and terminates when a coil is experiencing a field of 0.071 Wb/m^2, which is equivalent to an induced e.m.f. of 1.84 V. at 10,500 rev/min.. In this machine, it will be remembered that there are two coils in parallel across each pair of adjacent segments, and their combined resistance will alter quite significantly with temperature.

The difference between the total power and the calculated armature power in Figure 6.10 can therefore be attributed to two sources. The first is a heating loss in the short-circuited coils themselves. The second is an additional heating loss at the brush contacts. Clearly, the maximum induced voltage across the two segments is very much larger than the normal brush contact voltage drop. This can be accounted for by a non-uniform current density flowing from the brush to the segments.

Since the electric vehicle was to be powered by one wheel motor unit in each rear wheel, a duplicate machine was made at the same time. However, this second motor had no special connections to the armature, and so equalisers were included for every other commutator segment. The brush and segment dimensions are such that only two segments are short-circuited by a brush at any time. It is unlikely, then, that the equalisers will alter the effect of the induced voltages in all the short-circuited coils. The same test and calculations were performed for this motor, and the results are shown in Figure 6.11. At a speed of 10,500 rev/min., the difference between the total power and the calculated armature power is 134 W., which is quite close to the value of 156 W. found for the first motor.

The major difference with the second machine is that the mechanical power losses are much higher than were those of the first. The reason for this was discovered when it was disassembled after the test. It was reasonable to assume that neither windage nor brush friction would vary greatly from one machine to another, since the clearances between rotor and stator, and the brush

Figure 6.11. Second wheel motor's performance with no load.

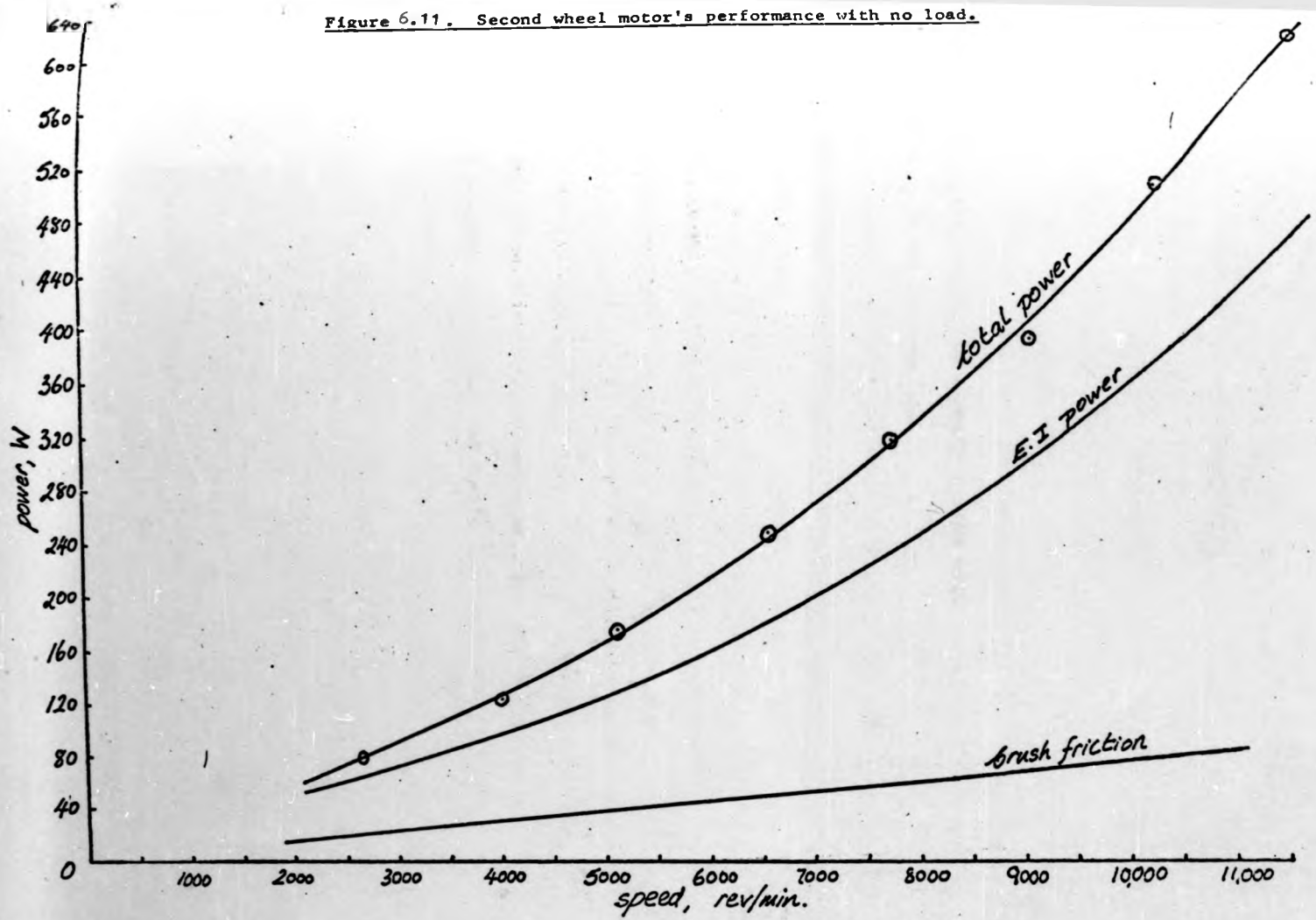

pressure, were approximately the same in each. The bearings also were found to be in the same condition. However, the photographs of each side of the armature show that considerable damage has occurred (Figure 6.12).

Firstly, the commutator itself no longer has a smooth finish, but shows the effects of considerable sparking. This confirms the conclusions already reached with regard to commutation. Secondly, it can be seen that the armature coils in one region have generated enough heat for the epoxy resin to crack. It will be remembered that the heat deflection temperature of this mixture is about 150°C. This damage has occurred mainly around the end-windings, at both ends of the active region. These positions are the most vulnerable in this respect, since they carry the greatest concentration of armature conductors. The outer layer of conductors is then lifted beyond the normal position of the armature's surface, due to the expansion of this layer and those beneath it. This has been sufficient to cause some conductors, and some epoxy resin, to rub against the stator. The result for this motor was the additional mechanical loss already noted.

The heat generated in these regions may be caused directly by the current flowing in each coil when it is being commutated, and also by the conduction of heat, mainly through the copper, from the brush contacts. Before it was possible to study this further, the same fault had occurred in the first wheel motor.

The normal mechanical power losses in a Disc-Armature motor running at 10,500 rev/min. do not appear to be excessive in magnitude. However, at speeds much greater than this, the windage

Figure 6.12: Second wheel motor's armature, after testing with no load.

will increase quite rapidly. This may well be the limiting factor on the operating speed, if the commutation losses are overcome. The latter have been described, and their effects noted, and it is now clear that further investigation of the variation of bar-to-bar voltage in the commutated coil is most important for this machine to progress. This phenomenon will not be peculiar to the high speed wheel motor, and it may well occur also in the fan motor, for example. However, that machine runs at only 2730 rev/min., at which speed this loss may be negligible. In fact, in Section 6.1, all the fan motor's power losses were adequately accounted for.

It should be mentioned that, in the fan motor, the close proximity of the flux return ring to the winding may provide the armature coils with just sufficient self-inductance for the coil current to reverse in the normal way during commutation. The other important factors that will determine the manner of this reversal are the field distribution in the angular direction, and the dimensions of the brushes and commutator segments. Nevertheless, the main criterion for good commutation is that this should occur in a minimal field, so that no significant bar-to-bar voltage is generated. Clearly, the importance of each of these factors must be determined, and this could have an effect on the design of the magnet system, which hitherto has neglected this phenomenon.

6.3. Speed capability of the Disc-Armature machine.

To conclude the remarks about the suitability of this type of armature disc to run at high speeds, the results of some over-speed tests are reported. A test rig was constructed so that the armatures of the fan and wheel motors could be driven by a belt from another machine, at higher speeds than normal. In this way, the stators of the Disc-Armature prototypes are not involved, so they will not be damaged should the armature burst. The speed was measured using a magnetic perception head connected to an impulse tachometer.

For the wheel motor's armature, a steel band was shrunk onto the commutator, since this was only designed to operate at the normal running speed of 10,500 rev/min.. We are more concerned with the epoxy resin, to determine whether this needs reinforcing with carbon fibres, for example. In fact, this armature achieved a speed of 14,500 rev/min., without showing any damage, although it can be seen from earlier tests that windage will be quite large at this speed. The commutator band was then removed to restore the armature to its original form. This was then run continuously at 10,500 rev/min. for 2½ hours, and still no damage occurred. It can therefore be concluded that this armature does not require reinforcing, and further, that the damage described in the previous section was due to armature heating rather than to the centrifugal force.

An armature from the fan motor was then assembled in the test rig. This was gradually accelerated until, at a speed of 15,500 rev/min., cracking occurred. The extent of this is shown

in Figure 6.13, as the major cracks are in the radial direction on the return ring's side of the disc. The density of the iron powder ring is approximately four times that of the epoxy resin mixture used for encapsulating the winding. Therefore, the most probable cause of the cracks is the variation of the centrifugal force in the axial direction. Thus, the return ring end of the rotor has parted from the phosphor bronze bearing, but the commutator end has not. It may be concluded from this that a symmetrical disc design, as in the wheel motor, is preferable for operation at high speeds.

Both of the armatures for the wheel motors had to be balanced. Small weights were added inside the outer rim that houses the end windings. However, the fan motor armature used in this test was not balanced, and it is interesting to note that no excessive vibrations were experienced up to the speed of 15,500 rev/min.. This indicates that the epoxy resin moulding is reasonably homogeneous throughout its volume, containing very few air bubbles. The encapsulation process appears to have succeeded well in this case. Also, the thickness and homogeneity of the flux return ring must be approximately constant, and this was due to great care being taken in preparing the mixture and compacting it evenly.

The tests performed on these two types of Disc-Armature motor have shown some of the advantages and some of the limitations of the machine. It is now possible to see for what applications designs can be confidently prepared, and what criteria to use, and also for what operating conditions further study and experiments are needed.

Figure 6.13: Fan motor armature after operating at 15,500 rev/min.

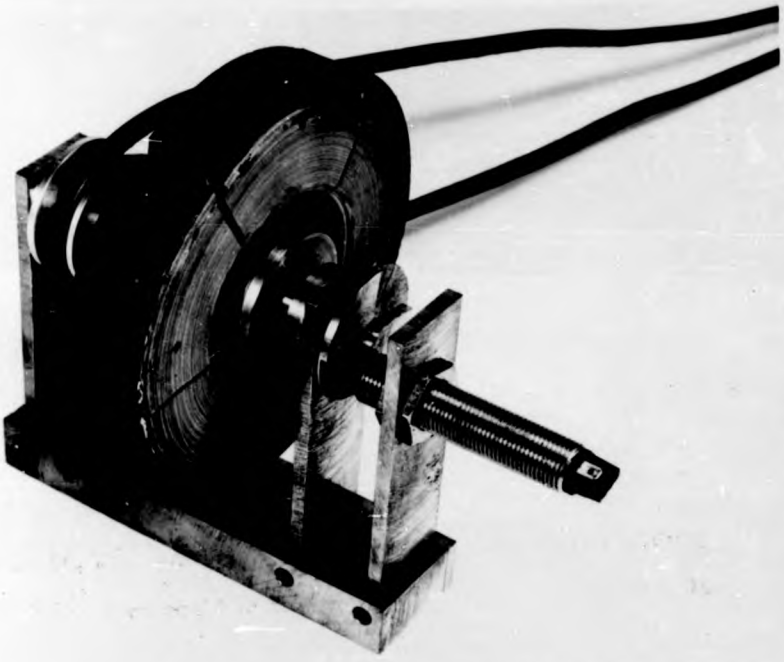

7. CONSIDERATIONS FOR MACHINE DESIGN.

7.1. Selection of magnet dimensions.

The importance of treating the Disc-Armature machine as a three-dimensional problem has been demonstrated already. In particular, Figures 3.17 and 3.18 show the field distribution in the radiator cooling fan motor at one of the conductor layers. The latter gives the radial distribution, and indicates that the field at radii R_1 and R_2 (Figure 3.7) is approximately half its maximum value. That occurs at a radius slightly greater than the average radius, as might be expected from the discussion in Section 2.3. This shows a clear need to optimise the design of the axial-field machine in the radial direction. If the ratio of R_2 to R_1 is increased, there will be a greater length of active conductor, but there will also be a greater waste of useful flux available in the air-gap.

The most common criterion for relating R_1 to R_2 is to maximise the armature power. This power, E.I, must firstly be obtained in terms of specific electric and magnetic loadings. These are defined so that they do not vary with a machine's dimensions, but, when multiplied by which, will give a measure of the machine's total electric and magnetic loadings. They are therefore used to separate the expression for armature power into terms that are independent of machine dimensions, and a function of R_1 and R_2.

In conventional machine theory, the specific magnetic loading is identical to the average useful flux density in the air-gap, $\overline{B}$. The value of $\overline{B}$ will depend on the permanent magnet material used, but it will be approximately constant if the pole face area is

altered. However, the theory developed for the Disc-Armature motor in Section 2.3 has shown the flux density at a given point, $\underline{B}_{i,j}$, to be inseparable from the radius of that point, r_i. If this is so, then a specific magnetic loading, independent of machine dimensions, can never be defined. For the purpose of producing optimum designs, therefore, the assumption will have to be made that $\underline{B}_j$, correctly defined by Equation 2.4, is independent of r_i.

The average e.m.f. in a conductor, E_c, will be found, as before, using Equation 2.3 to be:

$$E_c = \frac{p}{2.\pi}\int_0^{\frac{2\pi}{p}} e_j.d\theta$$

$$= \frac{w(R_2^2 - R_1^2).}{2}\cdot\frac{p}{2.\pi}\int_0^{\frac{2\pi}{p}} \underline{B}_j.d\theta$$

The specific magnetic loading, $\overline{B}$, can be recognised in this expression as the average value of $\underline{B}_j$ over a pole pitch. $\overline{B}$ can then be substituted to give

$$E_c = \frac{\overline{B}.(R_2^2 - R_1^2).w}{2} \qquad (7.1)$$

For the purpose of designing a machine, it is better to re-write Equation 7.1 in the manner of Equation 2.14. Hence, the armature e.m.f., E, is given by

$$E = \frac{\overline{B}.\pi.N.(R_2^2 - R_1^2).Z}{a} \qquad (7.2)$$

The specific electric loading, A_c, must make it possible to find, from the machine dimensions, the total electric loading in the armature. Conductor current, I_c, is approximately independent of machine dimensions, but the number of conductors, Z, will depend upon R_1. A_c is therefore defined as:

$$A_c = \frac{I_c.Z}{2\pi R_1} \qquad (7.3)$$

I_c is related to the armature current, I, by the number of parallel paths, a. The armature power can therefore be found from Equations 7.2 and 7.3 as

$$E.I = \pi.w.\bar{B}.A_c.(R_2^2 - R_1^2).R_1 \qquad (7.4)$$

Remembering that it is an approximation that $\bar{B}$ and A_c are independent of machine dimensions, Equation 7.4 can be differentiated with respect to R_1 to find its maximum value. This occurs when

$$R_2 = \sqrt{3}.R_1 \qquad (7.5)$$

In any electrical machine, the armature current contributes both to the armature's power and to its heating losses. Equation 7.5 has provided a criterion for selecting the ratio of the radial dimensions in an axial-field machine, based upon the maximum value for E.I. It is possible to show that the heating losses cannot be minimised by any particular relationship between R_1 and R_2.

The heat developed in one conductor, Q_c, allowing for a proportion of end-windings, is found from Equation 4.12 to be

$$Q_c = I_c^2.\frac{4.\rho}{\pi.d_c^2}\left[(R_2 - R_1) + \frac{\pi}{p}.(R_2 + R_1) + C_1\right]$$

The total I^2R_a heat in the armature, Q, can then be found using this expression and Equation 7.3. The current density in the conductors, J_c, is also used because, like the specific loadings, it is approximately independent of machine dimensions. Hence :

$$Q = 2.\pi.A_c.J_c.\rho.R_1\left[(R_2 - R_1) + \frac{\pi}{p}.(R_2 + R_1) + C_1\right] \qquad (7.6)$$

Differentiation of Equation 7.6 with respect to R_1 shows that, for a minimum of Q to exist, p must be less than π. However, it is not possible to find a relationship between R_1 and R_2 in this range such that R_1 is less than R_2. The criterion of maximising the armature power, that yielded Equation 7.5, is therefore the only valid way of relating R_1 and R_2 for a Disc-Armature machine. This criterion, though, only applies to the radial direction, and it will be equally important to find a corresponding result for the angular direction, that gives some guidance as to what pole arc/pole pitch ratio should be used.

As was mentioned in Section 2.1, it is fortunate that the choice of the number of poles to be used in any design is limited. A value is chosen by experience, paying attention to the resulting coil shape. Thus, the pole pitch is selected, and the pole arc can be varied until an optimum value is found. Increasing the pole arc will increase the pole face area, and hence also the useful flux. However, this gain becomes less as the pole arc approaches the pole pitch, due to an increase in the leakage flux between adjacent magnets. This leads to a poorer utilisation of the magnet material.

When optimising the design in the radial direction, it had to be assumed that $\overline{B}$ was independent of machine dimensions. In the angular direction, this assumption would appear to be even less valid, since the leakage flux will increase rapidly as a pole arc/pole pitch ratio of unity is approached. However, it will be assumed that the intrinsic magnetisation is independent of all dimensions, and so Equation 3.25 can be used to give the field distribution in the air-gap. The evaluation of this expression,

by the program "Normal Fluxplot", was described in Section 3.4. The pole arc is varied by altering the value of α (Figure 3.7) in the upper integration limit of Equation 3.25.

The radiator cooling fan motor will again be used as an example of this calculation. The field distribution at one conductor layer is plotted over half the pole pitch at some different radii. Figures 7.1, 7.2, and 7.3 are the results at 41mm., 47mm., and 59mm. radius respectively. Each figure shows the effect of various pole arc/pole pitch ratios, α', on the field distribution. It should be noticed that 47 mm. is approximately the average radius of the active conductor lengths, and 59 mm. is R_2 for the fan motor.

These three figures illustrate what has already been described. That is, at any given position in the air-gap, an increase in the pole arc will increase the flux density. However, the total gain in flux density, represented by the differences in the areas under the individual curves, does not match the additional magnet volume. This is another way of demonstrating the growth of leakage flux caused by bringing adjacent magnets' edges closer together.

The original intention was to optimise the machine's design in the angular direction. However, it must firstly be decided which criterion should be employed. If, as with the radial direction, maximum armature power is required, then Equation 7.4 indicates that $\overline{B}$ must be maximised. This will occur when α' is unity, and each set of magnets is constructed by magnetising a complete toroid alternately in zones. This criterion clearly has no regard for the best utilisation of the magnet material, and there will be considerable leakage between adjacent poles.

Figure 7.1 : Angular field distribution at 41mm. radius in the fan motor, for various values of pole arc/pole pitch ratio.

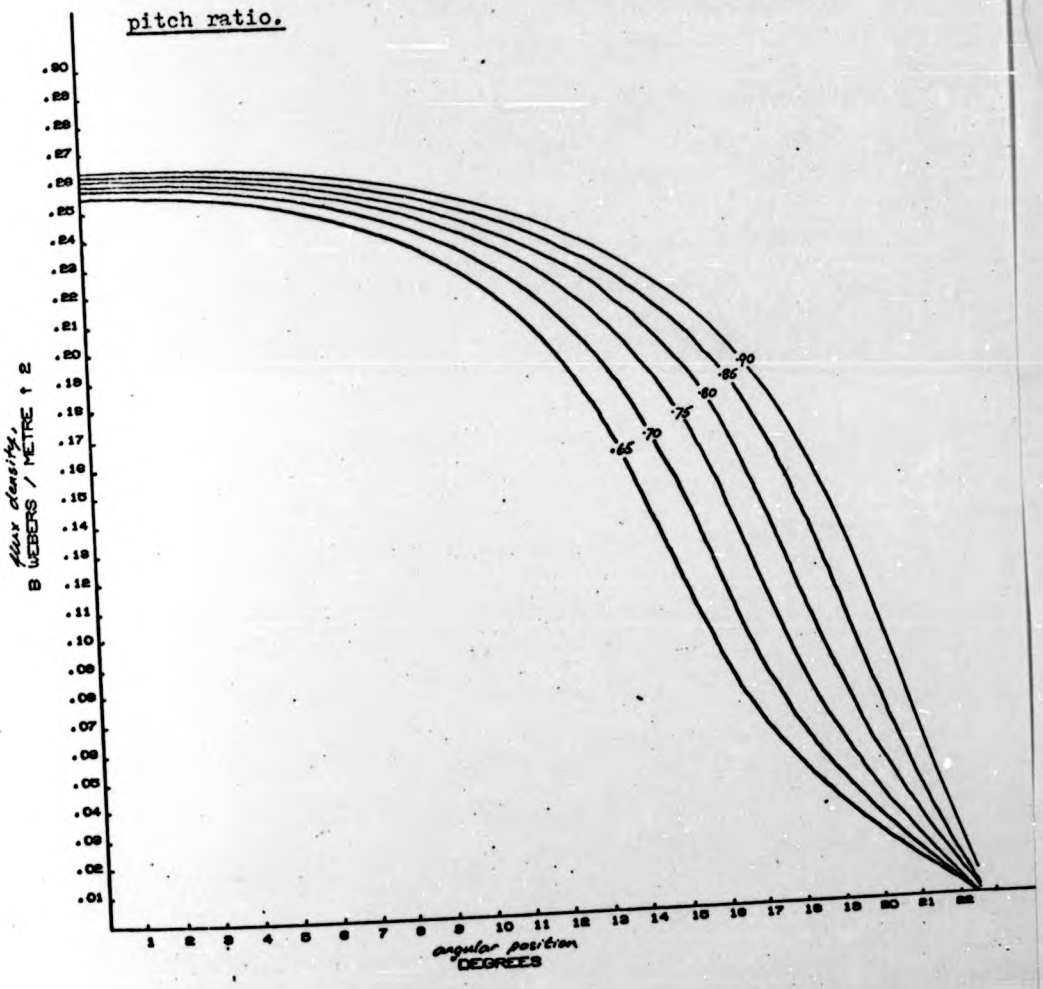

Figure 7.2: Angular field distribution at 47mm. radius in the fan motor, for various values of pole arc/pole pitch ratio.

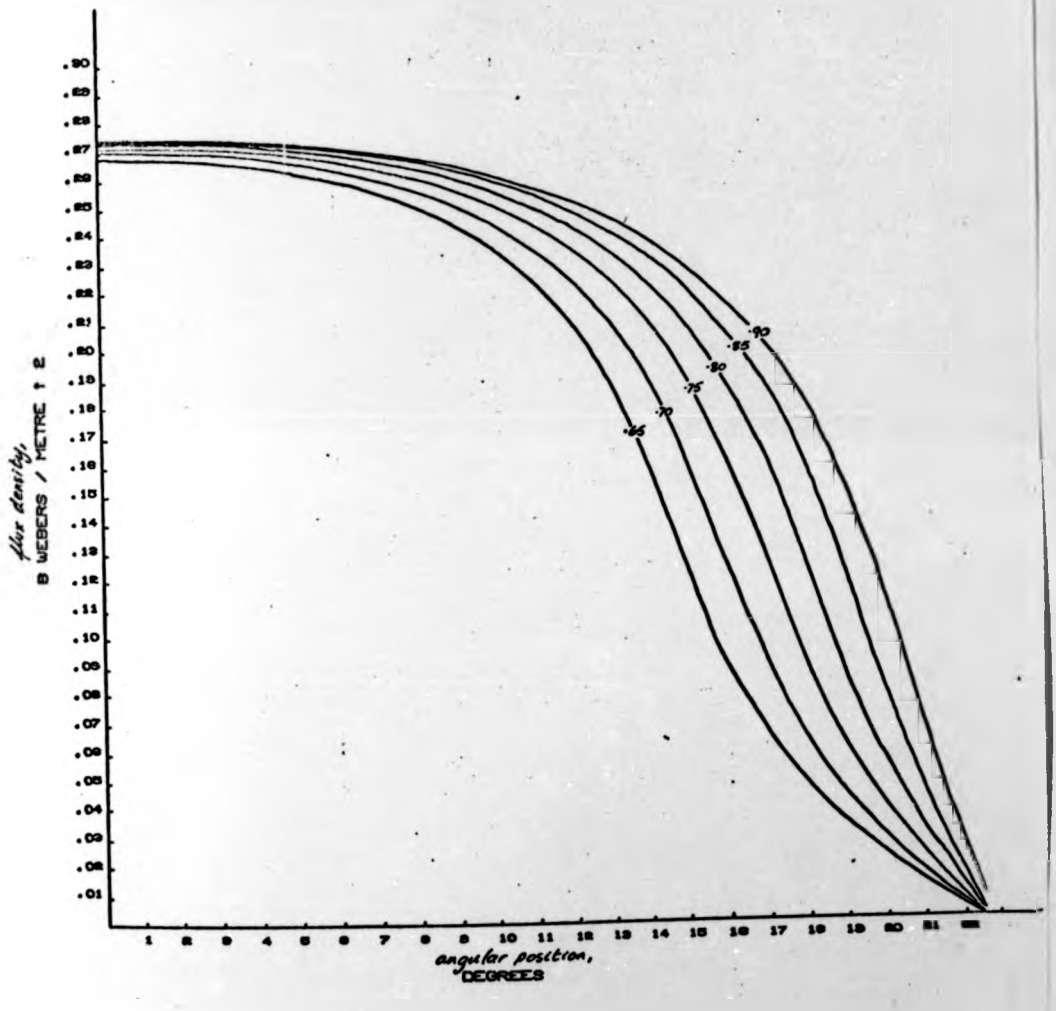

Figure 7.3: Angular field distribution at 59mm. radius in the fan motor, for various values of pole arc/pole pitch ratio.

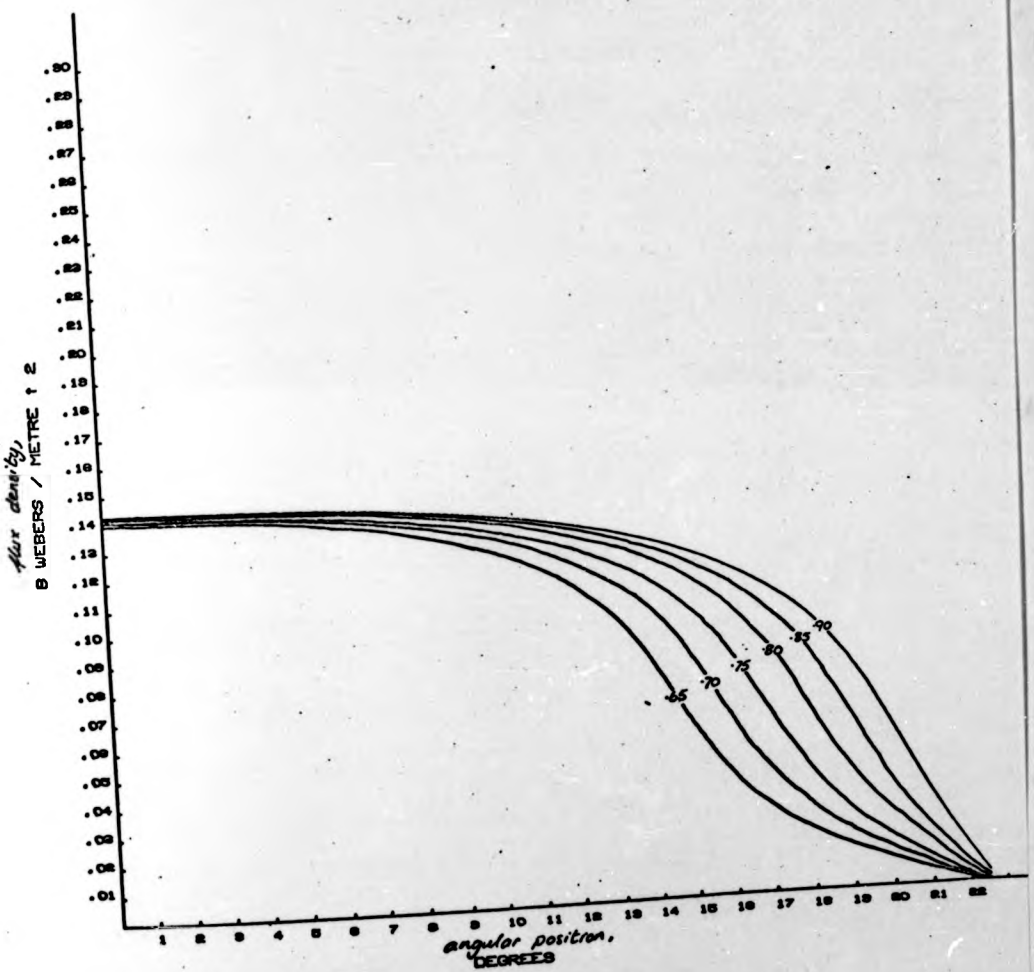

It is possible to take the calculations a stage further and to determine the e.m.f. in each armature winding path, for different values of α'. This procedure was adopted throughout Chapter 4, using the programs "Fluxcalc" and "Tlwave". The results are left to be multiplied by the appropriate factors to give either e.m.f. or torque. Figure 7.4 shows these results for ratios between 0.65 and 0.90. These curves indicate again the declining gain in armature power as α' is increased towards unity.

An alternative criterion for the magnet design might be to maximise the power-to-weight ratio of the magnet material. The power would be measured by the magnets' contribution to the armature power, and the weight would be directly proportional to the pole arc. Thus, Figure 7.4 can be used to deduce the variation of power-to-weight ratio with pole arc/pole pitch ratio. Figure 7.5 shows that the former decreases with the latter over the whole range considered.

It must therefore be concluded that neither the criterion of maximum armature power, nor that of maximum ratio of armature power to magnet weight, can be employed in this type of machine. An attempt has been made to take account of the feeling that pole arc/pole pitch ratios near to unity are wasteful of magnet material. However, a consideration of the magnet power-to-weight ratio indicates that very small values for α' are preferable. The motor design clearly requires a balance between these two criteria.

In fact, it must not be overlooked that other criteria may be important. For example, the maximum permissible magnet weight, or the maximum cost of its material. However, it is less likely

Figure 7.4. Variation of pole arc/pole pitch ratio for fan motor: effect on e.m.f. and torque.

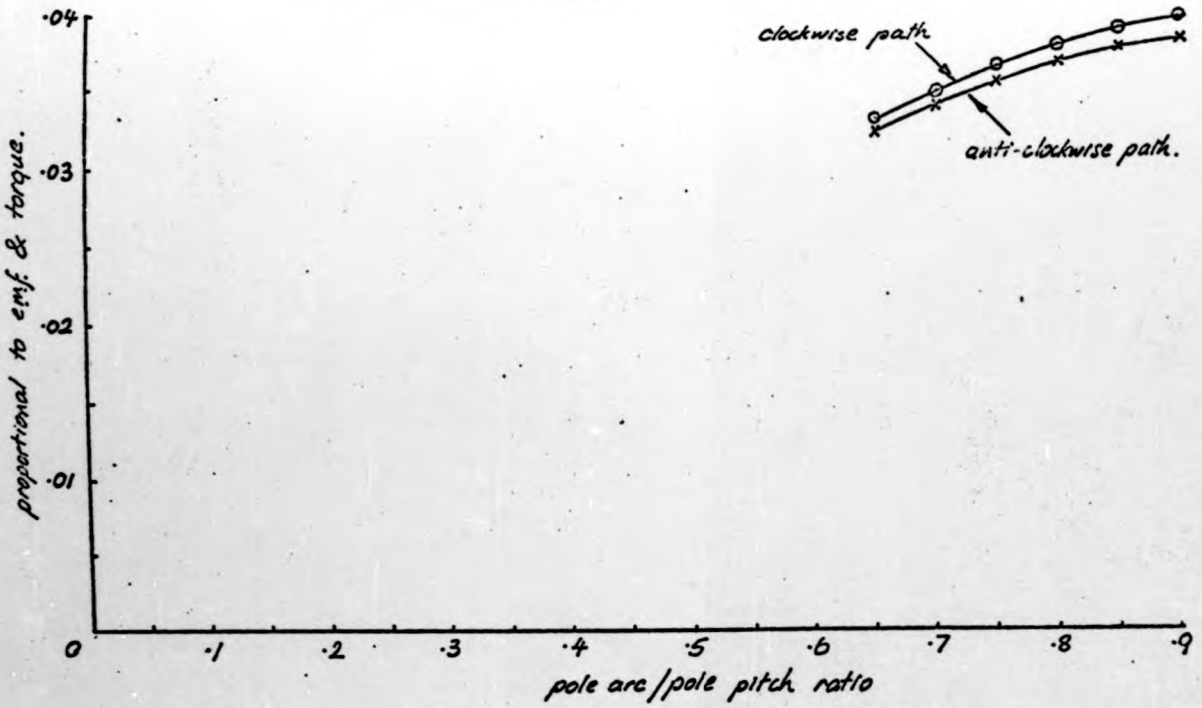

Figure 7.5. Variation of pole arc/pole pitch ratio for fan motor: effect on power-to-weight ratio.

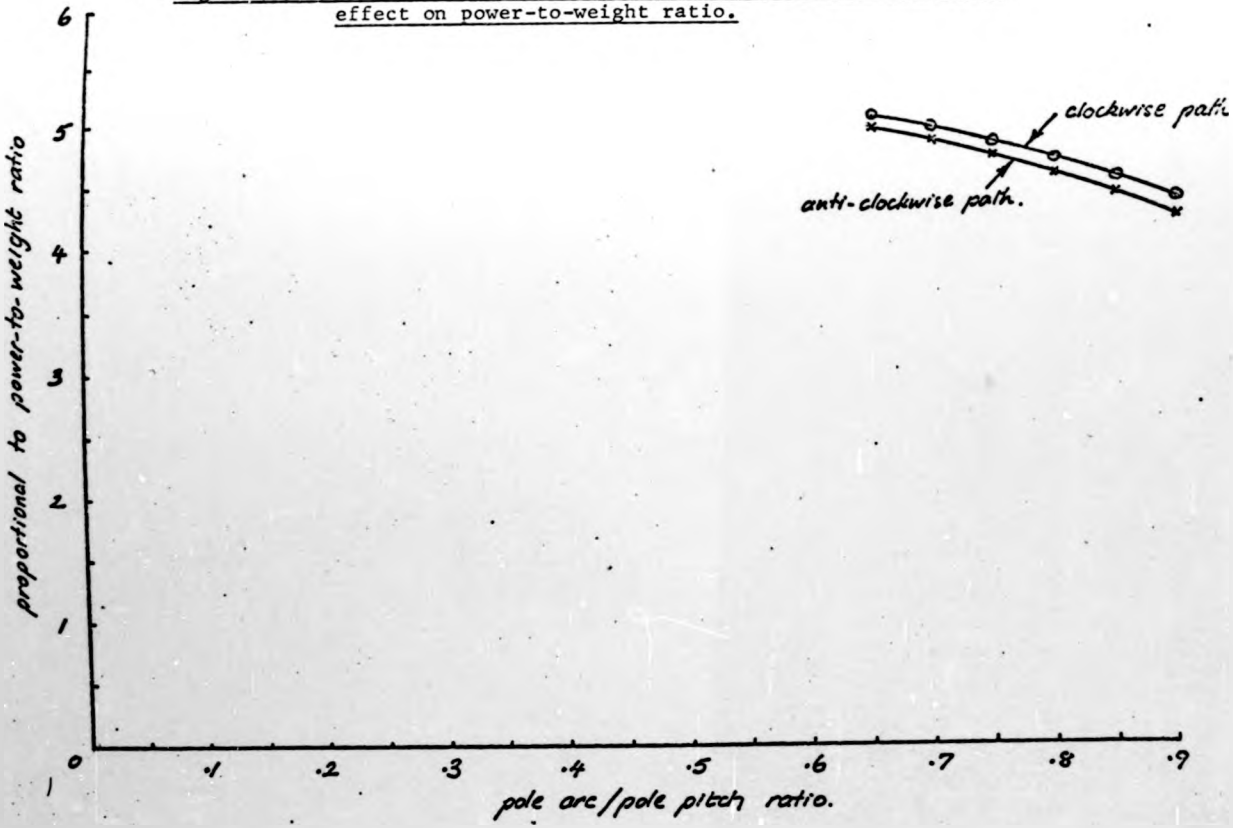

that these will be required. It can then be found that a multiplication of the curves in Figures 7.4 and 7.5 does yield a maximum at $\alpha' = 0.8$ (Figure 7.6). This is therefore the optimum ratio for achieving the maximum combination of armature power per unit volume of magnet material and useful flux density.

7.2. Relationship between magnet and copper volumes.

The determination of an optimum value for α' has considered only the volume of the magnet material. Also, any new design criteria based on the weight or cost of the magnets alone have been discounted. However, the armature power (Equation 7.4) has contributions from both the magnetic and electric loadings of the machine, and so any required output might be obtained from a variety of designs. These would achieve different relative contributions from each of the loadings. The proportions would be selected to meet some new criterion for the whole machine. For example, because the wheel motor is part of the vehicle's unsprung weight, its total weight is important. The volumes of permanent magnet and copper should therefore be related in an attempt to minimise this. This procedure could easily be extended to calculate minimum cost of these materials, as might be important for the fan motor.

The effect of a change in the magnet volume, V_m, on the copper volume, V_c, will therefore be determined. In particular, a new criterion for choosing the pole arc/pole pitch ratio will be sought. Firstly, the dependence of armature current on V_m is found. The variation of armature current with speed will be:

Figure 7.6. Variation of pole arc/pole pitch ratio for fan motor: combination of power-to-weight ratio with e.m.f. or torque.

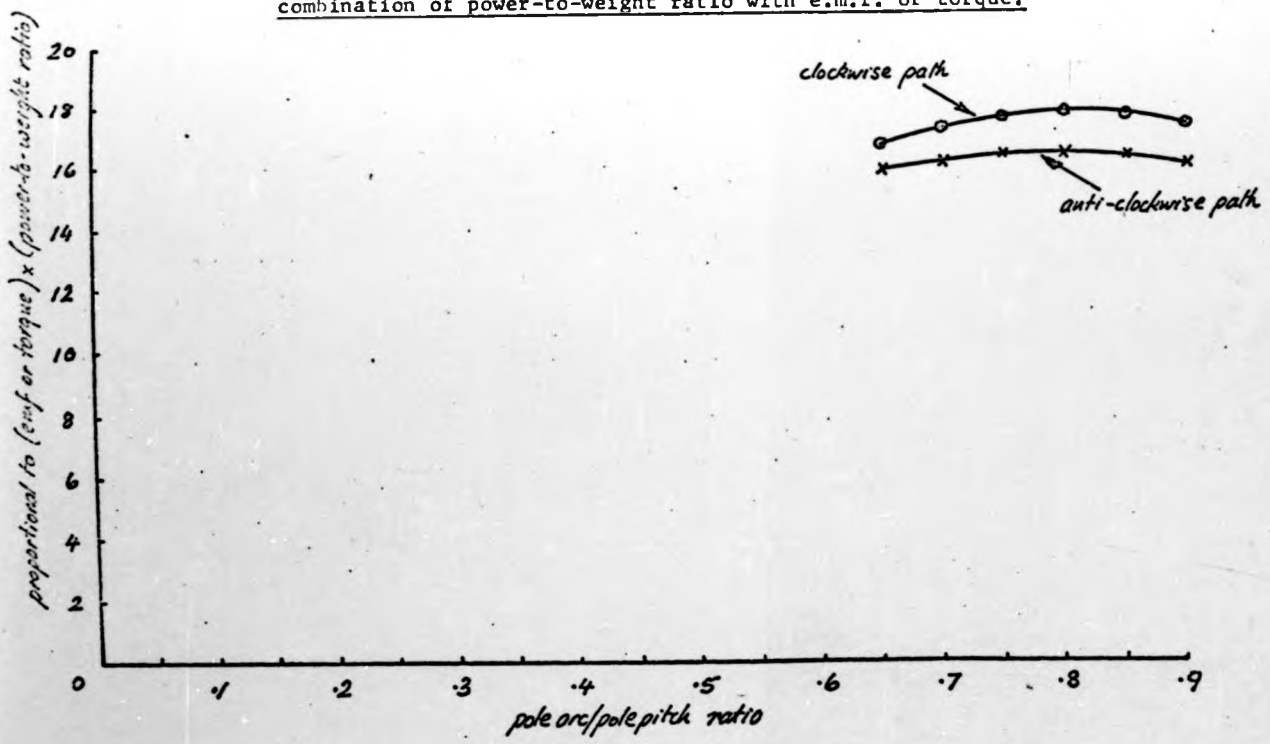

$$I.R_a = V - \frac{\phi.p.Z.N}{a} \qquad (7.7)$$

ϕ is the total useful flux per pole, and it can be related to the useful flux density in the air-gap, $\overline{B}$, by

$$\phi = \overline{B}.A_{pp} \qquad (7.8)$$

where A_{pp} is the active area of one pole pitch. Combining Equations 7.7 and 7.8 gives

$$I.R_a = V - \left(\frac{p.A_{pp}.Z}{a}\right)\overline{B}.N \qquad (7.9)$$

If the pole arc alone is varied, then the terms in brackets in Equation 7.9 will be constant. Those terms, together with $\overline{B}$, vary with α' as described by Figure 7.4 for the fan motor. As when armature heating is considered, I must be obtained in terms of the conductor current density, J_c. Since the number of parallel paths is a,

$$I = a.A_c.J_c$$

also,
$$R_a = \frac{\rho.l_c}{a^2.A_c}$$

where l_c = the total length of armature conductor.

$$\therefore \quad I.R_a = \left(\frac{\rho.J_c}{a}\right).l_c \qquad (7.10)$$

A comparison of Equations 7.9 and 7.10 shows that a variation of α' alone does not affect the cross-sectional area of the copper used. This is because it has been assumed that a change in current density should not occur if the machine dimensions are altered. If, however, the radial dimensions are altered at the same time as α', then the total length of conductor will change.

A small change in the active conductor length, $R_2 - R_1$, would clearly alter A_{pp}, which is no longer a constant. A larger variation might also affect Z and a, and it will be assumed that the changes are small enough for this not to occur. Also, the constant C_1 in Equation 4.12 will be ignored, and l_c can then be written as

$$l_c = Z\left[(R_2 - R_1) + \frac{\pi}{p}.(R_2 + R_1)\right] \qquad (7.11)$$

Also, the area A_{pp} is given by

$$A_{pp} = \frac{\pi}{p}.(R_2^2 - R_1^2) \qquad (7.12)$$

If the relationship of Equation 7.5 is used, then A_{pp} can be written in terms of l_c from Equations 7.11 and 7.12.

$$A_{pp} = \left(\frac{2.\pi}{p.k_r^2.Z^2}\right) l_c^2 \qquad (7.13)$$

where $$k_r = (\sqrt{3} - 1) + \frac{\pi}{p}.(\sqrt{3} + 1)$$

Equations 7.9, 7.10, and 7.13 can then be combined to relate l_c, $\bar{B}$, and N.

$$\left(\frac{\rho.J_c}{a}\right) l_c = V - \left(\frac{2.\pi}{k_r^2.a.Z}\right) l_c^2.\bar{B}.N \qquad (7.14)$$

Equation 7.14 shows that a variation of the pole arc/pole pitch ratio can be used in two ways. Alone, l_c will not be affected, and so the motor speed will change with α'. Varied together with $(R_2 - R_1)$, l_c will change if N is constant. The aim is to study the latter, since the speed of a motor is usually one of the design parameters. Equation 7.14 is therefore re-arranged in the form of Equation 7.15.

$$\left(\frac{2.\pi.N}{k_r^2.a.Z}\right)\bar{B}.l_c^2 + \left(\frac{\rho.\underline{J}_c}{a}\right)l_c - V = 0 \qquad (7.15)$$

ρ and $\underline{J}_c$ are very much smaller than any of the other constants, and so the second term in Equation 7.15 will be negligible. This therefore reduces to

$$\bar{B} = \left(\frac{k_r^2.a.Z.V}{2.\pi.N}\right)\frac{1}{l_c^2}$$

It is, however, more informative to use the direct relationship between l_c and R_1 (Equation 7.11) to re-write this expression as:

$$\bar{B} = \left(\frac{a.V}{2.\pi.N.Z}\right)\frac{1}{R_1^2} \qquad (7.16)$$

Equation 7.16 shows that the volume of copper can only be altered by adjusting R_1. For given output parameters, copper can be saved if the magnet volume is increased, and vice versa. However, alterations to the magnet volume must involve both the radial and the angular dimensions. For example, if a reduction in l_c is desired, this is achieved by reducing R_1. A corresponding increase in $\bar{B}$ must take place in accordance with Equation 7.16. For the new R_1, curves of the form of Figure 7.4 will give the variation of $\bar{B}$ with α', and so the required value of α' can be selected.

Since this method can only be used for small variations, its use will be somewhat limited. Larger variations may require a new winding design, involving different values for Z or a, and since α' must change quite considerably, new values for the pole number might eventually have to be considered. Nevertheless, Equation 7.16 does indicate that, for a small increase in copper volume, a much larger reduction in magnet volume will follow. This would be particularly useful in the case of rare earth magnets, since they are so much more expensive than copper at the present time.

8. CONCLUSIONS AND FURTHER WORK.

In this thesis, there has been extensive coverage of the calculation of the field due to permanent magnets. For the high coercivity ceramic ferrite type used in the fan motor, there was good agreement with the experimental results. The measured value of the torque per unit of conductor current showed the accuracy of the summation, in the manner of the winding arrangement, of the flux cut by the elements of each conductor. This also relied upon the correct use of image and adjacent poles, which were therefore shown to be a good substitute for the iron powder flux return ring.

However, some errors in the theory were indicated in the case of the alloy material, Hycomax III. The magnetisation tests on these magnets revealed that there was considerable leakage flux between adjacent magnets. Furthermore, it was evident that this was coupled with a transverse field within the material, that was rotating the magnetic domains. There are many commonly used permanent magnet materials that will exhibit this effect, and so further study to produce a more accurate theory for this type would be most worthwhile. Some of the observations already made can be used as a starting point.

It has already been shown that for some materials, the intrinsic magnetisation $\underline{M}$ is not constant, but varies linearly with $\underline{H}$. Also, the interior of the magnet has been treated like an air gap, and $\underline{H}$ was calculated at any point from the surface distribution of pole strength. It was assumed that this distribution only existed on the pole faces, but a direct solution of Laplace's

Equation indicated that there should also be sources on the pole sides. The variation of $\underline{M}$ with $\underline{H}$ will be different in the anisotropic and transverse directions, and the relationships may not even be linear, but tests on the material can establish the required characteristics.

A suggested procedure for determining the correct surface distribution is to commence with that used so far, and to progressively correct it. At each stage, the magnitude and direction of $\underline{H}$ is calculated around the boundary, and the normal and tangential components of $\underline{M}$ are found from the known characteristics. A new surface distribution is therefore defined, and the field is recalculated. This should continue until the changes at each stage are only slight.

A similar method might be used to study the flux distribution within the iron powder flux return ring, for it will be remembered that pressing only takes place in the axial direction. The test results for the field carried by this material, and its eddy-current and hysteresis losses, are encouraging for this and perhaps other electromagnetic applications. Measurements of the B-H characteristics in each direction should be accompanied by more conclusive results for the losses. The latter was not achieved in the fan motor, because of the axial field construction, and so further work on iron powder composites should be with a conventional machine design, to eliminate the thrust force. The manufacture of a more complicated shape than the ring has not yet been achieved. The advantage of a slotted structure to the volume of magnet material has been mentioned, and this profile requires the use of the

iterative solution for the useful field. The image poles have to take on more irregular shapes, for the determination of the magnet's potential distribution, but experimental plots should reveal what accuracy is required.

It may be possible to include iron powder in all the epoxy resin of the disc, if the positions occupied by the conductors are sufficient to prevent the flux from travelling in the circumferential direction before it has passed through the same conductors. Compaction could not be used for this, though, as the conductors'' insulation would be damaged. A new method of manufacture would have to be found, and it is unlikely that such a high percentage of iron powder would be achieved as with the ordinary ring. Also, the conductors need to be held against one surface, so a more immediate solution might be found if the return ring was not included in the armature. The loading of the armature with iron powder would then reduce the effective air gap length, and benefit the volume of magnet material.

The performance of the wheel motor has demonstrated a peculiarity of the Disc-Armature machine, that occurs because the coils have very little self-inductance. The variation of the bar-to-bar voltage of a short-circuited coil can lead to very high losses, but these were not noticed in the fan motor. A resistance at the brush contact of 0.081 ohms was found to account for the motion of the commutator over the brushes. With the fan load, for example, this is equivalent to a voltage drop of 0.77 V., which compares well with the manufacturers' estimate of 1 V.,

when it is considered that the latter also includes the static voltage drop at the contact. It may then be wondered what has become of the commutation loss in this machine ? The method that was developed to calculate the induced e.m.f. as the armature is rotated may be useful for investigating this.

It will be remembered that the connections between the fan motor's armature conductors and its commutator segments were misplaced by half the angular pitch of a segment. The effect of this will be either to advance or retard the commutation, depending on the direction of rotation. In this case, the commutation is advanced, and a coil is under the influence of the pole it has just passed for all the time it is short-circuited. The current through the coil, the segments, and the brush will therefore be into the segment approaching the brush, assisting the commutation. For rotation in the opposite direction, there would be a concentration of current in the trailing edge of the brush, which would cause considerable sparking. It is this difference that prevented the direction of rotation of the fan from being reversed, a test that would have provided a point on the other side of the speed vs. current characteristic, and given more information about the thrust bearing loss. However, the brush contact resistance would clearly have been changed.

It may be, then, that a simple solution to the commutation problems of the Disc-Armature machine has already been found. It is recommended, though, that before another high speed motor is designed, this method of calculating the angular variation of e.m.f. should be developed to investigate the effect of various

displacements of the winding from its "correct" relationship to the commutator. This is equivalent to rocking the brush-gear, a proceduro that is common in conventional d.c. machines. However, it is expected that the angle of displacement in a Disc-Armature motor will not be dependent upon the load current, and should therefore suit a wider range of operation than a conventional one without interpoles.

There is still much to be done before a reliable Disc-Armature machine can be manufactured, that fully utilises all of its advantages over more conventional types. However, as has been illustrated by the fan motor, a most satisfactory design can be produced if not all the criteria are not strictly adhered to. In fact, this machine is now successfully completing many hours of testing by an industrial user.

This thesis has covered much of the theory relating to the Disc-Armature motor, and has reported some interesting experimental results. However, this is a new type of machine, and what has been investigated is not exhaustive; it is only a beginning.

displacements of the winding from its "correct" relationship to the commutator. This is equivalent to rocking the brush-gear, a procedure that is common in conventional d.c. machines. However, it is expected that the angle of displacement in a Disc-Armature motor will not be dependent upon the load current, and should therefore suit a wider range of operation than a conventional one without interpoles.

There is still much to be done before a reliable Disc-Armature machine can be manufactured, that fully utilises all of its advantages over more conventional types. However, as has been illustrated by the fan motor, a most satisfactory design can be produced if not all the criteria are not strictly adhered to. In fact, this machine is now successfully completing many hours of testing by an industrial user.

This thesis has covered much of the theory relating to the Disc-Armature motor, and has reported some interesting experimental results. However, this is a new type of machine, and what has been investigated is not exhaustive; it is only a beginning.

9. REFERENCES.

1. British patent no. 1.231,782.

2. Campbell, P.; "Design of a commutatorless Disc-Armature motor for electric car", Undergraduate thesis, University of Warwick, 1970.

3. "Hybrid buses get ahead faster than cars", Elect. Rev., 7 Jan 1972, p.20.

4. Clayton, A.E.; "Performance and design of d.c. machines", Pitman, 1959, Ch.2.

5. Carter, F.W.; "Note on air-gap and interpolar induction", Jour.I.E.E., 1900, vol.29, pp.925-933.

6. Smith, G.D.; "Numerical solution of partial differential equations", O.U.P., 1965, Ch.2.

7. Sommerfeld, A.; "Electrodynamics", Academic Press, 1952, Ch. 12, p.80.

8. Dwight, H.B.; "Tables of integrals and other mathematical data", Macmillan, 1962.

9. Stark, P.A.; "Introduction to numerical methods", Macmillan, 1970, Ch.6.

10. Gould, J.E.; "Some aspects of permanent magnet d.c. motors", Trans.I.E.E.E., June 1970, vol. MAG-6, no.2, pp.275-8.

11. Shobert, E.I.; "Commutation", Trans.A.I.E.E., Dec.1962, no.63, p.594.

12. Permanent Magnet Association ; "Magnetic properties and design data for standard P.M.A. materials", Sheffield, 1972, Tech. Bulletin No.1.

13. Stott, G.; "Iron powder compacts for electromagnetic applications", M.Sc.thesis, University of Warwick, 1971.

14. Permanent Magnet Association ; "Magnetising of permanent magnets", Sheffield, 1966, Tech. Bulletin No.7.

15. Clayton, A.E.; "Performance and design of d.c. machines", Pitman, 1959, Ch.11.

16. Bleaney, B.I., and Bleaney, B.; "Electricity and magnetism", O.U.P., 1965, Ch.5.

17. Robnor Paints Ltd. ; Private Communication on mixture reference PX.153G, Swindon, 2 July,1973.

18. British Standard BS 2782.

19. "Electric Vehicle Traction Motor", Physics exhibition handbook, March 1972, pp.57-58

20. Campbell, P.;"A new wheel motor for electric commuter cars", Elect. Rev., 10 March 1972, vol.190, no.10, pp.332-3.

21. Campbell, P.; "Electric car differentials", Engineering, July 1972, p.713.

22. Campbell, P.; "Current problems for electric cars", I.E.E.Stud.Q.J., Sept 1972, vol.42, no.169, pp.80-82.

23. Campbell, P.; "Prospects for the d.c. disc-armature motor", 8th. Univ. Power Engineering Conf., University of Bath, Jan 1973.

24. "Good design will get more out of electric cars", Elect. Rev., 4/11 Jan 1974, vol.194, no.1, p.19.

25. Campbell, P.; "'Pancake' shaped d.c. motor for efficient fan drives", Elect. Rev., 8 March 1974, vol.194, no.8, pp.211-212.

26. Campbell, P.; "Energy conservation in electric vehicles: the d.c. Disc-Armature motor", European Conf. on Electrotechnics, Amsterdam, April 1974, paper A 5-1.

27. Campbell, P., and Corbett, A.E.; "The pancake motor", Automotive Des. Engng., July/Aug 1974, vol.13, pp.34-5.

28. Campbell, P.; "Energy conservation in electric vehicles", Electronics and Power, 5 Sept 1974, vol.20, no.5, pp.634-636.

29. Campbell, P.; "Developments in small axial-field machines", International conf. on electrical machines, City Univ., Sept 1974, paper E6.

30. Campbell, P.; "Principles of a permanent magnet axial-field d.c. machine", Proc.I.E.E., Dec.1974, vol.121, no.12, pp.1489-1494.

31. Campbell, P.; "The magnetic circuit of an axial-field d.c. electrical machine", Intermag conference, April 1975, paper 17-6.

32. Simons, S.; "Vector analysis for mathematicians, scientists, and engineers", Pergamon, 1964, Ch.8, p157.

APPENDIX I: Relationships between $\underline{B}$, $\underline{H}$, and $\underline{M}$ for permanent magnets.

There is often confusion about the relationship between the basic magnetic vectors $\underline{B}$, $\underline{H}$, and $\underline{M}$. This thesis is based upon Equations 3.1, 3.2, and 3.3, and these are of the form given in Bleaney & Bleaney (Reference 16).

If a current circulates in a loop, having a current density $\underline{J}$, the resulting magnetic field will be related by Ampere's law:

$$\text{curl } \underline{B} = \mu_o \underline{J} \qquad \text{(AI.1)}$$

In magnetic materials, the intrinsic magnetisation, $\underline{M}$, is caused by magnetic dipoles, and is alternatively called the magnetic dipole per unit volume. These dipoles can be represented in an atomic model by circulating currents, of density $\underline{J}_m$. $\underline{M}$ is then caused by $\underline{J}_m$ in a similar manner to $\underline{J}$ causing $\underline{B}$:

$$\text{curl } \underline{M} = \underline{J}_m \qquad \text{(AI.2)}$$

In a magnetic medium that is also electrically conducting, Equation AI.1 should be re-written to include $\underline{J}_m$, which must also obey Ampere's law:

$$\begin{aligned} \text{curl } \underline{B} &= \mu_o(\underline{J} + \underline{J}_m) \\ &= \mu_o(\underline{J} + \text{curl } \underline{M}) \\ \therefore \text{curl}((\underline{B}/\mu_o) - \underline{M}) &= \underline{J} \end{aligned} \qquad \text{(AI.3)}$$

From Equation AI.3, the magnetic field is defined as:

$$\underline{B} = \mu_o(\underline{H} + \underline{M}) \qquad (3.1)$$

such that $$\text{curl } \underline{H} = \underline{J} \qquad \text{(AI.4)}$$

In the permanent magnets of the Disc-Armature machine, there are no circulating electrical currents (other than the dipole

APPENDIX I: Relationships between $\underline{B}$, $\underline{H}$, and $\underline{M}$ for permanent magnets.

There is often confusion about the relationship between the basic magnetic vectors $\underline{B}$, $\underline{H}$, and $\underline{M}$. This thesis is based upon Equations 3.1, 3.2, and 3.3, and these are of the form given in Bleaney & Bleaney (Reference 16).

If a current circulates in a loop, having a current density $\underline{J}$, the resulting magnetic field will be related by Ampere's law:

$$\text{curl } \underline{B} = \mu_o \cdot \underline{J} \qquad \text{(AI.1)}$$

In magnetic materials, the intrinsic magnetisation, $\underline{M}$, is caused by magnetic dipoles, and is alternatively called the magnetic dipole per unit volume. These dipoles can be represented in an atomic model by circulating currents, of density $\underline{J}_m$. $\underline{M}$ is then caused by $\underline{J}_m$ in a similar manner to $\underline{J}$ causing $\underline{B}$:

$$\text{curl } \underline{M} = \underline{J}_m \qquad \text{(AI.2)}$$

In a magnetic medium that is also electrically conducting, Equation AI.1 should be re-written to include $\underline{J}_m$, which must also obey Ampere's law:

$$\text{curl } \underline{B} = \mu_o(\underline{J} + \underline{J}_m)$$
$$= \mu_o(\underline{J} + \text{curl } \underline{M})$$
$$\therefore \text{curl}((\underline{B}/\mu_o) - \underline{M}) = \underline{J} \qquad \text{(AI.3)}$$

From Equation AI.3, the magnetic field is defined as:

$$\underline{B} = \mu_o(\underline{H} + \underline{M}) \qquad (3.1)$$

such that

$$\text{curl } \underline{H} = \underline{J} \qquad \text{(AI.4)}$$

In the permanent magnets of the Disc-Armature machine, there are no circulating electrical currents (other than the dipole

currents), so $\underline{J}$ will be zero, and Equation AI.4 becomes:

$$\text{curl } \underline{H} = 0 \qquad (3.3)$$

In some treatments, the constant μ_o appears on the right-hand side of Equation AI.2, as it does in Equation AI.1. This leads to a different form for Equation 3.1, which is not used here.

The Biot-Savart law can be written in the form:

$$\underline{B} = \frac{\mu_o . q . (\underline{v} \times \underline{r})}{4\pi \, r^3} \qquad (AI.5)$$

where $\underline{B}$ is the flux density due to a charge q travelling with velocity $\underline{v}$ in the direction $\underline{r}$. Using the vector identity

$$\text{div}(\underline{a} \times \underline{b}) = \underline{b}.\text{curl } \underline{a} - \underline{a}.\text{curl } \underline{b} \ ,$$

Equation AI.5 becomes:

$$\text{div } \underline{B} = \frac{\mu_o . q}{4\pi} \left(\frac{\underline{r}}{r^3} . \text{curl } \underline{v} - \underline{v} . \text{curl } \frac{\underline{r}}{r^3} \right) \qquad (AI.6)$$

The dipole equivalent currents in a permanent magnet are steady, and so curl $\underline{v}$ is zero. Furthermore, it can be shown (Reference 32) that curl $\frac{\underline{r}}{r^3}$ is also zero, so that Equation AI.6 becomes the familiar Maxwell's Equation:

$$\text{div } \underline{B} = 0 \qquad (3.2)$$

APPENDIX II: Direct Solution of Laplace's Equation.

The solution of Laplace's Equation, $\nabla^2\psi(x,\theta) = 0$, within the boundary OABC of Figure 3.3 is achieved by separating the two variables.

$$\psi(x,\theta) = X(x).\Theta(\theta) \qquad \text{(AII.1)}$$

Considering first the θ-direction, the solution must be periodic, and will have the general form

$$\Theta(\theta) = J.\cos\lambda\theta + K.\sin\lambda\theta \qquad \text{(AII.2)}$$

The values of J, K, and λ are determined from the boundary conditions $\psi(x,0) = 0$ and $\psi(x,C) = 0$. Hence, Equation AII.2 becomes

$$\Theta_n(\theta) = K_n.\sin\frac{n\pi\theta}{C} \qquad \text{(AII.3)}$$

where n = 1,2,3, etc.

This is true for both areas 1 and 2 in Figure 3.3.

The solution in the x-direction will be slightly different for each area. Area 1 will be considered in detail. λ is common between the solutions in each direction, and so that in the x-direction corresponding to Equation AII.3 will be exponential. It is given by

$$X_n(x) = L_n.\sinh\frac{n\pi}{C}(x - x_o) \qquad \text{(AII.4)}$$

where x_o, a constant, is zero from the boundary condition $\psi(0,\theta) = 0$.

The total solution is found by combining Equations AII.1, AII.3, and AII.4, and summing for all values of n :

$$\psi_1(x,\theta) = \sum_{n=1}^{\infty} k_n.\sin\frac{n\pi\theta}{C}.\sinh\frac{n\pi x}{C} \qquad \text{(AII.5)}$$

The final boundary condition is the potential distribution on

the magnet face, defined as $\psi(\theta)$ along the line HI. In Equation AII.5,

$$\psi(\theta) = \psi(H,\theta)$$

$$= \sum_{n=1}^{\infty} k_n . \sin \frac{n\pi\theta}{C} . \sinh \frac{n\pi H}{C}$$

from which the sine Fourier coefficients of $\psi(\theta)$ can be recognised as

$$k_n . \sinh \frac{n\pi H}{C} = \frac{2}{C} \int_0^C \psi(\theta) . \sin \frac{n\pi\theta}{C} \, . d\theta \qquad \text{(AII.6)}$$

The complete solution in area 1 is therefore given by substituting Equation AII.6 into Equation AII.5, from which Equation 3.7 is obtained.

The solution in area 2, given by Equation 3.8, is found in a similar way, allowing for the slight difference in the x-direction.

APPENDIX III. Materials for a rotating flux return ring.

The attachment of the remote flux return ring to the fan motor armature was done after the moulding operation. This was to give time for a variety of materials to be tested. The thickness of this ring is only 3 mm., and most of the flux travels in the axial and circumferential directions. If a laminated construction is to be employed, therefore, it is most effective for the laminations to run circumferentially. Such a ring was made for the fan motor (Figure A.3.1), though its manufacture in this shape was difficult.

One thou thick nickel iron strip was used, and firstly this was laminated. It was then wound onto a stainless steel band, supported on a plate of the same material. This stainless steel was able to withstand the high annealing temperature of 1050°C. The annealing was performed in a sealed oven in an atmosphere of hydrogen. This ensured that a standard core of the nickel iron strip was produced, having a saturation flux density of 1.44 Wb/m^2. An outer steel band was shrunk on, and the support plate removed. The ring was finally dipped in epoxy resin to give it additional rigidity for the subsequent tests.

Because of its large diameter and small thickness, the laminated ring was difficult to handle throughout its manufacture. This could make it unattractive to use in a small economical machine such as the fan motor. Some tests had already been done on iron powder compacts (Reference 13), and it was felt that this type of material offered a more convenient solution. The method of manufacturing rings from this material was briefly as follows.

It was found that merely to compress iron powders did not give a good mechanical strength. Epoxy resin was therefore added in a small quantity. This gives good adhesion between individual particles, and its high electrical resistance should reduce the

Figure A.III.1 Laminated nickel iron flux return ring.

eddy-currents in the bulk material. The epoxy resin was diluted with the acetone for mixing with the iron powder, and because the viscosity of resin decreases as the temperature is raised, this was performed on a hot-stage. The mixture was then dried, and finally powdered. An amount was measured into the mould and compressed at a pre-determined pressure. The percentage of epoxy resin to add initially, and the pressing pressure, are determined by the required saturation flux density in the material. Reference 13 predicts this mixture, of 24 parts of iron powder to one part of resin (by weight), to saturate at 1.6 Wb/m^2, which is greater than its designed operating flux density in the motor of 1.3 Wb/m^2.

Two types of iron powder were used for these rings. One was a carbonyl, having spherically shaped particles, and the other an electrolytic with flaky particles. The higher resistivity of the carbonyl was attributed to an assumed point contact between the particles, though it will be shown in Chapter 5 that the total power losses are quite similar in each type. The epoxy resin must interlock better with the flaky particles, because the electrolytic powder mixture was found to have a greater mechanical strength. This made it very easy to handle after manufacture, without damaging its shape.

It was mentioned in Section 2.2 that it had not been possible to press a slotted structure on one face of the ring. This would have reduced the effective air gap, and hence the required magnet length. The difficulty arises because different thicknesses are being pressed in different regions, and a very complicated die shape is required to ensure an even compaction. It was found that the roots of the teeth were very brittle, but this might be overcome by radiusing all the corners in the die.

PPENDIX IV. Construction of the Disc-Armature machine.

A.IV.1. Design of the stator components.

No attempt will be made to give a comprehensive account of the design procedure for a Disc-Armature motor. However, there are some particular problems that are worthy of mention, that only occur in a machine of this type. Those that concern the stator design arise because the field is in the axial direction, because permanent magnets are used, and also because certain design criteria are applied.

For the radiator cooling fan motor, it has already been noted that the inclusion of the flux return ring in the armature creates a force of attraction between the rotor and stator. This will also occur in a conventional machine, but it is only with an axial field that this force must be overcome for dis-assembly. This is also true for the Disc-Armature machine with an iron-free rotor, for the two stator halves have to be separated. There is equal difficulty in assembly, and some guidance has to be provided when the two halves come together. In the wheel motor shown in Figure 2.3, one stator half located inside the other for a distance of 12 mm.. These components, together with the armature, appear in Figure A.IV.1. Two holes can be seen in the magnet backing plate of the right-hand stator half, close to the periphery. Screws are inserted from outside, through these and another pair of holes, past the armature, to bear on the opposite stator half. In this manner the components are jacked apart, or alternatively brought together. A similar procedure is required for the fan motor.

Figure A.IV.1. Wheel motor's stator halves and armature.

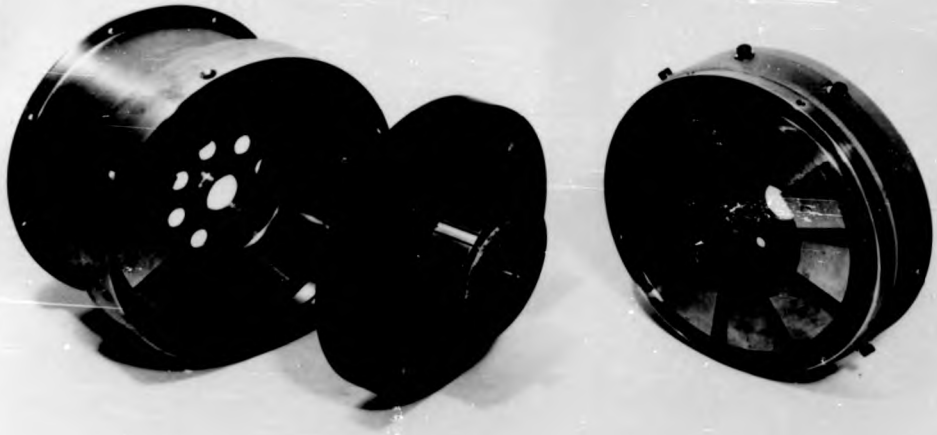

There would not be this difficulty if the magnets were magnetised after assembly of the machine. However, this does not justify the inclusion of magnetising windings. The alloy magnets in the wheel motor produce a greater field on open circuit than do the ceramic ferrites in the fan motor. This led to particular difficulties with the former, when they were positioned on the backing plates. The addition of each subsequent magnet, being already magnetised, led to an unbalanced circumferential force until the complet set was correctly in place. It was eventually found easier to attach each set before magnetisation, and then to magnetise each stator half before assembly.

A magnetisation jig with a profile to match one set of magnets was constructed, and the backing plate completed the magnetic circuit. The plates' thickness had originally been designed to accommodate a flux density of 1.3 Wb/m^2, thus operating well below saturation of the mild steel. However, to fully magnetise the magnets, a much greater flux density will be reached in the plate. An additional mild steel ring was therefore clamped to the back of the plate for the magnetisation process.

Frequently in the design of Disc-Armature motors, it is the brushes and commutator that cause an embarrassing increase in the overall length. In the fan motor, this was overcome by locating the brushes between adjacent magnets, but this is not always possible. For the wheel motor, Figure 2.3 shows that approximately half the volume occupied by the motor alone is allocated to the commutator and brush-gear. Had a face-type commutator been used, the overall length of the machine could have been reduced by using constant force springs. These were, in fact, employed in the wheel motor,

and Figure 2.3 shows that they take up very little space, so that the motor's diameter at the brush-gear could have been reduced. These springs have the advantage of giving a constant brush pressure, regardless of their extension. This dispenses with any mechanism for adjusting the pressure to the required value. Each spring is fixed to the inside of the brush-holder by a rivet, and is unwound in a slot alongside the brush.

The use of these springs requires the brushes to be in position before the stator halves and armature are assembled. They are loaded from the commutator side, and Figure A.IV.1 shows that they must be held back before the armature is inserted. The terminal leads can be used to do this.

A.IV.2. Design and manufacture of the armature.

The rotor of the Disc-Armature machine is the most novel component, and considerable time was spent in improving its method of manufacture. The final method will be described here, with reference to some unsuccessful attempts, though it should be remembered that this applies to the production of prototypes, and not necessarily to mass-production.

Once the individual coils are assembled as the winding, they are soldered to the commutator. The wheel motor's commutator was a production item, but that for the fan motor was designed to use the armature moulding process to complete its manufacture. The unmoulded fan motor armature is shown in Figure A.IV.2, and this can be compared with the general arrangement, Figure 2.4. A band of copper is left above the segments to support them until after moulding,

Figure A.IV.2.Fan motor armature winding and commutator.

when this is machined off leaving adjacent segments insulated from each other. The cross-sectional shape of the commutator, which allows a close fit with the end-windings, relies upon the adhesive property of epoxy resin to hold the segments in place. As an additional precaution, a band of epoxy resin is formed above the risers. For the soldering operation, a wooden jig is used to hold the winding against part of the mould, and the commutator in its correct position above the winding.

Epoxy resin has a number of attributes as an encapsulating material for electrical windings. Its adhesive properties are well-known, and it also has excellent electrical and mechanical characteristics. It keeps good dimensional stability, and it is possible to dilute the percentage of resin without significantly degrading these properties. This is usually done by adding marble flour, of which these armatures have a quantity equal by weight to the resin (In addition, the hardner is 0.8 parts by weight to that of the resin). The mixture used has a coefficient of expansion of approximately 4.75×10^{-5} /°C (Reference 17), which is greater than that for copper. If this were not so, the heating of the armature conductors during operation of the machine would crack the epoxy resin.

Since there is only a small clearance between rotor and stator over a considerable radial distance, it is important that the armature disc does not distort. The safe operating temperature for the resin, below which this will not be significant, is called the heat deflection temperature (Reference 18). For any mixture, this can be set within certain limits by the curing conditions. The heat deflection temperature of this mixture lies between 130°C and 190°C.

However, it will be towards the lower end of this range, as the curing schedule used was 16 hours at 65°C, 4 hours at 110°C, and then 2 hours at 150°C. It has been shown (Reference2) that the normal operating temperature would be in the region of 75.8°C, and so the armature using this mixture should be quite safe from distortion.

There are three principal methods of moulding a component such as this armature. Compression moulding is only used for large parts, and intricate details cannot be formed. The resin is placed in the mould, and heat and pressure are applied so that the material softens, fills the mould, and then hardens. It would be particularly difficult to achieve a close tolerance on the axial disc thickness with this method, for which it is much better to retain a fixed cavity shape throughout the process.

Injection moulding, which is quite similar to transfer moulding, is the most suitable method for mass-production. The resin, in granular form, is heated to plasticity in a cylinder, and then forced into the temperature-controlled mould. There is no difficulty in maintaining a good dimensional accuracy, and a rapid rate of production is possible. However, when thin sections are being moulded, the resin may cool too rapidly and a complete fill may not be achieved, or internal stresses may develop. This could be a problem over the active region of the armature disc, where the presence of the conductors can occupy most of the volume.

The final method is casting, which involves the greatest amount of hand labour. It is, however, the simplest method to use for prototypes, though precautions have to be taken to remove air bubbles. This is achieved by placing the mould in a vacuum chamber, and gravity feeding the liquid epoxy resin into it from within the

chamber. A specially equipped chamber was used for the disc armature prototypes, having remote control to release the resin. The mould also had to be designed to suit this equipment.

A.IV.3. Armature mould design.

The armature mould for the fan motor will be described in detail, and that for the wheel motor is quite similar. The general arrangement of the former is shown in Figure A.IV.3. The phosphor bronze bearing and the commutator are shown in position in the mould, but the flux return ring is not included. At the time the mould was designed, it had not been decided from which material to make the return ring, and so a recess was formed into which it could be fixed at a later stage.

The bearing fits tightly between the upper and lower plates of the mould, preventing any epoxy resin from fixing it to either. This is the main problem with the mould design, and particular care has to be taken with the commutator, which is of a fragile shape until it is encapsulated. The copper band, holding the segments together, is pulled into the groove, and held there. It is not possible to put a taper on the final surface of the segments, though this is required to facilitate an easy extraction from the lower mould plate. However, it is essential that the flow of resin is not impeded around the segments during moulding, so that a complete fill is achieved. Therefore, a cavity is left around the outer surface of the commutator, so that it is completely encapsulated within a protective layer of resin. This prevents damage to the segments due to adhesion when the armature is extracted, and the excess resin can be turned off at a later stage.

Figure A.IV.3. General arrangement of fan motor mould.

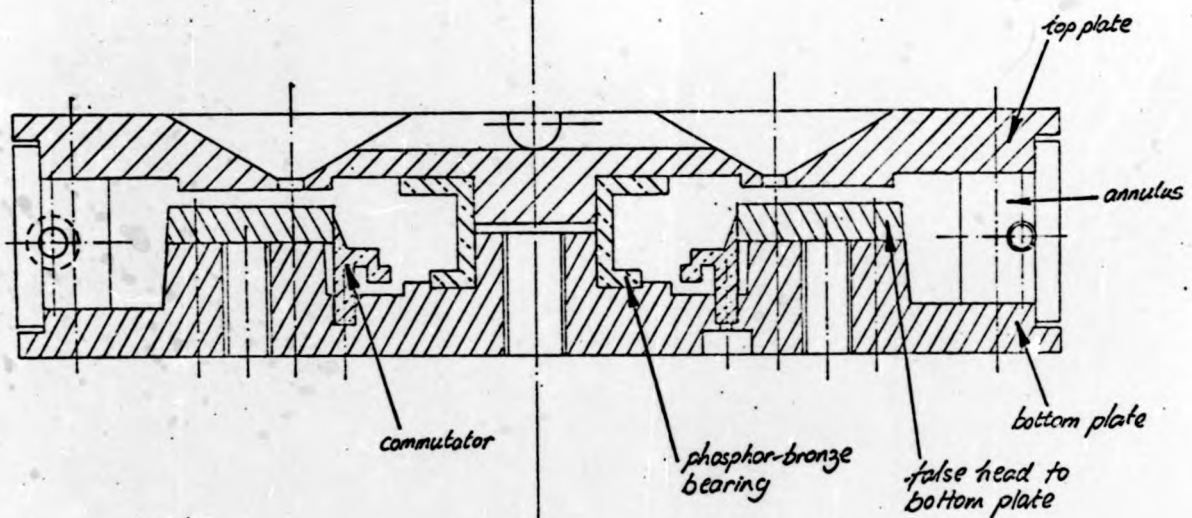

To ease the removal of the armature from the mould, all long edges that lie in the axial direction are offset slightly from this axis. The most suitable taper was found to be 3°, which was large enough to be of some assistance to this, and also small enough not to interfere with the machine's designed dimensions.

The mould was made from five parts, to ensure there was no undue strain on the armature during disassembly. These can be identified in Fig. A.IV.3, and are shown for the mould partially dismantled in Fig. A.IV.4. It is, in fact, possible to use just two parts for the mould, but it will be shown that this does not always produce successful results. To commence the disassembly, a separate annulus to the mould is used. This is in two identical halves, held together with screws. Fig. A.IV.4 shows one half on each of the upper and lower plates. The screws are removed, and a screwdriver is inserted in slots to lever the two halves apart.

The fifth part is a false head on the lower mould plate, shown separately in Fig. A.IV.4. Throughout disassembly of the mould, this remains in contact with the armature, to ensure that the active disc face maintains its correct shape. It cannot be removed until the protective layer of resin is removed from the commutator. After the annulus has been removed, the upper plate is jacked away using the threaded hole through the centre of the lower plate. The false head is then released, and the lower plate is jacked away from this using the other four threaded holes in that plate (Figure A. IV.4, top right). The extraction is eased by applying a release agent to all interior surfaces before moulding, and by sealing all joins between parts with silicone rubber.

Figure A.IV.4. Mould parts for fan motor's armature.

Despite the evacuation of the mould cavity before pouring in the epoxy resin, considerable care has to be taken to ensure that a complete fill is achieved. The apparatus used pours the resin into four cones in the top of the mould. Figure A.IV.5 shows these in the assembled fan motor mould (right) and wheel motor mould (left). Excess resin is allowed to flow between the cones. The diameter of the holes through which the resin flows must be about 4 mm., being large enough to permit a reasonable flow rate, and also small enough not to release the conductors from their positions below. It can be seen from Figure A.IV.4 that these holes emerge in the region of the active lengths of conductors, where coil sides are held together by tapes (Figure A.IV.2). It will therefore be difficult for resin to flow to the large cavities around the end-windings, despite these being evacuated. Slots are therefore cut from the pour holes to these regions, and these are offset greatly from the radial direction so that conductors are not released from their correct locations.

Figure A.IV.5: Assembled moulds for wheel motor (left) and fan motor (right).